



**Politecnico
di Torino**

Politecnico di Torino

Corso di Laurea Magistrale in Ingegneria Aerospaziale

A. a. 2022/2023

Sessione di Laurea luglio 2023

**A fluid dynamics study
using image processing of
scallop on dissolving hard candy**

Relatori:

Stefania Scarsoglio (Politecnico di Torino)

Sander Gerard Huisman (University of Twente)

Candidato:

Giorgio Santanatoglia

Ai miei nonni

Sunt enim duo praecipua ad cognitionem rerum parandam obstacula:
pudor, qui fumum offundit animo, et metus, qui, ostenso periculo,
dehortatur ab adeundis facinoribus. At his magnifice liberat stultitia.
Pauci mortales intellegunt ad quam multas alias quoque commoditates
conducat numquam pudescere et nihil non audere.

Moriae encomium, Desiderius Erasmus Roterodamu

Abstract

The surface morphology of dissolving and/or melting bodies in a fluid is of interest in many applications.

Studies on the topic are useful not only for clarifying the physical phenomena involved, thus enabling more accurate mathematical models, or for increasing the predictability in engineering applications. But also for providing new tools in geomorphology and planetary geology to better estimate the initial fluid flow conditions that gave birth to coherent structures on the surface of underground rocks.

The surface pattern formation is strongly correlated with the forces exchanged between the fluid and the solid body. Indeed, on one hand, a body melting or dissolving in a quiescent fluid induces flows. On the other hand, the boundary layer plays a key role in the body surface erosion and in the near-wall fluid diffusion. This coupled phenomenon is referred to as *self-sculpting*.

The results of a parametric experimental study based on the dissolution of hard candy in natural convection are here proposed and commented.

The main varying parameters being considered are the inclination of the object and the salinity of the fluid. But also the convexity of the surface and the possible presence of V- or U-shaped incisions on the surface are introduced for drawing attention on and suggesting possible future research proposals.

The surface pattern formation of first flutes followed by scallops is confirmed. Thanks to image data processing, a study on the body regression rate and an investigation on the characteristic size and on vertical and horizontal wavelengths of the coherent superficial structures is conducted. The results obtained from the photos are then commented on the basis of hydrodynamic stability theory, which is introduced at the beginning of the thesis.

Final general comments on the results and the work conducted, together with suggestions for possible successive experimental works, are finally provided.

Table of Contents

Introduction and Objectives

CHAPTER 1: Multiphase flows and self-sculpting

1.1. Introduction.....	15
1.2. Stefan’s problem.....	24
1.3. An overview of hydrodynamic stability.....	29
1.4. Evidence of self-sculpting in the real world.....	37

CHAPTER 2: Current Understanding of Scalloping

2.1. Scalloping on ice.....	41
2.2. Scalloping on gypsum.....	50
2.3. Scalloping on salt.....	70
2.4. Scalloping on hard candy.....	76

CHAPTER 3: Experimental Activity

3.1. Hard candy manufacturing.....	83
3.2. Experimental set-up.....	92
3.3. Evidence of surface patterning.....	100
3.4. Lighting set-up.....	115

CHAPTER 4: Image Data Post-Processing

4.1. Side photos.....	117
4.2. Front photos.....	135

CHAPTER 5: Results and discussion

5.1. Results from side photos.....	159
5.2. Results from front photos.....	169
5.3. A possible physical mechanism behind scalloping.....	176
5.4. Scallops as a self-organizing system.....	181

Conclusion and Recommendations

Bibliography

List of Figures

Acknowledgement / Ringraziamenti

Introduction and Objectives

The present thesis aims to provide further understanding on the topic of the morphology that firstly appear and then evolve on the surface of dissolving bodies in an initially quiescent fluid.

At first glance, it may appear that research on melting and dissolving phenomena is not needed. Mainly because there is the habit that, since these phenomena happen every day, i.e., ice cubes melting in water, then they must be known for sure.

But most of the people are induced to think in this way, since they expect from the science classes attended at school that an easy and deterministic relation describes the physical system. Something like: *by increasing the difference in temperature between the solid body and the environment, the solid melts faster.*

But it will appear evident in the next chapters, that this is not so easy as it looks like...at all.

For example, just think about the same problem of a solid melting in a liquid environment, but with the possibility of changing now the salinity of the liquid and not the temperature. The solid dissolves faster?

Furthermore, it should be taken into account that most of the laws thought at schools describing melting and dissolution, like Fourier's thermal conduction law or Fick's law of diffusion, were proposed respectively in 1822 [1] and in 1855 [2]. But the theory of the boundary layer was proposed by Ludwig Prandtl only in 1904 [3].

If, for the sake of argument, boundary layer did not exist, the two mentioned theories would have provided a very clean and concise way to mathematically describe the evolution of the problem. But as will be seen, considering the existence of the boundary layer, the results are not at all those expected a priori.

Just to give a clue, when speaking of ice melting in quiescent water, most of the people would expect that the surface gets rounder and rounder, and smoother and smoother, with its volume retroceding uniformly till is completely melted. There is a similar expectation for a solute dissolving in a solvent. Instead, movement of the initially quiescent water near the wall of the solid is induced by hydrodynamic instabilities. The instability is caused in turn by the difference in temperature

(melting) or concentration (dissolving) between the liquid and the solid. Therefore, the established movement of water near the wall, strongly affects the shape of the body, but at the same time the shape of the body strongly affects the near-wall fluid dynamics. In summary, the surrounding fluid is not merely a passive agent, even if it is initially quiescent. Therefore, the surface of the solid becomes rougher and dimplier in the process. This is totally unexpected with the classical theories of thermal conduction or of solute diffusion that do not consider the existence of boundary layer; thus, neglecting the importance of the fluid in the process.

There is like a reminder to Karl Popper's analogy between (some) scientific theories and buildings built on unsecure foundations.

And recently the topic has received great renovated interest.

Potential applications of the present study could be addressed to geomorphology and planetary geology. Because a surface morphology driven by solutal convection is found in soluble rocks.

Therefore, the idea is to study the evolution of the pattern on the surface of a dissolvable body, in a controlled environment in a laboratory, to start creating a model that may in the future allow to estimate the initial fluid flow conditions that gave birth to coherent structures on the surface of underground rocks visible today. Obviously, further studies need to follow this one, in order to accomplish this ambitious goal.

Since this is an aerospace engineering master's degree thesis, the author of the present thesis dares to suggest that, if such a model is achieved one day and confirmed in geomorphology, then it might even be extended to planetary geology. Indeed, it is known that NASA is working on the project *Planetary Cave Rovers* [4] to explore planet caves. And there is even intention to use AI-guided drones (if the planet has an atmosphere, even rarefied) to do so [5], since they allow to reach, take photos and map caves, which are usually inaccessible places for rovers and which are not visible by orbiters.

The present work is organised in five chapters.

In the first chapter, a necessary introduction to the topic is provided. The chapter explains why the topic is considered within the domain of multiphase flows, what is the Stefan's problem and why it is important in the study of melting and dissolving phenomena. Follows an introduction to the hydrodynamics instabilities needed to understand why the initially quiescent fluid starts to move. Follows a brief collection of photos showing the rough and dimply surfaces mentioned before. In the second chapter, a general and exhaustive overview of the physical mechanisms behind the surface morphology on different materials is given. This is the core chapter with a rich bibliography to draw on.

In the last final three chapters, it will be given emphasis on the work, both made of experiments and of coding, carried out for six months at the *Physics of Fluids* group of the *University of Twente* by the author of the present thesis. Additional three months of post-processing followed.

To be more precise, the third chapter explains comprehensively how to repeat the experimental activity described in the thesis. The experimental activity carried out is entirely based on image processing as the principal tool for investigating the physical phenomenon. Indeed, the usual experimental techniques used in fluid dynamics, i.e., hot-wires, cannot be applied within the freezing-melting or the solute near-wall region. While PIV techniques have greater chances as PLIF to be applied in the near future.

The fourth chapter explains the two codes written to process the front and side photos taken in the experiments. The former is about a thousand lines long, while the latter is a little less than three thousand lines long.

In the last chapter, conclusions will be drawn based on the image data that were processed. Results will be commented. A physical explanation of the mechanism behind the surface patterning observed in an inclined block of hard candy is supposed and proposed. Based on the proposed mechanism, it will be explained why scalloping has the potentialities to be considered a self-organising system.

CHAPTER 1: Multiphase flows and self-sculpting

1.1 Introduction

Multiphase flows are ubiquitous in our surrounding environment.

Evidence of their presence ranges from the troposphere, where clouds dynamically evolve, to the Earth's crust, where geophysical flows transport mass and deposit sediments over long distances, as in snow avalanches and in pyroclastic flows, or well deep underground, as in groundwater flows. It is evident that many environmental multiphase flows are connected to the water cycle, which is essential to life on Earth. In addition to natural phenomena, multiphase flows are present in many key processes of the main energy industries, as in electrolysis, nuclear reactors, oil and gas industries processes. Thus, a deep understanding of the phenomena associated with multiphase flows is of great importance, if not even a necessary condition, for a better and sustainable development of our society.

It is clearly not possible to treat exhaustively the fluid dynamics and the actual and possible future applications of multiphase flows in a single document.

The present document focuses only on multiphase flows of liquid-solid mixtures associated to the dissolution or melting of a body in a fluid. In the following chapters, emphasis will be given to the study of dissolution of a body in a quiescent liquid and of the related self-sculpting phenomena, that leads to the initial formation of flutes, to their metamorphosis into scallops and to the final surface pattern. But before treating in detail the apparently easy, but in reality complex phenomenon, it is better to provide a definition of multiphase flows and of self-sculpting, and to introduce some common geometries created on the surface of a solid by self-sculpting processes and by sculpting processes driven by a forced external fluid.

A multiphase flow is any fluid flow consisting of more than one phase or component [6]. Where a *phase* is, in thermodynamics, a chemically and physically uniform or homogeneous quantity of matter [7].

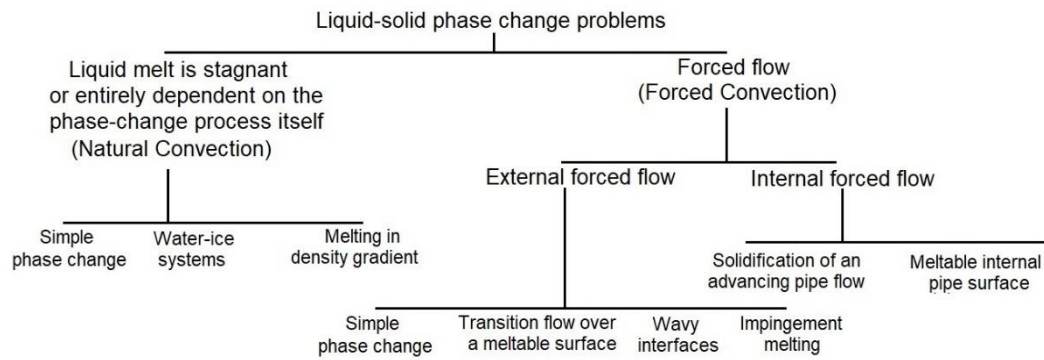


Figure 1 Possible originating interfaces in liquid-solid phase change problems.

As well introduced in [8], in a multiphase system made of a solid and a fluid, either being a liquid or a gas, similar geometries can arise from erosional effects of an external flow on the surface of an erodible solid body. And as will be thoroughly explained successively, similar geometries can arise even if the fluid is initially quiescent, but there is a presence of a temperature or concentration gradient within the considered physical system. As shown in *Fig. 1*, the similar geometries described in the paper are grouped considering the convection regime and, in case of forced convection, if the acting flow is internal or external.

It is easier for the reader to imagine the erodible solid body as a block of ice, while regarding the flow, it can be either considered as a liquid or a gas. Indeed, the final effects are the same; only the dimensions of the shaped surfaces change due to the different order of magnitude of the viscosity of the fluid.

In case of an external forced flow, a first distinction is given by the external velocity module. If the external velocity is very low and the heat conduction normal to the wall is predominant with respect to the conduction along the fluid flow, alias the Reynolds and Nusselt numbers are very low, then the problem reduces to one that primarily concentrates on the nonlinear nature of a transient phase-change process. On the other hand, if the external velocity is not negligible, the effects of erosion in shaping the surface are important. In this case, two cases are distinguished according to the direction of the external flow with respect to the normal direction of the local surface.

If the flow is directed almost parallel to the region of surface considered, it will gradually erode the surface. A greater local regression of the surface due to erosion

is expected moving downstream from the trailing edge. If the flow remains laminar, apart from an upstream region, the regression of the downstream body surface is almost constant and limited in value. The cutting surface is similar to a pinnacle.

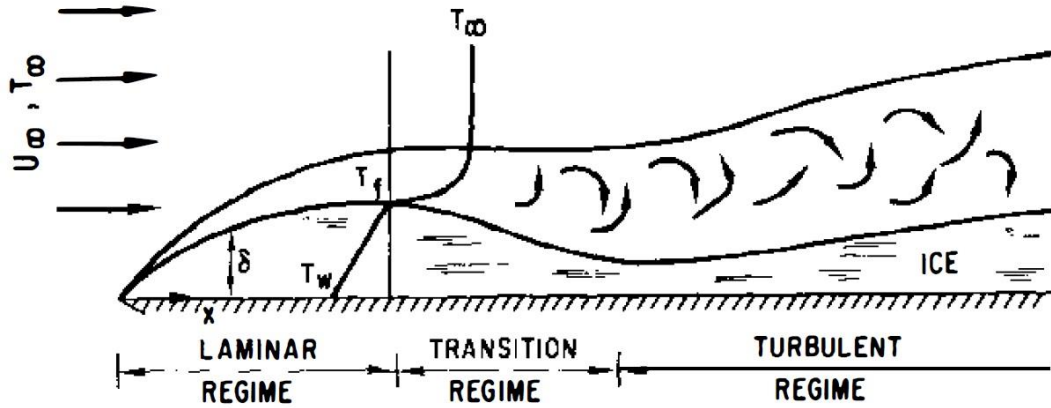


Figure 2 Steady-state ice-layer profile on a flat plate, indicating various flow regimes [3].

Instead, if the laminar flow reaches at a coordinate the critical Reynolds number, then at this transition coordinate there is a substantial increase in the heat-transfer coefficient due to turbulent mixing. This causes a marked decrease in the meltable solid thickness, which results in a region of unfavourable pressure gradient. Due to the unfavourable pressure gradient, the conductive heat transfer of the fluid drastically decreases in the formed valley. Therefore, the smooth transition results in a gradual increase in the Nusselt number, whereas the step transition results in a peak in the Nusselt number. Cheng et al. [9] also confirmed that heat-transfer rates are 1.5 to 2.5 times greater and that laminar-to-turbulent boundary-layer transition occurs at Reynolds numbers as much as an order of magnitude lower with respect to the relative parameters for a flat surface of the same material. The latter is a clear reminder of the undisputed necessity of anti-icing techniques to guarantee airworthiness in adverse cold environments associated with freezing rain conditions.

Instead, in case of a concentrated flow directed non parallelly with the local surface, there is a strong asportation of material due to the impingement. In this case the flow coherent structures within the jet mark the surface, leaving an indication of their dimensions. This is the case of warm jets impinging on a meltable solid surface. Yen & Zehnder [10] showed experimentally that the penetration rate of a free water jet into a solid block of ice is essentially constant and linearly dependent

on the bulk water temperature. Gilpin [11] highlighted that two different ablation modes exist for any given set of externally controllable parameters. In the *slow mode*, relatively larger cavities are produced with smooth rounded shapes at stagnation points, while in the *fast mode*, the cavities have smaller diameters and rough cylindrical surfaces. It is evident that the new surface morphology depends entirely on the jet flow properties and not on the properties of the fluid surrounding the jet and the solid body. There could even be vacuum in place of a surrounding fluid. Indeed, a clear example of fast ablation mode for an impinging jet on an erodible surface is offered by exhaust jets of retrorockets of landers when in proximity of a planet's surface.

An external flow directed almost parallel to the local surface, whose velocity is greater than the one associated to the case of nonlinear nature of a transient phase-change process and at the same time smaller than the one associated to the case of transition flow over a meltable surface, may generate a wavy surface geometry. Clearly, in order for wave patterns to develop, there must be a maximum in the heat-transfer rate in the trough regions between the waves and a minimum in the heat transfer rate at the crest region [8]. Furthermore, if the waves are not in static positions, then the heat-transfer rate must occur in the downstream half of the trough. Indeed, turbulence, and therefore heat transfer, are damped in regions of accelerating flow (favourable pressure gradient) and enhanced in regions of decelerating flow (adverse pressure gradient). The measured heat transfer rates for flow over a rippled surface are found to be 30 to 60 percent larger than those for flow over a flat or small-amplitude wavy surface of the same material [12].

Regarding internal flows applied to liquid-solid phase change problems, it is just worth briefly mentioning that, in the problem of solidification of an advancing-pipe flow, the freezing length increases with time [13]. Indeed, time is an independent variable of these models, since the solidifying crust thickness depends not only on the local convective heat exchange but on the time of arrival of the flow front as well.

The reason why the author added in *Fig. 1* the case of a meltable internal pipe surface is that it is similar to the case of a dissolvable internal pipe surface. The

author will motivate the possible interest in studying such a geometry in the final chapters.

Having treated briefly the possible cases related to forced convection, it is now worth providing a definition of self-sculpting and discussing the geometries shaped in the natural convection regime.

Self-sculpting [14] can be defined as the phenomenon of solid boundary's time-evolution due to the interaction between the solid being sculpted and the flow which had been induced by gradients created by the presence of the same solid.

The definition is at first abstruse. So, a description of the main phases in time of the long-lasting phenomenon is here provided. Basically, a solid body is immersed in a quiescent fluid. It is either supposed that the solid body is soluble in the surrounding fluid or that the temperature of the surrounding fluid is higher than the melting point of the solid body. The two conditions may even apply at the same time, as happens for ice in salty water. In the former case there is a non-null concentration gradient while in the latter case there is a non-null temperature gradient. If the two conditions are superimposed, obviously the two aforementioned gradients are both non-null. The gradients are higher getting closer to the surface of the solid body. At the same time the gradients decrease while getting further from the body surface and are null for positions farther than a critical distance, as shown in *Fig. 3*. Even only one non-null gradient is a sufficient condition to induce a flow. The flow is induced in order to reach the minimum energy state of the system, alias the equilibrium of the system, by increasing the entropy of the overall closed system, alias the number of different possible combinations of Boltzmann microstates. The latter means that, in order to reach the biggest number of combinations of Boltzmann microstates, the molecules initially within each separated phase (which is a homogeneous system) must disperse into a single heterogeneous system (made of the first two phases, thus multiphase) where they have a higher number of possibilities to interact chaotically. The induced flow by the gradient(s) acts on the solid body in the same way of an external forced flow on a solid body, as previously treated. With the main and big difference that the surface geometries being sculpted are unique with respect to the ones associated with an external forced flow, because the effects become in turn the

causes. Indeed, in case of a geometry being sculpted by an external flow, the sculpting phenomenon is mainly forced from the outside. In case of a self-sculpting geometry, the external flow has been initially induced by (the different properties of) the body, through a non-homogeneous and non-null gradient.

The induced flow in turns affect the melting and/or dissolution process at the local surface of the body, with two main effects: a modification in time of the thermal and/or concentration gradient and of the solid boundary. The perturbed gradient together with the evolved solid boundary affect the near-wall flow. In turn, the near-wall flow affects now differently the gradient(s) and the solid boundary, modifying them with a different perturbation. The cycle starts again. It is good to keep in mind that the perturbations of each cycle are not said to be constant. Indeed, the time-evolution of the process, and thus the mathematical model describing it, as will be further explained in the following chapter, is non-linear.

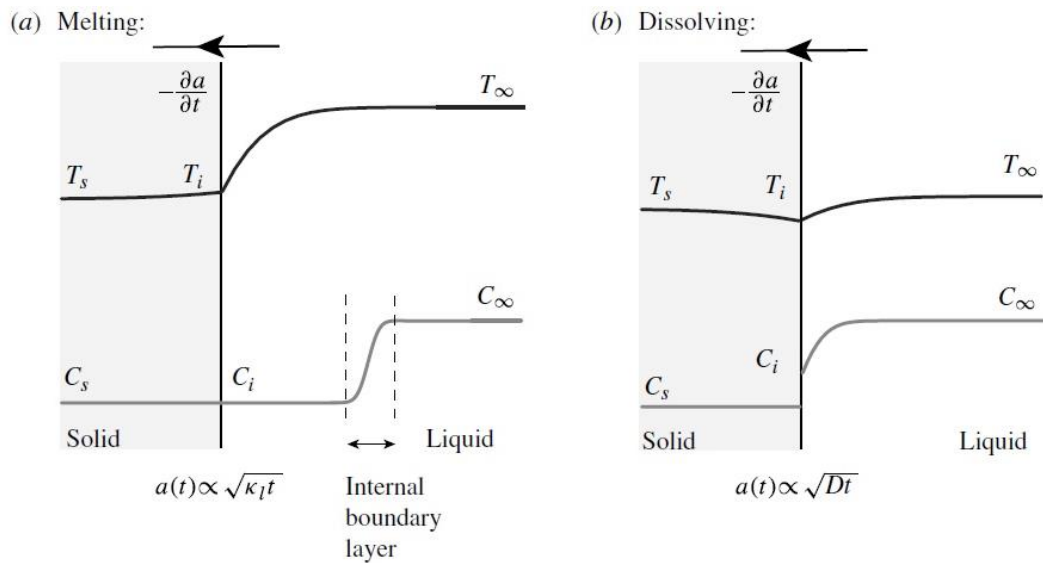


Figure 3 Temperature and concentration gradients in the case of melting and of dissolving [15].

Fig. 3 illustrates schematically the distribution of temperature and concentration in the near-wall domain. It is worth noting that, to guarantee the best possible generalization in the discussion of the melting and dissolving problems, both temperature and concentration gradients are taken into account simultaneously. Anyways, in the absence of convection, the rate of ablation is controlled exclusively by thermal diffusion for melting and solutal diffusion for dissolving.

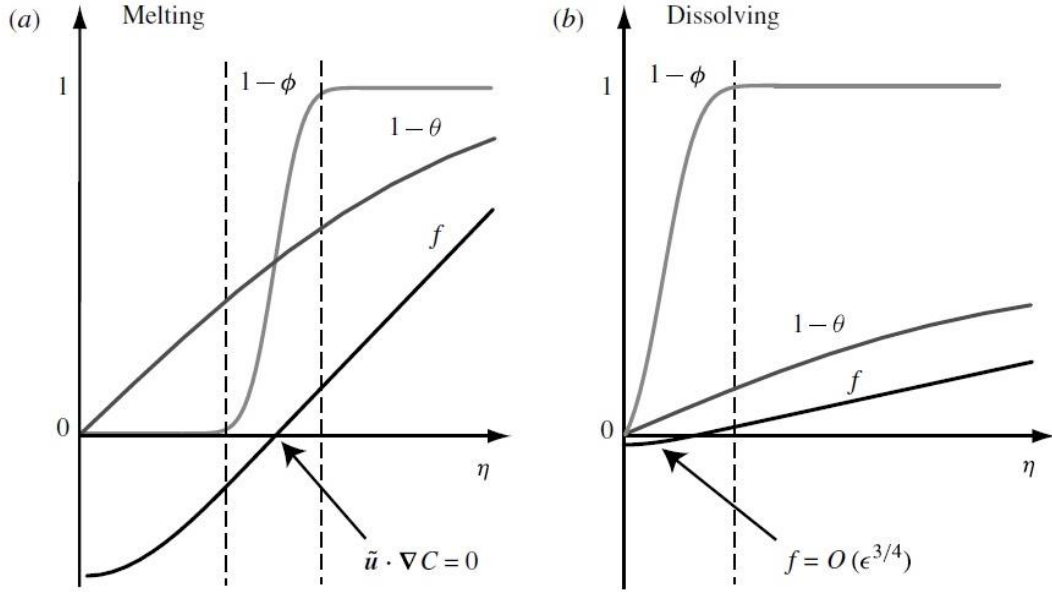


Figure 4 Near-wall temperature, concentration and streamfunction profiles for large Le [15].

Fig. 4 shows the case of large Lewis number (Le), which is equal to the ratio of thermal diffusivity to mass diffusivity. In the melting case, large solutal gradients are confined to a thin diffusive boundary layer, where the advective transport $f \rightarrow 0$ yields a broad fresh layer close to the interface. While in the dissolving case the solute gradient ϕ is large and f is small close to the interface.

Conservation of heat across the solid-liquid interface is expressed by the Stefan condition, as quantitatively explained in the next paragraph:

$$\rho_s l_f \frac{\partial \alpha}{\partial t} = \rho_s c_s \kappa_s \left. \frac{\partial T}{\partial y} \right|_{y=a^-} - \rho_l c_l \kappa_l \left. \frac{\partial T}{\partial y} \right|_{y=a^+} \quad [1]$$

Where l_f is the latent heat of fusion and ρ_j, c_j, κ_j are the density, heat capacity and thermal diffusivity of the solid ($j=s$) and the liquid ($j=l$) phases.

On the other hand, conservation of solute across the interface is expressed by:

$$\rho_s (C_i - C_s) \frac{\partial \alpha}{\partial t} = -\rho_l D \left. \frac{\partial C}{\partial y} \right|_{y=a^+} \quad [2]$$

Where D is the solutal diffusivity.

The two conditions allow either the heat flux or the salt flux to control the rate of change $\dot{\alpha} = \partial \alpha / \partial t$.

In the self-sculpting phenomenon two governing and contrasting processes can be observed at the same time: *natural insulation* and *natural mixing*. As the terms suggest, the former is responsible for a reduction in the gradient, thus in the local surface regression rate, while the latter is responsible for an enhancement of the gradient, thus an increase in the local surface regression rate.

A more detailed explanation of the corresponding regions of natural insulation and natural mixing on a self-sculpting body will be given after the introductory chapters.

Anyways, to conclude the dissertation on the possible self-shaped geometries in natural convection, some of the main parameters to take into account which differentiate the fluid dynamics, thus the body-fluid interaction with the following possibility of modifying the final geometry are here provided.

A major variable which is possible to play with in experiments and computational models is the relative body-fluid density, which decides the vertical direction of the problem. This determines the side of the body where dissolutional self-sculpting is expected: the side where the net surface, between the weight force and the buoyancy force, points outward the body.

The local relative density between the melt/dissolution layer and the fresh water plays a key role both in water-ice systems and in systems driven by vigorous compositional convection, which were already illustrated in *Fig. 1*.

In the case of water-ice systems, varying the salinity of water, it is possible to indirectly vary the water density while keeping its temperature constant. This is what happens in multiphase systems driven by vigorous compositional convection, when a strong difference in density is obtained. For ice-water system, though, this density difference can happen more easily, since the freezing point and the maximum density of pure water are respectively 0°C and at 4°C, thus the temperature window is very narrow. So, a small increase in the water temperature or a modification of its salinity can cause different vertical directions of the problem and corresponding different surface geometries.

On the other hand, when the solid and the liquid are of different materials, the melting/dissolving solid produces a sharp density interface, with a correlated sharp gradient, that may provide the controlling mechanism for natural-convective

movement of the melt/concentration layer and the liquid adjacent to the solid surface. By varying the local relative densities of the melt/concentration layer and of the fresh water, it is possible to play on the direction of the melt/concentration layer induced by the compositional convection, but the efforts are bigger with respect to the ice-water systems. For some solid bodies of a given certain material, it may even be necessary the use of liquids made most of alcohol or directly the use of olive oil. Anyways, since the mechanism is the same for ice-water systems, or for systems where the compositional convection is enhanced on purpose, a single explanation will be offered in paragraph 2.1 and not before the introduction of some hydrodynamic instabilities of interest in paragraph 1.3.

The present paragraph is concluded with a legitimate question that the reader may now arise: why the term “self-sculpted phenomena” is referred to phenomena where the body finally dissolves/melts entirely? Indeed, when referring to sculptures, most of us involuntarily think about also monuments or decorative friezes. All artistic works known for lasting in time, even under the action of atmospheric agents. Obviously when speaking of a solid volume being sculpted, we would refer to a still existing solid volume. The answer relies on the fact that, even if in all the experiments that will be illustrated in the following paragraphs, the solid body is finally completely dissolved/melted, in the real world the effects of self-sculpting are still visible in the present day. It is like stopping the experiment or the computational analysis at a general instant of the final stage. The “final stage”, as will be clarified in the following chapters, is an interval in which the self-sculpting phenomenon has reached a characteristic length scale, thus the forms being sculpted, if considered statistically, are quite homogeneous and do not vary their size no more in time. Many of the visible effects of self-sculpting in the real world are shown in paragraph 1.4.

1.2 Stefan's problem

Stefan's problem is intrinsically associated with the study of multiphase flows.

In its classical formulation, it describes the time-evolution of an initial free boundary between two phases of a material undergoing a phase change [16]. It was formulated by Jožef Štefan around 1890 [17].

For an exhaustive demonstration of formulation of the problem and for non-classical formulations applied to problems involving more than two phases, the author invites to read other references which treat the topic specifically. A suggested recent book covering the life of the scientist while providing a chronicle on his discovery is [18].

Most of the information provided in the rest of the paragraph are taken mainly from [19] and [20]. It is firstly provided an introductory explanation of the mathematical formulation in 1D of Stefan's problem applied to a solid melting in a liquid of the same material in a cylindrical volume, as firstly formulated by Štefan in [17].

Let's consider at an initial time $t = t_0$ a spatial domain \mathfrak{A} divided by a planar interface \mathfrak{D} , at initial surface position $s(t = 0) = s_0$ into two subdomains:

$\mathfrak{A}_1 = \mathfrak{A} \cap \{x < s_0\}$ filled with water and $\mathfrak{A}_2 = \mathfrak{A} \cap \{x > s_0\}$ filled with ice. It is assumed that the temperature is a function of the spatial coordinate only, $T(x)$. The position of the interface at a generic instant t is denoted by $s(t)$ and the interface is hypotised to remain planar.

An initial free boundary value problem between two phases of the same material undergoing a phase change is described by a parabolic set of partial differential equation (PDE). Since a portion of the boundary is a priori unknown, the free boundary, two boundary conditions must be prescribed on it, instead of only one, to obtain a well posed problem.

When a change of phase takes place, a latent heat is either absorbed (melting) or released (solidification). The heat is said to be *latent*, or hidden, because in phase changes, energy enters or leaves the system without causing a temperature change in the system.

The first boundary condition, applied to all the boundary of the body, is based on the assumption that temperature is continuous in the spatial domain, thus the temperature at the outer body surface $s(t)^+$ is the same as the temperature at the inner body surface $s(t)^-$ at all instants:

$$T(s^+(t), t) = T(s^-(t), t) = T_0, \forall t \quad [3]$$

Let's consider a generic portion of the interface with area \mathcal{S} . Since the solid is melting, the interface is advancing in time into the space domain previously occupied by the solid phase. Thus, at a later time $t_1 > t_0$, the interface occupies a position $s(t_1) > s(t_0) = s_0$. It is assumed that there is no heat source or sink in the domain \mathfrak{A} . The heat Q required to melt the melted volume $\mathcal{S} \times (s(t_1) - s(t_0))$ is:

$$Q = \mathcal{S} \times (s(t_1) - s(t_0)) \times \rho l_f \quad [4]$$

Where l_f is the specific latent heat of fusion and ρ is the density of the material.

While the heat flux through the interface between the two phases can be quantified thanks to Fourier's law:

$$\Phi_Q^\pm = -K^\pm \times DT^\pm(s^\pm(t)) \quad [5]$$

The superscript \pm is to differentiate between the upper (+) and the lower (-) side of the surface at the considered time. Where K is the conductivity of the material: K^- for the liquid and K^+ for the solid. By energy conservation, it is natural to assume that Eq. 5 is equal to Eq. 4 in the time interval $I_t = [t_0, t_1]$, when the latter is integrated on the volume of the solid body in I_t . Thus, it is possible to write:

$$\begin{aligned} \mathcal{S} \int_{t_0}^{t_1} \left[-K^- \frac{\partial T^-}{\partial x}(s^-(t), t) + K^+ \frac{\partial T^+}{\partial x}(s^+(t), t) \right] dt \\ = \int_{t_0}^{t_1} \int_{\mathfrak{D}} [-K^- DT^-(s^-(t), t) \cdot \hat{\mathbf{x}} - K^+ DT^+(s^+(t), t) \cdot \hat{\mathbf{x}}] d\mathfrak{D} dt \end{aligned} \quad [6]$$

Dividing both members by \mathcal{S} and comparing such modified second member with Eq. 4, then Eq. 6 can be rewritten as:

$$\int_{t_0}^{t_1} \left[-K^- \frac{\partial T^-}{\partial x}(s^-(t), t) + K^+ \frac{\partial T^+}{\partial x}(s^+(t), t) \right] dt = (s(t_1) - s(t_0)) \rho l_f \quad [7]$$

Dividing both members by $(t_1 - t_0)$ and taking the limit $t_1 \rightarrow t_0$, Eq. 7 ends up with

$$\lim_{t_1 \rightarrow t_0} \frac{1}{t_1 - t_0} \int_{t_0}^{t_1} \left[-K^- \frac{\partial T^-}{\partial x}(s^-(t), t) + K^+ \frac{\partial T^+}{\partial x}(s^+(t), t) \right] dt = \rho l_f \lim_{t_1 \rightarrow t_0} \frac{s(t_1) - s(t_0)}{t_1 - t_0} \quad [8]$$

By applying the *Intermediate Value Theorem*, the *Extreme Value Theorem* and the *Mean-Value Theorem for integrals*, it is possible to rewrite Eq. 8 as:

$$\rho l_f \dot{s}(t_1) = \lim_{t_1 \rightarrow t_0} \frac{1}{t_1 - t_0} \times (t_1 - t_0) \times \left[-K^- \frac{\partial T}{\partial x}(s^-(\tau), \tau) + K^+ \frac{\partial T}{\partial x}(s^+(\tau), \tau) \right] \quad [9]$$

Where τ is a generic instant of the interval I_t , thus $\tau \in [t_0, t_1]$.

But since $t_0 \rightarrow t_1$ and the function $\mathfrak{S}(\tau) = \left[-K^- \frac{\partial T}{\partial x}(s^-(\tau), \tau) + K^+ \frac{\partial T}{\partial x}(s^+(\tau), \tau) \right]$ is continuous, thus $T \in C^1$, then given any instant $t \in I_t$, Eq. 9 is rewritten as:

$$\rho l_f \dot{s}(t) = K^+ \frac{\partial T}{\partial x}(s^+(t), t) - K^- \frac{\partial T}{\partial x}(s^-(t), t) \quad [10]$$

The partial derivatives in the spatial domain can be rewritten with the spatial domain variable in subscript position, while Newton's derivative formulation is left to highlight that this derivation is done in the time domain.

$$\rho l_f \dot{s}(t) = K^+ T_x(s^+(t), t) - K^- T_x(s^-(t), t) \quad [11]$$

Eq. 11 is called the *Štefan's condition* and is the second boundary condition, which must be applied just on the free boundary in order to obtain a well posed problem.

The classical 1D Štefan's problem represents a semi-infinite solid occupying position $0 \leq x \leq \infty$ at the solidification temperature T_f (the subscript standing for freezing). An assumption needed is that any volume change in the solidification should be ignored. Furthermore, since at the fixed boundary of the solid phase

$x = 0$ there could be many different flux functions depending on the temperature value, it is assumed that the temperature in the solid phase is being constant. This is not other than a Cauchy boundary condition. Thus, the problem is to find the temperature distribution in the liquid phase and the location of the free boundary $s(t)$. It is worth remarking that even if two phases are present, the said problem is called *classical one-dimensional one-phase Štefan's problem* since it is only the liquid phase which is unknown. Such problem is described by the following set of PDE and conditions in the two sub-domains and in the free boundary.

Liquid region \mathfrak{A}_1 $0 \leq x < s(t)$	$\frac{\partial T}{\partial t} = \frac{K}{C\rho} \frac{\partial^2 T}{\partial x^2} = \alpha \frac{\partial^2 T}{\partial x^2}$	Heat equation valid in $0 < x < s(t), \forall t > 0$
	$T(0, t) = f(t)$	Cauchy's boundary condition $\forall t > 0$
	$T(x, 0) = T_f$	Initial condition
Free-boundary $x = s(t)$	$\rho l_f \frac{ds}{dt} = -K \frac{\partial T}{\partial x}$	Štefan's condition
	$s(0) = 0$	Initial position of the melting interface
	$T(s(t), t) = 0$	Dirichlet's condition at the interface: freezing temperature
Solid region \mathfrak{A}_2 $s(t) < x < \infty$	$T(x, t) = T_f$	$\forall t, x \geq s(t)$

Table 1 PDE and conditions describing the two sub-domains and the free interface of the classical one-dimensional one-phase Štefan's problem.

The author strongly suggests reading [21], where the application of a computational model to similar physical phenomena treated in the present work is shown and where the previously demonstrated problem is introduced in dimensionless form, being described by the following set of equations.

$$\left\{ \begin{array}{l} \frac{\partial c}{\partial t} = \Delta c, \text{ in } \Omega_{liquid} \\ c = c_m, \text{ on } \Gamma(t') \\ V_n = \beta \frac{\partial c}{\partial t}, \text{ on } \Gamma(t') \\ c(x, 0) = c_0, \text{ in } \Omega_{liquid} \end{array} \right. \quad [12]$$

Where $t' = t/K$ is the rescaled time on the conductivity of the material, and

$c = (T - T_m)/\Delta T$, is the rescaled temperature with $\Delta T = \max_{t=0}(|T - T_m|)$ and T_m the melting point of the solid, V_n is the normal boundary velocity at the interface, β is the Stefan number. The Stefan number controls the dynamics of the dimensionless system.

It is not offered here a demonstration of the Štefan problem applied to a solid object of material A dissolving in a liquid of material B. But it is worth noting that the previous model is also able to describe the dissolution process. In this case the temperature field is replaced by the concentration field $\mathbb{C} \in [0,1]$. The parameter space for melting, solidification and dissolution is listed below, as in [21].

Process	β	Range of c_0	c_m
Melting	$-c_p\Delta T/l_f$	$[-1,0]$	0
Solidification	$-c_p\Delta T/l_f$	$[0,1]$	0
Dissolution	ρ/ρ_s	$[0,1]$	1

Table 2 Parameter space of the model described in [21].

Where for the dissolution process, ρ, ρ_s are respectively the liquid and the solid densities, while for the melting and solidification processes, c_p, l_f are respectively the specific heat and the latent heat of fusion (freezing) in case the process considered is melting (solidification). The subscript is the same since the latent heat of fusion is equal to the latent heat of freezing, only the direction of heat exchanged between the two phases changes.

1.3 An overview of hydrodynamic stability

In the present paragraph, the hydrodynamic instabilities useful for explaining the phenomena studied experimentally are presented. Those are the Kelvin-Helmholtz, the Rayleigh-Taylor, the Rayleigh-Bénard and the “solutal Rayleigh-Bénard instabilities”.

The Kelvin-Helmholtz theory is explained in the present paragraph thanks to the theoretical support provided by [22] [23].

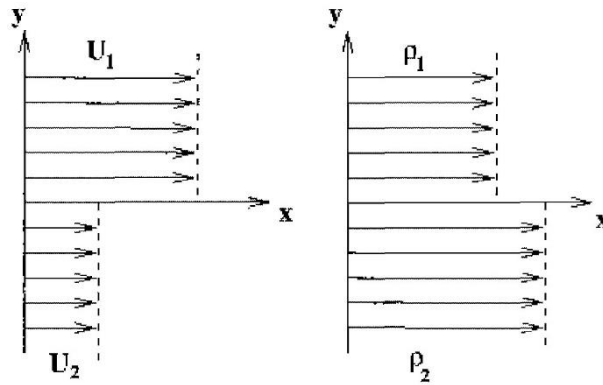


Figure 5 Sketch of a piecewise constant approximation to a shear layer. Fig. 2.2 in [22].

Two incompressible inviscid fluids in horizontal parallel infinite streams along the x direction of different velocities and densities with one stream above the other are considered. The upper fluid is numbered as 1 and the lower fluid is numbered as 2. The boundary between the two streams is supposed planar and at the vertical coordinate $y = 0$. The basic flow is completely described by velocity, density, pressure.

$U(y)$	$\rho(y)$	$p(y)$	
$U_1 \mathbf{i}$	ρ_1	$p_0 - g\rho_1 y$	$\forall y > 0$
$U_2 \mathbf{i}$	ρ_2	$p_0 - g\rho_2 y$	$\forall y < 0$

Table 3 Variation of the quantities describing the basic flow along the vertical axis.

The physical mechanism has been described by Batchelor [22] [24] in terms of the vorticity dynamics. Batchelor considered $U_2 = -V, U_1 = V$, with $V > 0$ and that

$\rho_2 = \rho_1$. In this way, the special case of a vortex sheet in a homogeneous fluid is being considered, as shown in *Fig 6*.

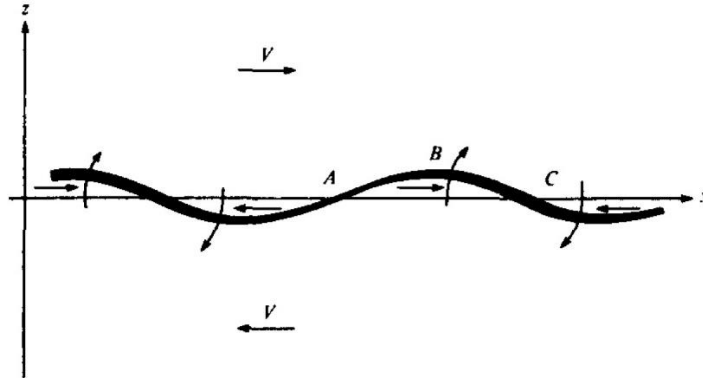


Figure 6 Growth of a sinusoidal disturbance of a vortex sheet with vorticity. Fig. 7.1.3 in [24].

Each vortex line induces a rotating flow with circulation equal to the strength of the vortex line. But at the same time, each vortex line has the fundamental property of being carried due to entrainment by the fluid. Thus, the vorticity $\frac{\partial u}{\partial y} - \frac{\partial v}{\partial x}$ of the vortex sheet is positive for $V > 0$. So positive vorticity is swept away from points like A and towards points like C because vorticity in parts of the sheet displaced downwards (or upwards) induces a velocity with a positive or (negative) x -component at any part of the sheet where $y > 0$ (or $y < 0$). The induced velocity at points like B due to each part of the displaced vortex sheet has positive x -component. Thus, the positive velocity accumulates at points like C and induces velocities concordant in $y > 0$ around such points thereby amplifying the sinusoidal displacement of the vortex sheet. These processes of accumulation of vorticity at points like C and of rotation of neighbouring points of the sheet will continue together, leading to exponential growth of the disturbance without change of the form of the disturbance, so long as the disturbance is small enough not to significantly change the flow basic state.

In addition to the physical mechanism, are here directly provided the formulas that allow to quantify the modes or the eigenvalues of the Kelvin-Helmholtz instability starting from the properties of the two flows.

Introducing $\alpha = \alpha_r + i\alpha_i$, the dimensionless wavenumber of instability along the x -direction, and $c = c_r + ic_i$, the wave velocity of the disturbance, it is possible to

define the dimensionless frequency of the disturbance as $\omega = \omega_r + i\omega_i$, where $\omega_r = \alpha_r c_r - \alpha_i c_i$ and $\omega_i = \alpha_r c_i + \alpha_i c_r$.

The dispersion relation formula for ω is:

$$\omega = \alpha \left\{ \frac{\rho_1 U_1 + \rho_2 U_2}{\rho_1 + \rho_2} \pm i \sqrt{\frac{\rho_1 \rho_2 (U_2 - U_1)^2}{(\rho_1 + \rho_2)^2}} \right\} \quad [13]$$

Which is a linear function of α . This means that the shorter the wave is, the faster it grows, although there is no fastest growing wave. Furthermore, since one root of the imaginary part of ω is positive for $U_1 \neq U_2$, the shear flow is always temporally unstable in an inviscid fluid and even if $\rho_1 = \rho_2$. This is the crucial point of the present introduction on the Kelvin-Helmholtz instability, which is at the origin of the Kelvin-Helmholtz waves.

To introduce the Rayleigh-Taylor instability, it is worth rewriting *Eq. 13* of [22] with the nomenclature used in [23]:

$$s = -ik \frac{\rho_1 U_1 + \rho_2 U_2}{\rho_1 + \rho_2} \pm \left[\frac{k^2 \rho_1 \rho_2 (U_1 - U_2)}{(\rho_1 + \rho_2)^2} - \frac{\tilde{k} g (\rho_1 - \rho_2)}{\rho_1 + \rho_2} \right]^{1/2} \quad [14]$$

Eq. 13 is of greater practical interest, but *Eq. 14* is more useful for theoretical considerations. Let's neglect the different additional quantities \tilde{k} , which is the total wavenumber, and s , which are the two perturbed fluid system modes. *Eq. 14* allows to extend the reasoning initiated with the flow shown in *Fig. 5*, assuming that there can be *internal* gravity waves in the flow.

Indeed, if the basic flow is at rest $U_1 = U_2 = 0$, *Eq. 14* becomes:

$$s = \pm \left[\tilde{k} g (\rho_2 - \rho_1) / (\rho_1 + \rho_2) \right]^{1/2} \quad [15]$$

There is instability if and only if $\rho_1 < \rho_2$, that is, the heavier fluid rests above the lighter fluid. Otherwise, if $\rho_1 > \rho_2$, then there is stability. Rayleigh recognised the influence of gravity on stratified flows, but was only Taylor to expand the model as in *Eq. 16*, recognising the importance of general accelerations other than gravity.

$$s = \pm \left[\tilde{k} g^* (\rho_2 - \rho_1) / (\rho_1 + \rho_2) \right]^{1/2} \quad [16]$$

Where g^* is the net vertical acceleration of the system.

Considering two non-viscous fluids at rest not satisfying the Rayleigh-Taylor stability condition ($\rho_1 > \rho_2$), they develop in time in order to reach a stable

Rayleigh-Taylor condition. To do so, small perturbations at the interface are generated. Basically, the boundary surface separating the two flows ripples. The physical mechanism is based on the baroclinic torque created by the misalignment of the pressure and density gradients at the perturbed interface. [25]

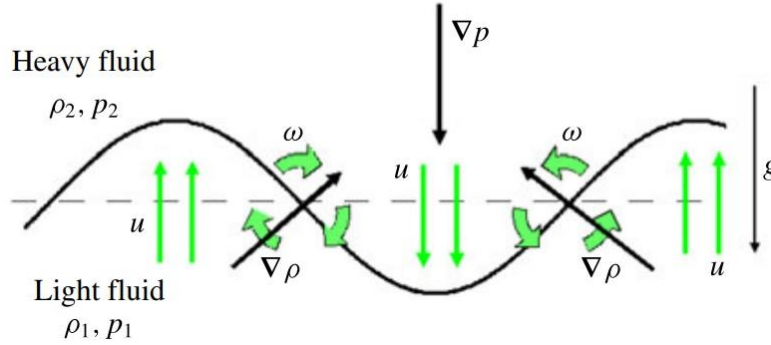


Figure 7 Visualization of the vectors acting in a Rayleigh-Taylor instability [20].

The magnitude of the baroclinic torque can be calculated from the inviscid vorticity equation:

$$\frac{D\omega}{Dt} = \frac{1}{\rho^2} \nabla\rho \times \nabla p \quad [17]$$

As shown in *Fig. 7*, for a given unstable configuration there is a specific harmonic component of the initial perturbation, for which the torque on the interface creates vorticity that will tend to increase the misalignment on the gradient vectors. This, in turn, creates additional vorticity, thus leading to further misalignment. Therefore, the physical system made of the two fluids evolves till a Rayleigh-Taylor stable condition is reached. In the stable configuration, the vorticity, and thus the induced velocity field, is in a direction that decreases the misalignment and therefore stabilizes the system. For example, this happens in response to *surface* gravity waves. This last example is useful to understand how the Rayleigh-Taylor instability and the Kelvin-Helmholtz instability are in some phenomena strongly related to each other.

Before passing to the discussion about the Rayleigh-Bénard instability, it is worth providing here some results shown in [26] regarding the Rayleigh-Taylor instability in fluid layers under an inclined plane. In this peculiar study, the flow is found to be linearly temporally unstable for strictly positive values of the inclination angle α of the plane.

The most unstable modes were calculated to be:

$$k_{max} = \frac{1}{l_c \sqrt{2}} \sqrt{\sin \alpha} \quad [18]$$

With a corresponding maximum wavelength:

$$\lambda_{max} = \frac{2\pi\sqrt{2}l_c}{\sqrt{\sin \alpha}} \quad [19]$$

Where l_c is the capillary length of the problem and is defined as:

$$l_c = \sqrt{\gamma/\rho g} \quad [20]$$

If $\alpha = \pi/2$, which corresponds with the notation used in [26] to a surface perfectly horizontal, *Eq. 19* degenerates in the canonical Rayleigh-Taylor instability $\lambda_{max}|_{\alpha=\pi/2} = 2\pi\sqrt{2}l_c$. According to Brun et al., concluding from *Eq. 19* that the critical angle that prevents the instability to form is $\alpha_{crit} = 0$ is just a crude interpretation that does not take the absolute-convective transition into account. Basically, a flow is said to be *convectively unstable* if the amplified perturbations move away from the source or *absolutely unstable* when the amplified perturbations invade the entire flow. In Brun et al.'s work, the critical value of inclination yielding absolute-convective transition is α^* and is calculated from the equality:

$$\sqrt{\sin \alpha^*} \tan \alpha^* = \frac{3l_c}{\tilde{u}^* h_i} \quad [21]$$

α^* is thus found to be an implicit expression decreasing with the ratio h_i/l_c , such that only surface tension and gravity effects influence the problem through the capillary length. Indeed, the fluid viscosity is considered to not affect the absolute-convective transition, because it intervenes linearly both in the flow rate and in the droplet formation time, such that its contribution cancels out when considering the relative contribution. In *Eq. 21*, $\tilde{u}^* = \frac{1}{\sqrt{27}} \sqrt{34 + 14\sqrt{7}}$ while h_i is the initial thin fluid film thickness.

In summary, the study published in [26] shows that the flow under an inclined plane is always linearly temporally unstable, unless $\alpha = 0$ thus the plane is perfectly vertical, and two instability cases are always possible for $\alpha \neq 0$: convective or absolute instability. In the first case, perturbations are found to decrease as they are

carried away by advection, despite the unstable nature of the flow. In the second case, the instability is strongly enough to overcome the flow.

It is now the right time to introduce an instability related to thermal convection within a fluid: the Rayleigh-Bénard (RB) instability.

This instability arises when a fluid is heated from below. Since a warmer volume of fluid is also denser, it may look at first obvious that the dynamics of the system would evolve as an inverted Rayleigh-Taylor instability. Not at all. The instability develops in a characteristic and coordinated movement of flow, through the manifestation of Rayleigh-Bénard cells. Those cells are convective rolls that cover entirely the region of the fluid domain which is experiencing a temperature gradient and each cell is counter-rotating with respect to the adjacent ones. The force that drives the convective flow is the buoyancy of the heated layer, whose magnitude is related to the difference in temperature between the top and bottom layers. The complexity of the problem becomes apparent when one recognizes that the temperature distribution is greatly altered by the convective flow itself, whose aim is to carry as much heat from the bottom of the layer to the top. In other words, the force that drives the flow is subject to modification by the flow [27]. Furthermore, it can be said that the system, by generating a much more efficient energy transport through convection, tends to resist the external perturbation and tries to return back to the equilibrium state. For the last two reasons, the formation of RB cells in nonequilibrium thermodynamics is considered as a self-organizing system [28].

However, as pointed out by Rayleigh's analysis, it is worth remembering that RB cells do not form every time there is a temperature difference in a fluid surrounded by a warmer bottom and cooler top layer, as in the mathematical model proposed by Bénard. Because viscous drag and heat diffusion contrast the birth and growth of RB cells. Indeed, if the former is equal to the buoyant force, there can be no motion, and at the same time the latter tends to dissipate the temperature gradient that drives the convective flow. Thus, the gravitational potential energy liberated by the sinking of denser fluid and the rising of lighter fluid must be greater than the energy dissipated by drag and diffusion in order to ensure the onset of a convective flow. The relation of these effects can be expressed as a dimensionless ratio: the

buoyant force divided by the product of the viscous drag and the rate of heat diffusion. Convection begins when this dimensionless number, called Rayleigh's number, exceeds a critical value specific for the considered physical system.

$$Ra = \frac{g\beta\Delta TL^3}{\alpha\nu} \quad [22]$$

Where it is here recalled that: g is the acceleration due to gravity, β is the thermal expansion coefficient, $\Delta T = (T_s - T_\infty)$ is the difference between the surface temperature (corresponding to the warm layer in the previous discussion) and the quiescent temperature (corresponding to the cold layer in the previous discussion and in real problems to the temperature of the fluid in the far field with respect to the heat source), L is the characteristic length of the problem, α is the thermal diffusivity, ν is the kinematic viscosity.

The Rayleigh-Bénard instability was introduced mainly to clarify what is referred in some papers [29] [30] as *solutal* Rayleigh-Bénard instability. The author underlines that neither Rayleigh nor Bénard applied their theory to model the induced convection caused by a concentration gradient in a fluid. Furthermore, to the author's knowledge, there is not an actual agreement among the international scientific community on the use of the term and even little is found when searching for mentions from different and independent research groups on this instability. Therefore, an alternative explanation to the one proposed in [30] of the phenomena related to the self-sculpting on the downward face of an inclined block of hard candy is provided in paragraph 5.3, using only the other aforementioned instabilities. It is not correct to read the previous lines as a critic to the authors or the work discussed in the papers which mention this instability; it is not the author's intention to do so.

Anyways, the main reason for listing this instability in the present paragraph is because the experimental work presented in the present thesis is mostly based right on the work carried on in [30]. So, it is necessary for the comprehension of the following chapters to understand at least what is meant with solutal Rayleigh-Bénard instability.

In a few words, the solutal RB instability is a modified RB instability driven by a concentration gradient instead of a temperature gradient. As clarified in *Fig. 45*, some authors use the terminology of solutal RB instability to refer to a cellular structure, organised on the dissolving surface, which is made of a repeated geometry of peaks delimitating valleys. The peaks act as detaching points for the dissolving plumes, while in the valleys the solute is collected and transported by the solutal liquid layer towards the adjacent plumes. *Fig. 45* clearly shows that the regression rate is higher in the valleys than in the peaks, due to the higher concentration gradient. Even if the velocity is higher, and thus a greater erosion, could have been at first expected close to the peaks, this is not apparently the main contribution to the phenomenon.

The solutal Rayleigh number associated to the solutal RB convection is written as:

$$Ra = \frac{\Delta\rho g \delta^3}{D\eta_f} \quad [23]$$

Where $\Delta\rho$ is the apparent density of the fluid in the solutal film, g is the acceleration due to gravity, δ is the characteristic length of the problem which is represented here by the thickness of the destabilising film, D is the diffusion coefficient, η_f is the mean viscosity inside the film. It is evident that the variables $\Delta\rho, \delta, \eta_f$ are referred to the *film*, which is the solutal liquid layer surrounding the diffusing solid object and separating the diffusing solid object from the liquid solvent.

1.4 Evidence of self-sculpting in the real world

As explained in the first paragraph, self-sculpting processes are mainly associated to solid bodies melting and/or dissolving in a liquid in natural convection.

Notable examples of self-sculptures in nature are icebergs melting in the ocean and dissoluble rocks under the exogenous process of chemical weathering. As will be explained in the next chapter, the most common dissoluble rocks are salt (halite), gypsum and limestone. The chemical weathering process can happen in the underground or in the aboveground environment. Examples of mineralogical underground self-sculptures are scallops and flutes in karst environment, while examples of mineralogical aboveground self-sculptures are so called pinnacle and tower karsts. While in the self-sculpting process of underground rocks, water may be in contact for very long period with the rocks' surface, due to the presence of underground aquifers, in the same process happening aboveground, water may even be cyclically deposited on the rock surface due to atmospheric agents, i.e. rain, haze, snow. For a broader and extensive dissertation on geological sculpting and on karst geomorphology, the author suggests respectively [31], especially the 6th chapter, and [32].

Some photos of notable effects of self-sculpting in nature are proposed in the present paragraph. The photos are coupled with an image describing the relative fluid dynamics involved in the self-sculpting process.

Since sculpting due to externally forced flows was mentioned in the first paragraph, it is good to mention at least some evidences of these natural processes.

Aeolian processes land-form characteristic shapes as dunes, ripples on the surface of a dune, barchanoid ridges and even more. Similarly, fluvial deposition and erosion sculpt riverbeds [33], leaving prints with coherent length scales [34].

Recently, even the morphology of meteorites left by the ablation due to the atmosphere entry was studied [35]. In conclusion, even if this type of shapes is not the object of the present study, it is worth mentioning its existence for suggesting eventual future experimental studies, using a wind or water tunnel, of the sculpting geometries and their characteristic length scales.



Figure 8 Scalloped iceberg near Paulet Island, Antarctica. © Phillip Colla.

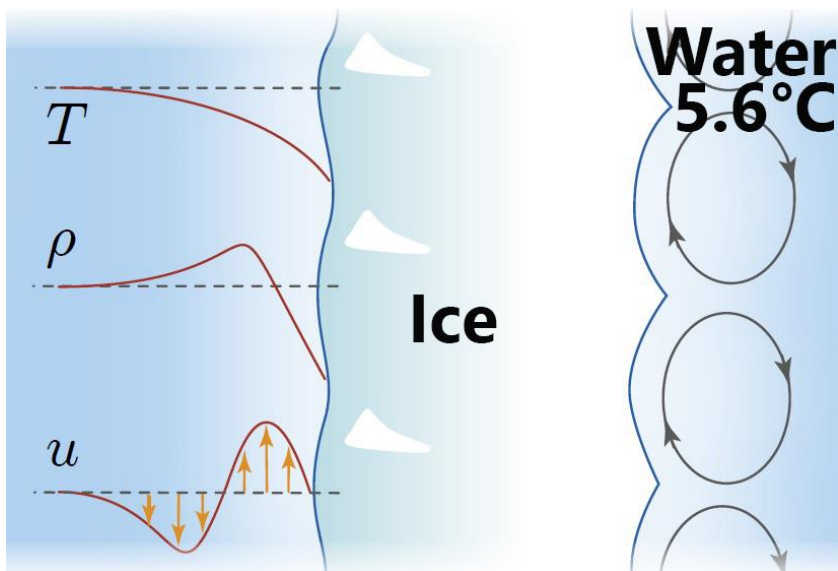


Figure 9 Model of ice scallop due to vigorous compositional convection.



Figure 10 Pinnacle karsts in the Tsingy de Bemaraha National Park, Madagascar. © Arthus Bertrand.



Figure 11 Tower karsts in Guilin, Guangxi province, China. © VCG Photo.

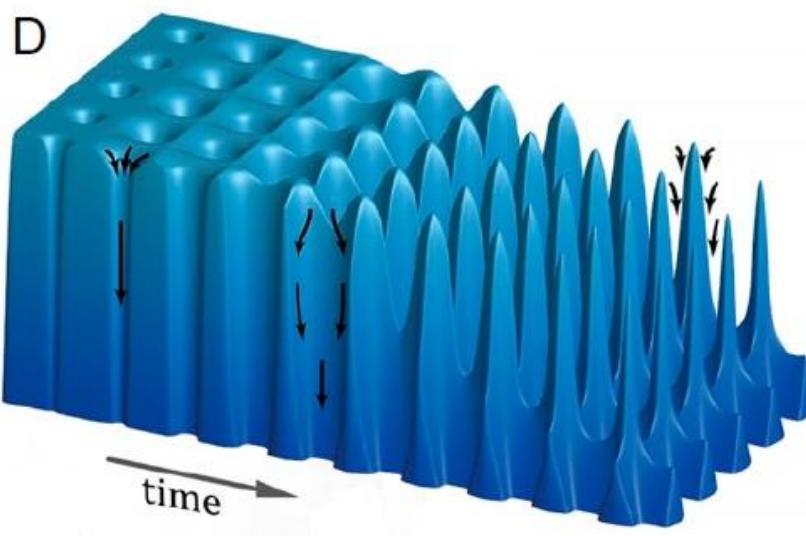


Figure 12 Bed-of-nails morphology from dissolution of an initial porous media. [31]



Figure 13 Speleogens in a cave in Borneo. [32] © Dave Bunnell.



Figure 14 Sala degli Scallops (transl. “The room of scallops”), Grotta della Lupa, Majella, Italy.



Figure 15 Another image of smaller speleogens.

CHAPTER 2: Current Understanding of Scalping

2.1 Scalping on ice

Glaciers and ice melting is one of the actual grand challenges in environmental fluid dynamics [38].

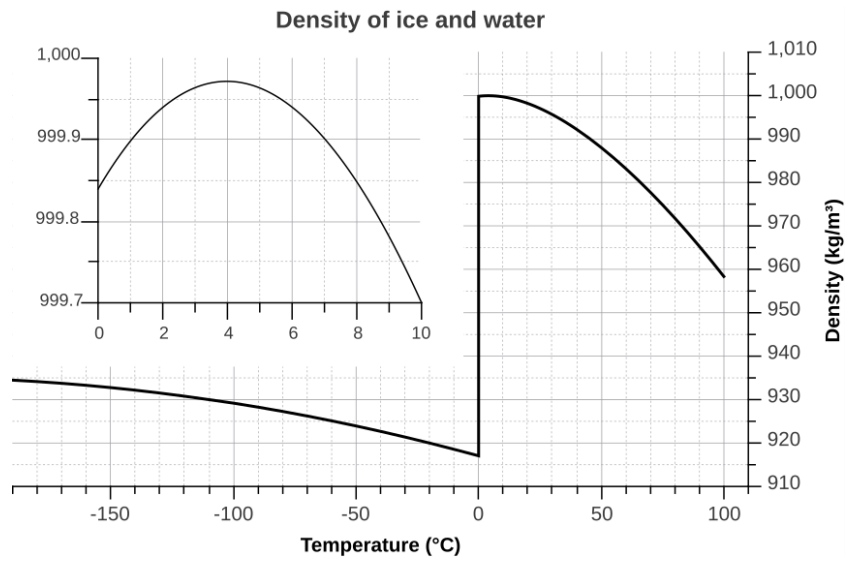


Figure 16 Graph of $\rho_{H_2O}(T)$. [34]

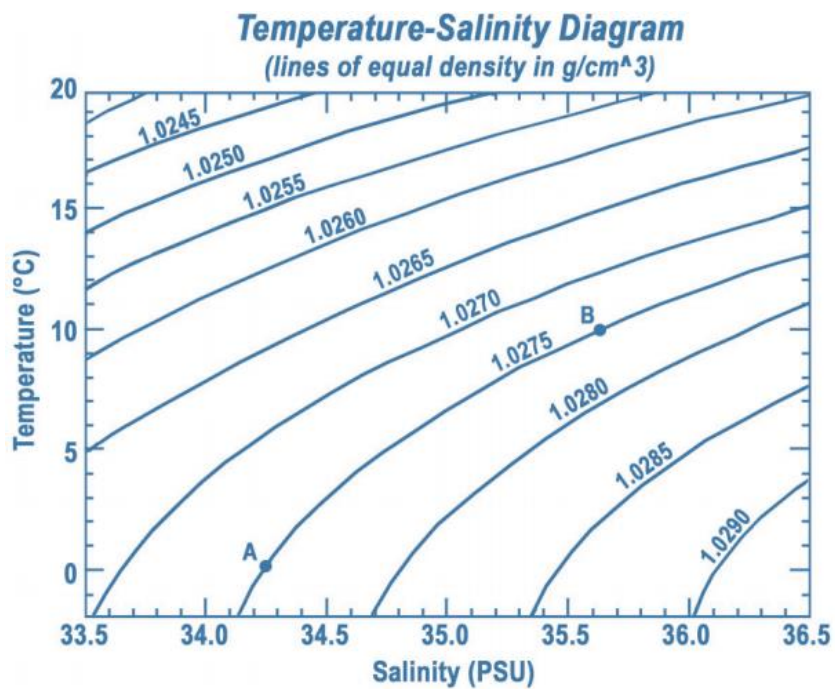


Figure 17 Temperature-salinity diagram of H_2O .

Melting or freezing of water at temperatures near 4°C is peculiar. This is not because of a strong interaction between convection and phase change. Instead, it is due to the fact that thermal convection in water near its freezing point is distinguished from more common convective systems, since the density of water is not linearly dependant on temperature, as shown in *Fig. 16*, but attains a maximum value at about 4°C [8]. An empirical law for calculating seawater density based on the values of its salinity and temperature is provided in [40].

Therefore, as already anticipated in the first paragraph, for ice-water systems, a small increase in the water temperature or a modification of its salinity, as shown in *Fig. 18*, can cause different vertical directions of the problem and corresponding different surface geometries.

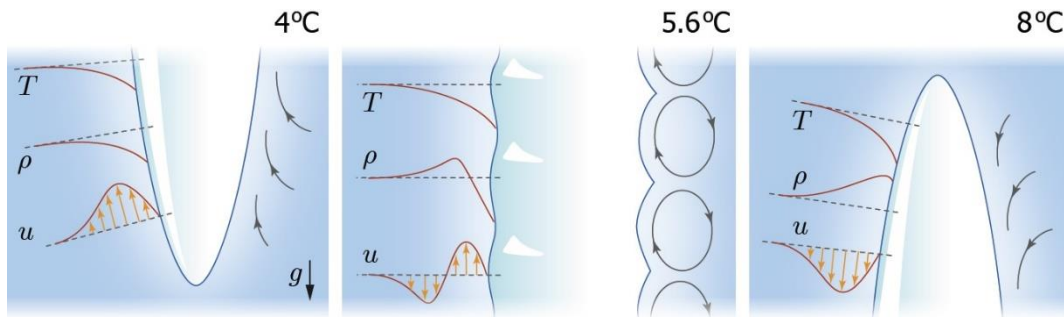


Figure 18 Possible ice surface melting patterns driven by a buoyancy gradient.

A lighter melt layer is directed upward if fresh water is at 4°C, while is denser and thus directed downward if fresh water is at a temperature greater or equal than 8°C. If the temperature of fresh water has an intermediate value, the shear flow originated at the interface of the two vertically layered fluid, the lighter melt layer which is closer to the ice surface and the denser fresh water, generates a Kelvin-Helmholtz instability, sculpting the surface with characteristic scallops.

Furthermore, also the local inclination of the considered body surface is a strong variable of the problem. Therefore, considering a symmetric body, the behaviour on the surface pointing downward is different with respect to the behaviour of the surface pointing upward. A confirmation of this different behaviour is given in [41] [42], where it is noticed that the upper surface of an ice plate at the bottom of an aquarium becomes pitted, while the lower of a fixed ice plate in contact with the

water meniscus remains smooth. The former case is referred to as *melting from above*, while the latter case is referred to as *melting from below* in [42].

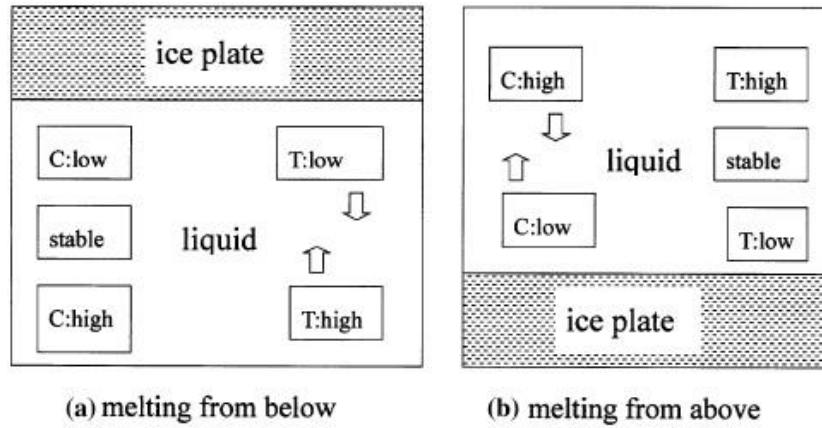


Figure 19 Sketch of the melting from below (a) and melting from above (b) configurations [42].

Basically, the distributions of temperature and of concentration cause stable and unstable conditions, respectively, in the liquid melt for the melting from above. Indeed, the predominance of the buoyancy resulting from the concentration distribution produces a vigorous convection. A pattern made of convective cells, similar to the one associated to the RB instability, develops, sculpting the initial flat surface into a pitted surface made of a small scale “mountain and valley” structure, as shown in Fig. 20. The structure has a width of approximately 1 mm [42]. Kerr [41] confirms a typical width of the pits of 1-2 mm.

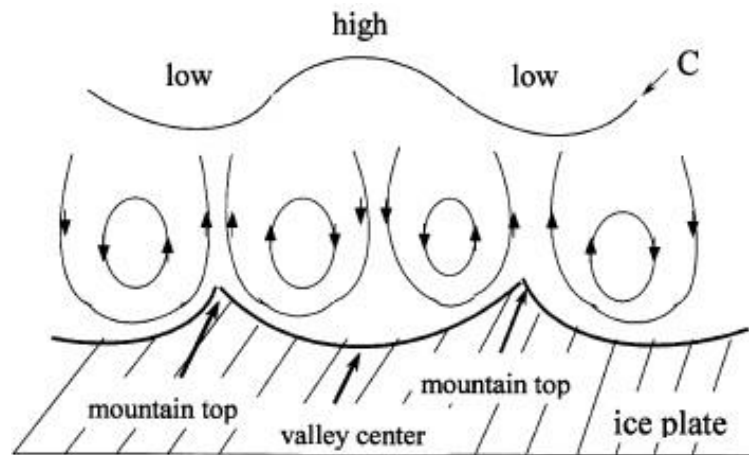


Figure 20 Sketch of convective cells and relative streamlines in the near-wall region of the “mountain and valley” structure. [37]

A vigorous upward flow is seen just above each “mountain top”, while a weak downward flow appears in proximity of the “valley center”. Upward and downward

flow velocities are respectively measured to be about 0.7 mm/s and 0.4 mm/s at the 20th minute since the start of the experiment [42]. A pair of small circulations develop between upward and downward flow. The small circulating vortices allow the entrainment of purer water in the concave region. Therefore, the concentration gradient is highest in the valley center. Once these vortices are established, they sum their diffusion-caused acceleration to the buoyancy acceleration. The superposition of these two accelerations is constructive. Therefore, these typical flows will considerably promote the melting of the ice plate to be 30% larger as compared to the numerically predicted results assuming a flat melting front, and also by three times larger compared with the results for melting from below and two times larger as compared to a vertical ice plate melting [42]. An increase in the melting rate on the same self-sculpting surface is confirmed also by Kerr [41], who measured a melting velocity at the top of the cavities about two and a half times greater than the melting velocity of the otherwise-flat interface. Kerr proposes a formula for calculating the overall regression velocity in such conditions:

$$V \sim \left(\frac{g(\rho_f - \rho_m)\kappa_f^2}{P\mu_m\mathcal{S}^4} \right)^{1/3} \left(1 + \frac{k_f}{k_m\mathcal{S}} \right)^{-1} \quad [24]$$

Where V is the overall melting velocity of the surface, μ_m is the dynamic viscosity of the melt, ρ_j, k_j are respectively the density and the thermal conductivity of the fluid ($j = f$) and of the melt ($j = m$), κ_f is the thermal diffusivity of the fluid, P is a dimensionless number defined on the ratio of the dynamic viscosity of the fluid to the dynamic viscosity of the melt, \mathcal{S} is the Stefan number. P is empirically calculated as:

$$P = \sqrt[3]{324} \left(\frac{\mu_f}{\mu_m} \right)^{2/3} \quad [25]$$

And the Stefan number for this problem is defined as:

$$\mathcal{S} = \frac{\rho_s L_s + \rho_s c_s (T_m - T_s)}{\rho_f c_f (T_f - T_m)} \quad [26]$$

Where L_s is the latent heat of the solid, c_j is the specific heat of the solid ($j = s$) and of the fluid ($j = f$), T_m, T_s, T_f are respectively the temperatures in the melt, in the solid and in the fluid.

Eq. 24 can be simplified to the following equation in case $\mathcal{S} \gg k_f/k_m$:

$$V \sim \left(\frac{g(\rho_f - \rho_m)k_f^2}{P\mu_m\mathcal{S}^4} \right)^{1/3} \quad [27]$$

The case $\mathcal{S} \gg k_f/k_m$ is equivalent to $h_T \gg (h_mk_f)/k_m$, where h_T, h_m are respectively the fluid and the melt layer thicknesses, which can be calculated as:

$$h_T \sim \left(\frac{P\mu_mk_f^2}{gV(\rho_f - \rho_m)} \right)^{1/4} \quad [28]$$

$$h_m \sim \left(\frac{PV\mu_m}{g(\rho_f - \rho_m)} \right)^{1/2} \quad [29]$$

Obviously, to calculate V , Eq. 24 or Eq. 27 is needed, with the former being more general than the latter but requiring κ_m . It is clear that in order to apply Eq. 27, the condition $\mathcal{S} \gg k_f/k_m$ or the condition $h_T \gg (h_mk_f)/k_m$ needs to be satisfied with the latter condition requiring V . They are basically the same condition defined on different parameters. In case the reader wants to use the secondly defined condition, the impasse is resolved using Eq. 27 to calculate V to calculate in turn h_T, h_m . Only now the second condition is tested: if verified, the assumption made on the use of Eq. 27 was correct, otherwise Eq. 24 needs to be used. Generally, for ice-water systems the condition is satisfied.

Kerr's work is useful not only for providing a formula to quantitatively estimate the overall regression rate of the melting solid-liquid system, but especially for introducing a dimensionless number that determines if the vigorous compositional convection can occur in the system. Specifically, in order to have vigorous compositional convection, the unstable compositional buoyancy of the melt needs to be always much greater than the stabilizing thermal buoyancy due to the heat that must be removed from the fluid to produce this melt. Thus, the ratio \mathfrak{R} of the buoyancies needs to satisfy the following condition, for a horizontal ice floor:

$$\mathfrak{R} := \frac{\rho_f - \rho_m}{\alpha(\rho_s L_s + \rho_s c_s (T_m - T_s))/c_f} \gtrsim 2.0 \quad [30]$$

Where α is the coefficient of thermal expansion.

Kerr suggests that the critical ratio \mathfrak{R}_c should depend also on the viscosity ratio μ_f/μ_m , expecting higher \mathfrak{R}_c for unequal viscosities, since the viscous coupling between the melt and fluid should then be reduced.

It is worth mentioning that Kerr conducted also experiments on a sloping ice floor and noticed two different convective regimes depending on a new critical ratio $\mathfrak{R}_c = 2.7$. It was found that if $\mathfrak{R} > \mathfrak{R}_c$, then the ice surface is cusped, otherwise the ice surface consists of a series of parallel grooves running down the slope. The critical ratio referred to the case of the sloping ice floor is higher than the one referred to the case of the horizontal ice floor, suggesting that the mixing efficiency of the compositional convection is hindered by the downslope flow in the thermal boundary layer. It is therefore anticipated that \mathfrak{R}_c is a monotonically increasing function of the slope of the floor [41].

So, comparisons of experiments made with different viscosities and additional experiments investigating the influence of the floor angle may further help in quantitatively refining Kerr's model.

Thus, it is evident that despite the existence of many studies on pressure-driven and shear flows, the possibility for topography to emerge between a horizontal melt or dissolving layer and a solid phase is not well understood. At least compared with the case of topography generation by RB convection.

In addition to topographies generated by buoyancy-driven layered flows, the aforementioned horizontal boundary layer can even be strongly affected by shear, such as under ice shelves. In the latter, the flow has high Re_* , St , Pr .

Higher Pr results in thinner thermal boundary layers, which could impact the near-wall dynamics, and higher St results in slower melt rates, which could significantly change how interface patterns couple with transient flow features. Two prominent studies conducted by Couston et al. [43] and by Claudin et al. [44] attempt to model the topography generated by this type of flow.

The key findings of [43] are a confirmation that streamwise topographical features emerge from uneven melting and freezing at a phase boundary also when the flow is driven by a pressure gradient and that the type of density stratification affects the characteristic amplitude and spanwise wavelength of the streamwise patterns. Furthermore, the mentioned paper computationally demonstrates that the crest-to-trough amplitude is of the same order as the viscous sublayer thickness for stable and neutral buoyancy-driven stratification and that it extends beyond the buffer

layer and into the log layer for unstable stratification. This spatial ratio, combined with a separation of scales between the topography lifetime and the diffusion time scale across the solid layer, suggests that the interface evolution is purely driven by the flow dynamics for stable stratification. While it is suggested an interplay between interface evolution and the fixed-temperature condition at the solid wall for neutral stratification and it is suggested an interface's amplitude saturation forced by the solid wall condition.

Claudin et al. [44] notice that the dissolution instability at the origin of the pattern is associated with an anomaly, and therefore an instability, at the transition from a laminar to turbulent hydrodynamic response with respect to bed elevation. Thus, suggesting a possible mechanism for the selection of the pattern amplitude.

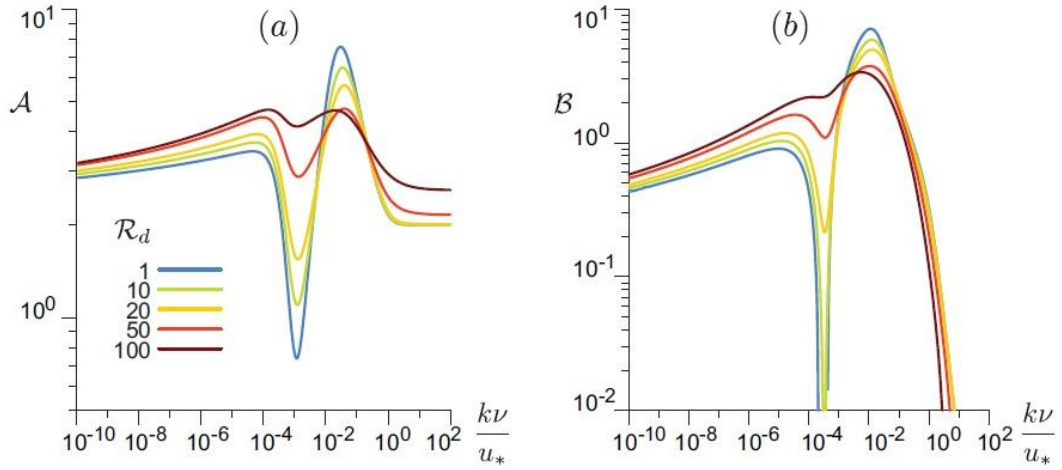


Figure 21 In-phase \mathcal{A} and in-quadrature \mathcal{B} shear stress components as a function of the wave number kv/u_* [44].

The novelty of the study is, by an investigation of a sinusoidally perturbed surface, that the coefficients encoding the in-phase and in-quadrature components of the sinusoidal bed modulation, which influence the basal shear stress, are found to be strongly dependant on the bed-roughness-based Reynolds number $Re_d = du_*/\nu$. In Fig. 21, the region associated to small wavenumbers $kv/u_* \lesssim 10^{-4}$ corresponds to the turbulent regime, while the region associated to wavenumbers $kv/u_* \gtrsim 10^{-2}$ corresponds to the laminar regime. It is clear that the region between the mentioned two corresponds to the laminar-turbulent transition regime.

In order to present the final results of the mentioned study, it is necessary to define a diffusion coefficient \mathcal{D}_t proportional to the turbulent viscosity:

$$\mathcal{D}_t := \frac{\ell^2 |\dot{\gamma}|}{\beta_t} + \frac{\nu}{\beta_v} \quad [31]$$

Where $\beta_t, \beta_v, \ell, |\dot{\gamma}|$ are respectively the turbulent and viscous Schmidt numbers, a van Driest-like mixing length and the strain rate modulus.

Therefore, for a constant \mathcal{D}_t corresponding to the laminar regime, the peak effect visible in *Fig. 21* increases the flux and thus the erosion at the crests of the sinusoidal solid surface. This is a stabilising situation. On the other hand, when turbulence is dominant, \mathcal{D}_t is not constant due to turbulent mixing. For corresponding small wavenumbers, turbulence is enhanced slightly-up stream of the crests of the sinusoidal solid surface, and hence there is stabilising erosion again.

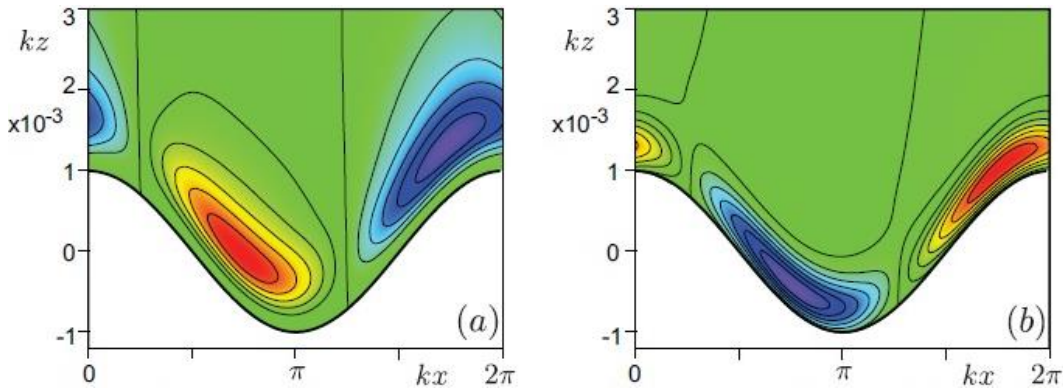


Figure 22 Isocontours of the diffusion coefficient (case a) and of the concentration (case b) within the fluid above a sinusoidally modulated bed (in white). Red (blue) regions correspond to a strong (weak) modulus [44].

Fig. 22 illustrates the stabilising effect associated to turbulence: strong mixing leads to a large vertical flux (case *a*) which reduces the concentration (case *b*).

An amplifying destabilising situation is found only for laminar-turbulent transition, since turbulence is shifted downstream by means of the adverse pressure gradient, enhancing mixing and thus erosion in the throughs. Hence explained how only the development of the instability increases the bed roughness, thus suggesting how the pattern eventually selects nonlinearly the wavenumber kv/u_* .

It is worth concluding the present paragraph briefly introducing the known effects of ice melting in a mixture. This can be extended to ice shelves melting, since between ice and oceanic water there is a salinity gradient.

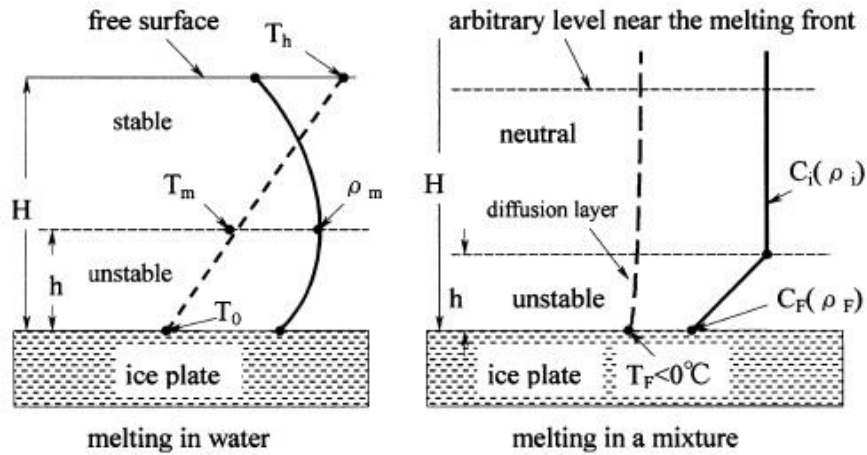


Figure 23 Stability of the density/concentration distribution in the region close to the ice surface. Sketches related to melting in water (on the left) and melting in a mixture (on the right) [42].

Sugawara et al. [42] confirm experimentally a different density/concentration distribution in the region close to the ice surface, as shown in Fig. 23. In the case of ice melting in water, the liquid region above the 4°C line is stable as seen from the density distribution. While in the case of ice melting in a mixture (made of 20 wt.% of CaCl_2), the mixture above the diffusion layer is neutral due to the uniform concentration/density.

Furthermore, ice blocks melting into a salinity gradient are expected to become vertically layered [45] [46], thus influencing the final shape.

Layering in sheared double-diffusive convection Rayleigh-Bénard is expected when the temperature field destabilises ($T_{bottom} > T_{top}$) while the salinity field stabilises ($S_{bottom} > S_{top}$) the flow [47].

2.2 Scalloping on gypsum

As anticipated in the final paragraph of the previous chapter, the most common dissolvable rocks are salt (halite), gypsum and limestone. It is good to discuss separately the experiments done to study scalloping on gypsum, since the experimental activity is done in water tunnel and thus in a forced convection regime. While the experimental studies on scalloping on salt are similar to the ones related to scalloping on hard candy, since they are performed in a natural convection regime.

Respectively, halite is a mineral made of $NaCl$, gypsum is a soft sulfate mineral of calcium sulfate dihydrate with chemical formula $CaSO_4 \cdot 2H_2O$, while limestone is a carbonate rock composed mostly of the minerals calcite and aragonite, which are both crystal forms of $CaCO_3$.

Mineral	Dissolution reaction	Solubility ($mg L^{-1}$)	Common range of abundance in waters ($mg L^{-1}$)
Gibbsite	$Al(OH)_3 + H_2O \rightarrow 2Al^{3+} + 6OH^-$	0.001	Trace
Quartz	$SiO_2 + H_2O \rightarrow H_4SiO_4$	12	1–12
Amorphous silica	$SiO_2 + H_2O \rightarrow H_4SiO_4$	120	1–65
Calcite	$CaCO_3 + H_2O + CO_2 \leftrightarrow Ca^{2+} + 2HCO_3^-$	60*, 400 [†]	10–350
Dolomite	$CaMg(CO_3)_2 + 2H_2O + 2CO_2 \leftrightarrow Ca^{2+} + Mg^{2+} + 4HCO_3^-$	50*, 300 [†]	10–300
Gypsum	$CaSO_4 \cdot 2H_2O \rightarrow Ca^{2+} + SO_4^{2-} + 2H_2O$	2400	0–1500
Sylvite	$KCl + H_2O \rightarrow K^+ + Cl^- + H^+ + OH^-$	264 000	0–10 000
Mirabilite	$NaSO_4 \cdot 10H_2O + H_2O \rightarrow Na^+ + SO_4^{2-} + H^+ + OH^-$	280 000	0–10 000
Halite	$NaCl + H_2O \rightarrow Na^+ + Cl^- + H^+ + OH^-$	360 000	0–10 000

* $P_{CO_2} = 10^{-3}$ bar.
[†] $P_{CO_2} = 10^{-1}$ bar.

Figure 24 Dissociation reactions and solubilities of some representative minerals that dissolve congruently in water at 25°C and 1 bar pressure [32].

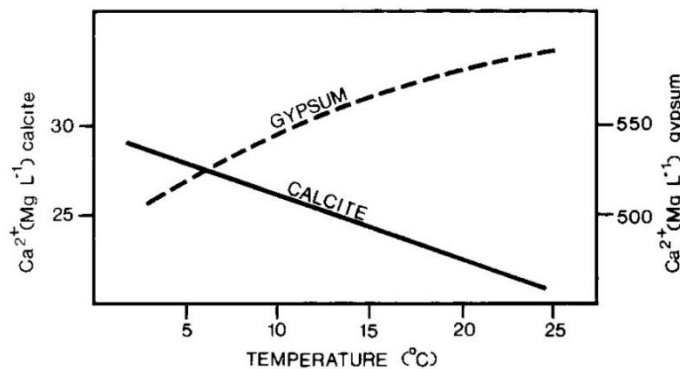


Figure 25 The solubility of calcite and gypsum in water at the standard atmosphere in the temperature interval ranging from 2°C to 25°C [32].

Patterns left on limestone surfaces were first remarked by Lugeon in 1915 [48]. With the only exception of Maxson [49], who in 1940 was the first to coin the word *flute* to indicate a *long, continuous grooves of concave cross-section* found on surface-rivers beds, and Bretz [50], who in 1942 was the first to suggest the use of cave patterns to *determine the direction of a cave stream flow*, only right after the Second World War interest on the topic exploded. Similar patterns started being observed also on the surface of ice caves [51] [52], thus suggesting that the phenomenon was not only associated to rocks. One of the most important contributions was historically made by Coleman [53], who in 1949 was the first to suggest the term *scallop* to indicate *a series of interrupted concavities*. The term replaced the misleading word *cup*, which had already been introduced by Bretz [50]. The aforementioned author's contribution was of interest also because they went further: Maxson remarked the possibility that scallops may *fix the position of vortices supplied by the turbulent flow*, even though without providing a physical explanation, while Bretz and Coleman suggested a possible *self-stabilizing interaction of vortices and scallops*. A second dark period for remarkable contributions followed. Only at the start of the '60s, the initial problem on the origin of cave patterns, which was mainly debated among geologists and speleologists, regained attention with a more systematic research approach based on the use of water tunnels. For nearly twenty years, erosion of gypsum by a forced external water current was extensively studied in order to try to provide a possible answer to some geomorphological questions still open. The major contributions were made independently by Curl [54] [55] and Allen [56] [57] [58]. They were representatives of two different theories regarding the origin of patterns: Curl supported the passive-bed theory, while Allen supported the defect theory.

As outlined in [59], the *passive-bed theory* of erosion marks postulates that the characteristics of the erosion marks are entirely determined by the dynamic properties of the fluid in contact with the surface, while the *defect theory* assumes that the position of each erosion mark is due to the initial presence of an irregularity or a defect at the surface. The latter also assumes an independent evolution for each mark and an increase of length and amplitude with time up to a limit set by the initial spacing of defects.

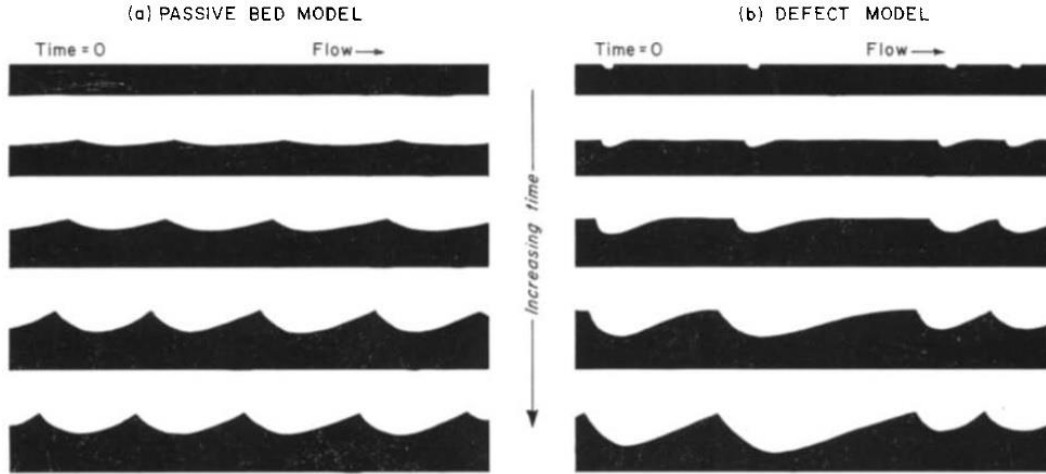


Figure 26 Changes of bed geometry with time according to the passive-bed theory (case a) and to the defect model (case b) [58].

In [54], Curl studies the mass transfer profile of a fixed flute pattern machined into Perspex when immersed in a forced water flow. Two viewpoints are highlighted in the study: the evolution in time of dimensionless parameters describing the pattern dimensions and the determination of stability conditions for the pattern geometry. The dimensionless analysis proposed is based entirely on averaged quantities and on stationary and homogeneous values, the latter due to the fixed and homogeneous pattern considered. So, the reader should keep in mind that the averaging sign is omitted in all the variables shown in the following formulas just to make the text more readable. By introducing the *stable flute period* \mathcal{L} , the diffusivity of the solute ions in the water \mathcal{D} , the width of the water channel H , and ρ, μ referred to the forced fluid, by dimensional analysis is found that:

$$N_f^* := \frac{\rho UL}{\mu} = f\left(\frac{\mathcal{L}}{H}, \frac{\mu}{\mathcal{D}\rho}\right) \quad [32]$$

Where $Sc = \mu/(\mathcal{D}\rho)$ is the Schmidt number, which controls the relative thickness of the mass and moment transfer boundary layers.

It is now evident, looking at the first ratio, that the dimensional analysis leads to the Reynolds number, as expected. But in [54] it is given a different name to this ratio: N_f^* , the *stable flute Reynolds number*. The author of the present thesis personally disagrees on renaming a corroborated and important physical dimensionless number so easily. But it must be said that there is a reason after all. Indeed, in Reynolds's notable pipe experiment [60], the Reynolds number is calculated for a given geometry (length scale) based on the density and the dynamic viscosity of the

flow considering, usually, the flow velocity as the variable input; thus it describes and allows to predict the fluid flow behaviour. While in Curl's study, the density and dynamic viscosity of the flow are given too, but in this case N_f^* is fixed and the aim is to find the relationship $L = f(U)|_{\rho, \mu, N_f^*}$. So, in addition to directly considering the usual outcome of the Reynolds number as a fixed parameter, also the main characteristic potential of describing the flow behaviour with the dimensional ratio is completely lost. Curl suggests a stable flute Reynolds number $N_f^* \approx 22500$. Therefore, *Eq. 32* states that the averaged flute period, is inversely proportional to the average flow velocity and thus that the averaged flute period depends on the flow properties.

In order to study a possible stable vertical height, Curl applies a dimensional analysis on the parameters acting in the perpendicular direction of the mean surface:

$$\frac{\rho y U}{\mu} = f\left(\frac{x}{L}, \frac{UH}{\mu}, \frac{\mu}{D\rho}\right) \quad [33]$$

Curl speculates that *Eq. 33* should not depend on Re_U and on Sc . The reasoning behind the first hypothesis is driven by the fact that, in presence of a highly disturbed flow region near a fluted surface, the flow disturbance produced by other surfaces of the channel is of less importance, except to the extent that other surfaces determine the average flow velocity in the region of the surface upon which the surface forms. Therefore, as long as L/H is small, *Eq. 33* should not depend on the Reynolds number calculated with the average velocity of the overall flow. The reasoning behind the second hypothesis is driven by the fact that, the Schmidt number, should not be important when it is large and the concentration boundary layer is extremely thin.

By applying the two aforementioned hypotheses, *Eq. 33* reduces to a dependence:

$$\frac{y}{L} = \frac{1}{N_f^*} f\left(\frac{x}{L}\right) \quad [34]$$

Eq. 34 allows to conclude that all stable flute profiles must be geometrically similar. Curl passes then to the analysis of the rate of solution of the pattern, doing a dimensional analysis of the average mass transfer coefficient \bar{k} over a full flute period, finding that:

$$\frac{\bar{k}L}{D} = f\left(\frac{L}{H}, \frac{\mu}{D\rho}, \frac{\rho UL}{\mu}\right) \quad [35]$$

The ratio \mathcal{L}/H is omitted because very small and *Eq. 35* is simply rewritten as:

$$\frac{k\mathcal{L}}{\mathcal{D}} = f\left(\frac{\mu}{\mathcal{D}\rho}, \frac{\rho U\mathcal{L}}{\mu}\right) \quad [36]$$

This time the Schmidt number cannot be omitted because the exchange of solvent between the surface and the mainstream is very rapid due to the mixing strengthened by the high turbulence levels induced by the scalloped wall. Therefore, the concentration boundary layer does influence the mass transfer rate perpendicular to the surface.

The dimensionless ratio on the left-hand side is the overall average Sherwood number Sh and represents the ratio of the convective mass transfer to the rate of diffusive mass transport. It is indicated in the following as N_S to underline that it is referred to the flute pattern. *Eq. 36* can thus be rewritten as:

$$N_S = f(Sc, N_f^*) \quad [37]$$

For a stable flute pattern $N_S = f(N_f^*)$ such that $N_S = N_S^*$ and constant. Specifically, $N_S \propto N_f^{1/2}$ for a fixed pattern and is found to be strongly dependent on the flute profile, especially along the lee slope:

$$N_S = c_f N_f^{1/2} Sc^{1/3} \quad [38]$$

Where c_f is a constant. For an approximately circular conduit of diameter d , the Reynolds number is calculated as $U\rho d/\mu$, allowing to rewrite a functional relation among the previously introduced dimensionless numbers as:

$$Sh = (N_S/N_f) \cdot Re \quad [39]$$

Therefore, the rate of solution of the pattern is inversely proportional to the flute period and hence proportional to the stream velocity when stability is attained. This means that the flute pattern will evolve in time to establish a constant Sherwood number. Furthermore, $N_S \propto N_f^*$ allows to conclude that stable flute patterns with small periods are propagating more rapidly than those with longer periods, if all other factors are kept constant, and that shorter flute periods should be more common than longer periods.

since the experiments discussed in the mentioned paper are performed at $Re_\tau \cong 2200$, which corresponds to $Re \cong 22500$; therefore it is very legitimate to doubt if the periodicity of the pattern is caused primarily by an erosional phenomenon, by the structures within the associated turbulence and by a characteristic separation-reattachment length associated to the forced convection than to a merely dissolving phenomenon.

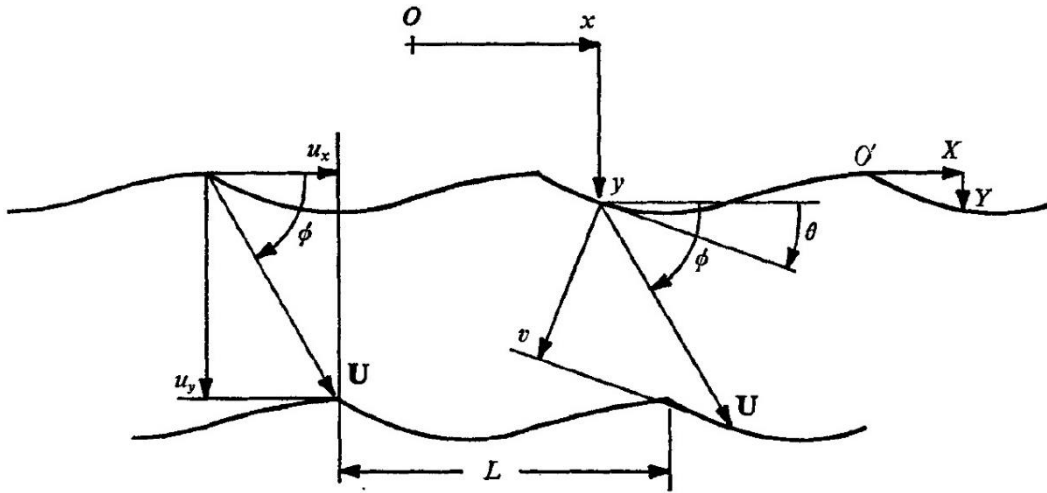


Figure 28 Flute geometry and dissolution-rate and characteristic velocity vectors [55].

Similarly to Eq. 40, using the notation shown in Fig. 28 for two different points on a stable profile, the propagation direction in terms of local conditions is given as:

$$\tan \phi = \frac{v_1 \sin \theta_2 - v_2 \sin \theta_1}{v_1 \cos \theta_2 - v_2 \cos \theta_1} \quad [41]$$

It is worth mentioning that the notation in [55] is different than the one proposed by the same author in [54]: in Eq. 41 ϕ, θ are respectively the propagation direction angle and the slope angle as used in [55], while in Eq. 40 which was proposed in [54] they are exactly the opposite.

Blumberg & Curl provide the multiplying factors of the formula mentioned earlier. The weighted formula is not mentioned here, both because of the doubt anticipated at the top of the present page and because their validity is more limited since they depend also on empirical constants.

The doubt anticipated at the top of the present page is supported also by Fig 29, where it is evident the contribution provided by turbulence. Fig. 29 evidences the main turbulent flow (1), the laminar free-shear layer (2), the laminar-turbulence transition and the relative entrainment (3), the reattachment (4), the recirculating

flow (5), the lee-slop boundary layer (6), the stream ward-slope boundary layer (7), the lee-slope boundary-layer separation with small eddies (8).

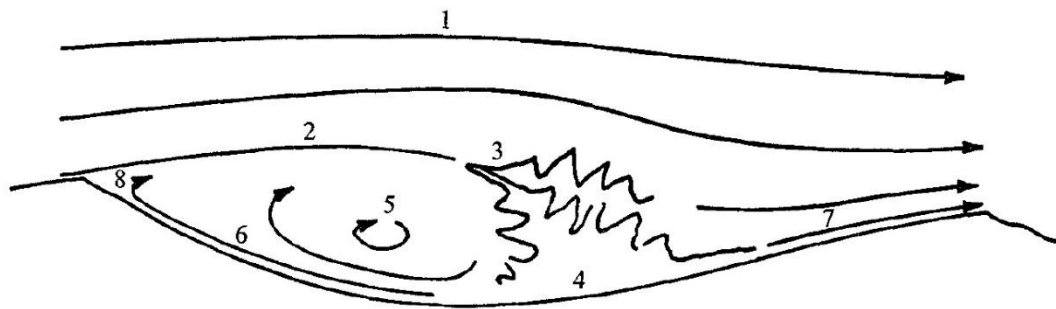


Figure 29 Characteristic flow regions over one flute period [55].

Overall, it can be said that Blumberg & Curl find a general agreement with the information provided before. The experimental results have been later confirmed [61] with in-situ measurement for the case of forced water flow in karst conduits.

Allen's explicit critic to Curl is that, apart from providing relations based on experiments, does not advance any physical reasoning to suggest why the flow velocity, flow dimension, fluid properties and rock diffusivity alone determined the wavelength of the flutes. As mentioned earlier, it is now even more clear that Allen is a supporter of the defect theory and thus endorses that the origin of flutes and scallops is due to the enlargement of initial inhomogeneities [56]. To prove this, shallow pits of circular plan and depth one-third the diameter were cut into the bed of a Plaster of Paris block. The block was then located in the test section of a water tunnel and a flow was forced. The experiments were carried out at Reynolds numbers between 7950 and 99400.

According to Allen, if the pit is sufficiently small in relation to the thickness of the laminar sublayer, the eddy within the pit remains laminar, otherwise the eddy in the pit is turbulent, as shown in *Fig. 30*. Both Allen and Curl thus agree on the idea that flutes and scallops are associated with a locally separated flow. But Allen argues that a scallop or a flute can arise at an inhomogeneity only if the rate of solution is for some reason greater at the inhomogeneity than on the surrounding bed, otherwise the inhomogeneity is erased by the flow in favour of a smooth bed.

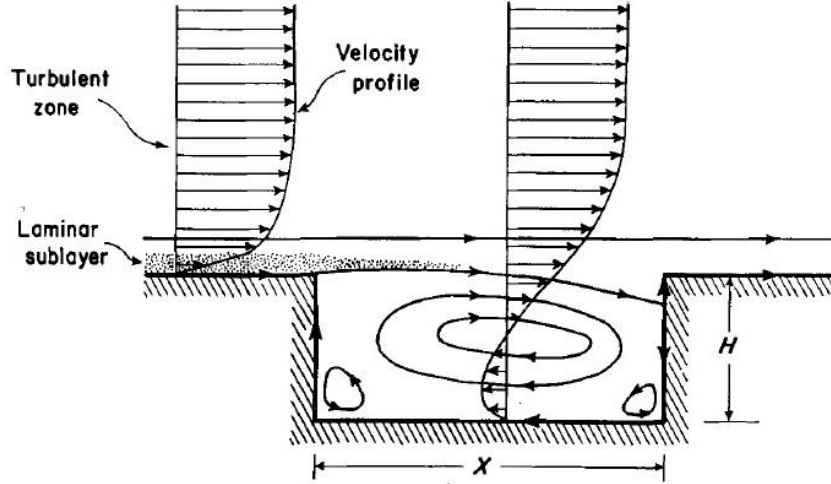


Figure 30 Idealised pattern of flow and associated flow velocity profile in a shallow cavity [56].

According to Allen, the critical condition is associated to the separation of the turbulent flow. Therefore, in [56] a relation, which is given in [62], for the critical diameter for the occurrence of a turbulent separated flow in a pit of cylindrical shape is recalled:

$$X_{crit} = 80Kd \left(\frac{1.25Ud\rho}{\mu} \right)^{-7/8} \quad [42]$$

Where K is a numerical constant to be determined experimentally.

It is worth noticing that $X_{crit} \propto U^{-7/8}$. This is expected because the separation is induced in the viscous sublayer, as shown in *Fig. 30*. And the viscous sublayer thickness decreases for an increasing value of the Reynolds number defined at a fixed position x on the streamwise direction Re_x , as shown in the following two formulas taken from [63]:

$$\frac{\delta_v}{x} = \frac{50}{Re_x \sqrt{c_f/2}} \quad [43]$$

$$\frac{\delta_v}{\delta} = 680 \frac{\ln^2 Re_x}{Re_x} \quad [44]$$

Using the hydraulic radius of the experiments as flow dimension d , it was found $K = 7.4$. Therefore, according to Allen, in a water tunnel with test section of diameter d , in order to have the formation of a pattern on the surface of plaster of Paris, the diameter of initial inhomogeneities must respect the following condition:

$$X > 7.4 \times 80d \left(\frac{1.25Ud\rho}{\mu} \right)^{-7/8} \quad [45]$$

Considering Eq. 42 as a criterion for the stability of pits in a plaster surface exposed to a turbulent water stream, it is possible to measure the depth of the pits at different time intervals. It is found that:

$$\frac{A(t)}{H} = 1.23 \left(-\frac{Vt}{H} \right)^{2/3} \quad [46]$$

Where $A(t)$ is the depth at a generic instant t , H is the initial depth, $(Vt)/H$ is a dimensionless ratio based on the mean velocity V with which the surface retreats.

The rate of growth of the pits is thus simply calculated from Eq. 46 as:

$$\frac{dA}{dt} = 0.82V^{2/3}H^{1/3}t^{-1/3} \quad [47]$$

Eq. 47 shows that larger initial inhomogeneities grow slightly faster than smaller ones. In all cases, however, the rate of growth gradually decreases with increasing duration of the experiment.

Furthermore, the non-dimensional length of the initial pits increases approximately as $(-Vt/d)^{1/2}$, while the non-dimensional breadth roughly as $(-Vt/d)^{4/5}$, as graphically shown in [58].

Even if Curl was the first to propose a time-evolution model for characteristic dimensions and geometry of the flute pattern with the related stability conditions, only Allen introduced order in the nomenclature (*Fig. 31*) of the patterns on the basis of the flow-structure phenomena.

As introduced in [57], from a morphological point of view:

- *Flutes* are isolated heel-shaped, wave-like solutional hollows of parabolic plan-form whose arms open out down-current.
- *Scallops* are saucer-shaped depressions of polygonal plan that are produced by the growth of flutes to the stage of interference.
- *Grooves* are shallow depressions several times longer than wide and elongated parallelly to the flow direction.
- *Ridges* and *furrows* are long, almost perfectly rectilinear structures with a remarkable regular transverse spacing which is a tiny fraction of their streamwise length.
- *Secondary flutes* and *secondary scallops* appear, in a few words, like intersecting flutes or scallops, respectively.

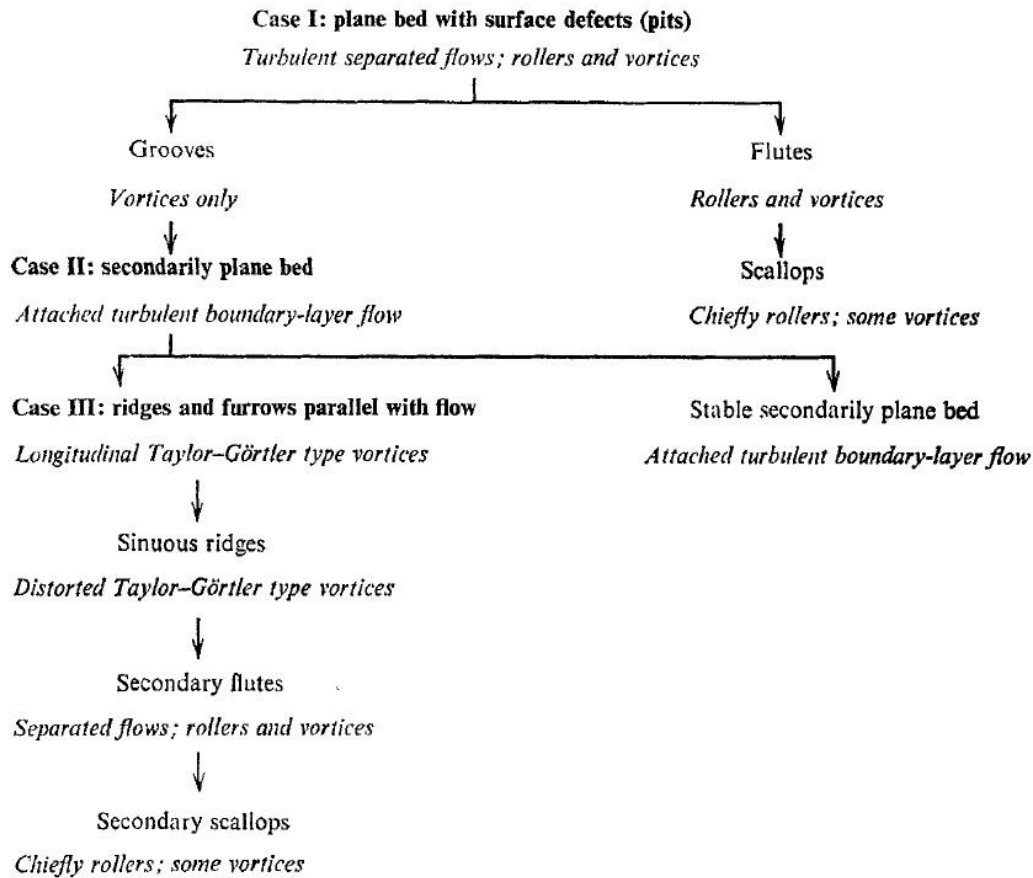


Figure 31 Scheme of instabilities and resulting bed forms and flow fields [57].

Allen's nomenclature is powerful and useful, with respect to all the previous nomenclatures coined, because the related classification is not merely based on a morphological point of view. Quite the contrary, it is based on a fluid dynamic reasoning and thus it provides a physical explanation of the final shape. The plaster bed is divided into the *primarily* and *secondarily bed*, depending on if the patterns are being sculpted by instabilities associated to the main or eventual secondary flow.

To analyse the aforementioned structures from the point of view of the respective fluid source, it is worth starting with the flutes, which are the first structures that appear on plaster of Paris in a forced convection regime. As shown in *Fig. 32*, the initial pit contains a separated flow and from its upstream rim sheds vortices into the current to form a wake extending a considerable distance downstream from it. The separate flow enhances mixing in the near-wall region thus a long narrow groove is hollowed out downstream from the pit, which itself undergoes at first a slight enlargement in the upstream and lateral directions.

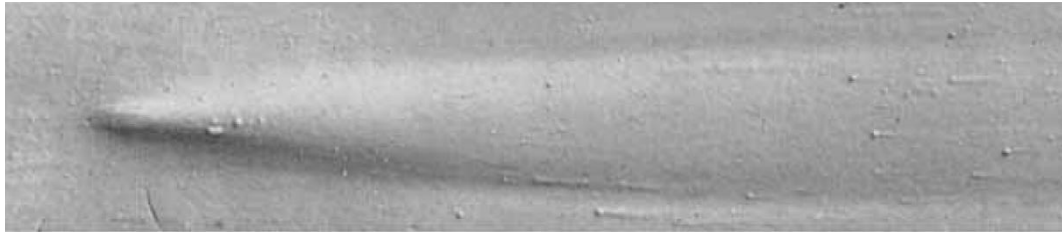


Figure 32 Mould showing a flute at $Vt/d = 1.5$. Current from left to right. The portion of the bed shown in the photo is 10 cm wide [57].

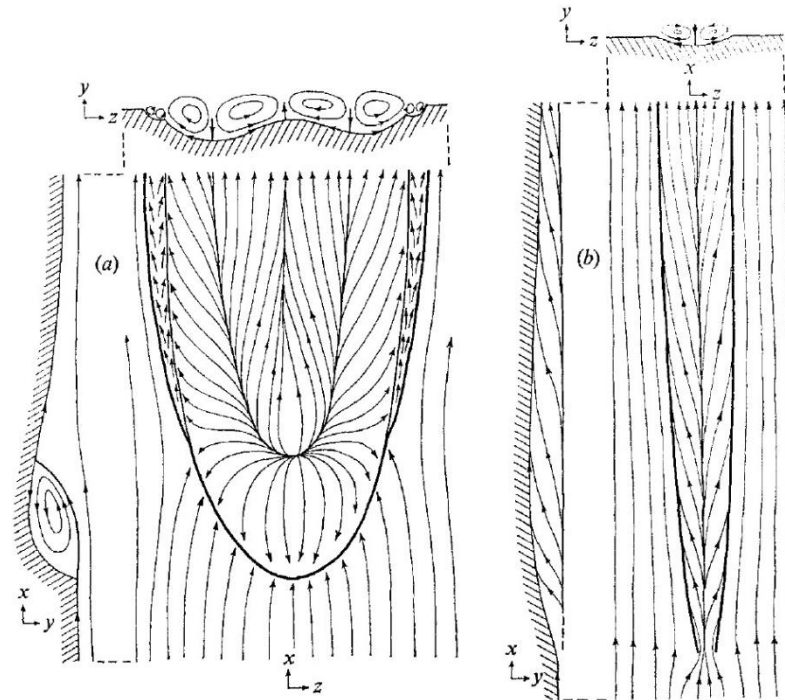


Figure 33 Schematic flow field displaying skin-friction lines and streamlines associated with mature flutes (case a) and mature grooves (case b) [57].

As shown in *Fig. 33*, there is a striking concentration of vorticity in the flow associated with flutes. Basically, the upstream part of each flute holds captive a closed separation bubble and along each flank lies a strong vortex that rises out of the mark to pass downstream and blend into the external flow. The median ridge of the flute is generally a zone of weak streamwise separation of flow. Therefore, the erosion rate is expected to be least at the crests of the ridges, where the local shear bed stress is least, and greatest at the axes of the furrows, where the local bed shear stress reaches a maximum.

The flow field associated with mature grooves is simpler: a pair of oppositely rotating and relatively weak streamwise vortices reattaching to the bed on the floor of the mark.



Figure 34 Rectilinear furrows [57].

In the case the defects originally present on the experimental plaster bed have dimensions smaller than the critical one, then all the bed is a secondary bed and becomes involved in another mode of instability, shown as *case II* in Fig. 31. Basically, this secondary bed is covered by ridges and furrows, as shown in Fig. 34. In several experiments, their crest-to-crest measured distance ranges between 0.71 cm and 1.05 cm with their transverse spacing being between 5 and 10 times their depth [57]. The difference between a ridge and a furrow is that the former has a sharper crest, while the latter has a more rounded crest. Therefore, the former may be associated in the field to *rinnenkarren* while the latter to *rundkarren*, two specific forms of *karren*. *Karren* is a German term used in geology and geomorphology to refer to small-scale solutional forms developed on limestone. Allen suggests successive experiments to verify a possible connection between ridges and furrows and Klineian streaks; but nothing more can be added on the connection. The grooves make angle projected onto a horizontal plane generally between 5 and 10 degrees relative to the streamwise elongation of the ridges. The ridge crests and the longitudinal axes of the furrows can be respectively interpreted as streamwise separation lines and lines of streamwise reattachment. The bed features appear to be associated with paired vortices similar to the Taylor-Görtler type.

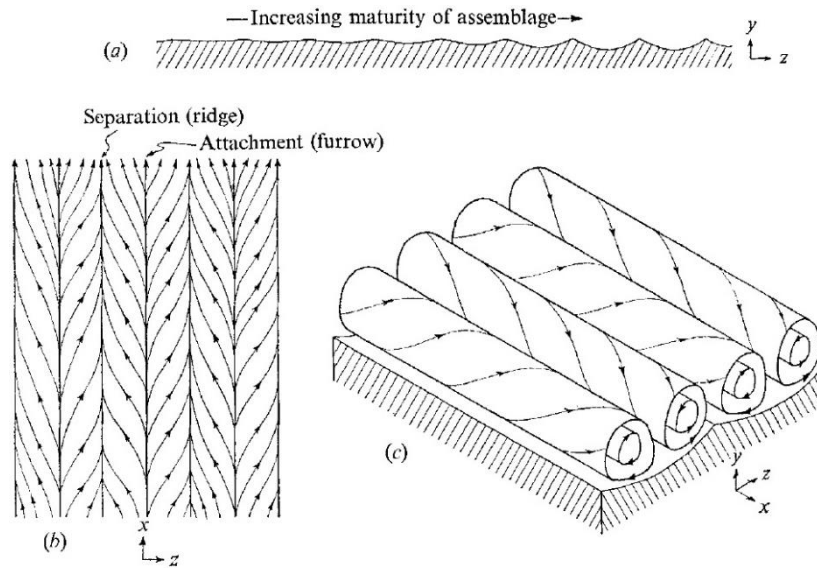


Figure 35 Features of ridges and furrows: (a) Evolution in time of the profile. (b) Schematic pattern of skin-friction lines. (c) Three-dimensional illustration of the flow-field [57].

The ridges and furrows described so far can undergo an additional instability, indicated as *case III* in Fig. 31. If this is the case, the crest-to-crest distance appears at first to shrink and widen along the stream direction. The rectilinearity is lost into a more or less regular sinuosity, which evolve in turn into a definitive asymmetry with respect to the stream direction. The sinuosity has a streamwise wavelength about 5-25 times the mean transverse ridge spacing. As the furrows widen, the vortices in the widening portion grow steadily larger and more vigorous, to the extent of substantially disturbing, and sometimes considerably suppressing, the flow in the vortices situated laterally, as shown in Fig. 36. In Fig. 37a the right furrow shows the kind of flow field associated with furrows at the stage of development of *case a* of Fig. 36. The furrows, as anticipated, may widen symmetrically about the flow direction or even show an asymmetrical hollow developing in the bed, which is *case b* of Fig. 36 and is illustrated in Fig. 37c. For sure, if the asymmetrical widening occurs, it always follows the symmetrical one. Therefore, the left furrow in Fig. 37b is the least advanced since it has only one vortex on a side. Thus, this furrow corresponds to a transition state preceding *case b* in Fig. 36, while the furrow on the right corresponds to *case c* in Fig. 36.

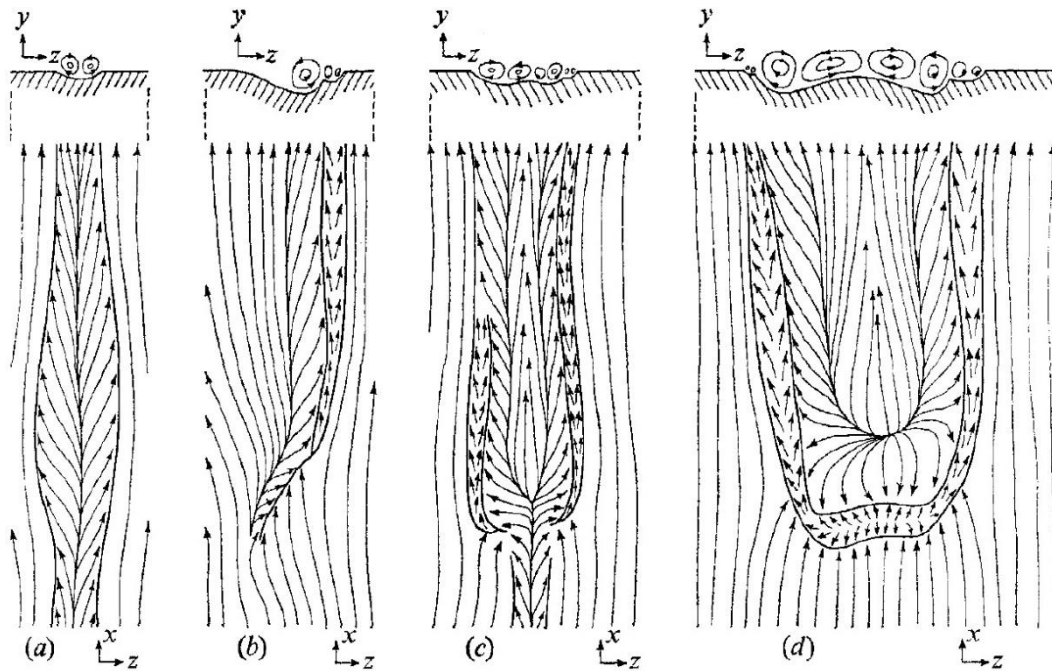


Figure 36 Schematic flow field displaying skin-friction lines and streamlines associated with stages in the development of secondary flutes from longitudinal ridges and furrows [57].

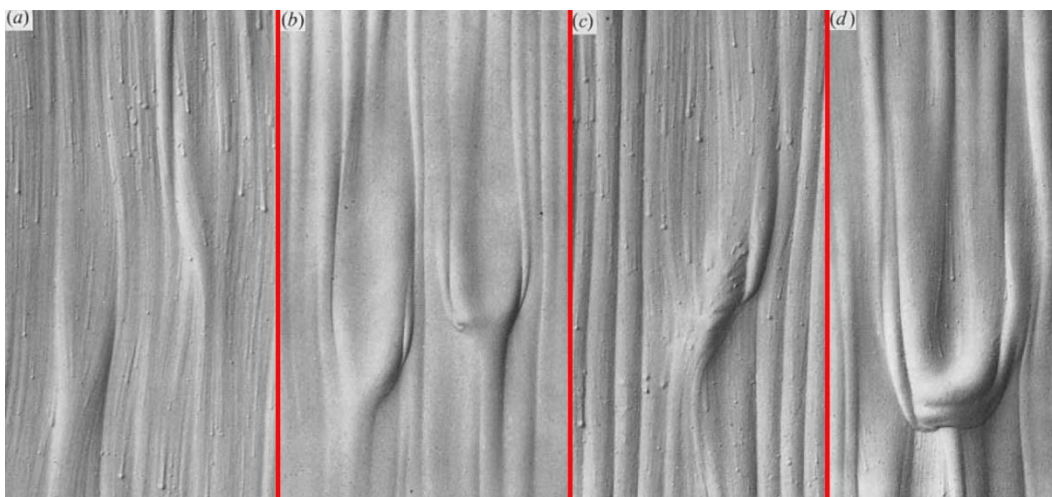


Figure 37 Moulds illustrating sequential stages in the development of secondary flutes by the higher-order instability of longitudinal ridges and furrows. They are not referred to the same furrow. Flow from bottom to top [57].

The structures shown in *Fig. 37b* are 3-4 times wider than the parent furrows. Furthermore, the cusped rim developed at the upstream end of the flank of each furrow is not yet continuous across the median line. The illustration of the flow field from *case c* of *Fig.36* suggests that there is a powerful vortex against each flank of the mark and a pair of weak vortices symmetrically arranged about a weak streamwise separation line on the crest of the median ridge. At the upstream end of the mark, the skin-friction lines of the main vortices make a relatively large angle

with the mean flow direction. If there are neighbouring secondary furrows, the one with the strongest flute enlarges engulfing them, through fusion of the cusped rims. Right before engulfing adjacent secondary furrows, the structure is approximately six times wider than its parent furrow. When the cusped rim fusion between adjacent furrows happens, a captive roller appears in the flow field associated with the mark and progressively strengthens. Further growth beyond the stage of *case d* of *Fig. 36* leads to the disappearance of the weak up-current furrow and the development of a parabolic shape in plan: a flute has now been attained.

To sum up, according to Allen, the broad spectrum of bed shapes that have been noted suggests an equally broad spectrum of flow phenomena associated with separated flows and makes it unlikely that a single mechanism of instability is responsible for the structures.

In conclusion, Allen even provided a classification of erosional marks found in rock or mud caves depending on their assemblage. Indeed, when erosional marks occur in association, the marks may be either scattered widely over an otherwise sensibly smooth surface, or so closely spaced as to interfere and share crests. Marks in the first category are described as *isolate* and in the latter as *conjugate*. Mark assemblages are in turn separated into *homogeneous* and *heterogeneous*. Usually, in a homogeneous assemblage, the marks are similar in shape and size; thus the linear scale of the individual mark can contribute largely to the linear scale of the assemblage. On the other hand, in a heterogeneous assemblage, the linear scale of the assemblage is larger than the linear scale of the marks themselves.

In the scheme shown in *Fig. 38*, dissolutional scallops, depending on their evolution in time, are in the categories of parabolic (broad form), polygonal (symmetrical) and polygonal (asymmetrical) and are within the bigger group of the homogeneous, conjugate assemblages. In speleology, scallops are rarely more than 20 cm and seldom less than 5 cm in length. The width is generally between one and two times the length, which is usually between four and eight times the amplitude. Ordinarily the crests of the marks are asymmetrically sharply cusped, thus suggesting a preferential flow direction. Assemblages of scallops are principally of

asymmetrically polygonal marks with subordinate numbers of parabolic and symmetrical polygonal structures. Very commonly in these assemblages the shared crests of the scallops join and culminate at sharp peaks on the bed.

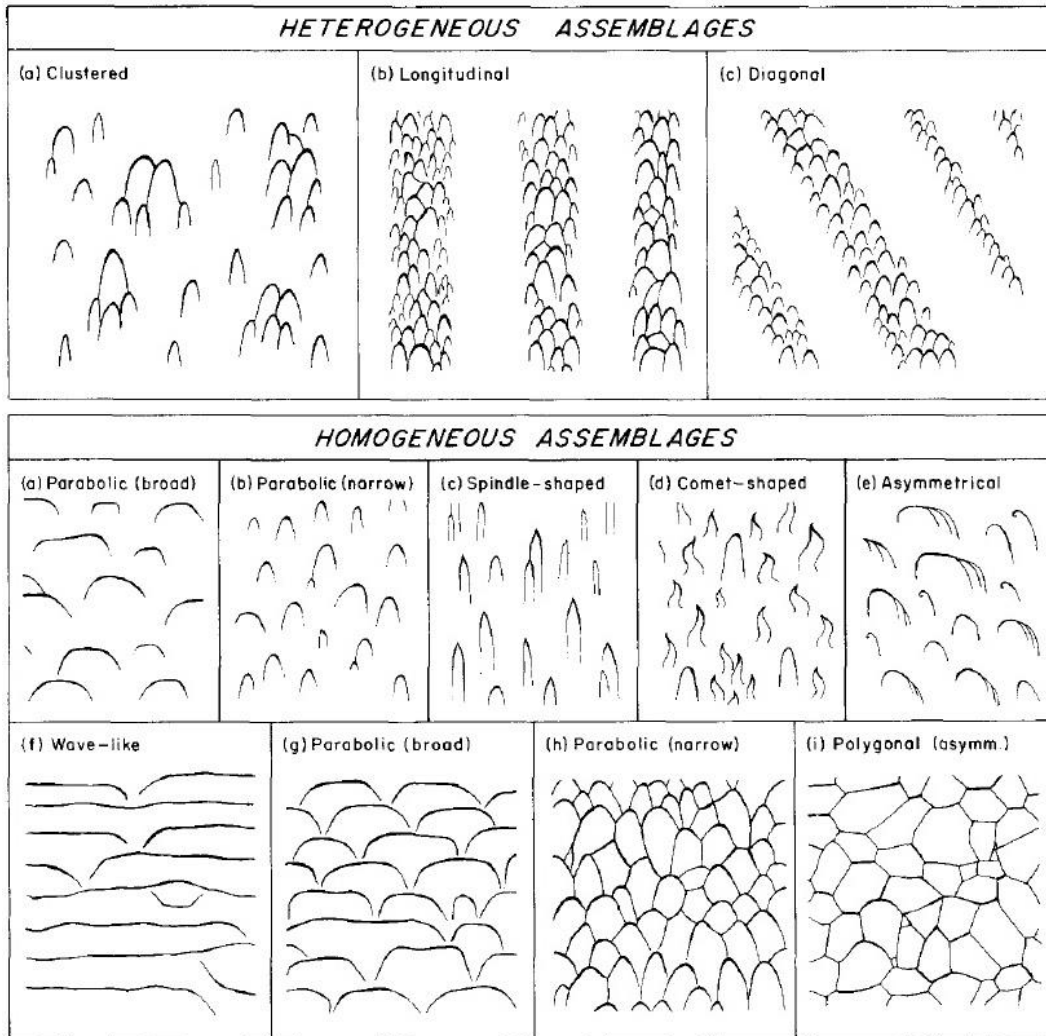


Figure 38 Cataloguing of assemblages of transverse erosional marks.
Current from top to bottom [58].

As sketched in Fig. 39, the commonest form of peak is the culmination of three crests about 120° from each other, one crest lying parallel with flow. Less commonly, four crests may culminate at one point or, in pairs, joint at the ends of a short transverse ridge of constant elevation along its length.

The cave markings known as flutes are rare compared to scallops. Their crests in plan vary from straight, through gently curved, to weakly sinuous, and in profile range from cusped to rounded. Flutes ordinarily occur in homogeneous, conjugate assemblages, with scallops found sometimes here and there in the assemblage.

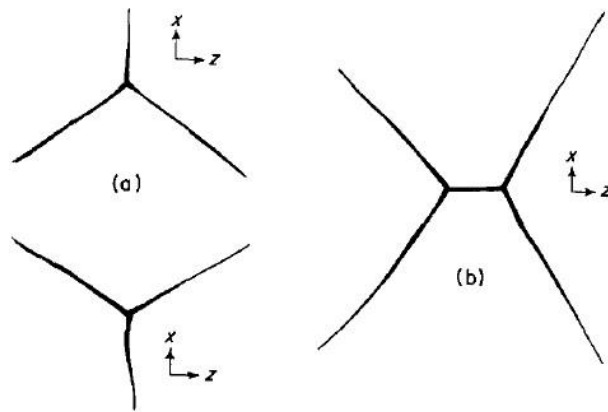


Figure 39 Pattern of crests, and their culmination (peaks), in assemblages of polygonal erosional marks [58].

The assemblages mentioned thus far are instantaneous. Instead, Fig. 40 proposes four stages of the time-evolution of an assemblage of marks of the same initial size but random spacing on a fixed surface.

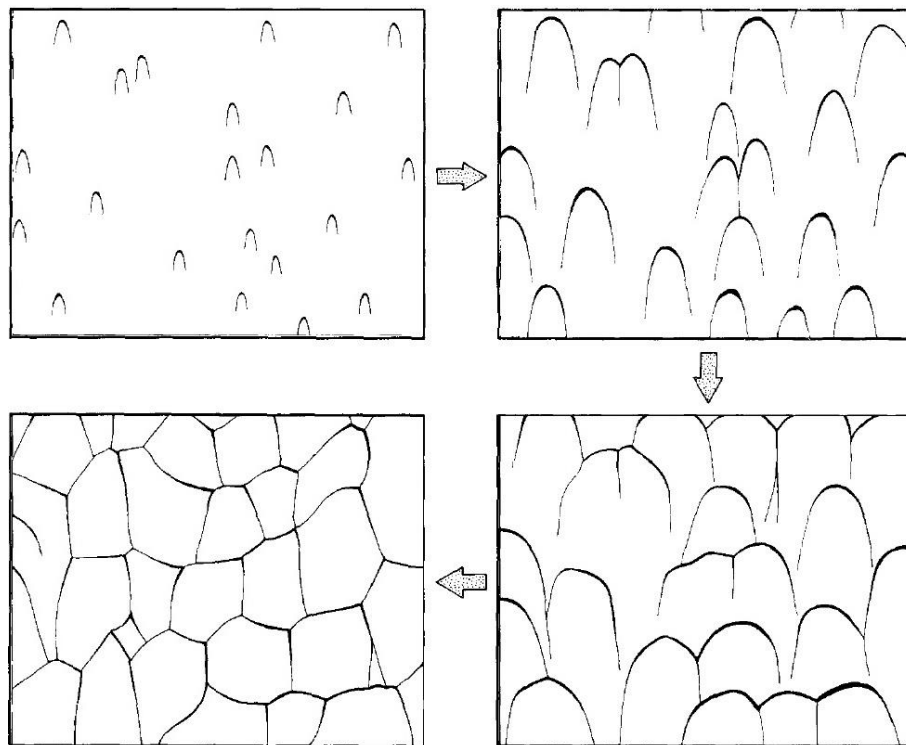


Figure 40 Expected development in time of an initial assemblage of transverse erosional marks. Current from top to bottom [58].

In early stages the marks do not interfere and a high proportion of the total bed area lacks marks. With increasing age, the marks grow larger and nearer so that eventually those initially closest merges to share rims. Therefore, there are now

small cluster of erosional marks scattered among isolated ones. But there are still large individual areas on the bed not yet impinged on by marks. By a late developmental stage, however, even these areas have been absorbed and the assemblage is now wholly of conjugate marks. Many individual marks retain their initial non-polygonal form till a relatively late developmental state, certainly to the earliest stage describable as conjugate. In later conjugate stages, however the erosional processes, which are now acting quasi-isotropically, are expected to give place to a polygonal form and straighten out the cusped crests shared by marks. The last stage shown in *Fig. 40* deserves a special comment driven by a substantial question: does this stage represent the final and unchanging state of the surface? The answer is affirmative according to Curl's stable flute theory. Therefore, this stage would be the greatest age that could be determined by inspection a posteriori of the surface. Instead, Allen supports the idea that when the surface reaches the conjugate state, erosional marks could be destroyed as well as created and that there is no significant evidence to say whether the two opposing processes would strike a balance expressed by a statistically constant size and spacing of marks independently of time.

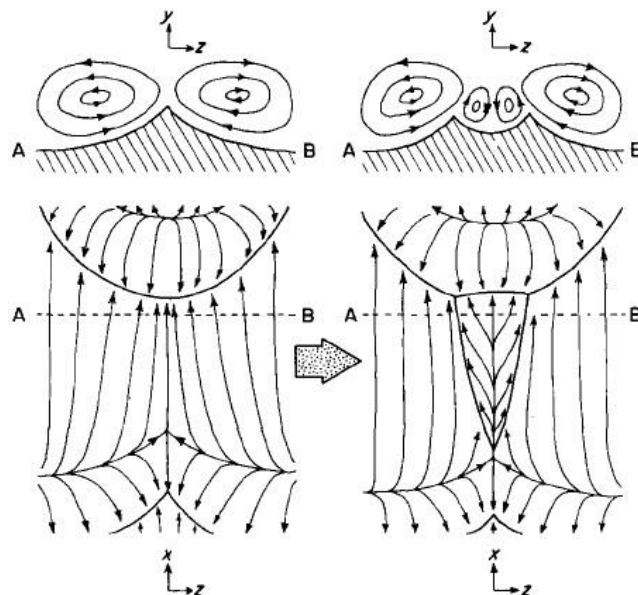


Figure 41 Conjecture on secondary vortices and bed furrows generated by flank vortices of conjugated marks [58].

The reason behind Allen's answer is mainly motivated by the distance between vortices of adjacent patterns. Indeed, to reach the conjugate state, the secondary

lateral vortices must merge into bigger vortices. This mean morphologically that erosional marks are so closely spaced that interfere and may even share crests, as shown in the left case of *Fig. 41*. It is interesting to note that such condition, corresponding to a cusp, is not admitted for a stable flute profile in Curl's theory. Anyways, the attachment line on one mark could advance downstream on the separation line of the next mark along the line of flow, as shown in the right case of *Fig. 41*, only if the flow field and pattern of erosion in the marks were substantially independent of each other. Allen points out that, since substantial independence has been established for migrating sand dunes [64], it cannot be neglected a priori a possible analogy also for erosional marks.

The author of the present thesis will compare the result found experimentally with the ones provided by Allen and Curl in the final chapter. Motivated comments about the similarities found and about the emerged limitations of the two mentioned authors' work will be provided as well.

2.3 Scalloping on salt

The renovated interest in performing experiments on salt dissolving in water is due to the offered potential for studying solutal convection in an initially quiescent fluid induced by dissolution.

Indeed, with respect to the aforementioned experiments involving ice or plasters: in the former, even if water salinity has an undisputed influence on melt-water density and thus on the surface melt instability, the phenomenon is mainly induced at the beginning by a temperature gradient and then driven by it. While in the latter, even if this is the case for dissolution to dominate, the experiments must be performed in an externally forced flow and thus the dissolution effects linked to the concentration gradient might be highly masked by erosional effects. Where *erosion* of surface due to a fluid involves two processes: *deflation*, which is the removal of surface loose particles by the flow and is linked to the near-wall velocity gradient of the clean fluid, and *abrasion*, which is the bombardment of the surface by sediments collected upstream and transported within the fluid. Therefore, for applications in geomorphological studies, experiments performed with salt in natural convection or with plaster in forced convection are respectively more correctly related to chemical weathering and aeolian/water erosion. The difference being that weathering does not usually include the transportation of the disintegrated rock and soil away from the site of the degradation [65].

The first observation of the pattern forming on a salt block when dissolving in a quiescent water has been scientifically reported for the first time in 1905 [66], where such pattern was called *figures de corrosion* and was found to have a cellular structure on the bottom surface of a horizontal salt block and a structure made of parallel stripes, which were called *stries de convection*, if the block was inclined. But it is not till recent decades that interest in possible studies arose again. Indeed, in addition to being a good test model for dissolution water caves [67] [68], salt is a good experimental model for solutal convection induced by dissolution [29] [69] [30]. The latter being a topic of recently renovated interest for the study of Darcy flows in porous media, one of whose engineering applications is found in CO₂ sequestration [70].

The principal papers mentioned in this paragraph are [29] [69], whose research was carried out by the same research group. These references are relevant because they pave the way for the next paragraph.

In [29] [69], the solutal convection induced by dissolution in water of a horizontal block of salt is investigated by means of numerical simulations. The reason behind the computational approach was preferred with respect to the experimental one is motivated by the following characteristic.

Despite the simplicity of the experimental configuration, immersing suddenly a dissoluble block into water or filling rapidly with water an aquarium in which the dissoluble block has been already posed, does not correspond to the classical problem formulation of the Rayleigh-Bénard convective instability. Indeed:

- Neither the concentration nor the flux at the boundaries is stationary forced in the initial base state.
- Due to the development of the concentration boundary layer by diffusion, the base state of the instability is time dependent.
- For the previous point, the convective flow starts after a specific duration.

Therefore, the standard methods of linear stability analysis cannot be used to predict the onset time, the associated wavelength and growth-rate of the convective instability.

Furthermore, the experimental investigation of the concentration boundary layer at the dissolving interface remains challenging due to its small size (about 100 μm) and the high concentration gradients; thus preventing the use of optical techniques. Calculating the thickness of the concentration boundary layer is important because the dissolution rate is set by its size, as it is for the temperature boundary layer in turbulent thermal convection.

Anyways, the physical problem can be understood as an advection-diffusion problem in the fluid, which is coupled with a moving solid boundary due to the dissolution and gravity precipitation of Na^+ and Cl^- ions in water [71]. The dissolution law at the interface is written as:

$$-\rho_s \frac{\rho_m - \rho_0}{c_m} \mathbf{v}_d \cdot \mathbf{n} = \alpha(\rho_i - \rho_m) = -D\nabla\rho|_i \cdot \mathbf{n} \quad [48]$$

Where $\rho_s, \rho_m, \rho_0, \rho_i$ are respectively the density of the solid, of the liquid at saturation, of the liquid in the absence of solute, of the liquid at the interface, c_m is the saturation mass concentration, α is the dissolution rate coefficient, \mathbf{v}_d is the dissolution velocity, \mathbf{n} is the normal vector to the interface directed outward from the liquid, D is the diffusion coefficient of the solute in the liquid. As can be seen, the dissolution rate depends on the value of the density ρ_i at the interface, which is modified by advection by the hydrodynamic flow in the liquid phase. Although the domain is static in this approach, the boundary condition involves simultaneously the module of the characteristic variable and its flux across the boundary, thus is non-classic. Furthermore, although the solutal convective instability corresponds to a nonstationary Rayleigh-Bénard convection problem, the global dissolution flux is experimentally found to be constant with time after some time has passed since the start of the experiment [72].

For salt, $c_m = 315 \text{ kg/m}^3$, $\rho_m = 1200 \text{ kg/m}^3$, $\rho_s = 2153 \text{ kg/m}^3$ from [29] and $\alpha = 5.0 \pm 0.4 \times 10^{-4} \text{ m/s}$ from [73].

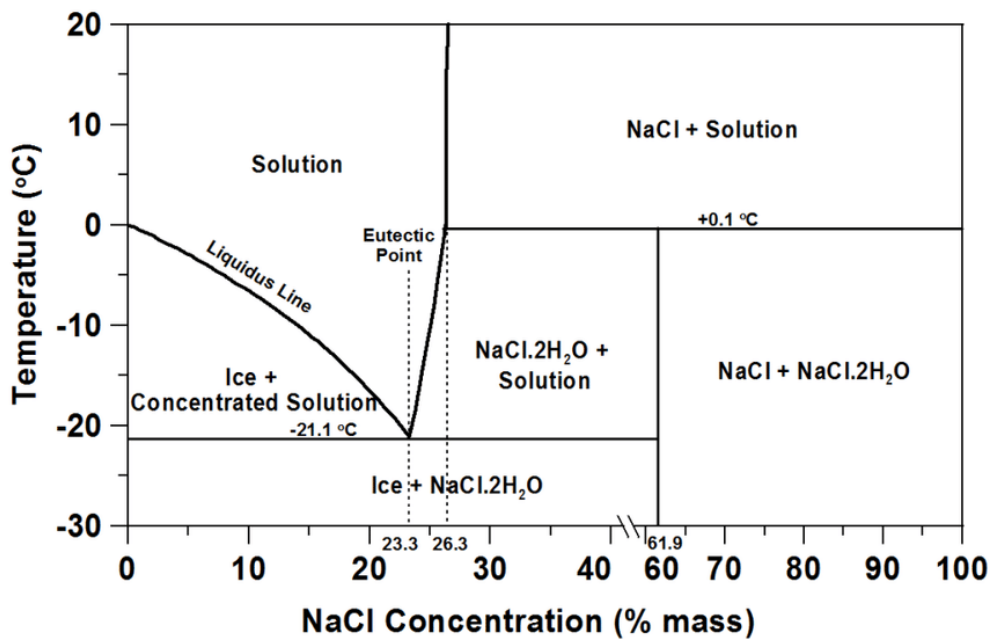


Figure 42 Phase diagram of NaCl-H₂O [74].

A different method to calculate c_m, ρ_m is using a state diagram, like the one provided as Fig. 42. To give an example of how to use it, this visually states that at the temperature of 20°C, 1 kg of water can fully dissolve a concentration of about 26.3 wt.% of salt, which corresponds to about 357 g of NaCl.

It is worth to mention that Eq. 48 was obtained from:

$$-\rho_s \mathbf{v}_d \cdot \mathbf{n} = \alpha(c_i - c_m) \quad [49]$$

Which considers in turn the linear relation $c = c_m (\rho - \rho_0) / (\rho_m - \rho_0)$ between the density ρ and mass concentration c of the solution, which is valid when only one chemical species is in the solution. This to remind that, when the dissolution of hard candy in salty water will be studied in the next chapter, there will be more than one chemical species in the solution.

Anyways, the importance of [29] [69] for the experimental study carried on is that, in addition to underline the non-classic RB problem and thus the points listed earlier, identify three regimes and propose formulas describing the related system dynamics.

The regimes identified are:

- *Diffusive regime* ($t < t_{onset}$).
- *Convection instability growth regime* ($t_{onset} < t < t_{qs}$).
- *Quasi-stationary regime* ($t > t_{qs}$).

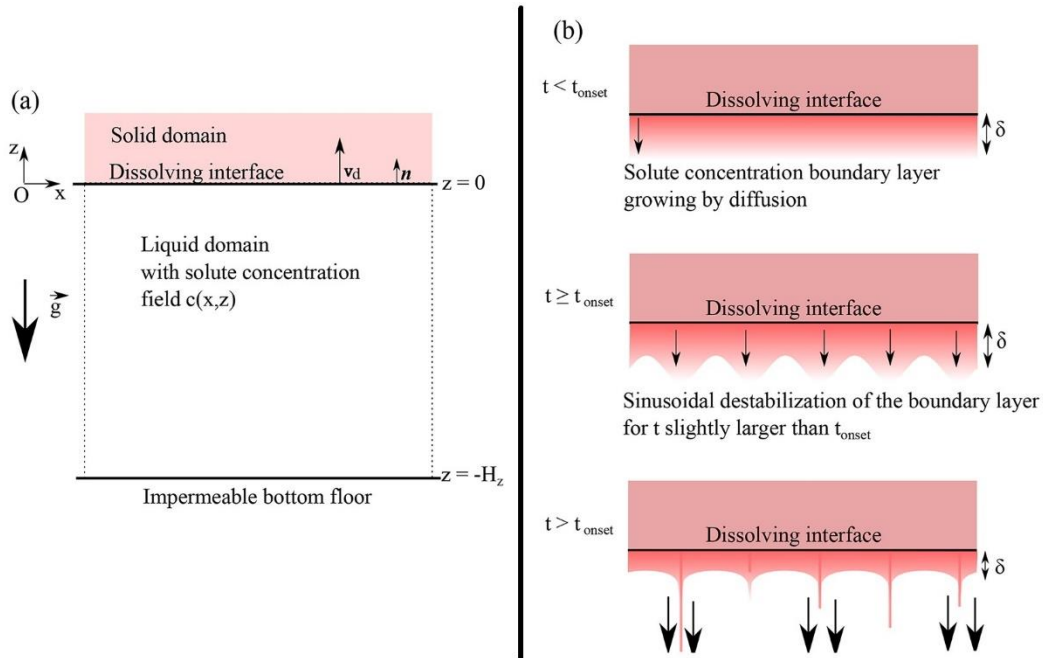


Figure 43 (a) Physical domain in the numerical simulation. (b) Solutal convection instability near the dissolving interface [69].

Whenever a soluble solid is put in contact with the corresponding solvent, it starts dissolving. The originating concentration layer grows until a critical thickness δ_{onset} is reached at t_{onset} . Only now the layer becomes unstable due to the buoyancy forces acting on the denser concentrated solution layer. Therefore, a buoyancy instability, analogous to the Rayleigh-Bénard instability where concentration replaces temperature, develops according to [29] [69]. The boundary layer adopts a sinusoidal shape with a wavelength λ_{onset} .

In [69], $\lambda_{onset} = 0.53 \text{ mm}$ is found both for the perturbed vertical velocity field and for the perturbed concentration field. The theoretical approach, which is used in the model to describe the convective instability under the action of gravity acceleration, relies on the Boussinesq approximation. This approximation requires that the variations of density with the solute concentration are negligible and is acceptable in the salt-water dissolving problem.

In a few words, in the intermediate regime the instability non-linearly grows in time, and concentrated plumes are emitted.

In the quasi-stationary regime, the plumes are intermittently emitted in the vicinity of the surface and the solute flux at the interface reaches a constant value on average. The characteristic timescale t_{em} of emission of filaments is measurable experimentally and follows the scaling hereafter proposed for the onset time. However, direct measurements of the onset time appear to be unreachable experimentally, as for the aforementioned concentration boundary layer thickness. The aforementioned asymptotic laws proposed in [29] for the second and third regimes strongly depend on the dissolving rate of the solid. Indeed, two cases are discernible: the *fast dissolving case*, which corresponds to a significant Damköhler number $Da \gg 1$, and the *slow dissolving case* corresponding to $Da \ll 1$. The Damköhler number compares the dissolution rate coefficient α with a characteristic diffusion velocity defined as D/δ and is defined as:

$$Da := \frac{\alpha\delta}{D} \quad [50]$$

When the Damköhler number is large, the dissolution is limited by the diffusion and the concentration at the interface is close to the saturation concentration. Instead, when the Damköhler number is small, the dissolution is limited by the chemical kinetics and the concentration at the interface is close to the initial

concentration of the solution. Given the aforementioned value of α , a block of salt dissolving in water is part of the fast-dissolving case. The asymptotic laws derived in [29] for the fast-dissolving case are:

$$\delta_{onset} \approx Ra_c^{1/3} \left(\frac{\eta D}{\Delta \rho g} \right)^{1/3} \quad [51]$$

$$\lambda_{onset} \approx \gamma Ra_c^{1/3} \left(\frac{\eta D}{\Delta \rho g} \right)^{1/3} \quad [51]$$

$$t_{onset} \approx Ra_c^{2/3} \left(\frac{\eta}{\Delta \rho g \sqrt{D}} \right)^{2/3} \quad [53]$$

$$\Phi \approx (Ra^{qs})^{-1/3} \left(\frac{g D^2}{\eta} \right)^{1/3} \frac{c_m}{\rho_m - \rho_0} \Delta \rho^{4/3} \quad [54]$$

2.4 Scalloping on hard candy

Hard candy, or *solid sugar*, has recently received a renovated interest to carry out experiments on the self-sculpting phenomena induced by dissolution in quiescent water [14] [36] [30] [75].

Undiscussed advantages to prefer hard candy over salt are for sure a cheaper cost, there is no mineral preferred orientation, the greater malleability, the lower dissolution rate, the higher saturation concentration in water.

Furthermore, hard candy is not opaque. Therefore, the pattern formation and evolution can be studied without the use of refraction, stereo-correlation or projection based optical techniques [76] or the involvement of tracing particles or colorants.

Obviously, nothing is perfect. Hard candy has disadvantages too: it is fragile when in the glassy state, its fragility can be easily influenced by atmospheric condition, its manufacturing process is more complex, the manufacturing process requires a control of the final temperature reached, it is difficult to manufacture a bubble-free final solid.

An advantage, and disadvantage at the same time, of hard candy is that its properties, i.e., opacity and viscosity, depend on the final temperature reached in the manufacturing process [77]. So, from a point of view, it is possible to play with the final temperature, for example till “burning the sugar” and thus discovering that it can become so opaque that eventual patterns forming on the surface are very difficult to detect if present, and at the same time discovering that after it is casted it takes much more time to solidify and during this time its viscosity is much lower than could be at first expected. But if this allows to vary some conditions using the same material, at the same time there is the opposed necessity of having the same material properties to increase the repeatability of the experiments. It is worth reminding that the dependence is not only on temperature or concentration, but also on the sugar used (i.e., glucose, fructose, ...). Anyways, to the author’s knowledge, there are no consistent surface viscosity changes in the final hard candy block manufactured. A more detailed explanation on the last statement and on the manufacturing of hard candy is given in paragraph 3.1.

The experiments described in the present paragraph are referred to [30], which constitutes the principal reference on the topic available today. They were carried out on a rectangular block of hard candy immersed in quiescent aqueous solutions. The experiments are performed varying the inclination of the block and the salinity of the solution.

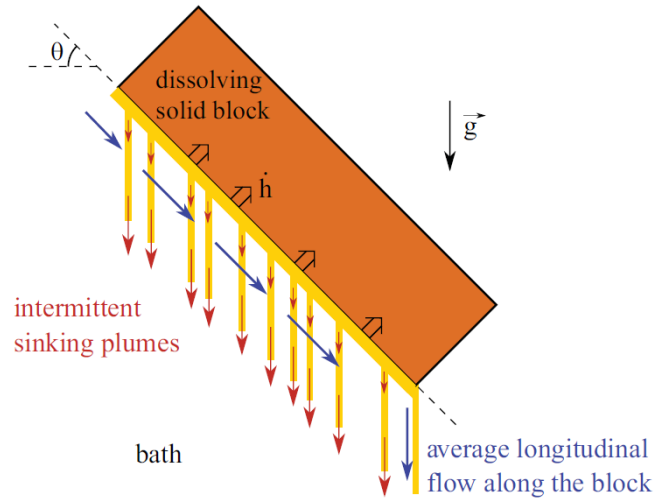


Figure 44 Schematic view of the dissolution-driven flow on an inclined block of hard candy [30].

The differences in solute transport depending on the orientation of the block interface go along with a different erosion velocity and shaping of the block walls. It is found that the solute flow along the block and the dynamics of patterns at the block interface have little if any influence on the global dissolution rate. In the mentioned paper, the experiments were carried out immersing a block of hard candy at room temperature at the center of a glass tank which was 40 cm long, 20 cm wide and was filled with the solution to a depth of 20 cm. A few seconds after immersion, longitudinal parallel stripes with an initial wavelength of 0.4 mm are observed [30]. The initial wavelength of longitudinal stripes λ_s , the characteristic growth time T_s for their formation and the global erosion velocity \dot{h} of the block wall pointing downward, where there is scalloping, are measured. Indeed, the block wall pointing upward is not scalloped, showing clearly how the solute layer at the interface is destabilised by gravity. Solute diffusion and viscosity stabilize the interface and tend to increase the solute layer thickness δ , while gravity drives the instability and tends to decrease δ by ultimately forcing the near-wall flow to detach. The

instability selects the thickness of the concentration layer and the wavelength of solute threads. It produces a modulation of the solute concentration at the interface, which shapes the dissolving block. The concentration at the interface of the block is larger above a thread than between threads. The block dissolves faster where the concentration at the interface is smaller. The respective higher and lower concentration is indicated respectively as (+) and (-) in *Fig. 45*.

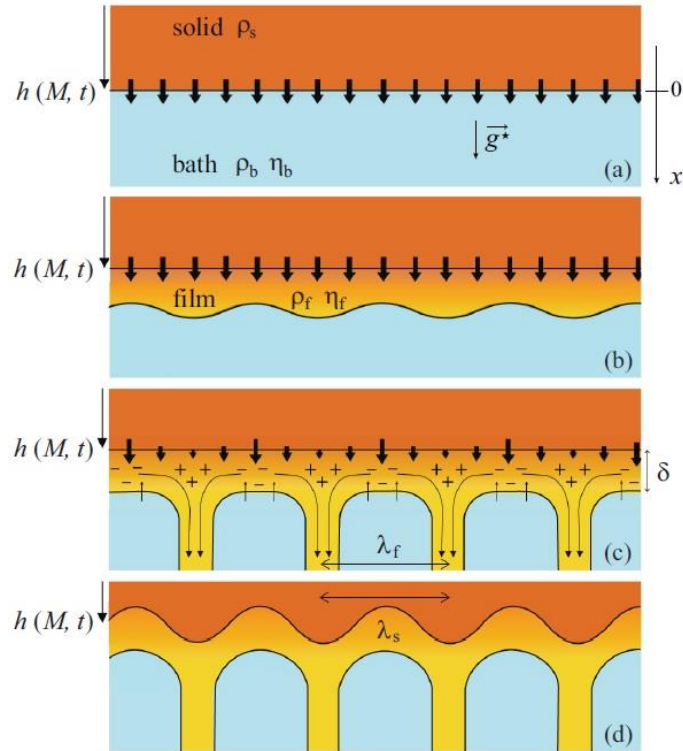


Figure 45 Evolution in time, from top to bottom, of the dissolution instability [30].

In [30] it is reported that the overall inclination of the bottom surface does not change over time, except for the region in the vicinity of the top corner. No explanation is provided. Furthermore, it is noted that the block dissolves faster at the interface facing downwards with respect to the interface facing upwards.

The characteristic time and length scales are said to depend on material, initial bath concentration and inclination of the block. It is reported that:

- The initial wavelength as the characteristic time for the stripes' formation increases with the bath concentration.
- The interface recedes faster when the concentration of the bath is smaller.
- The initial wavelength and growth time increase, and the interface recedes slower when the inclination angle with respect to the horizontal increases.

The second point, as will be explained in a while, could have been expected a priori. The scaling laws are derived balancing the dissolution-driven solute flux at the receding interface, the diffusion-dominated flux of mass at the solid interface, the advection flux of mass at the interface between the solute layer and the outer bath. Basically, to explain the code implemented in the mentioned paper, it is worth recalling the Stefan problem explained in paragraph 1.2 together with the used notation. The volume of the aquarium can be idealised in a spatial domain \mathfrak{A} made of three subdomains $\mathfrak{A}_1, \mathfrak{A}_2, \mathfrak{A}_3$ divided respectively by two interfaces $\mathfrak{D}_{12}, \mathfrak{D}_{23}$ at respective initial positions $s_{12}(t = t_{onset}) = s_{0,12}, s_{23}(t = t_{onset}) = s_{0,23}$, such that $\mathfrak{A}_1 = \mathfrak{A} \cap \{0 \leq x < s_{0,12}\}$ filled with water, $\mathfrak{A}_2 = \mathfrak{A} \cap \{s_{0,12} < x < s_{0,23}\}$ made of the concentration layer, $\mathfrak{A}_3 = \mathfrak{A} \cap \{x > s_{0,23}\}$ filled with the solid not yet dissolved. In order to take into account the existence of the concentration layer, and thus considering two interfaces instead of one, it is necessary that $t = t_{onset}$, and not simply that $t = 0$ like in the classical one-dimensional one-phase Štefan's problem explained in paragraph 1.2. Furthermore, another difference is that only the interface between the concentration layer and the outer bath is effectively a free boundary layer in a numerical simulation. Indeed, the thickness of the concentration boundary layer influences the dissolution rate, as anticipated in paragraph 2.3. While the interface between the concentration layer and the solid is basically fixed, in a numerical simulation, by the Damköhler number. As anticipated in paragraph 2.3, if $Da \gg 1$, then $C_i \approx C_{sat}$; while if $Da \ll 1$, then $C_i \approx C_b$. Where with C_i, C_{sat}, C_b are indicated respectively the mass concentration of the solution at the interface between the solid and the concentration layer, C_{sat} is the concentration of the saturated solution, C_b is the concentration of the outer bath. In physical words, the equilibrium between the dissolution kinetics and the diffusive flux sets the concentration at the solid interface. The authors of the mentioned paper assume a linear concentration profile in the concentration layer and a linear relationship between density and concentration. This allows to postulate scaling laws for the thickness of the concentration layer δ and for the already introduced variables \dot{h}, λ_s, T_s :

$$\delta \sim (3R_\lambda^2)^{1/3} \left[\frac{\rho_s}{\rho_s - \beta C_{sat}} \frac{D\eta_f}{(\rho_{sat} - \rho_b)g \cos \theta} \right]^{1/3} \left(\frac{C_{sat} - C_b}{C_{sat} - C_b \frac{\rho_{sat} - C_{sat}}{\rho_b - C_b}} \right)^{1/3} \quad [55]$$

$$\dot{h} \sim -(3R_\lambda^2)^{-1/3} \left[\frac{D^2(\rho_{sat} - \rho_b)^4 g \cos(\theta)}{\eta_f(\rho_s - \beta C_{sat})^2 \rho_s} \right]^{1/3} \frac{C_{sat}}{\rho_{sat} - \rho_0} \left(\frac{C_{sat} - C_b}{C_{sat} - C_b \frac{\rho_{sat} - C_{sat}}{\rho_b - C_b}} \right)^{-1/3} \quad [56]$$

$$\lambda_s \sim -(3R_\lambda^5)^{1/3} \left[\frac{\rho_s}{\rho_s - \beta C_{sat}} \frac{D\eta_f}{(\rho_{sat} - \rho_b)g \cos \theta} \right]^{1/3} \left(\frac{C_{sat} - C_b}{C_{sat} - C_b \frac{\rho_{sat} - C_{sat}}{\rho_b - C_b}} \right)^{1/3} \quad [57]$$

$$T_s \sim (9R_\lambda^7)^{1/3} \left[\frac{\eta_f^2(\rho_s - \beta C_{sat})\rho_s^2}{D(\rho_{sat} - \rho_b)^5 (g \cos \theta)^2} \right]^{1/3} \left(\frac{C_{sat}}{\rho_{sat} - \rho_0} \right)^{-1} \left(\frac{C_{sat} - C_b}{C_{sat} - C_b \frac{\rho_{sat} - C_{sat}}{\rho_b - C_b}} \right)^{2/3} \quad [58]$$

Where $R_\lambda := \lambda_f/\delta$, and is found in [30] applying Brown's [78] or Lister & Kerr's [79] wavelength of the Rayleigh-Taylor instability.

According to the former, $R_f \cong 3$, while according to the latter $R_f \cong 3.8$.

β is a dimensionless value that depends on the dissolving material. The values in Eq. 55-58 for hard candy and salt are provided in the same mentioned paper grouped in Table 4.

	β	$C_{sat} [kg/m^3]$	$\rho_{sat} [kg/m^3]$	$\rho_s [kg/m^3]$
Hard candy	1.06	968	1450	1540
Salt	1.96	317	1197	2348

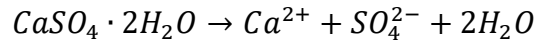
Table 4 Useful values for hard candy and salt to be used in the scaling laws Eq. 55-58 [30].

Before concluding the present paragraph, the author of the present thesis would like to do some remarks regarding the mentioned paper.

First of all, in the mentioned paper's abstract as in its second paragraph and in its eighth figure's caption, an experiment with plaster in aqueous solution is reported. Reading these parts of text, it appears that Cohen et al. performed an experiment of *buoyancy-driven dissolution of an inclined plaster block* and studied its *erosion rate and pattern formation*. But, to the author of the present thesis' knowledge, it is not possible to dissolve plaster in natural convection. This can be explained looking at the chemical formulas.

Gypsum, the soft sulfate mineral introduced in paragraph 1.2, is composed of calcium sulfate dihydrate: $CaSO_4 \cdot 2H_2O$. Gypsum, as explained in the

aforementioned paragraph, and shown in *Fig. 24*, is (somewhat) soluble in water with the following reaction.



Therefore, gypsum is already in a hydrated state with two molecules of water. In order to obtain plaster of Paris, which is calcium sulfate hemihydrate, the crystallization water of the hydrate needs to be removed. Thus, original gypsum is heated at a temperature between 120°C-180°C:



Where the arrow pointing up means that chemical species has been released as steam. Plaster of Paris is $CaSO_4 \cdot \frac{1}{2}H_2O$. If the reagents were heated up to a temperature higher than 600°C, then *dead burnt plaster* is obtained. Dead burnt plaster is nothing else than anhydrous calcium sulphate ($CaSO_4$).

Therefore, when water is added to the kiln-dried gypsum powder, aka plaster of Paris, it is readily absorbed and becomes incorporated back into the crystal structure. During this process the plaster of Paris crystallizes and hardens into a solid, releases heat, and increases in volume slightly. Therefore, it sounds very strange that a buoyancy-driven dissolution pattern may have been formed on the surface of plaster. The doubt is unfortunately not clarified by the lack of images of dissolving plaster in the mentioned paper, even though plots showing results of such experiments with gypsum are provided. Furthermore, the cited supplemental material at the end of the mentioned paper is not openly accessible.

Secondly, the author of the present thesis cannot unfortunately verify *Eq. 55-58*, since the intermediate passages are not provided. They honestly appear dubious due to the absence of dimensionless numbers, i.e., Re, Ra, \dots , and due to the exponentials.

Finally, regarding the second point mentioned at page 78, it could have been expected a priori that the interface recedes faster when the concentration of the bath is smaller. Doing a mental consideration, if only the concentration of the bath is changed and all the other parameters are left constant, then increasing the concentration of the bath, it means that there is more hard candy dissolved in the

bath; therefore the net concentration gradient between the concentration layer and the bath is smaller; therefore the block dissolves slower. The opposite happens for an increase in the concentration of the bath. Remaining on this topic, right before the fourth chapter of the mentioned paper, its authors highlight that the value Ω , defined as $\Omega := [C_{sat} - C_b(\rho_{sat} - C_{sat})/\rho_b - C_b]/(C_{sat} - C_b)$, increases with the bath concentration. This is quite evident rewriting Ω as:

$$C_{sat} - \frac{C_b(\rho_{sat} - C_{sat})}{C_b\left(\frac{\rho_b}{C_b} - 1\right)} \quad [59]$$

Where $C_{sat}, \rho_{sat} = const.$ and C_b can be removed. In this case the first derivative of Eq. 59 depends only on the quantity in curly brackets at the denominator. Recalling what said concerning on how to use a state diagram like the one shown in Fig. 42, it is evident that $\rho_b = f(C_b)$ and that ρ_b increases monotonically with C_b increasing. Furthermore, the lower and upper limits of these two quantities are $\rho_b > \rho_{H_2O} \cong 1000 \text{ kg/m}^3$ and $C_b \leq C_{sat} = 968 \text{ kg/m}^3$ for hard candy and $C_b \leq C_{sat} = 317 \text{ kg/m}^3$ for salt; thus $(\rho_b/C_b) > 1$. Therefore, also this dependence could have been a priori expected.

CHAPTER 3: Experimental Activity

3.1 Hard candy manufacturing

In order to carry out experiments with hard candy, it is obviously necessary to manufacture or, as commonly said, *cooking* it. The recipe used is the one proposed in [36]. Table sugar, corn syrup and water are combined together in volumetric proportion 8:3:2 respectively. Every candy is made of these ingredients. The author of the present thesis stresses that hard candy is not caramel [80], as sometimes wrongly found in the literature. Indeed, caramel is also made of milk or some of its derivatives. Due to the presence of proteins of milk's derivatives, the reactions involved in the manufacturing process are thus different, as will be explained in a while. To provide repeatable or comparable results, it is mentioned that the sugar and the corn syrup used in author's experiments is the fine-grain white table sugar produced by *Südzucker*[®] and the corn syrup produced by *Chung Jung One*[®], whose respective products are shown in *Fig. 46*. Demineralised water is used.



Figure 46 Sugar and corn syrup used in the following experiments.

There are different types of candies, like chevy-, cotton-, gritty-, gummy-, hard- or rock-candy, just to mention some. They all start by the same ingredients, but the final appearance is different and mainly dependent on whether sugar crystals are given enough time to form in the process [81] [82]. The time given to form also

Each grain of sugar consists of a small crystal made of an orderly arrangement of sucrose molecules. Sucrose is in turn a disaccharide made of glucose and fructose. When table sugar is put in contact with water, dissolution starts. The dissolution process involves two steps: firstly, water molecules bind to sucrose molecules; secondly, the (globally null) electrostatic distribution of the bound sucrose-water molecules, pull the sucrose molecules away from the sugar crystal and into the solution. This process, though, happens only for a small portion of the table sugar which has been put together with water and corn syrup in the pot, because sugar is present in supersaturated concentration. This is a chemical dynamic equilibrium. In order to dissolve more sucrose molecules, since the dynamic equilibrium is affected by temperature, it is necessary to increase the temperature of the system. Indeed, as stated by *Le Châtelier's principle*, a system that is shifted away from equilibrium acts to restore equilibrium by reacting in opposite to the shift. So, an increase in temperature causes the system to decrease its energy, in an attempt to bring the temperature down. Because the breakup of chemical bonds always absorbs energy, it cools the system down, so more sucrose molecules break apart and dissolve in the solution.

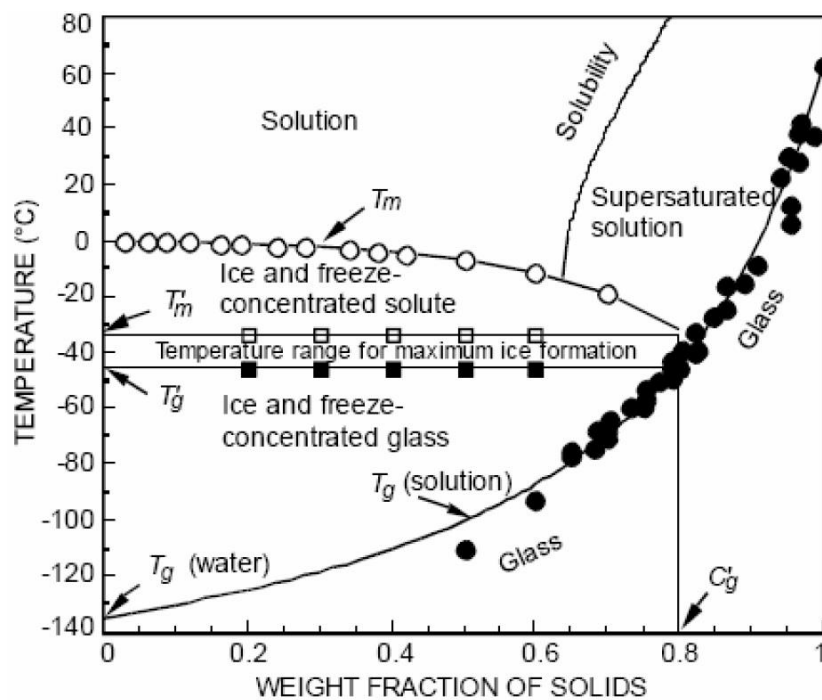


Figure 49 State diagram of sucrose. Adapted from [83] and shown in [80]. (Keep in mind that this is a state, and not a phase, diagram, since T_g is not a thermodynamic equilibrium event, in contrast to the melting transition).

But as shown in *Fig. 49*, when providing heat, it is necessary to take into account the corresponding state of sucrose. Indeed, as also mentioned in *Fig. 47*, increasing too much the temperatures means breaking even the intramolecular carbon bonds of sucrose molecules. This chemical event is referred to as *caramelization*. It is therefore now clear that providing heat to increase the dissolution process and providing (further) heat to break the intramolecular C-bonds of sucrose molecules are actions that should keep separated to obtain a final hard candy block with the wanted properties for the experiments discussed in the following chapters. Regarding the heating phase of the manufacturing process, it was mentioned before that caramel is involved in a different reaction with respect to hard candy. Indeed, since in the case of caramel there are milk proteins within the reagents, they take part in a reaction with the reducing sugars. This reaction is called *Maillard reaction*, happens at lower temperatures than the caramelization temperature and is responsible for the flavour and colour in most of bakery products.

Having concluded the chemical description of the heating phase of the manufacturing process, it is worth mentioning what happens in the so called cooling, setting or relaxation phase.

Once the saturated solution starts to cool down, it becomes supersaturated. A supersaturated solution is unstable so, as temperature decreases, sugar comes out of the solution forming crystals. The lower the temperature, the more molecules join the sugar crystals. Since a crystal is generally formed by a *crystal seed*, mechanically stirring the solution causes the sucrose molecules within the solution to be pushed into one another, forming crystal seeds throughout the syrup. This should be done, after the syrup has cooled down below 50°C. The resulting crystals are smaller when more of the crystal seeds are present, because the sucrose molecules can join any of a larger number of crystal seeds. Another solution to mechanically stirring is cooling the solution too quickly. This is what is done to manufacture candy blocks, which are then used in the present experiments. This can be done simply cutting off abruptly the heating source and leaving the viscous syrup to cool down in a mould at room temperature. In this case the syrup does not have time to form enough intermolecular interactions to grow into larger crystals. The rapid cooling has a second effect: the chemical structure remains amorphous. And

when an object has an amorphous structure, which is an irregular structure with no pattern, it has the property to appear glassy. Even if the overall structure is almost irregular, there can be some small regions where crystallization had time to happen. This can be proved by putting the hard candy block in a freezer and lowering the temperature slowly in order to do not crack the block due to a temperature shock. After a while, even if the cooling is done very gradually, the block will crack since these ordered regions have different orientations with each other and can thus induce a crack plane and a crack path between them. This can finally explain why when the caramelization temperature is reached or even passed, the final syrup is very less viscous, takes a way longer time to solidify and looks dark brown or black. In this case the intramolecular bonds of many sugar molecules are broken. So, the syrup cannot form at all intermolecular interactions to grow into crystals. Therefore, in this liquid state the broken molecules have even greater freedom to move and thus the internal frictional force between contiguous layers is even fewer; therefore, the lower viscosity. Burnt candy, assuming there are no bubbles within it, since it has no ordered regions, does not crack in a freezer. The author of the present thesis even left a block of burnt hard candy for a couple of weeks in a freezer of the laboratory and there were observed no cracks in it. On the other hand, doing the same with non-burnt hard candy, leads to the formation of cracks in the hard candy block within the first 24 hours.

Having said so from a molecular point of view, is here proposed a brief description of the corresponding actions to be performed in the cooking process.

The aforementioned ingredients, in the aforementioned volumetric proportion, are put in a pot and heated. The electric heater available allowed to set the power of the temperature to be reached. At the beginning, maximum power is set in power-mode, or a maximum temperature of 170°C is set in temperature-mode. The mixture is mechanically stirred every now and then, especially pushing the mixture from the inner perimeter of the pot toward its center. This is done because the temperature at the base of the pot is not uniform and because bubbles in the center tend to push the mixture toward the inner circumference of the pot. The mixture boils twice: at 100°C due to the boiling temperature of water and then there is a second increase

in bubbling at around 155°C-160°C due to the boiling of water molecules originated from the breaking of some sugar bonds. If power-mode was selected, when the first boiling is observed at 100°C, then it should be switched to 170°C temperature mode. Cooking is stopped when the syrup turns to be slightly-yellow/yellow. The syrup is poured into a silicon mould, while moving gently the pot from a side to the other to easily level the viscous syrup. The mould is put in a vacuum chamber in order to remove bubbles trapped within the viscous candy syrup. Depressurising the candy syrup, its volume will expand considerably. For this reason and to keep the candy syrup inside the lateral walls of the mould, the depressurisation process is done step by step. This allows the viscous syrup the needed time to expel the bubbles trapped within it and thus regaining a smaller volume. At the beginning, the syrup is depressurised at 800 mbar. Usually not more than ninety seconds are needed to the candy syrup to expel many bubbles and set to a certain height in the mould. Then, depressurisation to 700 mbar is reached. It is waited a few more, like in the previous step. Then, after these two fast and small depressurisations, a big depressurisation is set to reach 500 mbar. The sugar syrup stays at this pressure level for longer, not less than five minutes. If the escaping bubble-activity through the free surface of the syrup calms down, then a smaller depressurisation is applied in order to keep always the syrup in a bubble-escape state, thus also to prevent the syrup not passing from a viscous state into a rubber-like behaviour. Since it tends to increase viscosity very fast if left free to relax. Anyways, not more than eight minutes should pass since 500 mbar were reached, otherwise the syrup would be too viscous to incorporate the holder without deforming the free surface. Therefore, the valve of the vacuum chamber is opened and the holder is set in the mould. Before doing so, the holder is inserted in its support. The support of the holder is a holed metal block. The holder passes through the hole and is blocked by a lateral screw (*Fig. 58*). It is suggested to lower the holder inside the viscous syrup with the base steeply inclined, in order to push the smallest volume as possible and preventing a major volume of air gets trapped right below the base. It is strongly suggested to lower vertically the holder and minimize as possible horizontal movements of the holder in the viscous syrup. The holder should be put closer as possible to the smaller side of the mould to maximize the interrogation area for the

frontal photos. But also not too close; the rule of thumb is that there should be at least a centimetre and a half. The holder can be even positioned closer to an edge than the adjacent. The same rule of thumb applies considering the distance from both the sides having in common the edge. But this should be done only after some experience has been acquired, since an holder closer to an edge than the other has higher chances to crack the hard candy after a while. The base of the holder should not be placed too close to the base of the mould. As will be explained in the next paragraph and as already anticipated in the previous one, the regression rate at the downward surface is faster than the regression rate of the surface facing upward. Therefore, the base of the mould should be closer to the free-surface of the viscous syrup than to its base in contact with the mould. Till now the holder's support is fixed through the blockage of the screw close to the holder extremum which is opposite at the base. This allows to have an available longer length of the holder to manoeuvre it. A rule of thumb is to position the base at $2/3$ of the total height of the liquid syrup, with the reference system starting from the internal base of the mould, or instead at one centimetre deep from the free surface. Obviously, with increasing experience, more accurate positions can be better estimated. To do so, once the base of the holder is already within the syrup, the screw blocking the height of the metal holder along the metal support is unscrewed. The metal holder is left leaning on the walls of the mould, and the desired depth of the base is chosen by raising or lowering the holder through the hole of the metal holder. The screw is thus tightened and the height of the base set. Anyways, after the holder is placed in the mould, the vacuum chamber hatch is closed and an internal pressure of 300 mbar is set. Always keep in mind that, even if the holder was inserted inclined, a bubble might have been trapped right below the base of the holder. So, during the fast depressurisation to 300 mbar, the operator should be ready to stop the vacuuming process if a bubble starts raising out from the base of the holder and expanding way faster than the smaller ones within the viscous syrup. The process to reach 300 mbar can resume as soon as this bubble raises the surface and shrinks by dissolving the trapped air in the vacuum chamber environment. When this pressure value is reached, the syrup should be left in this condition for a little bit less than five minutes. Anyways, it is suggested not to keep using the vacuum chamber for more than twenty minutes

since the mould was firstly put in it right after the casting. The process may even be shortened if the escaping bubble activity is seen to calm down. Indeed, this is a symptom that candy syrup is getting quite viscous. The more viscous candy syrup gets, the more difficult it is to extract bubbles from it and also the more difficult it is to resume the initial volume condition once the vacuuming process is stopped. Therefore, whether there is even a doubt that at a preceding instant of the twentieth minute since the start, the escaping bubble activity is less energetic, the vacuuming process should be stopped immediately. Basically, as more time passes, the candy syrup cools down and since it is in a supersaturated condition as previously said, as can be seen from *Fig. 50*, its viscosity changes very rapidly [84].

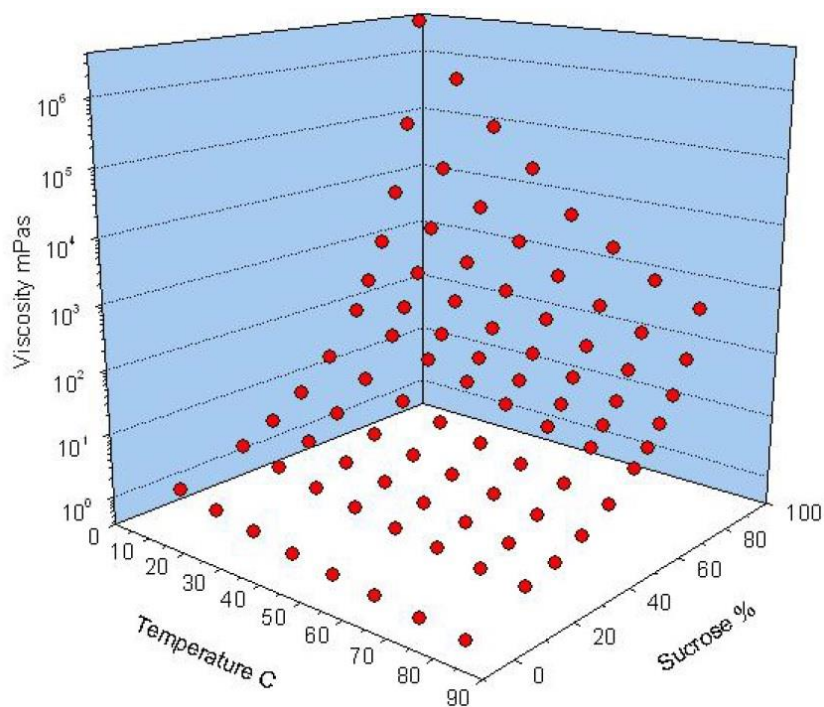


Figure 50 Dependence of the dynamic viscosity of sucrose solutions from temperature and weight concentration $\mu(T, wt. \%)$. Adapted from Table 6.3 in [85] and shown in [80].

The hard candy setting time is at least of three hours and a half starting from the end of the vacuuming. Obviously if more hours are waited the better it is. But waiting more than six hours, as some papers report, is neither necessary. Also because the longer time passes, after the sixth hour, the more probable is that the hard candy block may crack. If this is the case, and the temperature of the room has always been constant, it could be related to the humidity of the room. Basically, the crack may originate because the hard candy block is dehydrated with respect to the

humidity of the room. This implies that, unfortunately for the operator working with hard candy, it is not suggested to manufacture the block the day before. It is also worth noticing that, in order to reduce the probability of cracking when dropping the hard candy block in the aquarium, it would be better if the minimum water temperature is at least at 19°C or little higher. For the best reproducibility of experiments, water temperature should also neither vary too much. In the experiments shown in the present thesis, the usual water temperature range is 18°C-23°C.

In conclusion, it is worth answering a question that may arise reading the present paragraph: is the vacuuming process really necessary?

The answer obviously depends on the application. For the experimental study described in the present thesis, the answer is affirmative.

This is evident by looking at *Fig. 51*. The hard candy block shown in the figure is still rich of air bubbles. The bubbles are dispersed all over the face (front photo) and at different heights from the base (lateral photo). Furthermore, big bubbles are found at the faces of the parallelepiped, since they solidified first due to the contact with the cooler surface of the mould. This is obviously even worse for doing experiments aiming at studying the genesis of patterns on a surface.

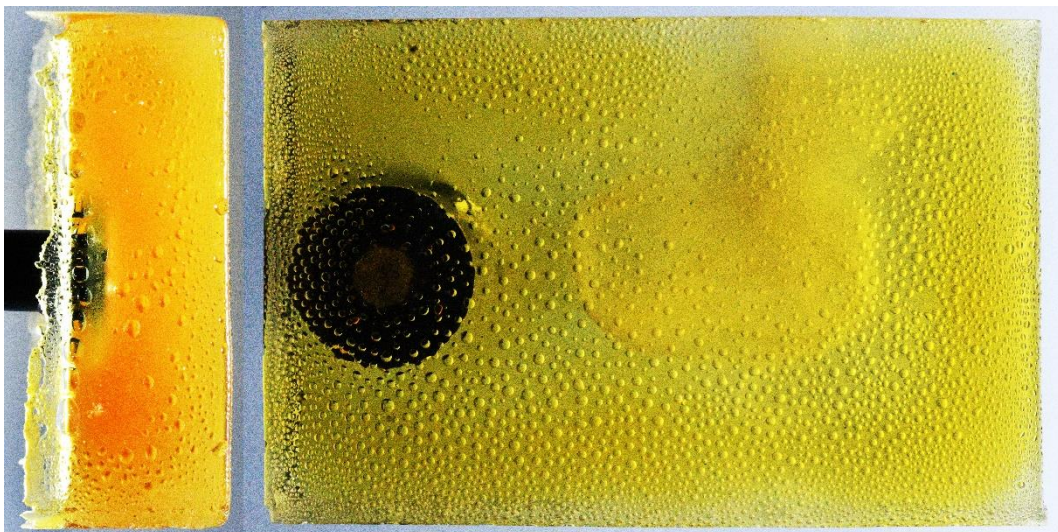


Figure 51 Lateral photo (on the left) and frontal photo (on the right) of the same hard candy block, whose dispersed air bubbles were not removed with the vacuum chamber. The base of the block is 134 mm long and 90 mm width.

3.2 Experimental Set-up

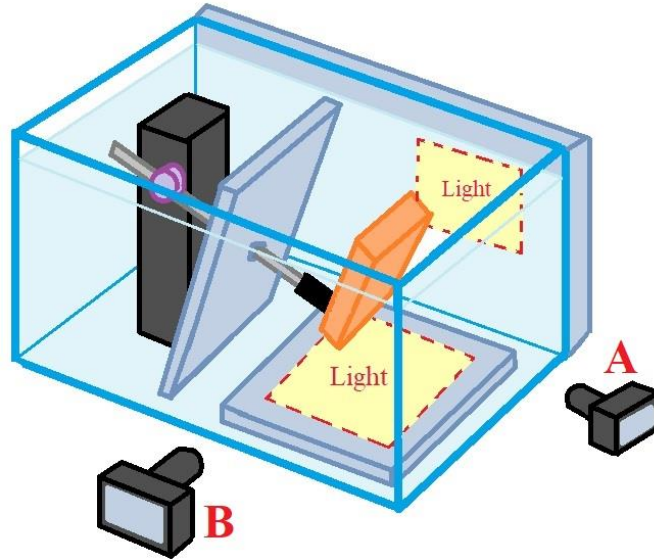


Figure 52 Illustration of the experimental set-up used for the experiments.

For the experiments in natural convection, it was used a water tank whose internal length and width are respectively 78.3 cm and 38.4 cm. The water height was set for all the experiments at 44.4 cm from the base of the tank, by placing on one surface a strip of tape.

For the nomenclature, the point of view of camera *A* is the *frontal*, while the point of view of camera *B* is the *lateral*.

A *Nikon D850* camera has always been used for taking the frontal photos. While for the lateral photos, it was used at times a *Nikon D850* or a *Nikon D5100*. Because of the inclination of the hard candy block, a wide-angle lens is suggested for the frontal photos. This allows to have a greater depth of field and thus have in focus all the surface ranging from the top to the bottom frontal face of the block. The lens mainly used for the frontal photos was a *Nikon Nikkor 50mm f/1.8D*. Rarely it was used instead a *Sigma Macro 50mm f/2.8 EX DG*. For the lateral photos is preferred instead a telephoto lens, in order to have a smaller depth of field. This allows to have in focus only the perimeter of the lateral surface of the hard candy block and thus not to take into account patterns or plumes detaching from the middle of the

frontal face. The lens used for this purpose was a *Carl Zeiss Milvus Makro Planar 100mm f/2 ZF.2*. All the lens mentioned thus far are fixed focal lenses.

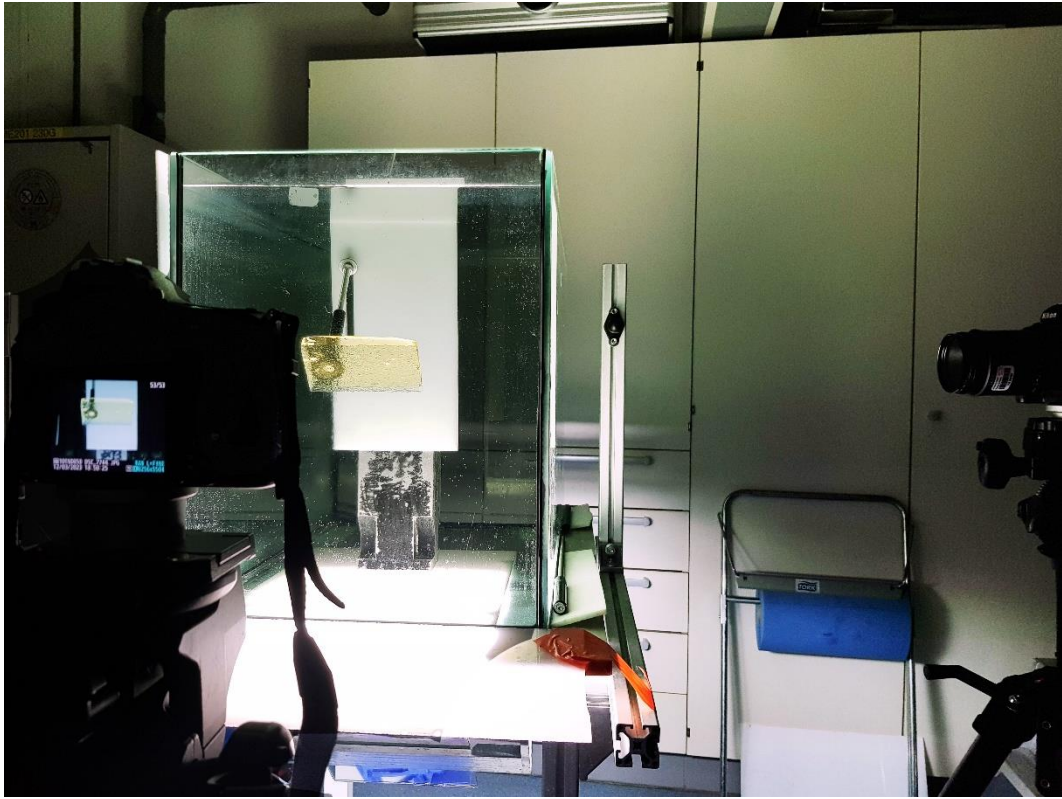


Figure 53 Photo of an experiment taken behind the point of view of camera A.

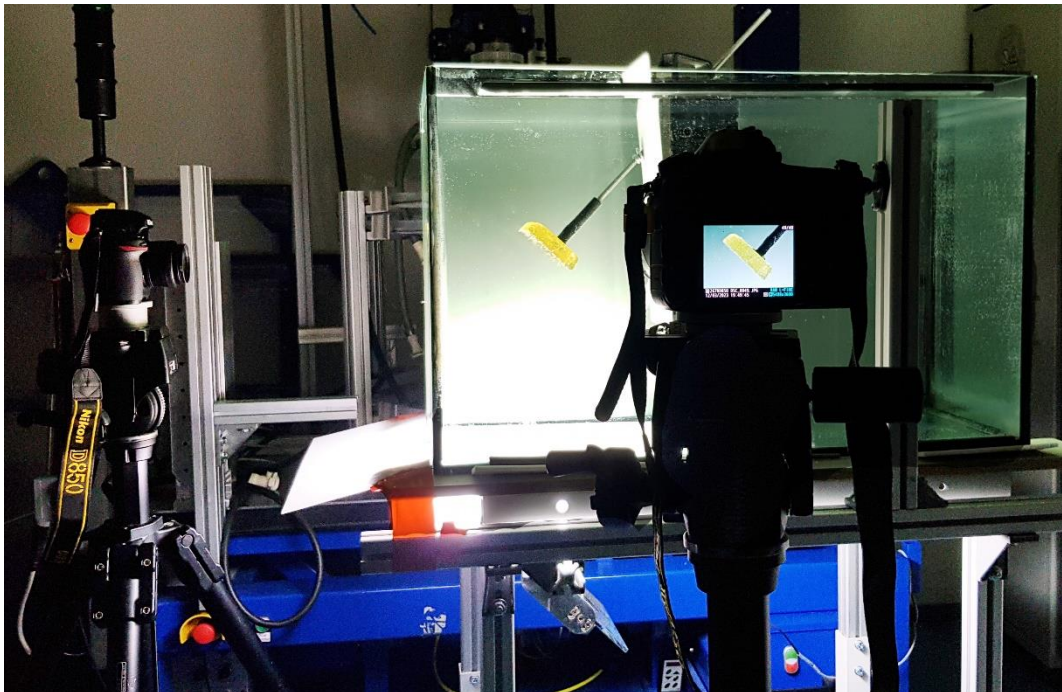


Figure 54 Photo of the same experiment taken behind the point of view of camera B.

Flexible moulds made of silicone rubber were made from scratch by the author of the present thesis. Two moulds have a rectangular base of size 133.5mm x 89.9 mm and 147.9 mm x 92.2 mm, respectively.

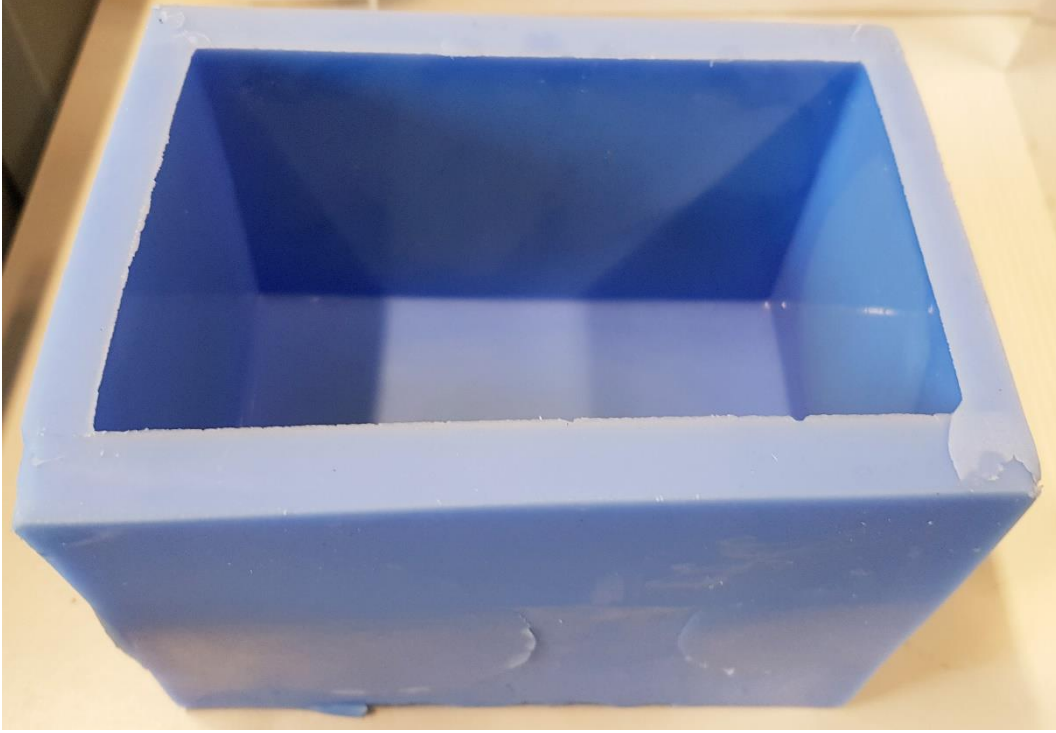


Figure 55 One of the two moulds with the rectangular base. (It appears distorted only in photo).

Also some flexible silicone-made bases, which can be leaned on the base of the two aforementioned rectangular moulds to change the geometry of the frontal face of the hard candy block, were manufactured. These flexible bases allow to have a final hard candy block with a 2D-harmonic surface or a convex surface (whose curvature is made from a circumference of diameter 17.0 cm). The 2D-harmonic surface is a square in plan view. It was realised pouring liquid silicone hardeners on a negative surface which was 3D printed in resin. The surface is described by the following function, where x, y, z are respectively the length, with and depth coordinates with respect to the horizontal plane of the mould and $\mathcal{L} = 95 \text{ mm}$ is the length of the side of the mould.

$$-2 \leq z[\text{mm}] \leq 2 - \left(\cos\left(5\frac{x}{\mathcal{L}} \times 2\pi\right) \cos\left(5\frac{y}{\mathcal{L}} \times 2\pi\right) \right) \quad [60]$$

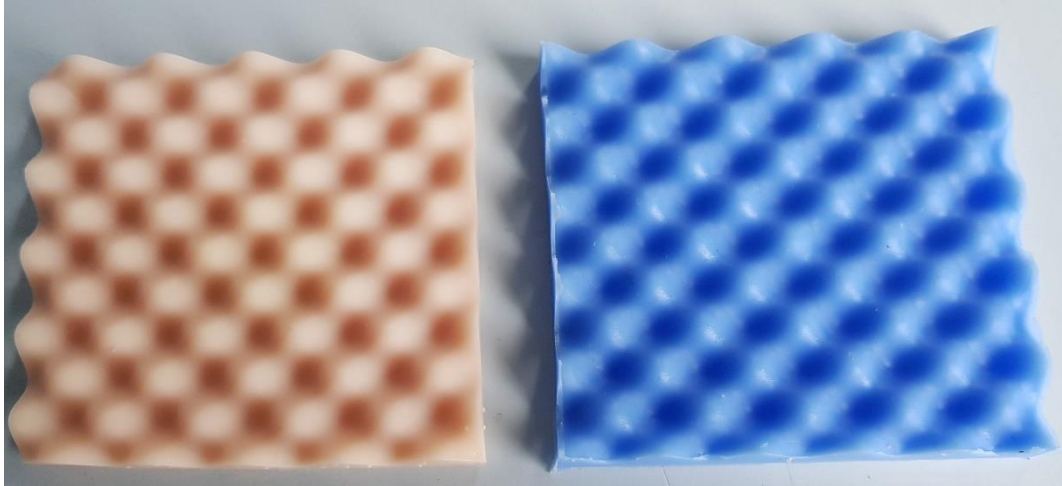


Figure 56 Harmonic surface. On the left there is the (negative) resin print on which the silicon mould base on the right was manufactured.



Figure 57 Concave mould base to realise a hard candy block with a convex face. In cross-sectional view the surface is an arc of circumference of diameter 170 mm. The two lines of points made of the extrema of the arc of circumference are 125 mm apart.

There were produced also silicone moulds bases allowing to have a V- or U-shaped longitudinal incision on the surface. The former (*Fig. 58*) more for an interest in the regression rate driven by bubbles (*Fig. 59*) than for tilting the local plane of the face pointing downward with a second angle.



Figure 58 “V-shaped” base mould.



Figure 59 Regression rate influenced by upward pushing bubbles.

Even if the configuration illustrated in *Fig. 59* appears at first banal, it is worth saying that there is an increasing interest in shapes sculpted by bubbly flows and not so much can be found in the literature. A bubble does not sculpt a surface through its upward pushing force, but rather by its interaction with the concentration or melting boundary layer. Indeed, extending this configuration to the case of melting ice would be of interest too since the thermal conductivity of air is lower than the one of water. Therefore, a bubble soon lies against a bump in the interface

from which it can be easily displaced laterally by the vigorous underlying thermal convection [41]. The curve connecting all the vertices of the cross-sections shown in *Fig. 59* becomes thus corrugated as time passes. Therefore, the interaction between the local lower temperature conductivity and the higher wetted surface area is not banal a priori.

Fig. 58 is also useful for showing the metal support of the holder (in black), which is needed till the candy syrup completely solidifies. The holder and its circular base are in plastic. The material and shape were not decided by chance. Plastic has a lower thermal conductivity than metal, therefore it does not vary its temperature when in contact with cooling hot candy syrup. This prevents the formation of cracks in the candy block which would be caused by thermal shock in case a metal holder were used. The circular shape of the base of the holder is a continuous surface without sharp edges. This furtherly prevents the formation of cracks, by minimizing nucleation points at eventual edges.

The *V-shaped* base mould shown in *Fig 58* has a dual *U-shaped* base mould.

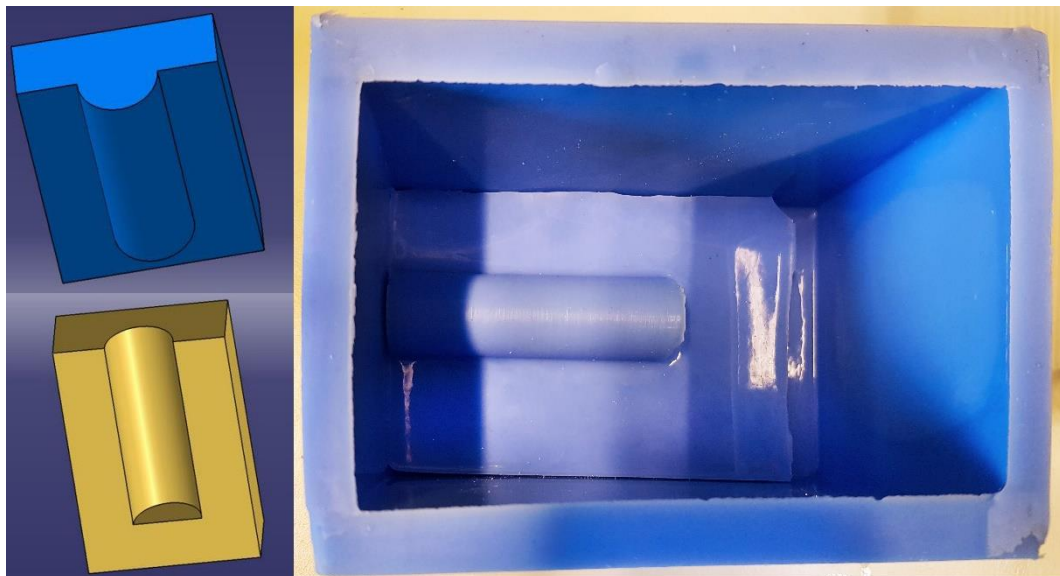


Figure 60 “U-shaped” base mould.

The base mould shown in *Fig. 60* allows to create a candy surface with a concave surface. The cross section of the concavity is a semicircumference with a diameter of 20 mm.

In addition to the previous moulds, there were realised also other three moulds. Anyways, they were not used for the experimental activity described in the present

thesis. A couple of the three moulds are cylindrical moulds with diameter of 52.8 mm and 34.7 mm respectively. The reason behind the non-canonical length is to be found in the cylindrical cans commercially available that were used as negative mould to manufacture the silicone positive mould. While the final mould created allows to create a half cross-section of a pipe.

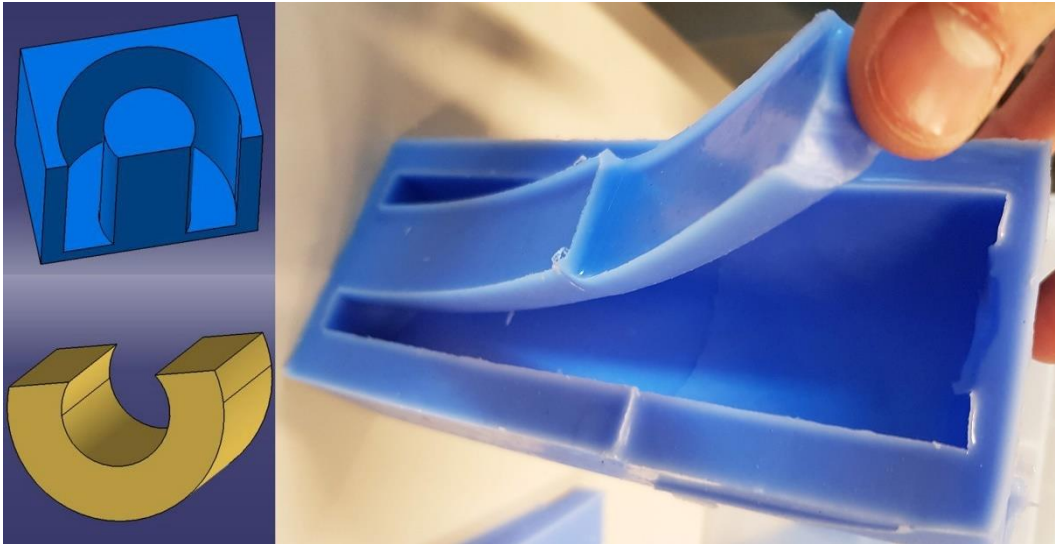


Figure 61 Mould to realise a half cross-section of a pipe.

In addition to the mould shown in *Fig. 61*, it should be remarked that a covering part exist. Basically, the complete mould is made of a covering and of the piece shown in *Fig 61* in the right photo. The idea is that at the beginning the two pieces should be kept joint using some tape. During the casting, candy syrup is poured from the hole which is on the right of the mentioned photo and at the top in the upper-left sketch. The mould is so placed vertically in the vacuum chamber with the hole pointing upward to extract the bubbles within the candy syrup. Once the syrup is solidified, the tape should be removed, together with the covering. Since the silicone mould is flexible, as shown evidently in *Fig. 61*, there should be no problem in extracting the half-pipe from the mould.

Since this mould was not used for experiments and that no tests, especially using the vacuum chamber, were made, the author of the present thesis expects that possible improvements are applicable and does not exclude a priori that some may be even necessary in order to use it. It was thought to provide anyways a brief description of the mould as a reference for possible future suggestions or implementation, or for sparking interest on similar mould geometries to realise

shapes that allow to study melting or dissolving internal pipe surfaces, as was anticipated in *Fig. 1*.

Before concluding the present paragraph, it is necessary to explain the factor used in the volumetric proportion of the hard-candy recipe and the water salinity levels chosen.

Regarding the former, this factor is stated here only for eventual readers that are continuing the experimental activity at the *Physics of Fluids* group of the *University of Twente* who may use some moulds created by the author of the present thesis. It is obvious that if different moulds are created in the meantime, then the internal volume of the mould is varied together with the factor. The ingredients are measured with a chemical beaker, their volume is expressed in millilitres.

Flat block mould	400:150:100 mL
Harmonic surface mould	480:180:120 mL
Curved surface mould	480:180:120 mL
U-, V-shaped sliced surfaces mould	640:140:160 mL

Table 5 Volume of hard-candy ingredients needed in base of the used mould.

Thanks to a balance accurate to the centigram, those can be translated in:

$$200 \text{ mL table sugar} = (196.82 \pm 0.15) \text{ g}$$

$$200 \text{ mL corn syrup} = (285.70 \pm 2.5) \text{ g}$$

$$200 \text{ mL NaCl} = (294.17 \pm 2.6) \text{ g}$$

Table 6 Volume-to-mass translation of ingredients in Table 5

The cited sodium chloride is necessary for changing the salinity of the water in the aquarium. Three levels were chosen for the experiments: no salt, 400 mL, 800 mL, which corresponds respectively and to salinity $S=0$ ppt, $S \approx 4.41$ ppt, $S \approx 8.82$ ppt, according to the formula:

$$S[\text{ppt}, 10^{-3}, \text{‰}, \text{mg/L}] = \frac{g[\text{NaCl}]}{g[\text{H}_2\text{O}]} \cdot 1000 \quad [61]$$

This allows to calculate the density of the water in the aquarium, thanks to the empirical formula given by Millero and Poisson [86], which since 1980 is the formula officially adopted by UNESCO as the International one-atmosphere equation of state of seawater.

3.3 Evidence of surface patterning

As soon as the hard candy block is placed tilted in the aquarium, stripes appear on the surface facing downward. For brevity, the surface facing downward and the surface facing upward will be called from here on the *frontal surface* and the *upper surface*, respectively. *Stripes* is the terminology used in [30], but since a roller is not expected at the point where this pattern originates and propagates downstream, these patterns may be called as *grooves* using Allen's nomenclature (*Fig. 32* and *Fig 33b*) [57].

This vertical flow pattern covers all the length of the frontal surface. Even if it appears regular in space, it is expected to be hydrodynamically unstable and does not last long. There is a critical distance along each groove where the layer under the inclined plane detaches. Looking from a lateral point of view, the grooves appear as a layer moving downward parallelly to the frontal surface, while the detaching points along the grooves are seen as plumes originating here and from the leading edge, alias upper side, of the frontal surface. At the beginning, this pattern is mainly a flow pattern, but it soon starts leaving corresponding traces on the surface. Indeed, it should be remembered from paragraph 2.2 that the flow field associated with a mature groove consists of a pair of oppositely rotating and relatively weak streamwise vortices reattaching to the bed on the floor of the mark, thus there is, even if small in magnitude, a sculpting wall shear-stress. In general, the flow pattern is more difficult to be taken in a photo with respect to the surface one. Some hints to do that will be given in the next paragraph. Anyways, the vertically predominant flow instability starts leaving on the surface some patterns which do not interfere with each other and that are well separated by big surface areas still flat. This configuration looks like the top-left sketch of *Fig. 40*. In the areas lacking marks, the grooves are more pronounced and still present. The grooves gradually disappear only after these small surface marks become visible along their vertical direction. Therefore, the pattern associated to the fluid structure is replaced by the corresponding superficial pattern. This implies that the superficial patterns spread also in the areas previously lacking them. This is equivalent to the top-right stage sketched in *Fig. 40*.

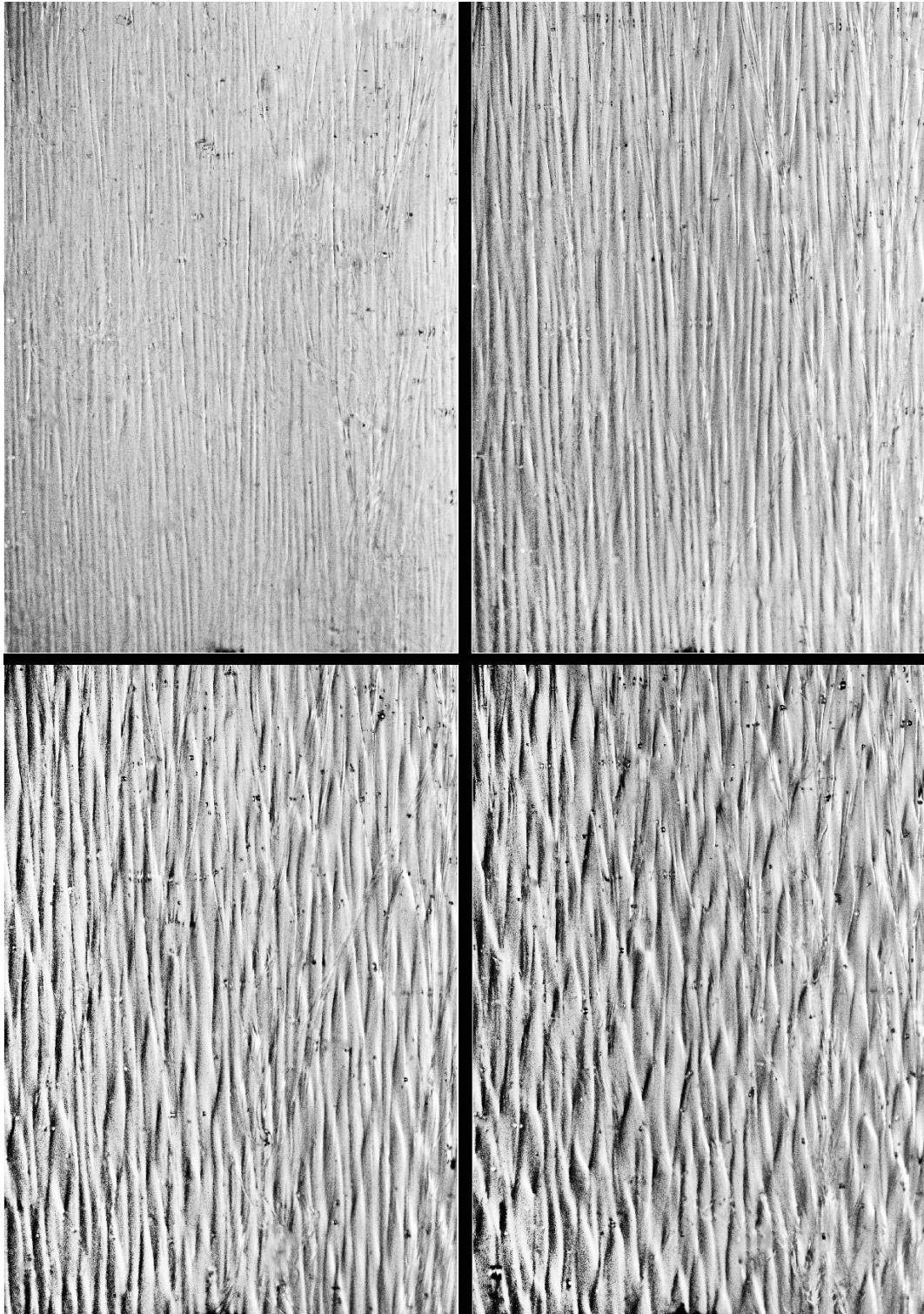


Figure 62 Evolution in time of the same fixed detail of surface. Each photo is taken after six minutes the preceding one. Photo order is: top-left, top-right, bottom-left, bottom-right. The block is tilted 60° with respect to the horizontal line and the water salinity is $S = 8.81$ ppt.

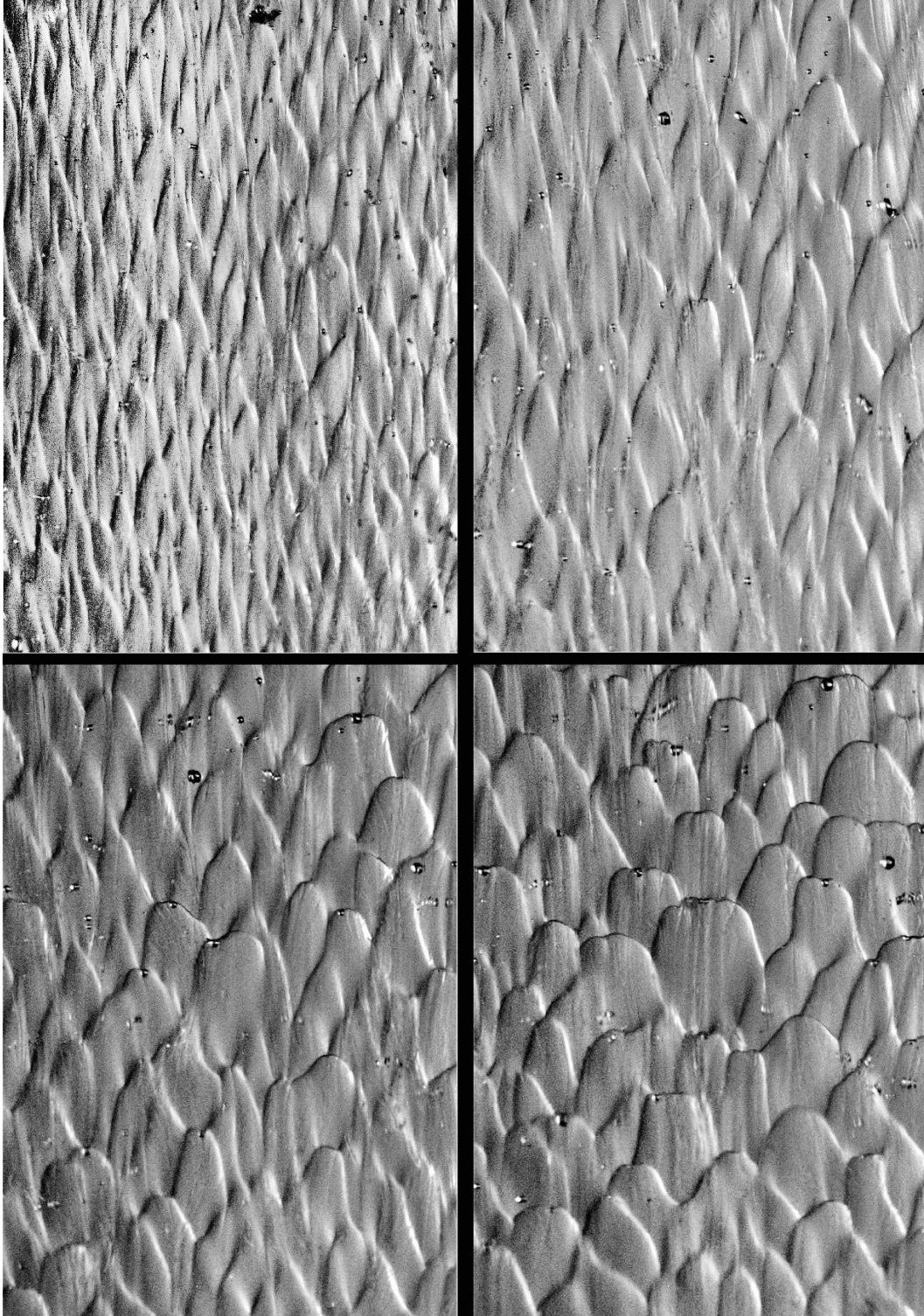


Figure 63 Evolution in time of the same fixed detail of surface of Fig. 63. The top-left photo is taken after six minutes the bottom-right photo in Fig. 63 was taken. The other three photos are taken at an interval of twelve minutes starting from the top-left photo. Photo order is: top-left, top-right, bottom-left, bottom-right. The block is tilted 60° with respect to the horizontal line and the aquarium water salinity is $S = 8.81$ ppt.

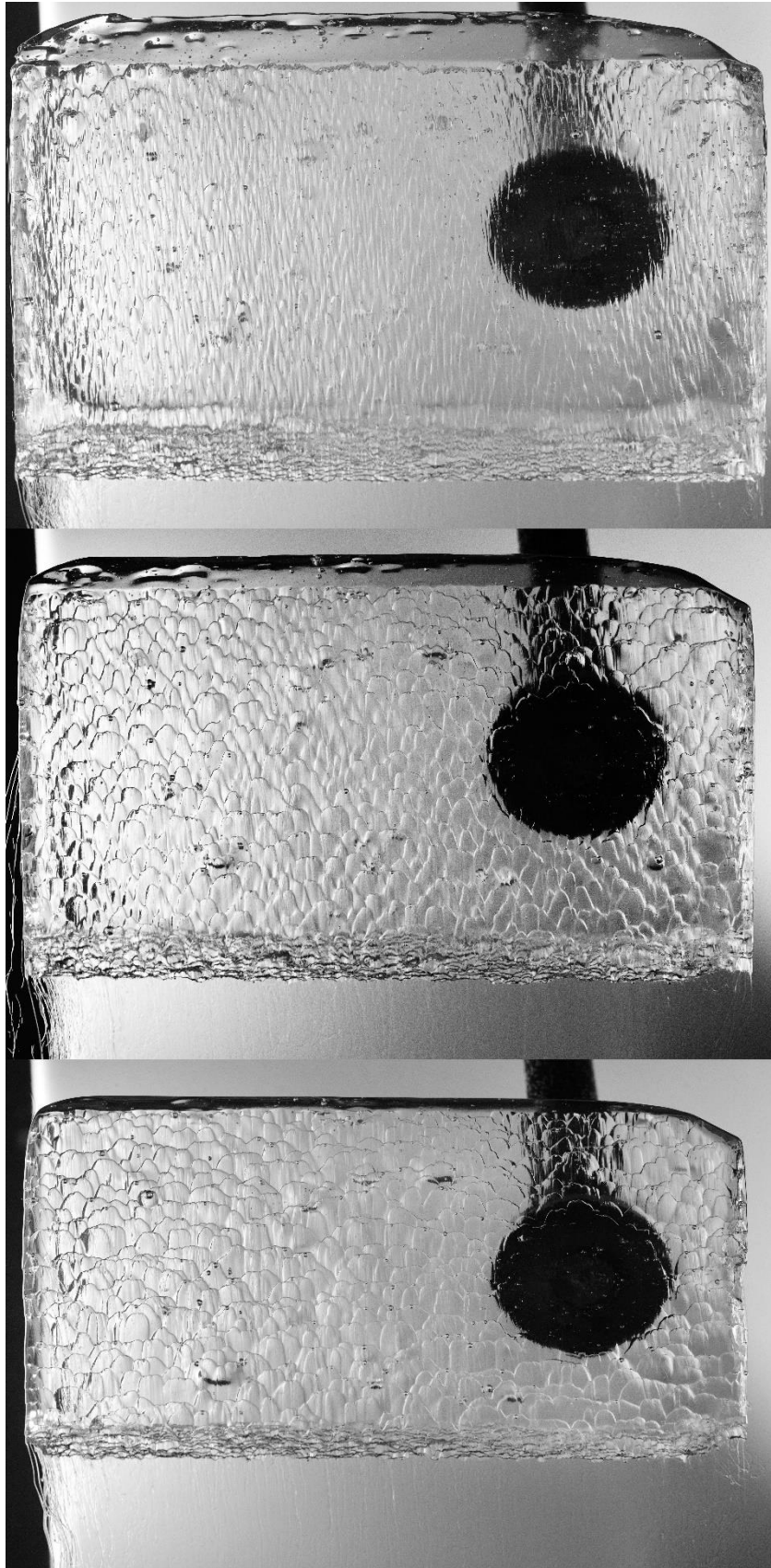


Figure 64 Evolution in time (from top to bottom) of the surface pattern on a hard-candy block inclined 60° with respect to the horizontal line with no salt added to the aquarium water.

It is worth noting the time interval between two sequential photos in *Fig. 62-63*. The pattern evolution rate is high at the beginning, due to the unstableness of the flow structures and relative surface pattern. While the rates decrease notably at an advanced time in an experiment. When this happens, like in the last two photos of the bottom line in *Fig. 63*, as will be quantitatively proved in the conclusive chapter, the wavelength of the pattern seems not to vary. Therefore, even if the final structure may appear more chaotic with respect to the seemingly equally spaced vertical grooves in the top-left photo of *Fig. 62*, the grooves are the representation of an hydrodynamically unstable flow and are visible only for a limited time interval, while the scallops are the visual result of the self-sculpting phenomenon which tends in time toward a hydrodynamically stable condition. This seems to be the condition of the bottom-right sketch in *Fig. 40*.

Observing the experiment from the point of view of the lateral camera, as anticipated in [30], the regression rate of the frontal and upper surfaces is higher in the upper region, alias the region close to the trailing edge of the surface, and it seems not to vary noticeable at the base, as shown in *Fig. 65*. This is related to the higher local concentration gradient that there is in the upper region.

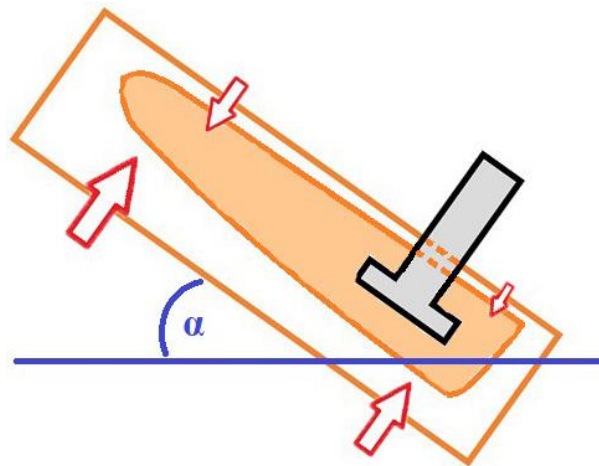


Figure 65 Sketch of the different regression rate depending on the surface considered and on the coordinate along the surface. Representation of the system of reference for the angle used.

Furthermore, the regression of the frontal region is tremendously greater than the regression rate at the upper surface, showing its dependence with the surface patterning. Indeed, the upper surface does not show any surface pattern, remaining smooth for all the duration of the experiments.

It was generally observed that, the higher the inclination, the longer it takes to reach the transition from grooves to scallops; in agreement with the Rayleigh-Taylor instability of a layer under an inclined plane [26].

During the experimental campaign, it was verified that the critical angle in order to have scallops is $\alpha_{crit} = 90^\circ$. This was done by using the base mould shown in Fig. 57 to create a frontal surface which is an arc of circumference and by placing this surface such that the axis of the circumference is horizontal, in order to have a local and continuous variable angle along the path of the solute layer. It was observed that scalloping forms only on the surface of the lower volume with respect to the horizontal line. In other words, this is the point where the local angle is $\alpha = \alpha_{crit} = 90^\circ$, since the normal to the corresponding local surface is exactly horizontal.

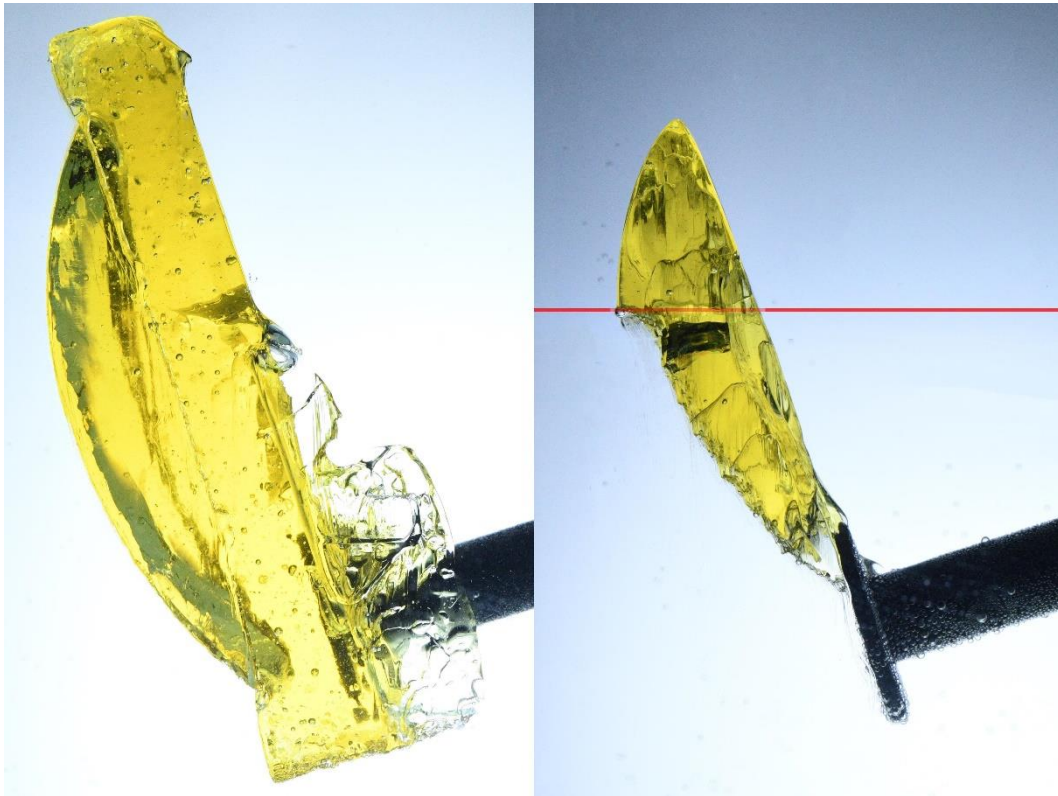


Figure 66 Lateral photos of the experiment to verify the existence and the value of α_{crit} . The two photos have the same spatial resolution. The photo on the right is taken 88 minutes after the first photo at the beginning of the experiment, which is shown on the left.

At the extreme case of $\alpha = 90^\circ$, which corresponds to the hard candy block completely vertical, there is no scalloping induced by the hydrodynamic instability of the concentration layer. After a long time, it might even happen that patterns are able to nucleate. But in this case, it is a phenomenon more driven by eventual

inhomogeneities that arise or are present since the beginning on the surface. Indeed, it is a very local phenomenon and the local patterns do not exhibit the properties of a homogeneous assemblage (*Fig. 38*).

This is helpful in anticipating one of the points that will be listed and motivated in the conclusive chapter: scalloping due to self-sculpting is not merely a pattern driven by inhomogeneities as Allen and the defect model theory assume.

As mentioned a moment ago about the scalloping on a vertical surface arising only due to the presence of inhomogeneities, are hereafter shown some photos (*Fig. 67*) of an experiment using a hard candy block whose internal bubbles were not removed through the vacuuming chamber. This allows to use the bubbles as initial inhomogeneities. In this case, four different phases in the development of the surface morphology are noticed. In a first phase (*Fig. 67a*), a fluid pattern similar to the aforementioned *stripes* is visible. If part of the print left from the bubble is a curve with only one maximum and continuous, i.e., a top-half semicircumference, only the two stripes originating at the horizontal extrema of the perimeter of the bubble are visible. In this case these two extrema are also the two points of local minimum of the top-half part of the print left by the bubble. If instead the part of the sign above the horizontal line passing through the two most distant points has more than a local maximum or is discontinuous, then the stripe originates also at the point of local minimum (as before, but in more than one then) or of discontinuity. It is evident that the stripe is none other than the separated solute layer. The point of separation is thus the top of the visible stripe. Differently from the stripes noted in [30] and mentioned at the beginning of the present paragraph as *grooves*, those do not cover the entire surface, but become less visible downstream. At a point, they are no more visible, symptom that the layer reattached. Basically, bubbles at the surface simply leaves a shallow cavity, as in Allen's model shown in *Fig. 30* and with the same fluid mechanics mechanism of separation. The vorticity associated to the separation pushes horizontally the flow. This works in constructive superimposition of effects with the lateral displacement of the layer induced by the top-half contour of the print of the bubble. Therefore, in a similar mechanism to the one shown in *Fig. 33*, the flow is driven from the maximum of the top-half print

toward the left and right local minima, or points of discontinuity, of the top-half rim respectively. And the following wake is seen.

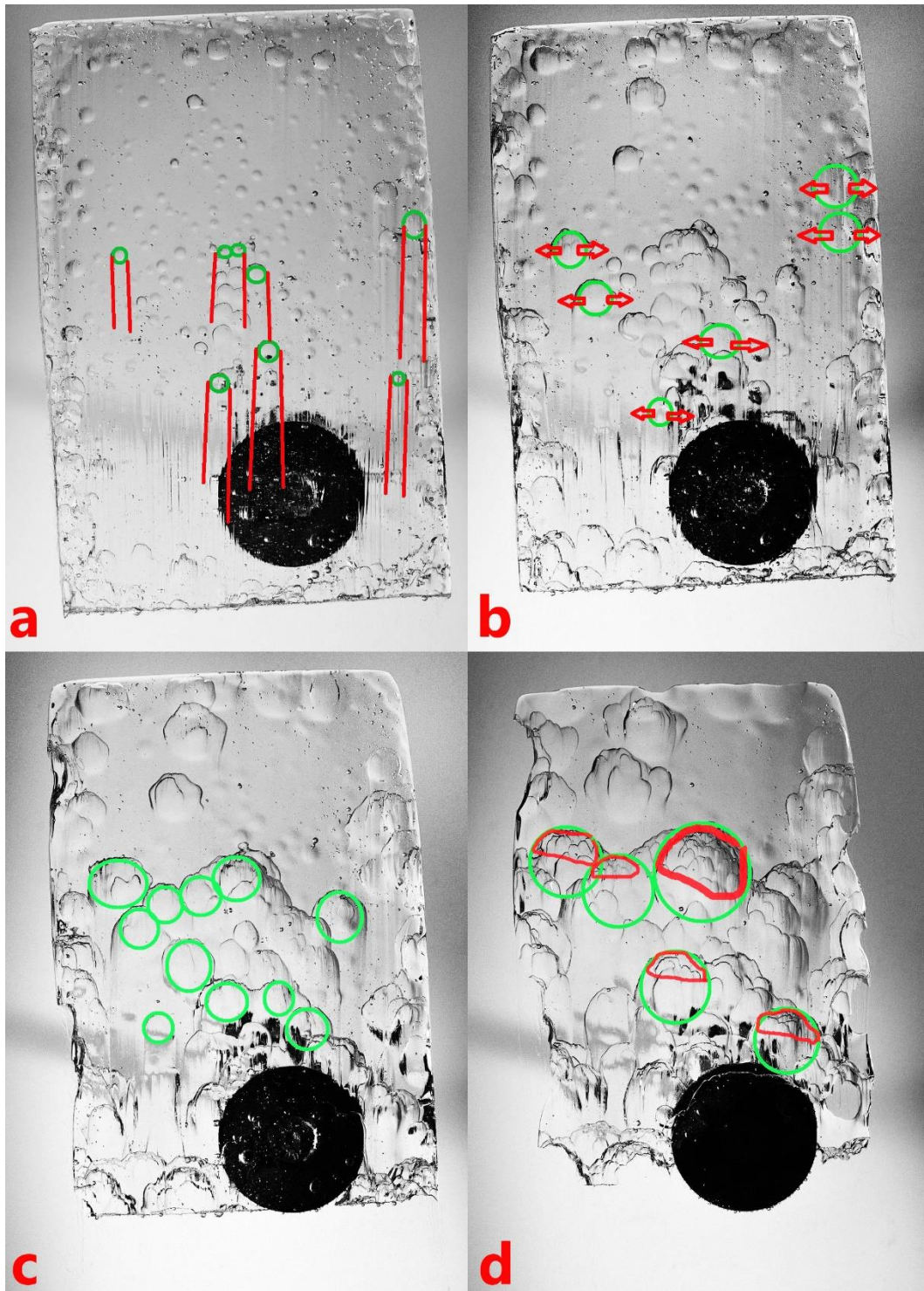


Figure 67 Evolution in time of the surface pattern on a vertical hard-candy block with initial surface inhomogeneities left by trapped bubbles. Time of acquisition of the photo since the start of the experiment: (a) 13 min., (b) 40 min., (c) 70 min., (d) 110 min. All the photos have the same spatial resolution.

The region in the pit is eroded faster due to the mixing and the mechanical shear-stresses associated to the separated flow. Furthermore, as just explained, the wake is formed by the vortices shed from the upstream rim. Thus, also these existing vortices contribute by laterally enlarging the initial shallow cavity left by a superficial bubble, as shown in *Fig. 67b*.

The shallow pits are now wider and deeper. It is important to notice that the pits do not have a planar base; therefore, the local curvature in the peak $\alpha_{loc} \neq \alpha_{crit} = 90^\circ$ and only now dissolution scalloping is able to evolve with the expected structure. The only and big difference is that the evolution is strongly limited within only regions whose surface points downward and which have an inclination smaller than the critical one. This explains why in *Fig. 67d*, scallops are present only in the upper part of the shallow pit. *Fig. 67c* shows how scallops originated by surface inhomogeneities, in addition to not covering all the surface, are delimited slightly above by a sharp upper contour which has a characteristic shape, similar to the one in cross-section of a “wide cupola”. Thus, it is still possible to see in it a resemblance of the initial shape of the surface inhomogeneity. Therefore, the scalloping self-sculpting process induced by bubble inhomogeneities on a surface initially inclined at $\alpha = \alpha_{crit}$ has a memory.

Resuming the started conversation on the mould (*Fig. 57*) used for realising the shape shown in the experiment *Fig. 66*, this is usually used for experiments in which the axis of the arc of circumference of the frontal surface points upward with the wanted tilt angle α , as shown in *Fig. 68*.

It is noticed that the flow is affected by the local curvature and, at least even more remarkably at the beginning of the experiment, two different regions are evident. The lateral regions, affected by a locally higher lateral tilt angle are even more unstable and thus have an anticipated groove-scallop transition. This is evident in the top and middle photos in *Fig. 68*. In the top photo, in the lateral regions there are already some single flutes here and there, some induced by the presence of a bubble or an associated inhomogeneity and some others by solute layer instability, while in the central regions only narrower and longitudinally elongated grooves are visible.

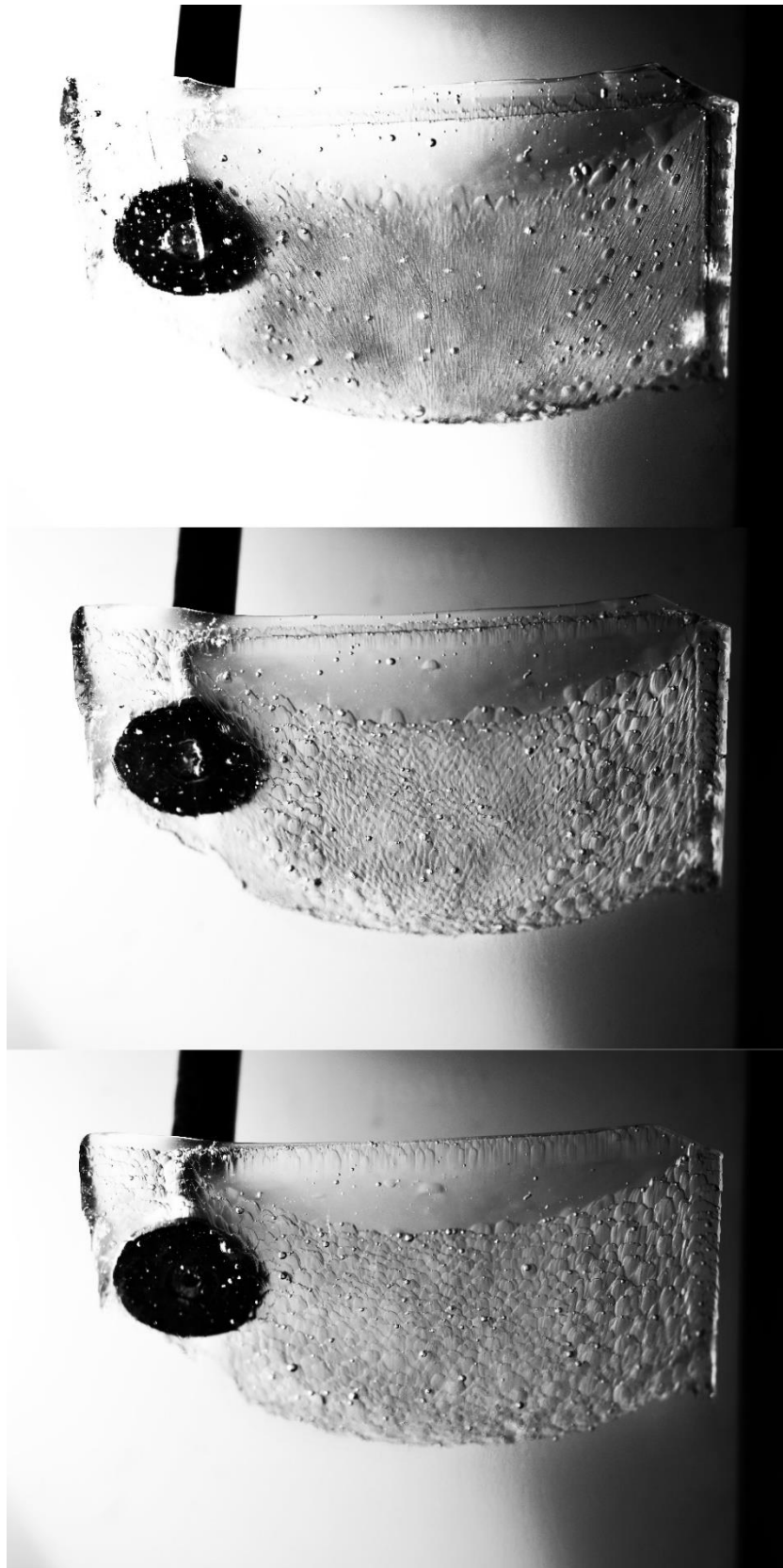


Figure 68 Evolution in time (from top to bottom) of the pattern on a convex surface on a hard-candy block inclined 45° with respect to the horizontal line with no salt added to the aquarium water. Each photo has the same spatial resolution and is taken 30 minutes after the preceding one.

It is worth clarifying that this is not related by chance to the bubbles' presence, since the same behaviour is found to repeat at the beginning of several experiments. Furthermore, as mentioned, not all the flutes are originated by bubble's presence and as clearly in the other two photos of *Fig. 68*, the pattern evolves and organises regardless of the initial homogeneities if the surface is inclined not at the critical angle and facing downwards.

In *Fig. 68b*, the scallops in the central regions globally point upward, while the scallops in the lateral region are tilted. This confirms that scallops can be used to indicate flow direction [53] [50]. But here it is noticed that this is true not only when they are found in nature in a speleological pipe, which may be experimentally modelled as Curl's and Allen's experiments where there is a flow directed mainly in a single forced direction, but also when there is a second angle involved. Indeed, in the experiments shown in *Fig. 64*, the only angle present is the one made between the direction of gravity and the normal direction of the local plane (which in this case coincides with the local direction of the solute mean flow). While in the experiment shown in *Fig. 68*, in addition to the same angle, there is a second angle made with the direction of the local mean flow.

While in my case it is easier to observe this in a convex surface pointing downward, since my phenomenon is driven only by solutal convection and gravity, the dual surface to verify a similar dependence applied to a forced convection regime may be thought as a curved concave surface. For example, like the shape of a centrifugal compressor.

Furthermore, *Fig. 68b* shows how the scallops formed laterally have a higher horizontal wavelength, alias are wider, with respect to those formed in the center. Recalling that scalloping has a memory, it is here evident how this is related to the previous stages when central scallops originated from more compacted vertical grooves, while each lateral scallops was able to evolve in a greater area due to the initial single flutes spread here and there. Furthermore, differently, from *Fig. 64*, here the lateral regions are more subject to a second acceleration whose direction is set by the second angle which it is recalled is related to the local curvature.

In *Fig. 68c* it can be seen how the central region has evolved more in time with respect to the lateral ones. Indeed, the central region's evolution reminds of the one

seen for a planar and inclined block (*Fig. 64*). While in the lateral regions, where the difference between the two aforementioned angles is more evident, the structure appears to evolve very fast at the beginning toward an equilibrium.

Fig. 70 shows the evolution in time of the self-sculpting pattern on a harmonic frontal surface of a hard candy block which is inclined 45° with respect to the horizon.

This confirms what anticipated for *Fig. 66-67*: the surface pattern is generated in the regions facing locally downward (in red in *Fig. 69*) and not in the regions with a local angle equal or greater than the critical angle (in blue in *Fig. 69*). Because in these red regions, the solute layer is Rayleigh-Taylor unstable and is able to separate, while in the blue regions, the local curvature of the surface keeps the layer attached.

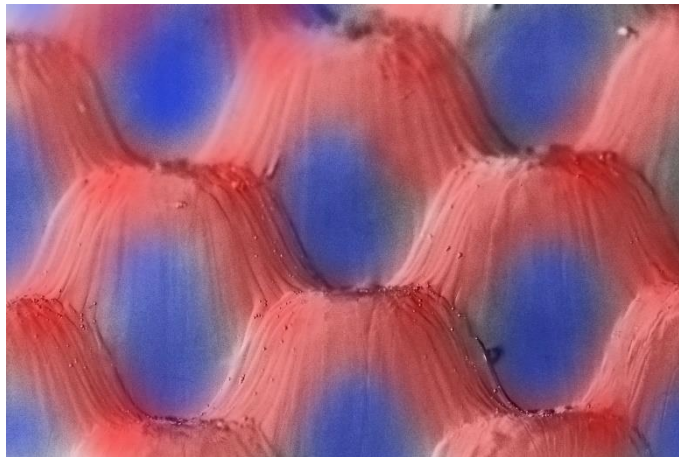


Figure 69 Detail of the top photo in *Fig. 70*. Regions camped in red point locally downward, while regions camped in blue point locally upward or are locally vertical.

It is worth calling now each blue region with the relative upstream rim a *harmonic cell*, since it is associated to the harmonic curvature imposed on the initial surface and in order to distinguish it from the term pattern, which is referred to the superficial self-sculpting process. Looking at the central photo shown in *Fig. 70*, the pattern within each harmonic cell has spread further toward the bottom of the harmonic cell, but it is still confined only in the upper half part of the harmonic cell. In the instants between the central and the bottom photo of *Fig. 70*, a process similar to the one described in *Fig. 67b* happens. Each harmonic cell widens, thus etches and digs the region facing upward of the adjacent harmonic cell.

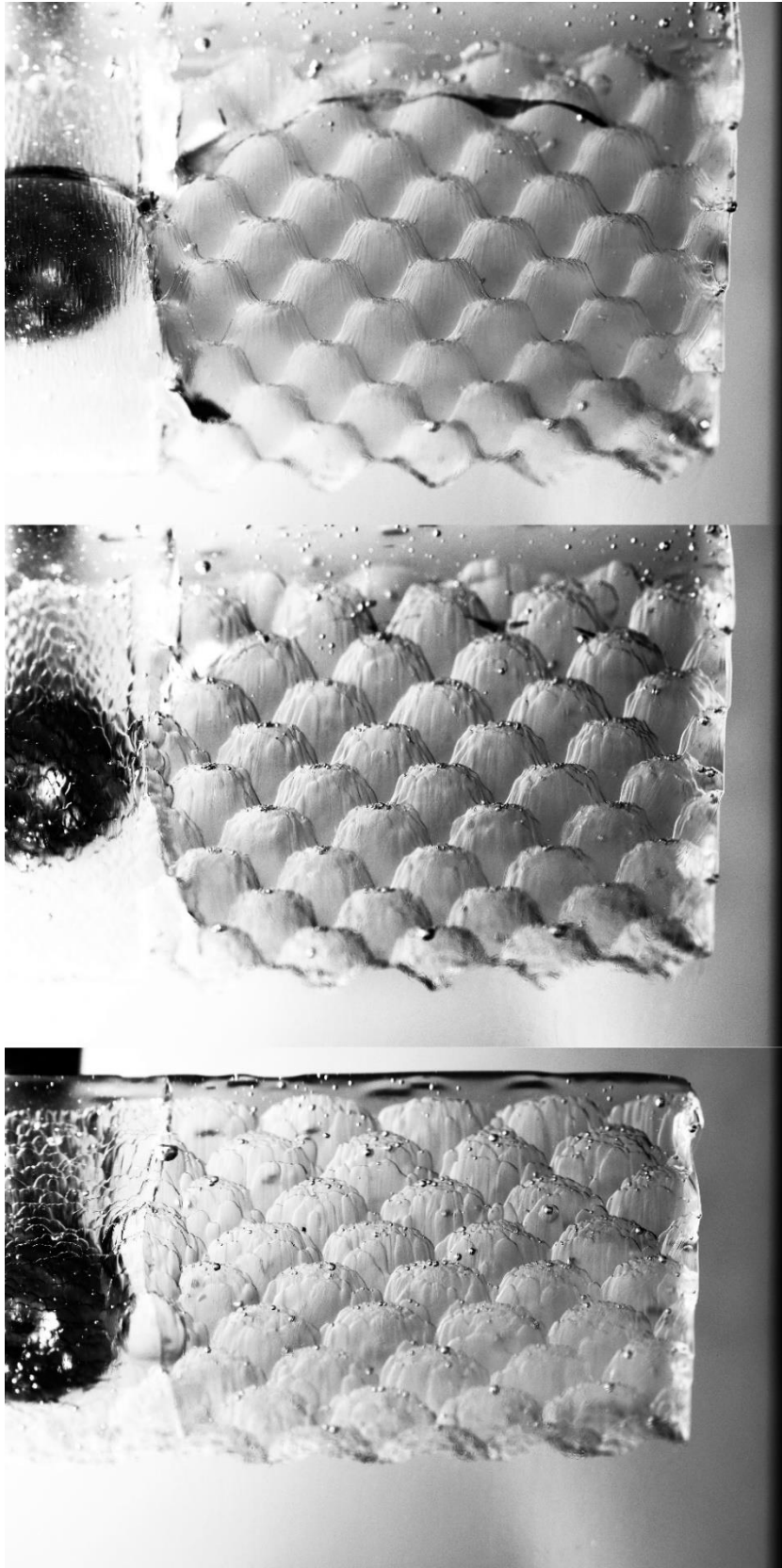


Figure 70 Evolution in time (from top to bottom) of the pattern on a harmonic surface of a hard-candy block inclined 45° with respect to the horizontal line with water salinity $S = 8.81$ ppt. Each photo has the same spatial resolution and is taken 30 minutes after the preceding one.

This is even more visible, because the three photos in *Fig. 70* have a lateral light source and their contrast was enhanced. It appears that the upstream rim is less sharp, by comparison of the photo in the middle with the one in the bottom. This is indeed explained by the local digging process by means of the vortices shed by each upstream rim. Therefore, each harmonic cell has a less sharp groove between its upward pointing region and the downward pointing region of the adjacent harmonic cell. This causes the lateral light to shade less and is thus highlighted by the less sharp contour.

The more uniform curvature allows internal scallops to extend from the left to the right side of each harmonic cell, being more present also in the central region of each harmonic cell. Only in the inner bottom of each harmonic cell the scallops are less packed. Even after an hour, like shown in the bottom photo, the scallops are still dependant from the initial imposed surface. The experiments end with a surface that has sharp crests corresponding to the initial harmonic maxima were located and nearly uniform flat bed corresponding to the initial surface depressions. It is worth noticing that the two final structures are said to *correspond* and not to be in the same initial position. Indeed, also this structure, as for the mentioned scallops of the experiments shown in *Fig. 64, 68*, appears to advance upstream. A greater physical explanation of this upstream motion will be given in paragraph 5.3.

In *Fig. 71*, is shown in three photos the time evolution of the self-sculpting pattern on a flat surface with a V-shaped longitudinal incision harmonic frontal surface of a hard candy block which is inclined 60° with respect to the horizon. The incision makes a right angle at the base and the two planes of the incision are inclined 45° toward the inside of the hard candy block with respect to its frontal surface. This shape is made from the mould shown in *Fig. 58*. The time evolution of the pattern is similar to the one observed in the lateral regions of the experiment done with a convex surface pointing downward (*Fig. 68*). The two geometries have in common the existence of the aforementioned second angle. But while in *Fig. 68*, this varies locally, in *Fig. 71* it is constant along the solute layer path. Therefore, the flutes spread here and there covering all the surface of the internal incision. In a few words, the pattern organises regularly and according to the flow direction.

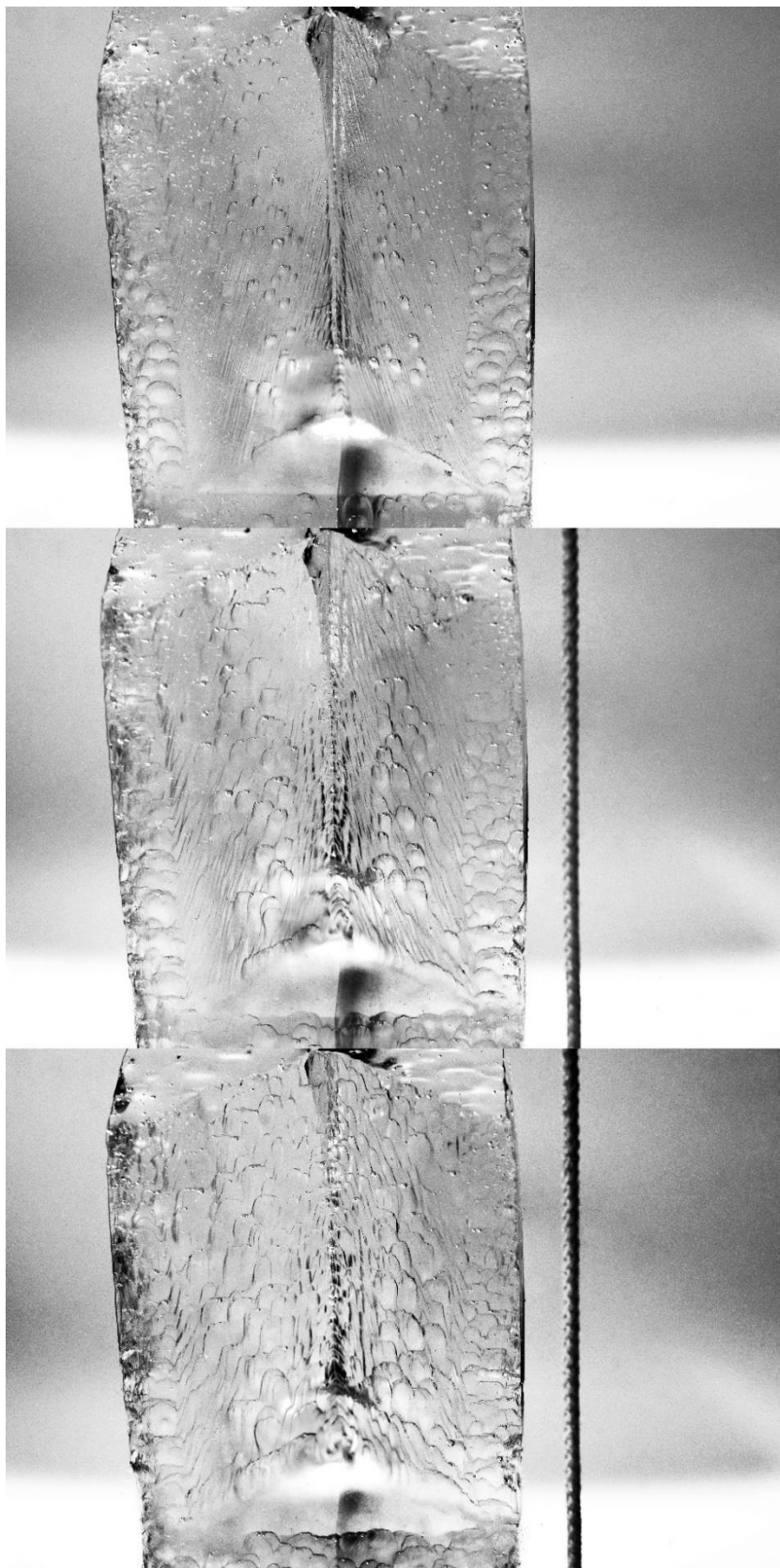


Figure 71 Evolution in time (from top to bottom) of the pattern on the surface of a V-shaped cavity of a hard-candy block inclined 60° with respect to the horizontal line and no salt added to the water. Each photo has the same spatial resolution and is taken 30 minutes after the preceding one.

3.4 Lighting set-up

Similarly to the final remarks left in paragraph 1.2, here is provided a description of the lighting set-up, mainly addressed to the readers who are effectively in the position of doing experiments on the self-sculpting of hard-candy. The readers who are not in the position of doing experimental activity on the topic, may understand better the difficulties associated in the lighting of such experiments in order to highlight the morphology created by an induced flow on the surface of a semi-transparent body. Those who are not interested in the topic at all, can even jump the present paragraph, without losing relevant information.

The author's interest in providing such information is driven by empathy to help others who should face similar conditions. Since different lighting setups had to be tested to optimise the subsequent image processing, it could be worth for some readers sharing here the advantages and disadvantages of those suggestable.

In a few words, two lighting setups are suggested among the several tried: a lateral horizontal-pointing lighting source and a bottom upward-pointing lighting source. With reference to *Fig. 52*, an opaque Plexiglas diffuser is placed between the light source and the hard candy block. In the case of the bottom light source, the diffuser is placed directly inside the aquarium at its bottom. While in the case of the lateral light, the diffuser is outside of the aquarium, leaning against the lateral side of it. An additional diffuser is right at the back of the hard candy block, from the frontal camera point of view, and is supported with some bolts by the inclined rod which is supporting also the inclined hard candy block. The diffusers are necessary both for diffusing the light and for having a homogeneous and clear background in the photos. Furthermore, the inclined diffuser also indirectly allows to break eventual thermal convective cells within the aquarium.

The lateral light is simply a spotlight, while the light at the bottom is a square LED panel, whose intensity can be varied through a potentiometer.

In order to visualise better the structures at the beginning of the experiment, like the stripes' and grooves' structure, it is suggested to use the lateral light and tilt the hard candy block slightly in the opposite direction of the light source. The author

underlines again that the tilt angle must be very low. In this way, since these structures tend to be aligned along a vertical line, a lateral horizontal-pointing light source highlights their left side shadowing the right one. In this way, a code to calculate the horizontal wavelength is very favoured in recognising these structures. If instead a horizontal upward-pointing light is used, most of the information on the initial structures is lost, since they become barely visible.

But as soon as the initial stripes' and grooves' pattern starts developing into spread flutes, then the situation is more critical, since in this case the left side of a flute is very bright with respect to the shadowed right side. The lateral light can be kept for the few initial minutes of this transition, but it is then suggested to switch the lateral light off and switch the bottom upward-pointing light on.

This is now necessary because the more stable patterns have a more predominant vertical wavelength than a horizontal one. Indeed, as already visible in the middle and bottom photos of *Fig. 64*, scallops tend to form horizontal clusters, even suggesting sometimes, especially in the final stages of the morphology evolution, ideal horizontal lines. Therefore, it is better in this case a light direction perpendicular to the main direction of the structure in order to highlight and shadow the opposite sides, applying the same idea illustrated earlier. This, as will be explained in greater detail in paragraph 4.2 is remarkably useful to not consider bubbles in the interrogation area of the frontal photos. Moreover, by the local grayscale or RGB intensity of a frontal photo, it is even possible to have a greater clue of the local inclination of the frontal surface with respect to the horizon, because light scatters differently.

There is no interest in going into a detailed description of other light set-ups which were tested. It is worth saying that using two lateral lights tilted toward the position of the hard candy block with respect to the frontal camera, and positioned slightly at its back, appears only a priori to be useful and in practice ineffective. The amount of light is too much, and it is difficult, even by reducing the diaphragm's aperture and using a telephoto lens, to visualise clearly surface patterns, because it is even difficult to see them with the naked eye.

CHAPTER 4: Image Data Post-Processing

4.1 Side Photos

In this paragraph a nomenclature associated to a lateral point of view of the experiments is used. Therefore, the frontal surface is now called *lower surface*, which is the surface pointing downward and subjected to scalloping. The upper surface retains the name.

The expected results from the post-processing of each image in the folder of the lateral photos taken in a general experiment in which a flat hard candy inclined block dissolves in water are:

- Object contour detection and region segmentation.
- Lower and upper surfaces' inclination.

These two raw results are related to the specific instant when the photo was taken. In order to study the physical phenomenon, the evolution in time of these raw results is computed, allowing to calculate:

- Evolution in time of the shape of the body, which is useful in case there is a convergence toward a universal shape [14] [87].
- Evolution in time of the lower and upper surfaces' inclination.
- Overall regression velocity $\dot{h}(t)$ and regression acceleration $\ddot{h}(t)$ of the lower and upper surfaces.
- Evolution in time of the local regression velocity $\dot{h}(x, t)$ along each of the two surfaces. In this case, the spatial domain is made of points which are spatially cross-correlated.
- Evolution in time of the FFT-analysed signal associated to the instantaneous local regression velocity $\dot{h}(x, t)$.

Each lateral photo is an input datum to the image data processing code. For the non-specialists, the operations explained hereafter, are all based on matrix operation.

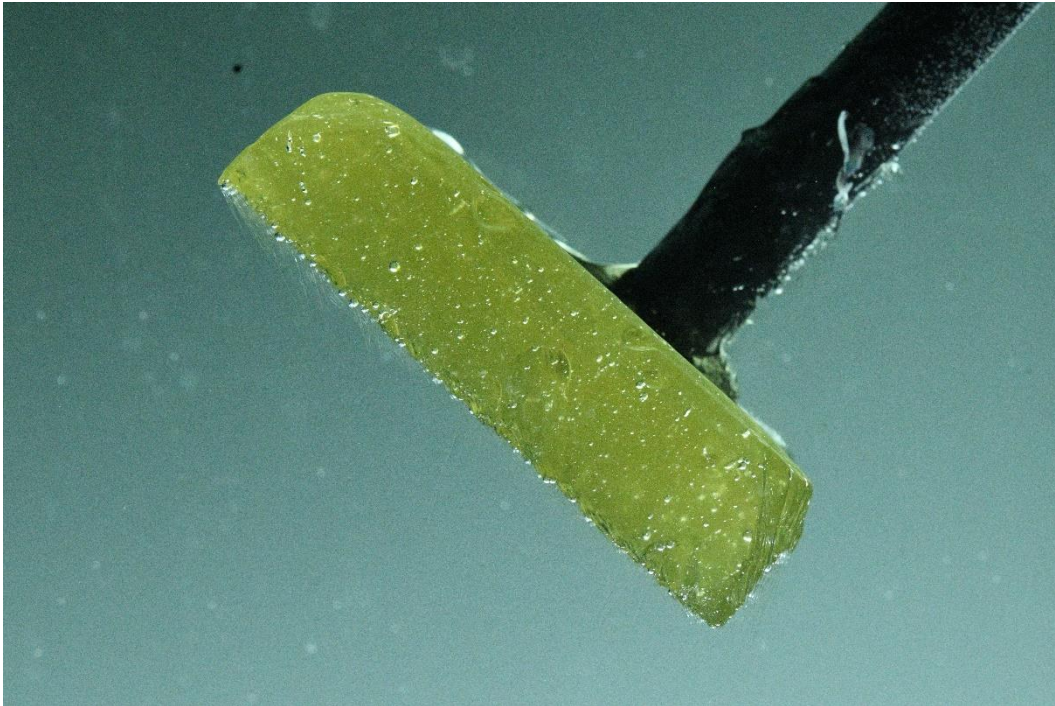


Figure 72 A generic lateral photo.

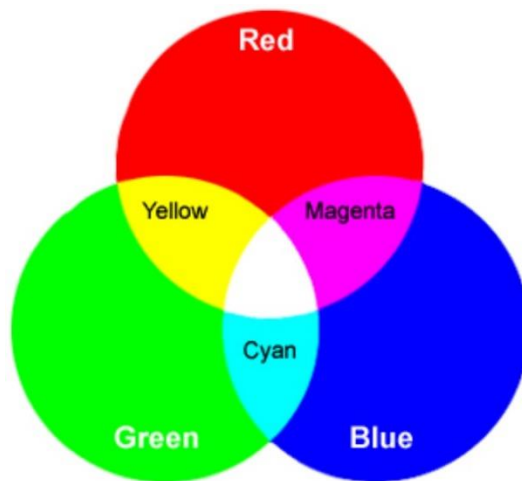


Figure 73 Additive synthesis of primary colours.

Because the photo is coloured, the matrix has dimensions $[N_R, N_C, N_{Ch}]$, where N_R is the total number of rows, N_C is the total number of columns and N_{Ch} is the total numbers of channels. In this case, the photo is an RGB image, meaning that there are three channels: red (R), green (G), blue (B).

The colour depth is stored in 8-bit, meaning that each pixel $p(r, c, i)$, with $r \in [1, N_R]$ and $c \in [1, N_C]$, has a digitalised intensity level $I(r, c, i)$ of the corresponding i^{th} channel in the range of $0 \leq I(r, c, i) \leq (2^8 - 1)$.

Since there is the interest in extrapolating the contour of a yellowish body in front of a cyan-blue background, the blue channel is multiplied by a constant and is subtracted from the red channel. This is equal to subtracting the secondary colour cyan ($C=B+G$) from the secondary colour yellow ($Y=R+G$).

The multiplication constant depends on the overall illumination in each experiment and decreases while time increases. The input photo is processed in parallel to optimise the boundary detection on a side of the lower surface and on the other side of the upper surface. For the lower surface the multiplication constant is not usually greater than 2.8, while it has usually constant and unit value for the upper surface. The reason for the reduction in the constant of the lower surface is that the hard candy block is smaller and smaller as time advances, thus it appears brighter and so the intensity level of the red channel of a pixel within the domain of the hard candy increases, while the intensity level of the blue channel remains almost constant for every pixel in the image for all the duration of the experiment. Furthermore, the difference between the upper and lower surface is related also to the higher presence of bubbles on the lower surface than on the upper as the time passes.

The remarkable advantage of the present method is that it does not need to do what in image processing is called the *background subtraction*. Basically, there is no need to subtract a photo taken when all the hard candy body is dissolved from the photo of *Fig. 73* in order to obtain a clear boundary. On the contrary, doing that penalises unexpectedly the result.

After the subtraction, the pixel intensity values are normalised. All the pixel values different than zero are set equal to one in the processed photo for the lower surface, while for the photo related to the upper surface the high-pass filter has a threshold usually about 0.4. So, each of the two photos is now binarized. This means that the pixels which are considered to be within or right on the boundary of the object have value equal to one, which corresponds to *true* in the terminology used by the *logical connectors* and is coloured white in a binarized image. While the pixels which are considered to be outside the boundary of the boundary of the object have value equal to zero, which corresponds to *false* in the terminology used by the logical connectors and is coloured black in a binarized image. The binarized photos (one optimised for the lower and the other for the upper surface) may also have white

regions not referring to the hard candy body. This happens only if there are some parts of the photo with a high intensity level in the red-colour band. An example of this is given by the plumb line inserted in the experiments to calculate the vertical direction. Therefore, in order to consider only the hard candy body, MATLAB's function `bwboundaries` is used followed by an if-statement, where only the boundary made of a greater number of pixels and for which the center of the photo is within the detected boundary is considered as the effective boundary of the hard candy block. A gaussian filter in the spatial domain is applied. The gaussian filter applied to the upper surface has a greater standard deviation σ , usually in the range 13-20, and sometimes is not fixed but is decreasing during an experiment due to the less rectilinear upper surface's boundary. While for the lower surface filter, the standard deviation is usually in the interval $\sigma = 2.5 - 3.5$. Since in the next step the gaussian filtered photo is furtherly binarized, the two actions combined can be seen as a diffusion in the spatial domain of the probability of finding the object. The higher the standard deviation of the gaussian filter, the higher the diffusion in the spatial domain. Thus, it is like asking the computer if a generic pixel is within a certain distance from the expected object; distance which is increased increasing the standard deviation. If the answer is true, then the pixel is coloured white, otherwise black. The binarization has a threshold value usually around 0.3 for the lower surface and usually 0.5 for the upper surface. The threshold is different because the upper surface is almost continuous and locally linear, and also because the previous standard deviation is quite big, therefore increasing the threshold is not necessary. While the lower surface is expected to be locally nonlinear and discontinuous, due to the presence of nucleating bubbles, the same surface pattern and dissolutional plumes. In *Fig. 74* is shown what said thus far, from the first binarization (on the left), the consequent gaussian filtering (in the middle), and the final further binarization of the so filtered domain (on the right). To be specifically, the binarized photo on the right has been multiplied by the original photo (thus the zeros remain zeros, while the white regions become coloured), to have a visual clue of the precision in recognising the lower surface.

In *Fig. 75* it is shown all the body detected from *Fig. 72* using the previous algorithm. It is worth reminding that since this process is parallel for the lower and

upper surface, then for every photo in input, two binarized photos, similar to *Fig. 75* but with the coloured region just white, are saved in output in a *.mat* file. We may still refer to these two as binarized photos, but it is easier and more correct considering them as binarized matrices made of zeros and ones.



Figure 74 Three main processes (optimised for the lower surface) to detect the body in the photo. On the left: binarization of the photo obtained by the subtraction of the blue channel from the red channel. In the middle: Gaussian filter applied to the previous photo. On the right: Binarization of the photo in the middle and multiplication by the original photo.



Figure 75 Object detected in the photo shown as Fig. 72 (optimised for the lower surface).

The next passage is to segment the different characteristic regions in the binarized matrices. In the matrix referring to the lower surface, the leftmost vertical column in which there is at least a cell different than zero is identified. The cell different than zero which is at the lowermost row is detected. The two coordinates of this cell

identify point *A*. The rightmost vertical column in which there is at least a cell different than zero is identified. The cell different than zero which is at the uppermost row is detected. The coordinates of this cell identify point *B*. In the matrix referring to the upper surface, the uppermost row in which there is at least a cell different than zero is identified. The cell different than zero which is at the leftmost column is detected. The coordinates of this cell identify point *C*. The lowermost row in which there is at least a cell different than zero is identified. The cell different than zero which is at the rightmost column is detected. The coordinates of this cell identify point *D*. In this way the vertices of the hard candy have been identified. It is worth considering now the binarized matrix as a photo, in which the closed region of ones is the hard candy body and the outer space made of zeros is the background. The two lines passing through points *A* and *B*, and through points *C* and *D*, are interpolated. They are both translated of a certain offset toward the center of the body. The boundary pixels of the detected body, which are lower (higher) than the interpolated line passing through points *A* and *B* (*C* and *D*) and in the interval between them is the lower (upper) surface contour. This is appended in the .mat file.

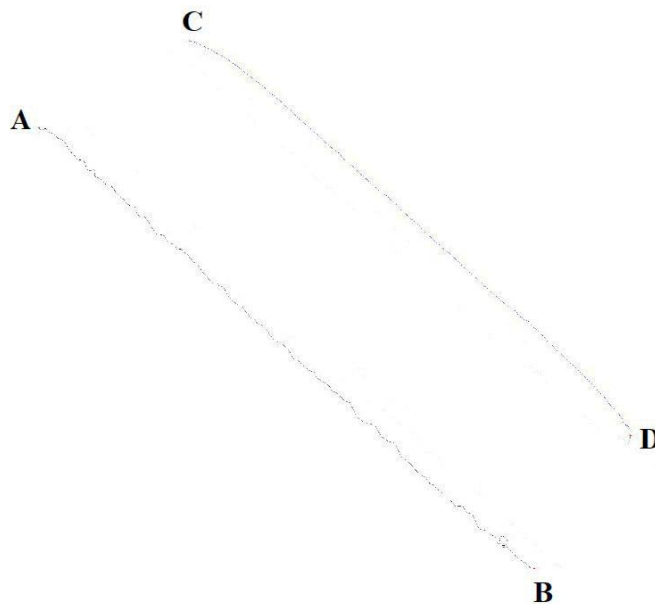


Figure 76 Lower and upper surface contours and relative extrema segmented.

The pixel points belonging to the lower and the upper surfaces' contour are then reordered, because MATLAB lists them by default with a similar logic used in TV monitors: from top to bottom and then from left to right. Instead, for a better processing of the images, it is preferred to have the points belonging to the contour of the two surfaces listed in ascending order according to the direction given by the solute layer: from A to B and from C to B respectively. To do so, the pixels are reordered taking into account 8-connectivity between a pixel and the other and assigning a priority in the selection of two possible nearby pixels given by the expected solute layer direction (from top-left toward bottom-right). This passage, even may appear secondary, is critical in order to have cross-correlated points to calculate the thickness regression rate and for performing the successive operations.

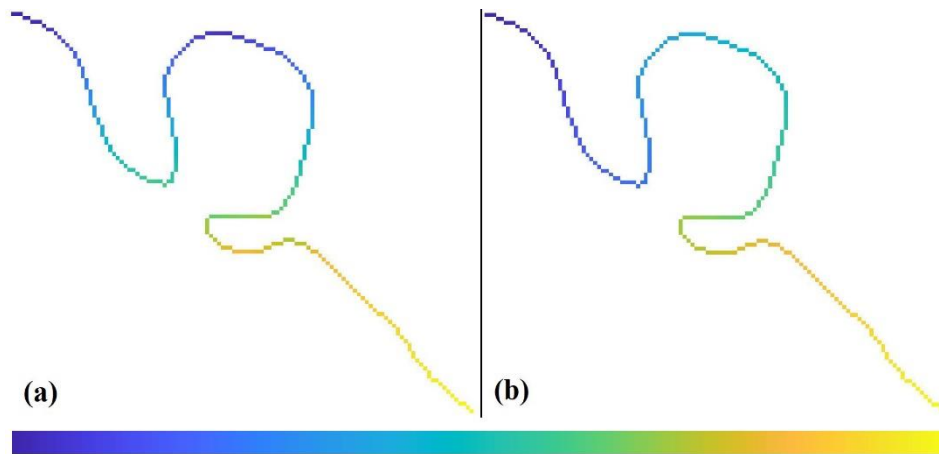


Figure 77 (a) Lower surface according from top to bottom as done by default by MATLAB. (b) Lower surface reorder in 8-connectivity along the direction given by the solute layer. The increasing pixel number is given according to the bottom colorbar.

The so reordered lower and upper surfaces' contour, together with their calculated inclination are appended in the .mat file. The inclination of the lower surface of the first photo, which is taken right after the hard candy block is immersed in the aquarium, is appended as inclination reference in the .mat file in memory.

In parallel, the acquisition time of the photo is stored in a separate .mat file as a matrix that has a total number of rows equal to the number of photos and two columns: in the left one there is the number of the photo and in the right one the related acquisition time. The acquisition time is taken from the *EXIF* (abbreviation of *Exchangeable Image File Format*). To access the acquisition time saved in the EXIF using MATLAB, the EXIF folder is first of all imported through the line of

code `I=imfindinfo('Photo_name')` and then the acquisition time is saved specifying in `DigitalCamera.DateTimeOriginal` the structure of the file previously imported. For example, in order to show it in the *Command Window*, it is requested only to write `string(I.DigitalCamera.DateTimeOriginal)`. Similarly, it can be saved.

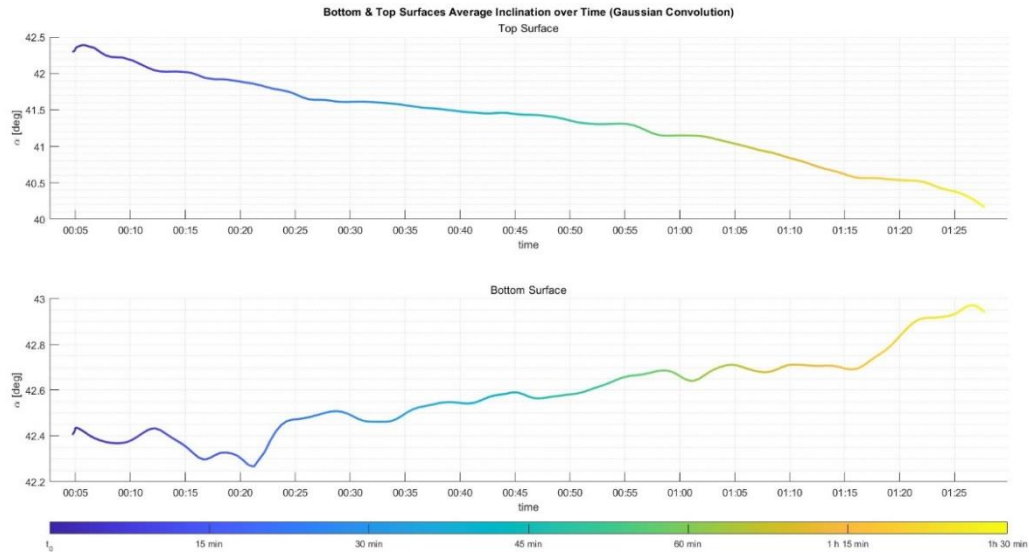


Figure 78 Variation in time of the overall bottom and upper surface of the dissolving hard candy.

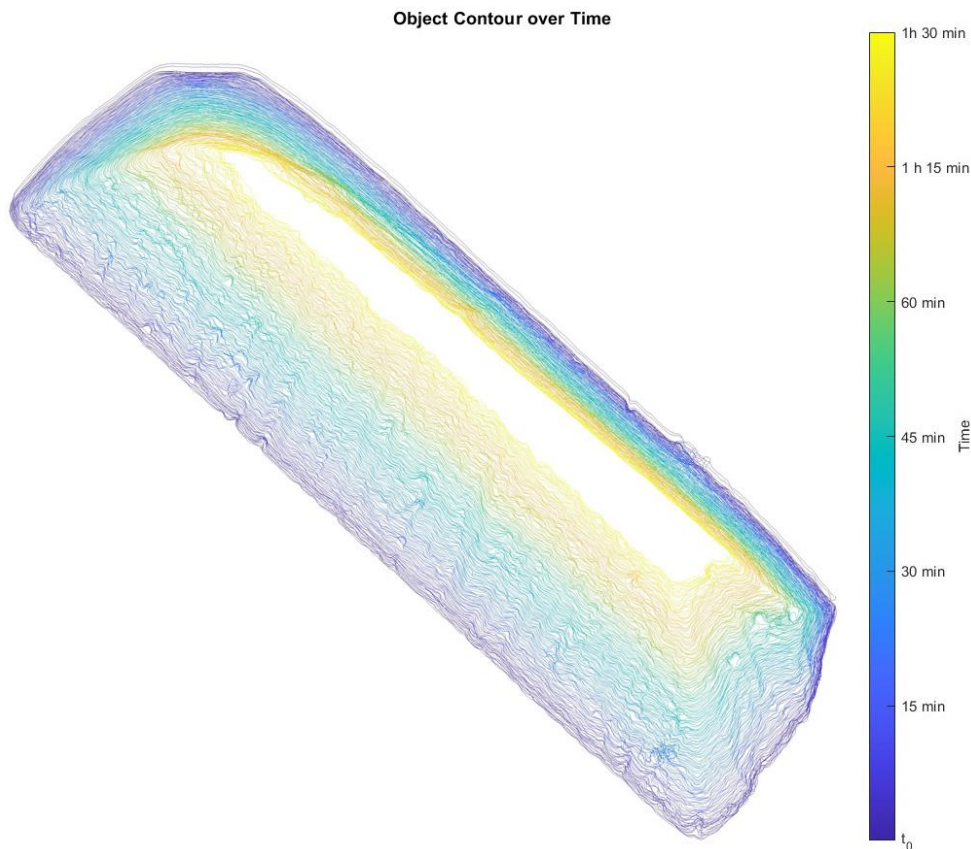


Figure 79 Evolution in time of the boundary of the dissolving hard candy block.

The vector made of the time instants when the photos are taken in the experiment, together with the value of the inclination of each photo and of the contour previously segmented, allows to plot the variation in time of the overall inclination of the bottom and upper surfaces (*Fig. 78*) and the evolution in time of the boundary of the dissolving hard candy body (*Fig. 79*).

A critical task is to calculate the thickness with respect to a fixed line for the lower surface's ordered curvature. In order to do so, the inclination of the lower surface of the hard candy in the first photo is loaded together with the position of point A of the boundary of the hard candy in the last photo. The line with same inclination as the initial surface is drawn so that it passes for the two coordinates of point A. The complementary angle to the one associated to the direction of the line is calculated. This angle decides the direction along which to calculate the thickness of the two significant surfaces of the hard candy. It is worth noticing that, since the line sketched and the complementary angle to this line are related to the angle of the lower surface of the hard candy in the first photo taken, then this angle is constant for all the photos. This is obviously necessary to calculate the thickness along a fixed direction. To measure the thickness, the code starts from each pixel belonging to the lower surface curvature and moves pixel-by-pixel toward the sketched fixed line along the thickness direction. For every step further from the initial pixel, the counter increases by one. When the moving pixel crosses the sketched fixed line, then the number reached in the counter is saved and the process is repeated for the successive pixel in the lower surface curvature. The process ends when the final pixel of the sketched fixed line is crossed by the moving pixel associated to the ordered lower surface. This is performed in MATLAB with an outer for-loop on the pixels of the lower surface curvature, an inner while-loop for the moving pixel, an inner for-loop to check the coordinates of every pixel of the sketched fixed line through two nested if-statements. Obviously this is not the only logic possible to do so; another one could have been finding the smallest cell of a vector created calculating in each cell the Euclidean-norm between the pixel considered on the lower surface and each pixel of the sketched fixed line. Anyways, the first logic allows to represent in *Fig. 80* the thickness so calculated. In this figure

the sketched fixed line is visible and the red stripes, which appear as an inner red texture, are the displacement along the thickness direction from each pixel on the lower surface to the corresponding intersection point with a pixel of the sketched fixed line.

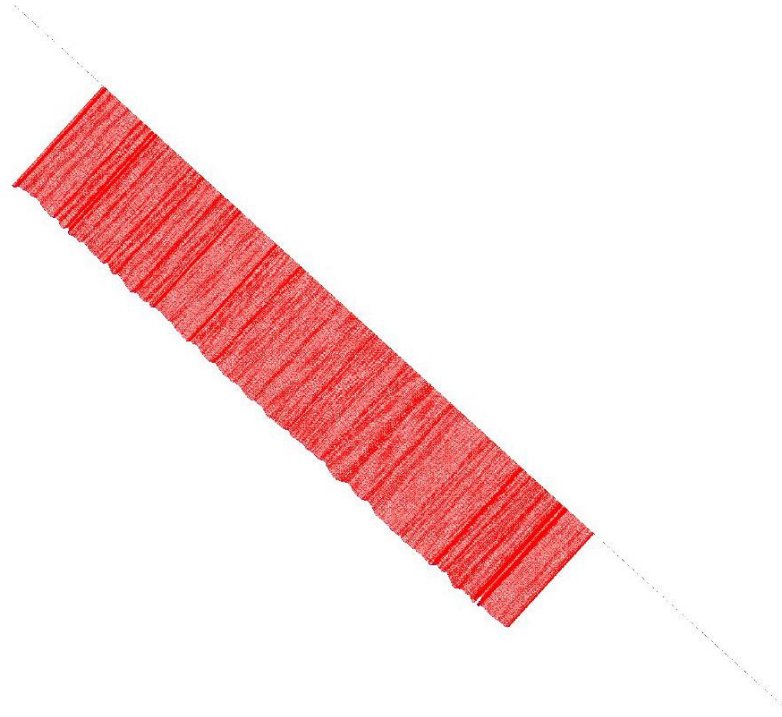


Figure 80 Distance calculated for each pixel of the lower surface with respect to the fixed line.

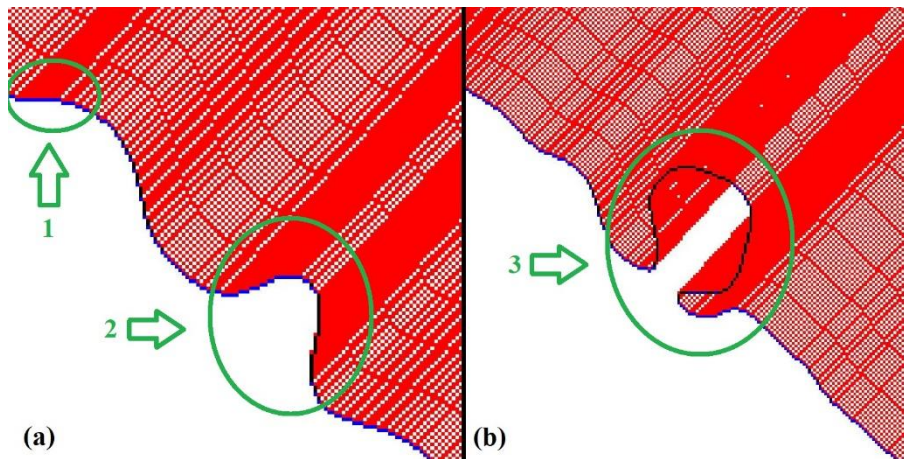


Figure 81 A couple of details of Fig. 80.

It is worth mentioning that it is better calculating the thickness starting from the body surface's points and not from the points of the fixed line, especially for the lower surface. Fig. 81 clearly shows why. In this way, when the surface contour has great local changes in the inclination, there are no points that are missed. It is worth

taking the opportunity to show the preciseness of the previous part of the code in calculating the boundary of the object. *Fig. 81b* is indeed the contour of a small bubble which was trapped within the hard candy block. Similar pits are found also when there are very bright regions in contact with the lower surface in the original photo. In the code it was preferred to remove them by subtracting the two primary colour-channels, since this helps in removing eventual bright spots due to bubbles. As will be explained in greater detail hereafter, the thickness calculated in *Fig. 81b* is not calculated merely as shown in the figure, but there is an implementation in the code to take into account impurities like the one showed; therefore it is not a problem.

The same process shown here for the lower surface is done for the upper surface. For each processed photo, for each hard candy body's surface, the coordinates of the two extrema on the fixed line that are crossed by the red thickness lines are saved. This allows to save the interval over which the thickness is calculated, passing from a variable system of reference in time, which corresponds to the coordinates of the points of the lower surface, to a fixed system of reference in time, which corresponds to the coordinates of the points of the fixed line. The rightmost left coordinate of the left extremum and the leftmost coordinate of the right extremum are calculated. These two coordinates identify the interval where the coordinates of the points of each hard candy body's surface are cross-correlated in the photos covering all the duration of the experiment. Indeed, the interval calculated for a photo taken at an advanced instant in the experiment is for sure smaller than the one calculated for a photo taken at the beginning of the experiment, since the body is shrinking due to dissolution. The same reasoning applies to a body shrinking due to melting. It is worth mentioning that calculating directly the interval based on the extrema of the final photo is not always a good idea. Furthermore, the computational cost associated in calculating the reduced cross-correlated interval is very low and at the same time stabilises even more the algorithm.

As anticipated before, the thickness calculated in *Fig. 81b* is not a problem. In the algorithm mentioned now is understood why. Basically, the thickness calculated thus far is not univocal. Indeed, in the thickness calculation, to a single pixel in the fixed line usually correspond more than one pixel on hard candy body's upper and

lower surface, respectively. Therefore, the previously calculated local thicknesses for each photo are saved in a matrix which has a number of columns equal to the number of the processed photos and a number of rows equal to the number of discrete pixels of the fixed line within the cross-correlated interval calculated before. When a pixel corresponds to more than one point, only the maximum value among the associated thicknesses is stored. At the beginning of coding, the mean value was saved instead of the maximum value; but it was then noticed that the maximum value stabilises more the code since dumps more eventual spurious numerical oscillations of the thickness value in the region of the surface's point considered in consecutive photos. In this way the stored thickness related to the lower surface's points in the detail shown in *Fig. 81b* is the one for all the points on the "outer" surface, since the thickness is univocal; this is noticeable since the red lines are quite equally spaced. In the "inner surface", corresponding to the pit and thus to points which are non-univocal with respect to points in the fixed line, only the maximum thickness is stored. Therefore, when the red thickness lines are more pronounced in colour, since they are calculated for three points (the outer effective surface point, a medium point associated to the recess, an inner point associated to the base of the bit), only the thickness of the outer point on the surface is stored. For the inner and univocal (middle) region of the pit, nothing can be done now with this algorithm. But again, this is not a problem, because this region is now more identifiable since the thickness presents a discontinuity along the coordinate of the fixed line. And discontinuities in functions are highly detectable.

Therefore, in the successive step, the mean thickness μ is calculated from the stencil made of all the thicknesses related to the surface points. The standard deviation σ is also calculated in order to fix an upper ($\mu + \sigma k^+$) and lower interval ($\mu - \sigma k^-$) where the thicknesses are considered correct. k^+, k^- are two multiplicative factors, such that $k^+ \neq k^-$ otherwise there is no change in the calculated mean value, that are set in order to cut off eventual discontinuities in the thickness curve. Two extrema are set in order to not allow the code to set very big multiplicative factors to cut off little discontinuities when the hard candy surface has no pits. Even if the code can work autonomously with good results in setting optimal multipliers within the given limited interval, for most of the results shown in the present thesis two

fixed multipliers were set manually for the photos of the same experiment, since this update in the code was done after most of the results were already calculated.

The mean thickness now calculated from the smaller and cleaner stencil made of the thicknesses related to the surface points that were within the aforementioned interval is updated and appended in the saving file. The thickness values outside of the interval are updated in the matrix made of univocal values with a constant and manually decided non-realistic value in order to easily detect it in the next algorithms and do not consider it.

The evolution in time of the value of the mean thickness calculated for all the points of the lower and upper surfaces allows to calculate the mean regression rate of the surface under consideration. Indeed, between two consecutive photos there is a constant interval of thirty seconds. Therefore, the mean regression rate is nothing less than the difference between two consecutive mean thickness values divided by the elapsed time interval between the two photos.

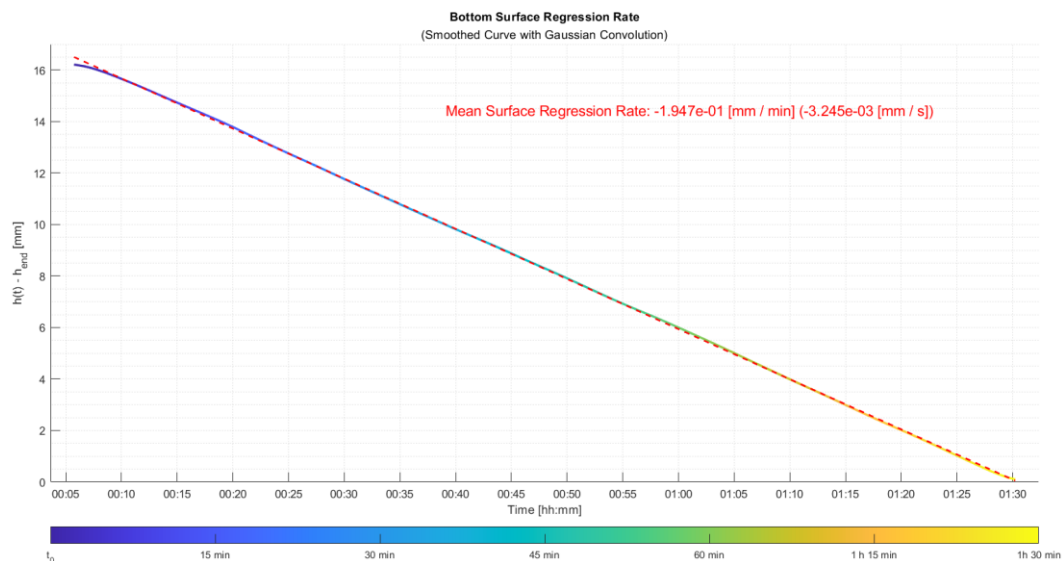


Figure 82 Evolution in time of the mean (lower) surface thickness. The red dotted line is the 1st order approximated regression-rate.

The shown parula-coloured curve has been gaussian filtered, with a very small standard deviation associated to the filter, in order to remove eventual discontinuities in the curve.

The parula-coloured curve is approximated with a 3rd order approximation, allowing to calculate in addition to the regression rate, which is a velocity after all, also the regression acceleration. This is useful to determine the position in time of

an eventual horizontal inflection point in the regression velocity curve, which corresponds, by definition, to the instant when the regression acceleration is null. Such cases are shown in Fig. 83-84.

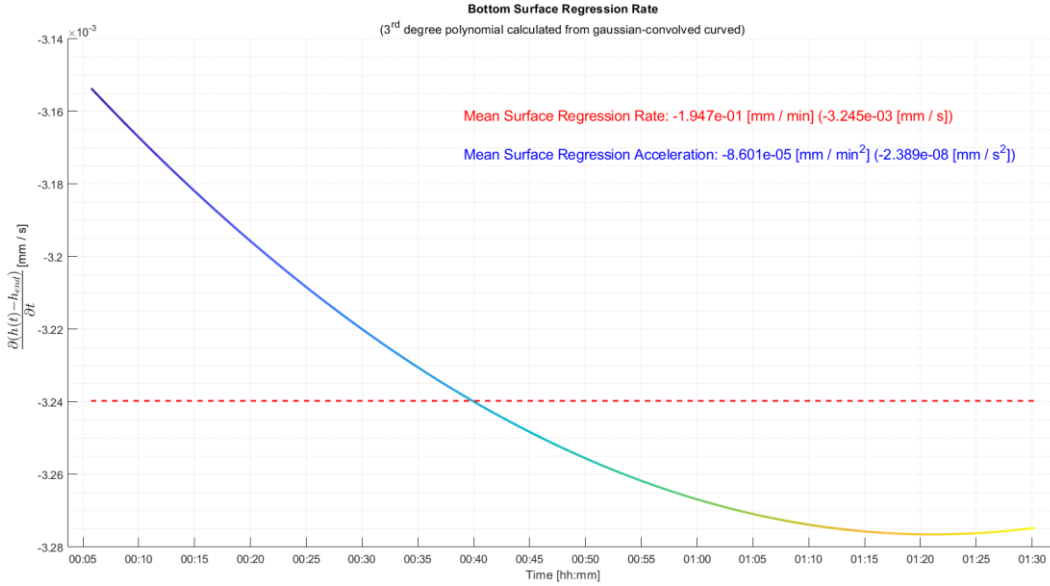


Figure 83 Evolution in time of the (lower) surface regression rate. The horizontal flex point corresponds to null regression acceleration. The horizontal red dotted line is the mean value.

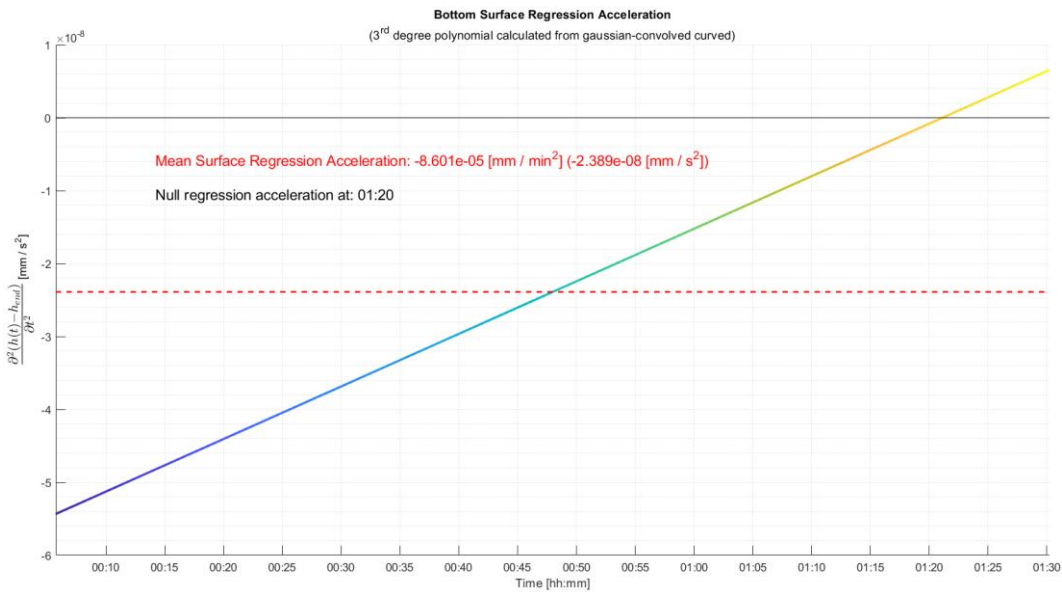


Figure 84 Evolution in time of the (lower) surface regression acceleration. The horizontal red dotted line is the mean value. The horizontal black line intersects the curve at the instant when the acceleration is null, which is the instant associated to the horizontal flex point in Fig. 83.

Furthermore, since the thickness values in the matrix are all univocal and referred to cross-correlated points, it is possible to calculate the regression rate along the coordinates of the cross-correlated interval. To do so, the averaged thickness is

calculated from the stencil made of the thicknesses of two consecutive photos, in order to dampen eventual spurious oscillations in the values. Furthermore, this averaging operation is done on non-nested “photos”. The mathematical term would be points, but this would be less clear since points are already mentioned to indicate the discrete pixel on the surface. Basically, what the author wants to underline is that in order to calculate the regression rate from consecutive averaged thicknesses, four photos are needed and not three. The reason is clarified hereafter:

$$\underline{h}(x, \underline{t}) = 0.5 \times (h(x, t_1) + h(x, t_2)) \quad [62]$$

Where $\underline{h}(x, \underline{t})$ is the averaged thickness and is referred to the intermediate instant between the initial ones $\underline{t} = 0.5 \times (t_1 + t_2)$. The intermediate instant is calculated in the algorithm when calculating the averaged thickness. The reason why the letter h is used is because, to be precise, this is more a distance with respect to a referenced line, thus a height, than a thickness. Anyways, if the regression rate of the averaged thickness is calculated from only three photos, in which one photo is common to both the two couple to do the averaging, the following cancellation happens:

$$\begin{aligned} \dot{\underline{h}}(x, \underline{t}_2) &= \underline{h}(x, \underline{t}_2) - \underline{h}(x, \underline{t}_1) = 0.5 \times (h(x, t_2) + h(x, t_3) - h(x, t_1) - h(x, t_2)) \\ &= 0.5 \times (h(x, t_3) - h(x, t_1)) \end{aligned} \quad [63]$$

This is not wanted and is equivalent to not considering the thickness associated to a photo (the nested one, which in the case shown is taken at the instant t_2). It is then clear that four photos are necessary to calculate the regression rate from the average thickness.

The local regression rate so calculated from the averaged thickness can be plotted in space along the coordinate of the body’s surface cross-correlated interval. Obviously, since it is of interest studying the evolution of this quantity, it is possible overlapping the curves coloured in different colours on the same graph. This is done in *Fig. 85*.

Since the local regression rate is similar to a resulting signal made of the superimposition of harmonic signals and noise, a discrete Fourier transform using a fast Fourier transform algorithm is computed on the signal. Every signal is

considered as made of two superimposed harmonic signals. Basically, they are the two highest peaks in the power density spectrum. Therefore, the evolution in time of the frequency, the relative wavelength, and the amplitude of the two signals is calculated and shown in *Fig. 86-88*.

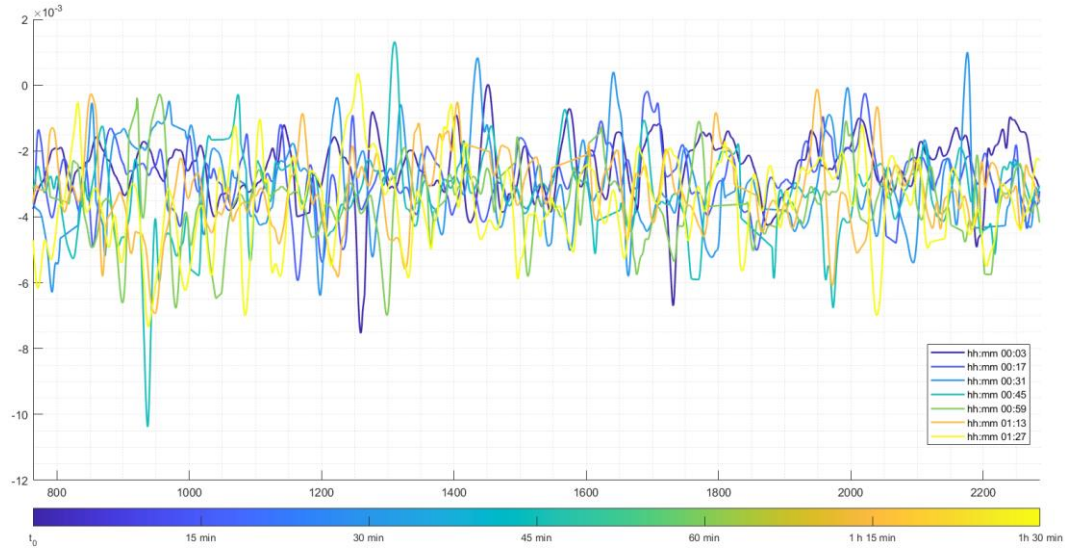


Figure 85 Evolution in time of the local regression rate along the coordinate of the body's lower surface cross-correlated interval.

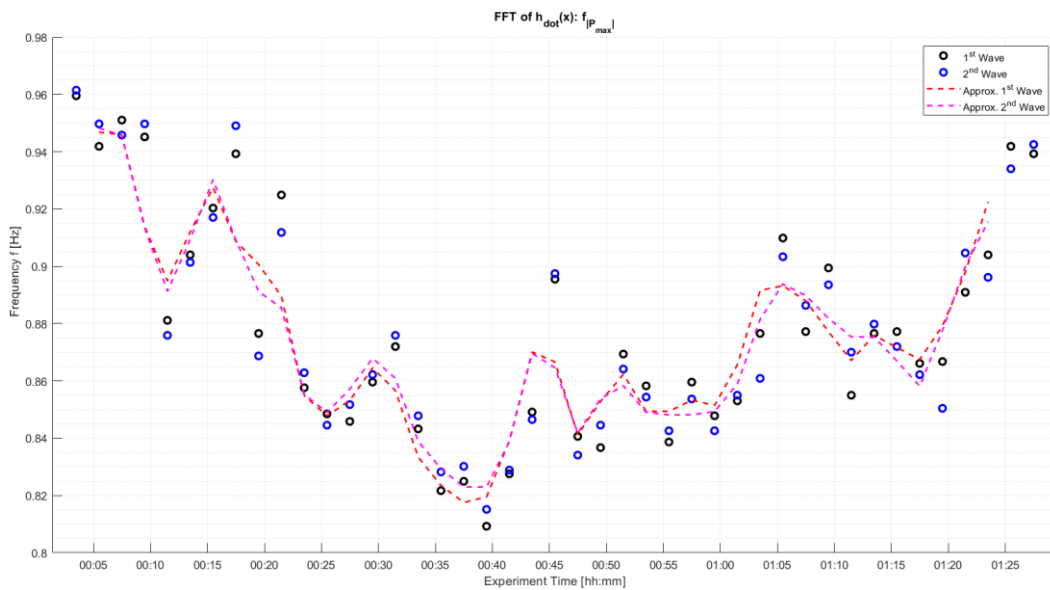


Figure 86 Evolution in time of the frequency of the two harmonic carrier waves found through FFT of the local regression rate defined in the body's surface cross-correlated space interval.

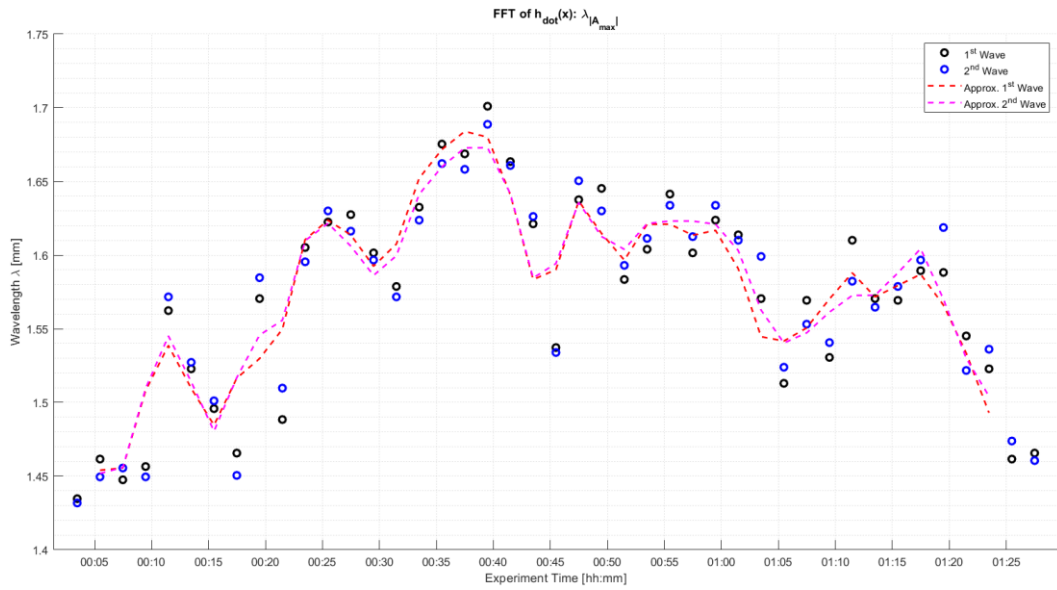


Figure 87 Evolution in time of the wavelength of the two harmonic carrier waves found through FFT of the local regression rate defined in the body's surface cross-correlated space interval.

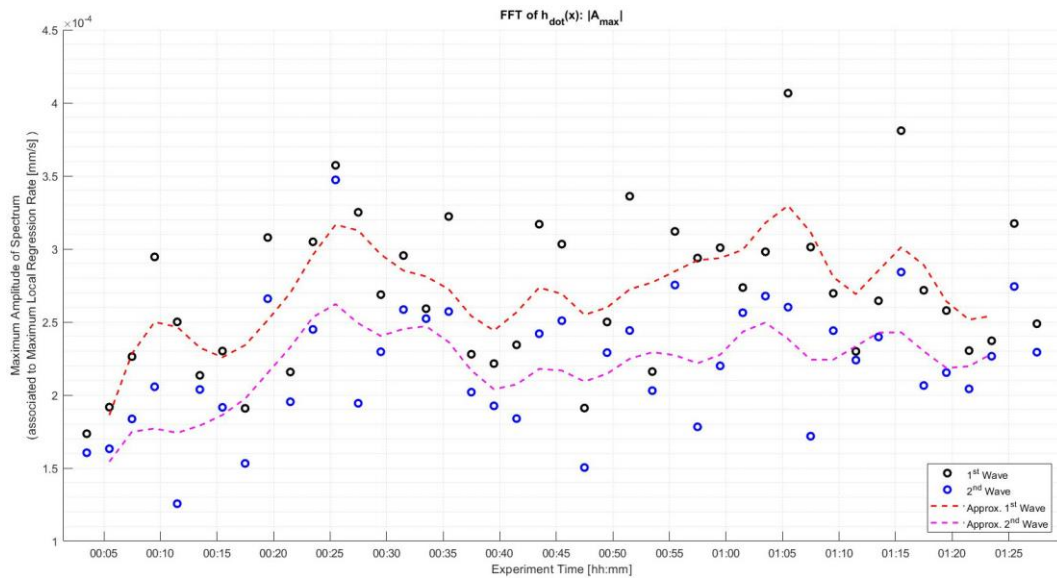


Figure 88 Evolution in time of the amplitude of the two harmonic carrier waves found through FFT of the local regression rate defined in the body's surface cross-correlated space interval.

The code for processing the lateral photos taken in each experiment is thus concluded.

4.2 Front Photos

The expected results from the post-processing of each image in the folder of the frontal photos of a generic experiment in which a flat hard candy inclined block dissolves in water are related to the morphology patterns on the frontal surface pointing downward.

The basic ideas behind the algorithm are sequentially:

- The pattern must be recognised.
So, that the coordinates of the pixels which constitute the pattern can be stored in a file in the memory.
- These coordinates must be grouped.
This is necessary because the pixels recognised as pattern are not a priori continuous. Therefore, one pattern may be made of different relatively close limited curves, each one made of 8-connected pixels.
- The curves belonging to the same group are numbered in order to satisfy a “virtual connection” between the curves.
Basically, the curves are still different closed *sets* in the spatial domain defined by the group, but this domain is a *topologic space* whose *components* (each entity defined before as *set*) are *connected*.
- Thanks to indices associated to the virtual connection of the previous step, the curves are connected such that they are a single geometrical set.
- The vertical distance between the sets (surface patterns) is calculated.
- The horizontal distance between the sets (surface patterns) is calculated.
- The ratio of the area occupied by the patten to the total area is calculated.

Eventually, the total area of the frontal surface can be used in combination of the known area of the side surface, which is calculated with the algorithm explained in the previous paragraph, in order to calculate the volumetric regression of the block in time.

Prior to processing the frontal photos, it is necessary to define the boundary of the interrogation area used. This can be done manually or automatically. Both the methods were used for processing the frontal photos. The two methods have in common that the lower horizontal side of the interrogation area moves upward linearly, while the upper horizontal side of the interrogation area moves downward linearly, while the upper horizontal side draws at the beginning a curve similar to an arc of hyperbola. Then when about fifty minutes passes since the beginning of the experiment, the position of the upper horizontal side in the photos can be considered almost constant. In the final photos of the experiments, at around eighty minutes since its start, the positions seem to move even downwards and not upwards because the hard candy block is quite thin then. When this happens, this usually identifies the last workable photo. It is also worth mentioning that the leftmost and rightmost sides of the rectangular interrogation area should stay enough far away from the physical boundary of the hard candy surface, in order not to consider boundary effects, such as local vortices due to the sharp edge of the block. In the present experiments, the left boundary is imposed by the position of the base of the holder, and therefore is usually fixed for all the photos of the experiment. For the right boundary, a hint is usually given by the presence in the final photos of a rounded top-right edge of the frontal surface of the hard candy block. The right boundary must be on the left on the rounded top edge, intersecting the top side when it is still quite rectilinear. Usually, the right boundary layer is kept fixed, in order to consider the same width for all the photos. But it may be also varied if wanted.

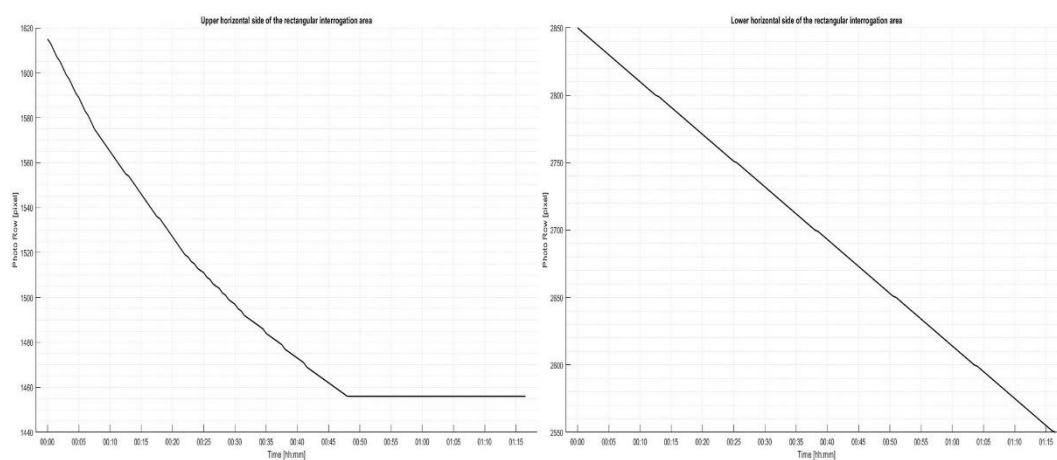


Figure 89 Evolution in time of the row position in the photos of the upper and lower horizontal side of the interrogation area. Be aware that the two photos are horizontally compressed.

Defined the evolution in time of rows and columns associated to the interrogation area, a generic input photo is shown in *Fig. 90*. The interrogation area is highlighted in red. It is worth keeping in mind that the spatial domain (*Fig. 91*) of the operations described hereafter is the one defined within the boundary of the interrogation area.

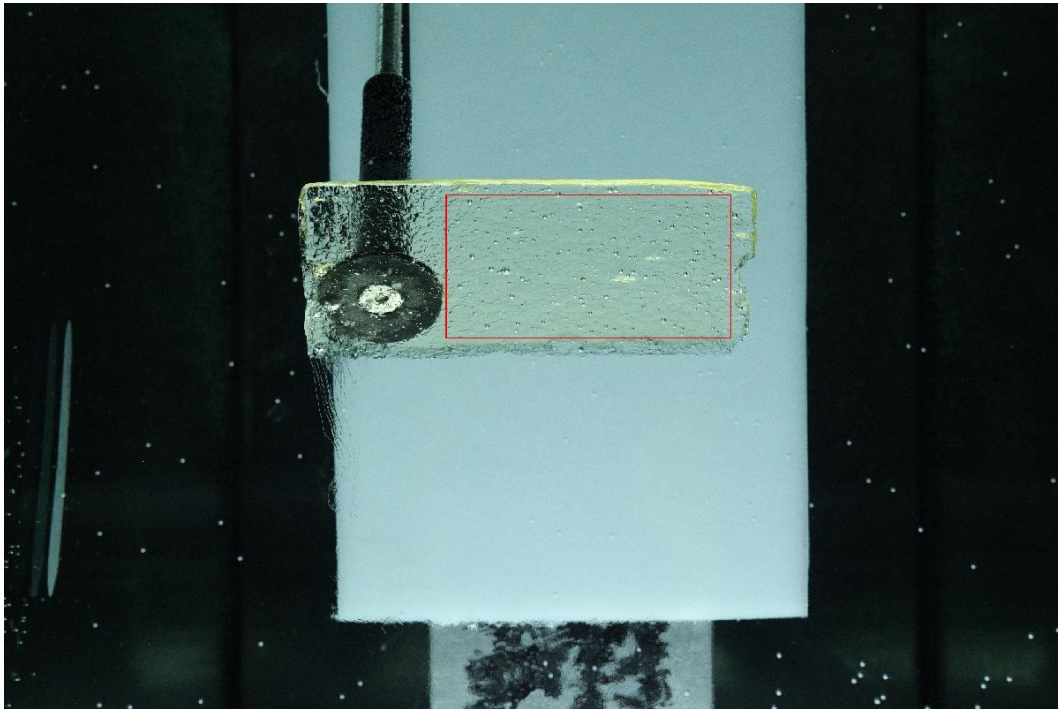


Figure 90 A generic front photo, with its rectangular interrogation area highlighted.



Figure 91 (Workable) spatial domain of the photo defined by the rectangular interrogation area.

The first pre-processing step aims to remove the bubbles present in the spatial domain. To do so, it is recalled that the light source is at the bottom of the aquarium and pointing upward. Therefore, bubbles have the property to be very bright at the bottom and very dark at their top. The initial photo is thus converted from RGB to greyscale and then a high-pass filter with a big threshold is applied in order to detect the bright pixels in the photo and save their positions in a temporary file. Usually, the big threshold is about 0.75 (it may look low, but keep in mind that the value is normalised) and it may range between 0.62 and 0.80 depending on the mean intensity of the pixels in the workable area. Once it is set, it does not change in time. The temporary file just saved is a binary matrix with the same number of rows and columns of the interrogation area. It is made of zeros, corresponding to pixels in the photo darker than the threshold, and ones, corresponding to pixels in the photo brighter than the threshold. A gaussian filtering with standard deviation $\sigma = 1.7$ and a subsequent binarization with threshold 0.3 is applied to this binary space. By doing so, the sets made of unitary cells in the domain made of zeros enlarge radially. This is done to consider a greater boundary of bubbles with respect to the effective one detected, and thus to cancel out also the shadowing of the bubbles that might have been remained undetected thus far.

A similar process is applied for the upper and brighter part of the bubbles. In this case the greyscale is inverted and an initial high-pass threshold about 0.62 in value is applied. The threshold may vary between 0.58 and 0.65. This is equivalent to considering a low-pass filter with a threshold of the order 0.38. The reason why the low-pass filter is not applied, despite its simplicity, is that MATLAB's function `im2bw` is implemented as a high-pass filter. Anyways, a gaussian filter with standard deviation $\sigma = 0.9$ and a subsequent binarization with threshold 0.25 is applied. This binary space related to the upper region of the bubble is summed to the binary space related to the lower part of the bubbles. Then a binarization with null thresholding is applied, in order to set all the cells with a value higher or equal than one to unitary value and leave the null cells unchanged. The binarized space thus obtained is shown in *Fig. 92*. The pixel coordinates corresponding to the points detected as within an upper and darker bubble's region are coloured in blue while the pixel

coordinates corresponding to the points detected as within a lower and brighter bubble's region are coloured in red in *Fig. 93*.

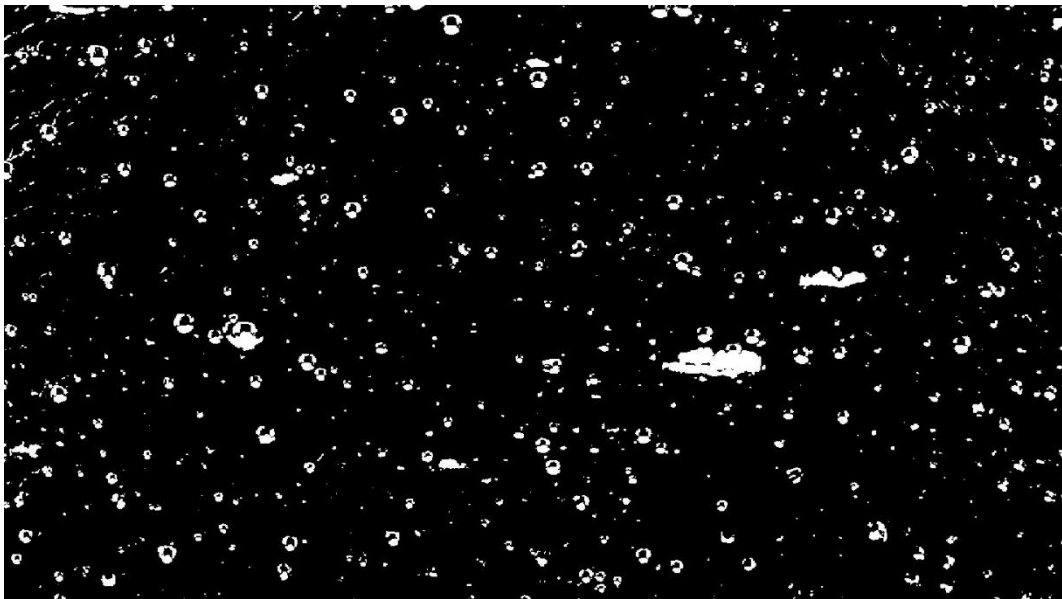


Figure 92 Binarized domain of detected bubbles and bright defects.

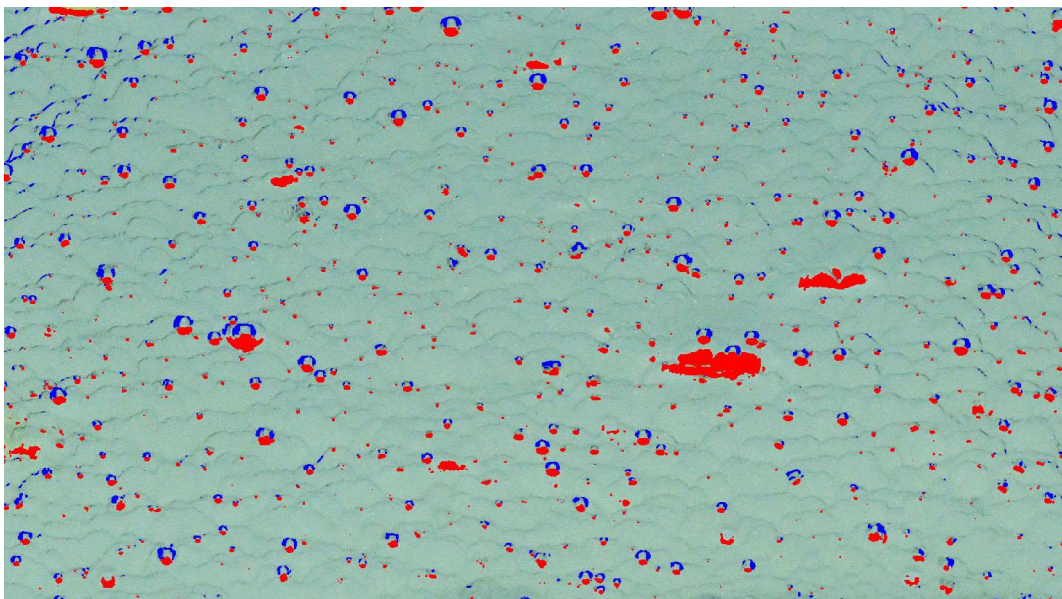


Figure 93 Binarized domain of Fig. 92 shown superimposed on Fig. 91, with lower brighter bubble's part coloured in red and upper darker bubble's part coloured in blue.

Eventual bright defects are, with satisfaction, detected too.

Since, as can be noticed looking at the upper-left corner, also some scallops are identified as the top darker part of the bubble, since they are darker with respect to the surrounding, a method is implemented to restore them in the workable domain of the photo. The condition to be satisfied is based on the distance with respect to

the corresponding lower and brighter region. Obviously, if a lower and brighter set does not exist at all, then for sure the set of darker points previously detected needs to be restored in the workable domain. *Fig. 93* is thus shown again as *Fig. 94*, where the restored pixels are coloured this time in green. The restored pixel corresponds now to null cells of the binarized matrix. This matrix is thus now saved in memory.

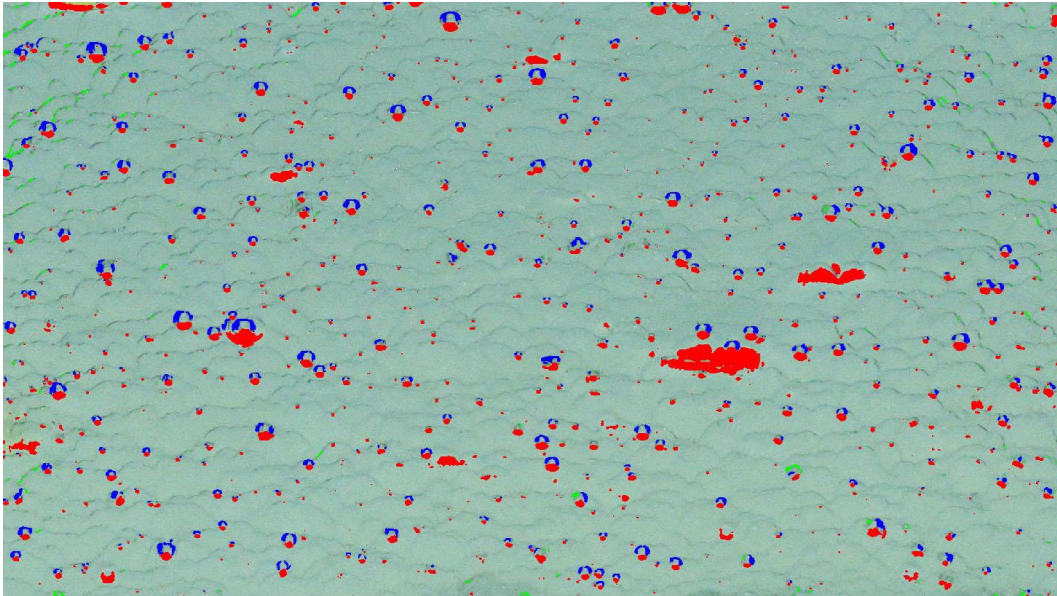


Figure 94 Red pixels correspond to bubbles' lower and brighter part, blue pixels to bubble's upper and darker part, green pixels to restored and thus again workable pixels previously counted among the blue ones. Green pixels can be more easily noted on the top-left corner of the image.

The time has come to explain how the surface pattern can be identified.

This code is not a continuation of the previous one. Only the binarized matrix from the previous code is directly loaded into the workspace and the original photo is imported as well and immediately converted in grayscale. The binarized domain, similar to the one in *Fig. 92*, is firstly gaussian filtered with standard deviation $\sigma = 1.3$, the result is multiplied by 12 and subsequently binarized with thresholding level of 0.3. Eventual holes present are filled with MATLAB's function `imfill`. The original photo is gaussian filtered too with filter's standard deviation $\sigma = 2$. It is useful to call here this filtered photo *B*. This is mainly done to remove salt and pepper noise. The unfiltered original photo is gaussian-filtered with a filter that has a very big standard deviation: $\sigma = 20$. Basically, the photo is very blurred (*Fig. 95*) after this operation and the overall intensity level decreases as well, as expected. This filtered photo is called here *A*.

The crucial step to detect the surface pattern is the subtraction of B from A .



Figure 95 Photo 'A'

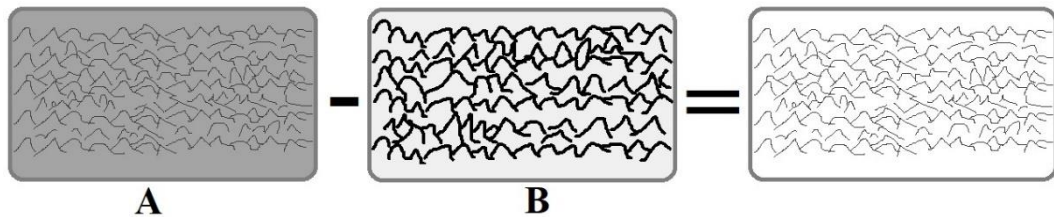


Figure 96 Visualization of the effects of the aforementioned image subtraction. Obviously, in reality, the surface pattern in A is not so evident and is neither so thick in B .

Fig. 96 visually explains why. Basically, B is quite similar to the original. Because the standard deviation is so low that the intensity levels remained pretty the same, except for the small regions characterising the salt and pepper noise which are removed. While the blurred photo, as anticipated, has a lower overall intensity level; in other words, the photo looks (more uniformly) darker. This is equivalent to say that the values of the cells of the matrix (of the photo) are smaller with respect to the original ones. It is very important to keep in mind that the regions without surface patterning are brighter than the confined regions where there is surface patterning. Therefore, when the two photos are subtracted, the regions where there is no surface patterning decrease a lot their intensity value in the gaussian filter, and thus have now a negative intensity value. While the confined regions of surface patterning do not significantly decrease their intensity level. Quite the contrary, since they are surrounded by many brighter regions, they slightly increase their

intensity level. Therefore, after the subtraction, their associated intensity values are still small, but positive in sign.

The pixels corresponding to white regions of the binarized matrix imported are automatically set to zero. While for the remaining, those that have a negative value are set to zero, while the remaining pixels with a still positive value, are all set equal to one, obtaining *Fig. 97*.

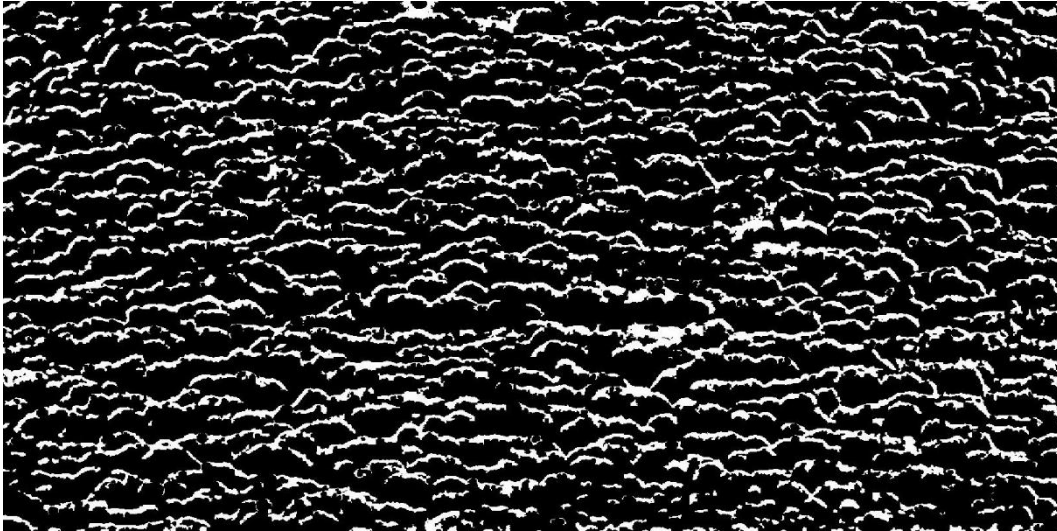


Figure 97 Binarized photo highlighting the detected regions of surface patterns.

It is now necessary to determine a more precise boundary of the surface pattern. Indeed, the one shown in *Fig. 97* is too thick: the single patterns are not discernible, and it looks thus almost impossible calculating the horizontal wavelength.

The light source located at the bottom and pointing upward comes in handy. Indeed, it outlines the quasi-horizontal contour of the patterns.

This allows to easily detect the row at which there is a surface pattern. In order to do so, the first derivative of the intensity value of each cell of the matrix is calculated along the vertical direction. Indeed, the contour of the surface pattern is evident to the human eye, because it has a discontinuity in the intensity value of nearby pixels. Each cell of the matrix made of cells that have the value of the first derivative is multiplied by each cell of the binarized matrix associated to *Fig. 97*. In this way, only the derivative within the regions of surface patterns is considered. The cells corresponding to regions outside the surface pattern are set to a known positive value, which has several orders of magnitude different than the expected first derivative. This is done to be sure that a cell where the derivative is null is not

wrongly considered as a cell not belonging to the domain of a surface pattern. For every column in the photo, the code starts from the first row till it finds a cell where the derivative is negative. The coordinate is saved in a vector named `scallop1`. The algorithm takes into account that the regions detected in *Fig. 97* may have more than one quasi-horizontal “leg”. Therefore, it is not possible to stop at the first negative derivative detected. Therefore, once the first negative derivative is found, the algorithm proceeds increasing the row number but without saving the position of other negative derivatives. As soon as it is found the pixel belonging to the outer region (the one coloured black in *Fig. 97*) that has the adjacent upper pixel in the inner region (coloured white in *Fig. 97*), the search for the negative derivative starts again. But in this case, the variable is saved in a different vector named `scallop2`. Again, the search for the first derivative stops till the pixel outside of the region which is connected with an upper pixel in the inner region is found. The search for the negative derivative restarts again, saving the coordinate to the vector named `scallop3`. In summary, the algorithm has a three-level redundancy to take into account three possible quasi-horizontal “legs” belonging to the same white region shown in *Fig. 97*. Obviously, prior to searching for additional legs, through the search of an outer existing pixel with null derivative, it is checked that the row is within the limits of the image to prevent the code from crashing.



Figure 98 Surface pattern (coloured in red, green or blue) calculated through first derivation of the intensity value along the vertical direction.

This procedure is repeated for every distinct white region in *Fig. 97*. The coordinates calculated in this way are shown in *Fig. 98*. The points belonging to *scallop1* are red, those belonging to *scallop2* are green, those belonging to *scallop3* are blue.

It is worth mentioning that before implementing definitely the algorithm based on the detection of the first coordinate along the column at which the first order derivative of the intensity value is negative, also algorithms based on the detection of the coordinate corresponding to the maximum negative derivative, of the last coordinate of consecutive coordinates having all in common negative derivatives, or of the mean coordinate of consecutive coordinates having all in common negative derivatives were tried. The one based on the first point at which there is a negative derivative is chosen since it accurately calculates the surface pattern boundary. Furthermore, with respect to the algorithms based on the mean value or on the maximum derivative, the calculated points belong to curves which are more probable to be 8-connected for longer distances.

But the problem of the connectivity remains after all, because:

- Each stencil associated to a white region of *Fig. 96* is made of coordinates that are not equally spaced.
- Even when the coordinates are equally spaced, they may cross each other.

The last point is evident in *Fig. 99*.

Indeed, these pixels cannot be directly used for the calculation of the horizontal or of the vertical distance between surface patterns.

In order to use them, two major implementations must be done:

- The stencil must be fixed into a stencil made of equally spaced points.
In order to do so, eventual missing points must be automatically added. After all, it may happen that in the image detection of surface patterns, a pixel might be lost. And even only one missing point is a sufficient condition for a non-equally spaced stencil.
- The patterns belonging to *scallop1*, *scallop2*, *scallop3* need to be reordered in a more efficient way.

This is needed in order to prevent the intersection of patterns and in order to consider patterns made of pixel coordinates simultaneously belonging to

each one of the three mentioned vectors. This is evident in *Fig. 99*, where red and some green points (or even some blue points with respect to green points) should be considered as a single entity before the intersection, while the remaining red points after the intersection should be considered as a separate entity.

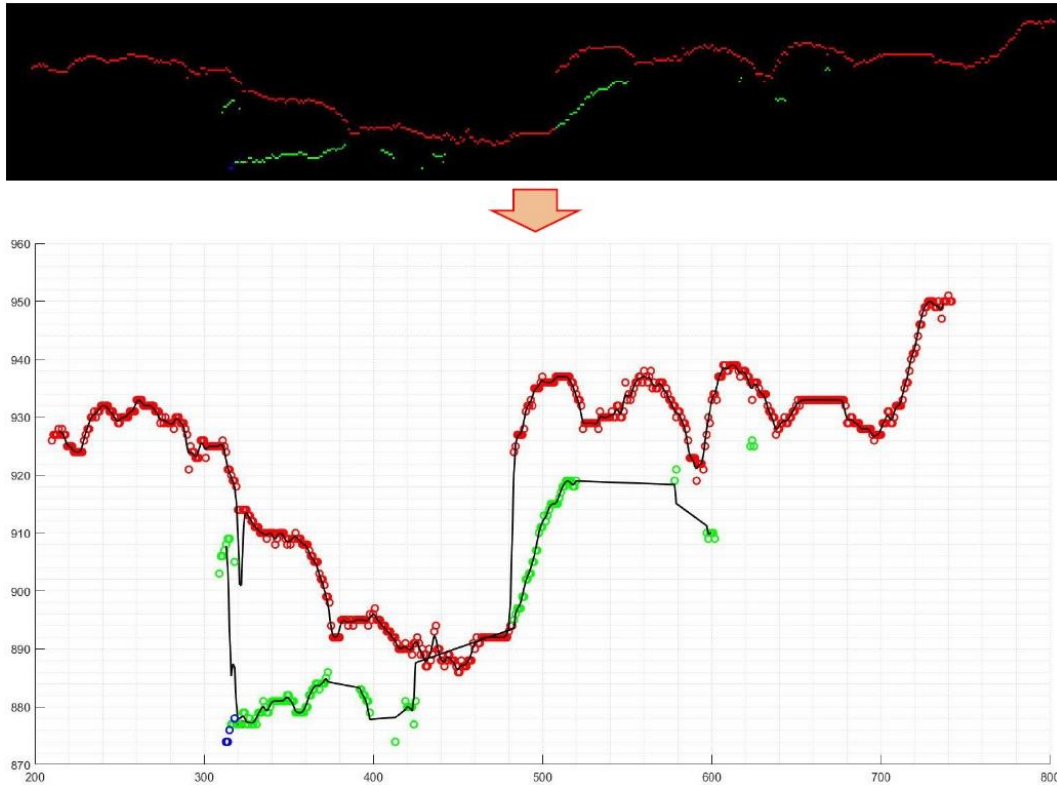


Figure 99 Working directly on the pixel coordinates associated to surface patterns is not possible. In addition to being discontinuous coordinates, they may even cross each other.

This task is not banal. Thinking about an idea to solve this, one suddenly finds out that the same idea may not be applied in other areas of the image or even that further ideas are necessary to close the problem. It is here proposed one algorithm that works very well. It was built after others did not succeed and thanks to the understanding of the limitations that made the other algorithms to fail.

The algorithm starts by considering *Fig. 98*. A null matrix is created. All the cells of the matrix which have the same coordinates of the points belonging to the three vectors shown in *Fig. 98* are equalised to one. A gaussian filtering with $\sigma = 1.2$ is applied to this binarized matrix. By doing so, *Fig. 100* is obtained. White pixels that are vertically or horizontally separated within certain geometrical constraints are connected, as shown in *Fig. 101-102*.

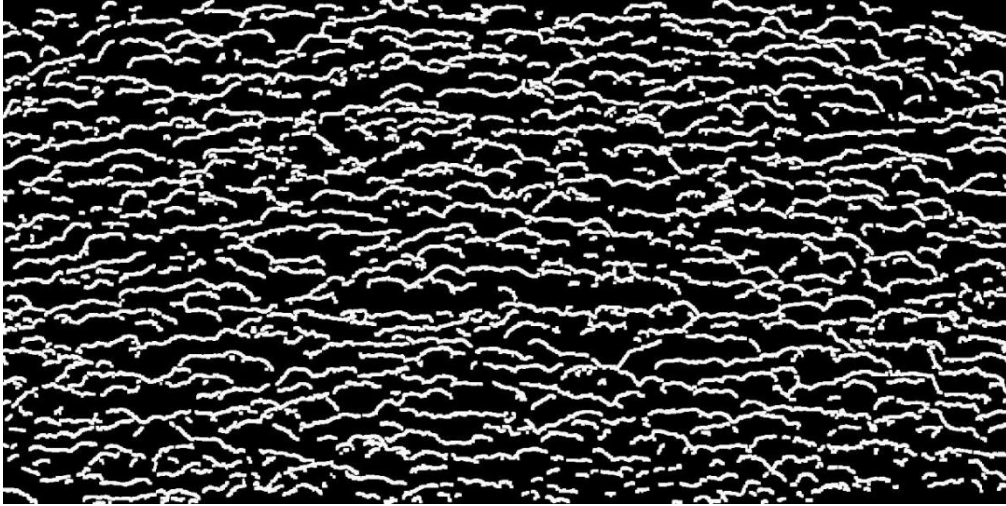


Figure 100 Gaussian filtering of the patterns shown in Fig. 98.

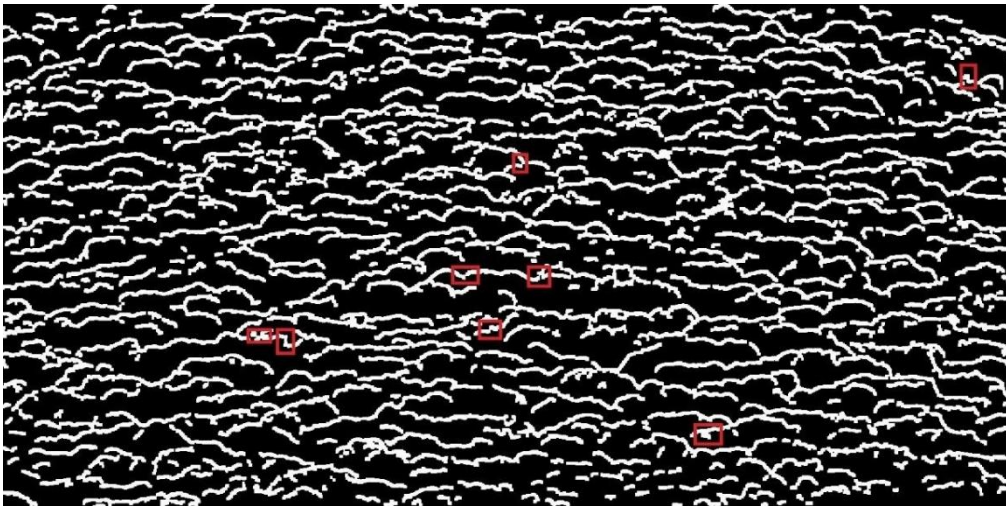


Figure 101 Sets separated by only one black row are connected. (Only some are marked).

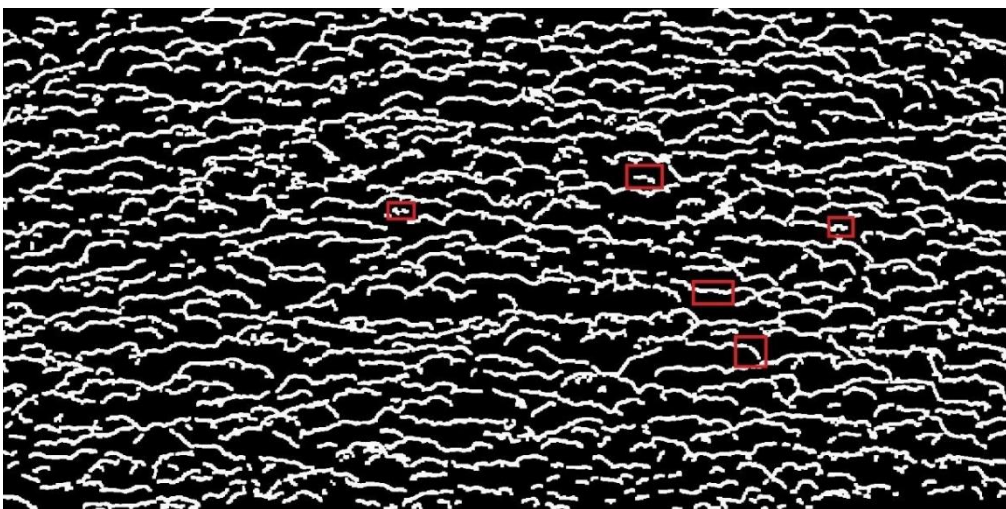


Figure 102 Sets separated by a maximum of three black columns are connected. (Only some are marked).

Skeleton by thinning of the binary imaged along a preferential direction is performed. Basically, for each furtherly-connected set from *Fig. 100*, it is calculated the mean pixel along the vertical direction. The result is shown in *fig, 103*.

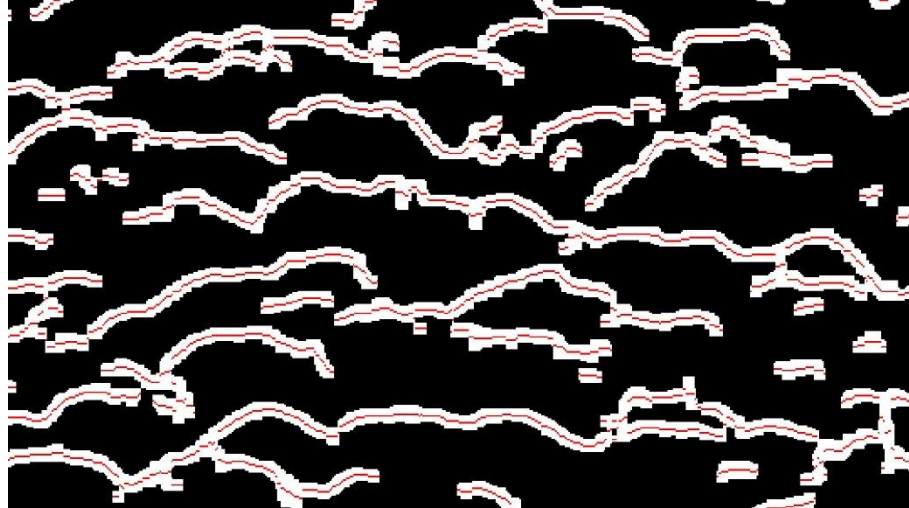


Figure 103 Detail of the calculated skeleton (in red) by thinning of furtherly-connected sets in *Fig. 100* along the vertical direction.

As done for *Fig. 100*, a gaussian filter is applied to the binarized matrix whose non-null cells are those with the same coordinates of the points belonging to the three vectors shown in *Fig. 98*. But this time the standard deviation of the gaussian filter is half of the previous one: $\sigma = 0.6$. Therefore, the widened sets in the photo are always within the widened sets of *Fig. 100*.

On the same image (*Fig. 104*) are considered in white the widened sets of *Fig. 100*, the lastly widened sets is coloured yellow, and the red, green and blue pixels associated to the patterns detected in *Fig. 98* are coloured in the same colour. The skeleton is coloured black. Furthermore, also the features in the image of dimensions 2×2 which have the property shown in *Tables 7-8* are coloured black.

1	0
0	1

Table 7 Feature n.1 detected in the photo.

0	1
1	0

Table 8 Feature n. 2 detected in the photo.

In other words, the cells corresponding to the skeleton and to the ones in *Tables 7-8* are set equal to zero. One detail of the resulted image is shown in *Fig. 104*.



Figure 104 Detail of the image obtained by furtherly-processed *Fig. 98, 100, 103*.

The operations of gaussian filtering and relative sets' connection allow to connect some domains initially non connected, while the operations with the skeleton and with the features shown in *Table 7-8* allow to separate some domains initially wrongly connected. But some domains are not yet optimally connected and some still needs to be connected.

All the operations described so far are a practical example of what in mathematics is defined as a *connected topological space*. In *Fig. 105*, the set Ω_1 of the spatial domain is connected, while the set Ω_2 is not connected but it is made of eight connected components. Basically, the algorithm is trying to pass from the condition associated to *Fig. 105b* to the condition associated to *Fig. 105a*, or in mathematical terms, to *transform each non-connected sets made of connected components into a connected set made of a single component*.

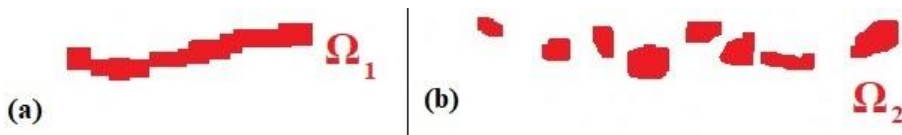


Figure 105 (a) A connected set. (b) A non-connected set made of connected components.

The final operations to connect the pixels of the surface patterns of *Fig. 98* are performed on the gaussian-filtered sets, shown in yellow in *Fig. 104*. Basically, for

each spatial domain defined by the white gaussian-filtered set, which is shown in white in *Fig. 104*, the leftmost yellow set is considered at the beginning. The algorithm calculates the distance and the angle of the segment between the rightmost pixel of the surface pattern within the leftmost yellow subset and the leftmost pixel of the surface pattern within all the remaining yellow subsets on the right. To have a connection, some requirements on the distance and the angle need to be satisfied. If they are not, the yellow subset considered is not connected and is thus removed from the ones to connect. Otherwise, the connected yellow subset on the right becomes the subset “on the left” and the operation is repeated till the rightmost pattern is reached. Obviously, when this condition is reached, not all the yellow subsets are still connected. Therefore, the cycle starts again from the leftmost among the remaining unconnected yellow subsets, till all the subsets are either connected or unconnectable.

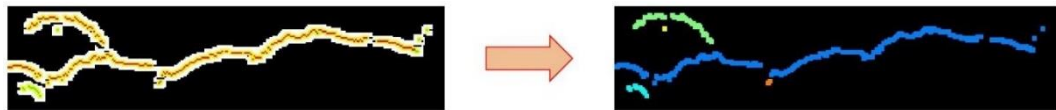


Figure 106 Connection of yellow subsets.

Fig. 106 shows one random result of the described operation. The final subsets that have a number of pixels of the surface pattern less than five are deleted permanently. This happens to the yellow and orange subsets on the right of *Fig. 106*.

For each yellow subset, eventual missing points are added by interpolating with a line the two extrema of the missing interval. In this way the stencil becomes equally spaced.

To calculate the vertical distance between surface patterns, since these are similar to quasi-horizontal lines, they are approximated by a horizontal line passing through the centroid of the coordinates of the pixels of the surface pattern. The length of the line is given by the horizontal extension of the surface pattern. *Fig. 106* shows a detail of the spatial domain where the horizontal lines approximating the surface patterns are visible. The reason why the author shows a detail and not the full picture is merely because when saving, or even only visualising, the full picture in MATLAB, most of the lines are automatically not shown by the program, and only

by zooming in the user can really see all the lines and thus see the vertical spacing between them.



Figure 107 Horizontal lines approximating the surface patterns detected and connected thus far.

Even if a characteristic vertical wavelength already appears in *Fig. 107*, directly calculating it for each column by advancing in the row numbers and saving the interval between every change of value in the binarized cell of *Fig. 107*, leads nowhere. Anyways, for clarity, it is shown in *Fig. 108* the result someone would obtain by doing so for a single photo.

Fig. 108 clearly shows two characteristics. The first one is that the interrogation area is not fixed for all the photos, but it evolves in time, being optimised for every photo. Basically, the upper and lower horizontal sides of the interrogation area evolve as in *Fig. 88*. This is more important for the upper limit, in order to let it evolve close to the leading edge of the frontal surface. This is visible in the photo by the quasi-linear region before the 200th pixel-row of the photo. If the interrogation area were fixed, only the region with the peaky curve of the gaussian convolution would have been visible, with a horizontal interval going approximately from the 100th to the 300th pixel-row of the photo. After all, it is not physically correct to directly focus on the middle of the frontal surface area neglecting its distance from the leading edge, because the solute layer starts descending from the upper side of the frontal surface. The second evident characteristic is the presence of the interval of linearity. This interval provides a further information: the growth distance from the leading edge needed by the

surface pattern to assume a coherent form in space. In other words, close to the leading edge of the frontal surface, the lines approximating the surface pattern have a longer (horizontal and) vertical spacing among them. And only at a certain position the lines start being more packed on the surface. The coordinate in the plot showing the transition from the linear to the peaky region highlights this change.

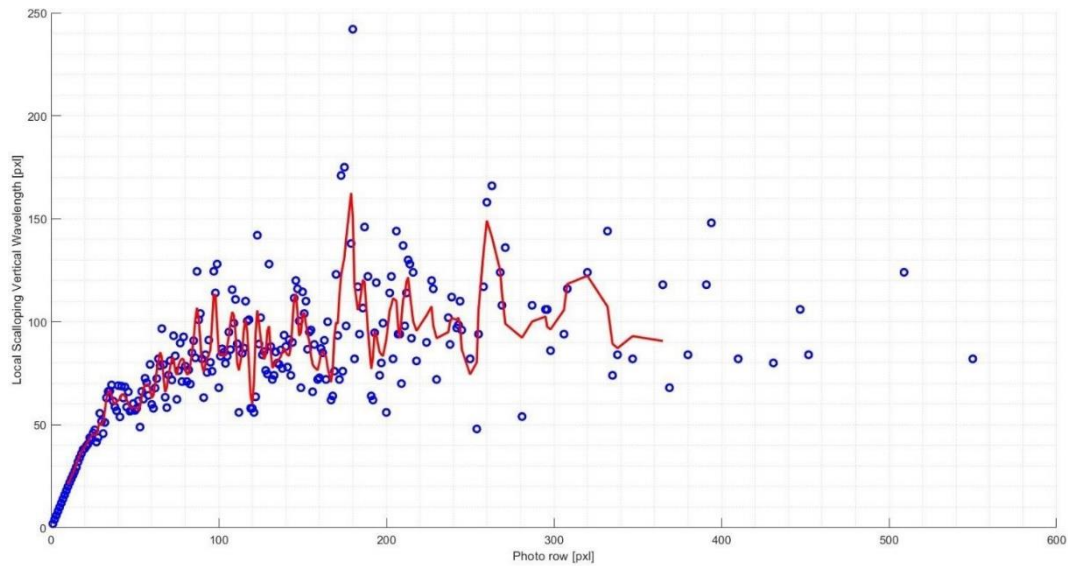


Figure 108 Vertical wavelength between surface patterns (approximated by horizontal lines) calculated by counting the peak-to-peak for each column. Adapted interrogation area in time.

But as anticipated, even if *Fig. 108* provides the useful information about the coordinate of the surface pattern's chaotic transition into coherency, is not very useful for determining the evolution in time of the vertical distance between surface patterns. Firstly, because *Fig. 108* is related to a single photo. This means, since an experiment lasts for ninety minutes and the photos are taken every thirty seconds, that 180 similar graphs are obtained...for a single experiment. Saving the peaks' position of every graph in a vector and plotting the evolution of the positions in time is only useful to see how a graphic with a high dispersion in the data looks like. Furthermore, by carefully looking at the peaks' value and position in *Fig. 108*, it is evident that there are more peaks than it should be. Indeed, if each peak's value is the distance between consecutive patterns, it is expected to find the successive peak in a position on the x -axis given by the sum of the previous peak's position plus its value. But this is not the case. After all, this happens because, looking at *Fig. 107*, when two lines partially overlaps their end parts in the same column, the peak-to-peak distance falls. This highlights the path toward a better algorithm: a

weighted peak-to-peak distance based on the number of pixels of the line sharing the same value.

This algorithm does not start counting the distance between the horizontal lines from the first row of the discrete spatial domain. Instead, each line has a spatial reference system. Therefore, the algorithm starts counting from each pixel of a horizontal line the vertical distance to reach the pixels of line(s) located downward. Since the initial line may have its end parts partially above surrounding lines or there might even be small segments between two very long lines, as shown in *Fig. 107*, if more than a distance is found for an initial line, these are weighted for the number of pixels sharing the distance value, and only the two distances associated to the two biggest number of pixels are taken into account. The value of the two distances is then averaged and stored for the known vertical coordinate of the initial line.

The evolution of the value along the rows of the photo is quite dispersed, as shown in *Fig. 109*.

The mean value μ and the standard deviation σ normalised to $(n - 1)$, where n is the number of dispersed points, are calculated. This allows to set the interval $[\mu - \sigma, \mu + \sigma]$, within which to consider the dispersed points. By doing so, eventual points that are very different than the mean and that would thus influence the gaussian convolution making spurious peaks are removed. The distribution of the points and the related gaussian convolution is shown in *Fig. 110*.

The same figure indicates with inverted violet triangles the position of the local maxima. This is plotted in a different graph (*Fig. 111*) as a set of vertical red lines, where the height of the lines corresponds to the vertical distance between consecutive surface patterns, and the position of the lines is the position of the upper surface pattern with respect to which the distance is calculated. This allows to overlap on the same plot the curve of the interpolated peak-to-peak points and its gaussian convolution, as shown in *Fig. 112*. Obviously, this is more a visual feedback, since it can be seen as the spread probability over a certain region of finding that surface pattern's vertical wavelength. By saying that this is merely a visual feedback, it is meant that the filtered distribution cannot represent the distribution of the peak-to-peak, since the distribution is expected to be a succession

of peaks, where the distance between two consecutive ones is exactly the value of the previous peak.

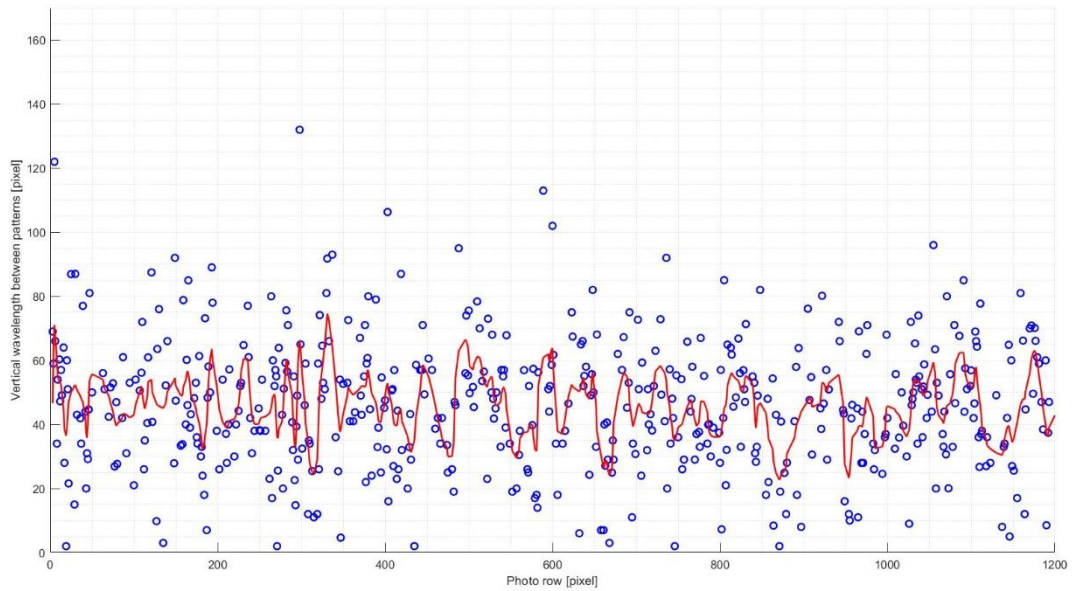


Figure 109 Dispersed points indication the distribution along the rows of the photo of the vertical distance between two horizontal lines, which approximates the surface pattern.

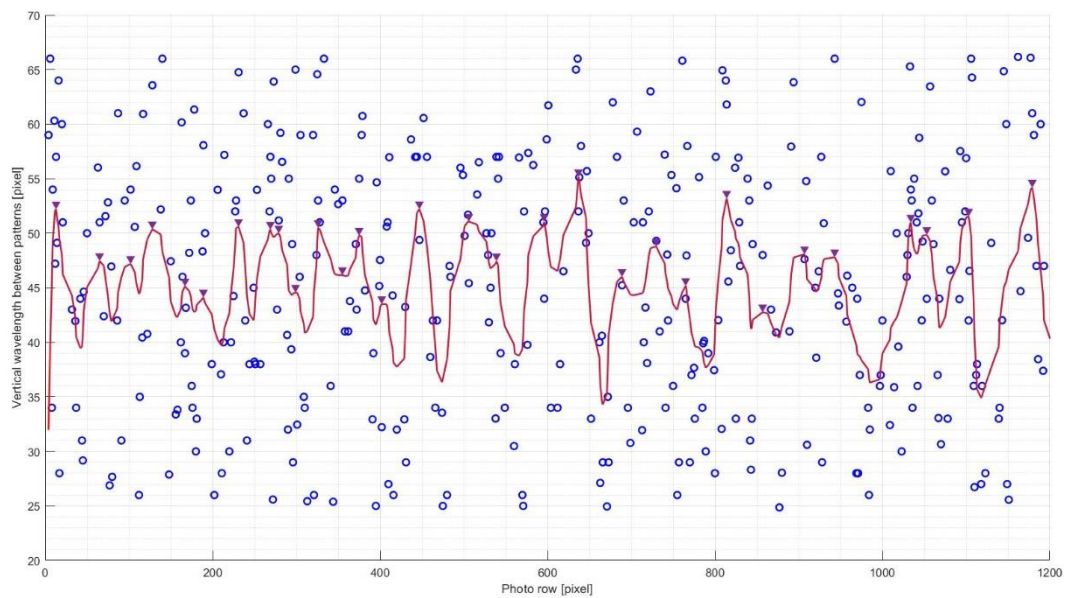


Figure 110 With respect to Fig.109, points outside the interval $[\mu - \sigma, \mu + \sigma]$ are not considered.

From Fig. 110 and especially from Fig. 111, it is clear how the peaks now calculated are more physically representatives of a wavelength. Indeed, between a peak and its successive there is a distance which is about the value of the peak.

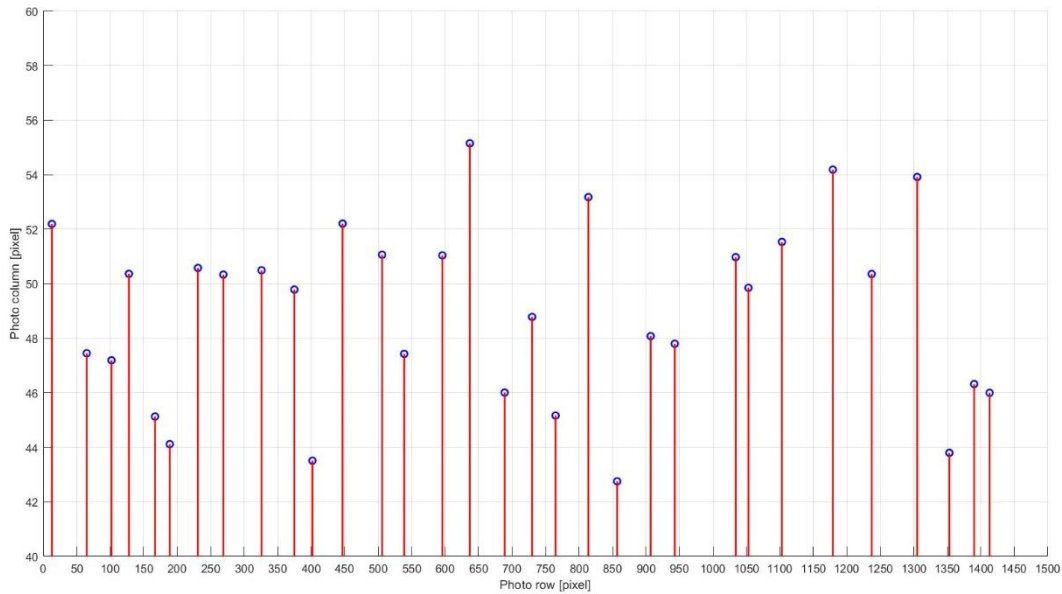


Figure 111 Peaks of Fig. 110 distributed along the vertical direction (alias the row) of the photo.

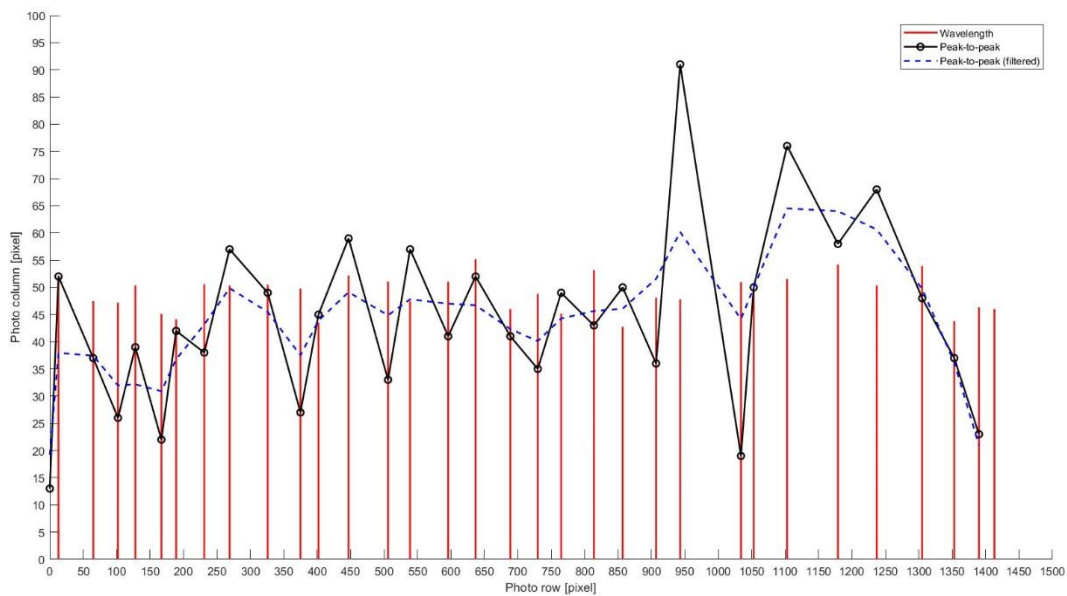


Figure 112 Interpolation of the peak-to-peak points (black) and its gaussian convolution (blue).

The final step is to plot the evolution in time of the peak-to-peak distribution along the vertical direction found for each photo. The result is plotted in a graph, Fig. 113, where the x -axis is still the vertical direction, alias the rows of the photo, while the y -direction is the temporal domain. The blue circles in Fig. 111 are thus plotted at the corresponding coordinate along a horizontal line.

The information on the vertical wavelength is in the figure, but it is hidden. To elaborate from the data the wanted information, it is necessary to remember that, as

shown in *Fig. 114*: firstly, the surface pattern is advancing upstream and, secondly, the related upstream velocity is so slow, that the cross-correlated position in the two photos of the same pattern is easily detectable even with the naked eye.

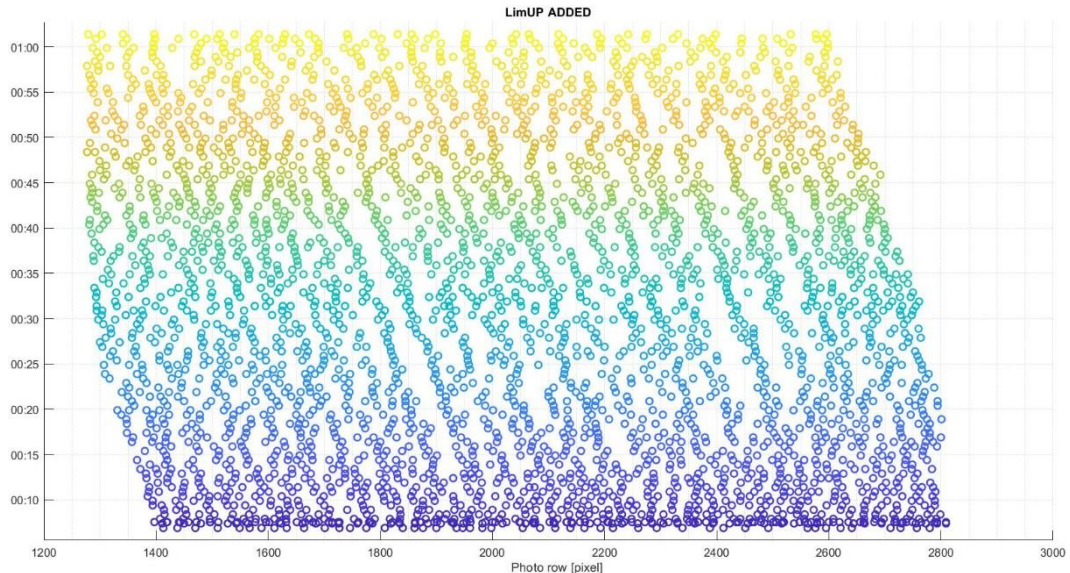


Figure 113 Evolution in time of the distribution of the peak-to-peak distance between surface patterns along the vertical direction.

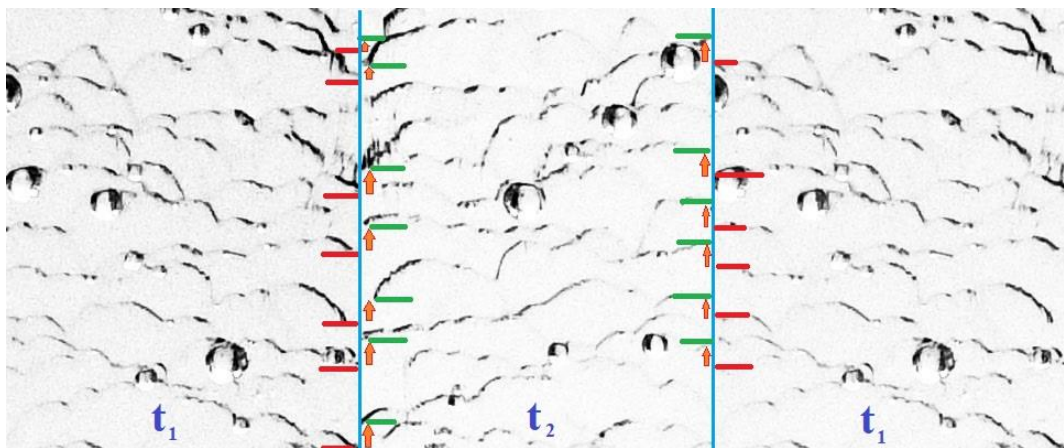


Figure 114 Detail of two photos taken at time instants t_1 and $t_2 = t_1 + 240$ s. The detail on the left and on the right is the same, while the detail in the middle is flipped horizontally to show the vertical displacement. The details are made of the same pixels of two different photos taken at different times at a fixed position. It is evident that the surface pattern advances upstream in time.

Combining in *Fig. 113* the information that the same surface pattern is expected to be in a slightly advanced position in the successive photo, it is possible to search for a hidden coherence in the apparently dispersed data. The information translates into grouping the points that are on leftward inclined lines. In other words, the algorithm is cross-correlating the peak-to-peak referred to the probable same

surface pattern that is shifted slightly upward in the following photos. *Fig. 115* shows the automatic implementation of the task.

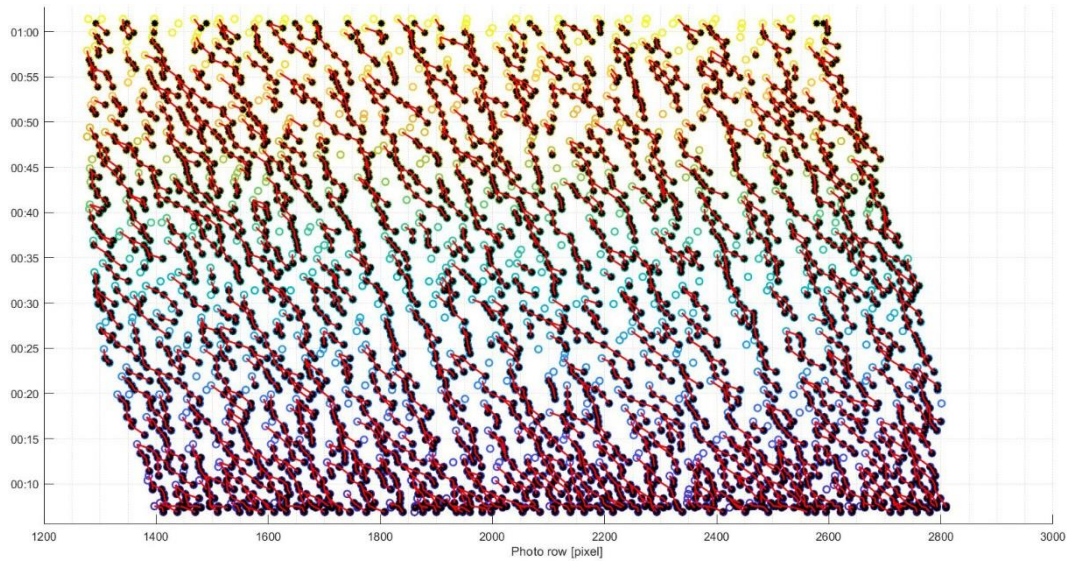


Figure 115 Cross-correlated peak-to-peak distances of the same upstream-advancing surface pattern superimposed on the distributed data shown in Fig. 113.

Therefore, *Fig. 115* provides the evolution in time and along the flow stream direction, starting from the leading edge of the frontal surface, of two quantities:

- The peak-to-peak distance associated to the surface pattern.
- The upstream-advancing velocity.

The first quantity can be calculated measuring the horizontal distance between a curve connecting cross-correlated points and the one at its right.

The second quantity is given by the local inclination of the curve connecting cross-correlated points.

All said thus far is related to the vertical peak-to-peak. The calculation of the horizontal peak-to-peak is done in a similar way. On each connected yellow subset, as the one shown in *Fig. 106*, a gaussian convolution with very low standard deviation is applied. The reason why the standard deviation must be very low is that otherwise it may dampen too much the maxim and the minima that we are interested in detecting. But at the same time, it is necessary because, even if the stencil is now equally spaced, it is not continuous. And it will never be continuous if a gaussian convolution or in general an interpolating function is applied because the stencil is by definition made of discrete points: the pixels of the photo.

This time the peak-to-peak distance is the distance between maxima of the gaussian convolution. It may happen that only a maximum is found, because sometimes the detected pixels are only one side of a single scallop. It was decided by the author to implement a conditional statement in the code to check if the condition of existence of only one maximum for a given yellow subset is satisfied. If the condition is true, then the maximum is not saved. Regarding the few cases when this happens, an attempt to calculate a horizontal wavelength could have been to calculate the distance with respect to the minima of the gaussian convolution. Anyways, the author preferred directly not to consider an eventual subset made of similar points, in order to have fewer data, but at least more accurate and reliable; together with a more stable code. Speaking of code's stability, the event that no maxima of the gaussian convolution are found is taken into account. The author has not checked if at this stage of the code there are subsets made of perfectly horizontal points. Anyways, if they may exist or not, there is a conditional statement that checks for the existence of no maxima. If the condition is true, then the corrupted subset is directly deleted. So, for each subset the maximum, mean and minimum wavelength are saved. It is usually preferred to work only with the mean horizontal wavelength. This distance is associated to the vertical position of the centroid of the subset. From here on the algorithm is the same as the one for the vertical wavelength since it works on a wavelength and the associated position on the vertical direction.

It is worth reminding that both the frontal code and the lateral code convert the pixel distance into a mm scale. For doing this, an algorithm that allows to manually draw a segment and that automatically displays the number of pixels within the drawn segment is used (*Fig. 116*). The algorithm is applied to a photo of a ruler hold parallel to hard candy's surface. Usually two measurements are computed, and their averaged value is used for computing the conversion factor.

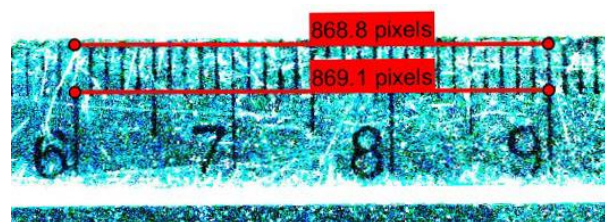


Figure 116 Algorithm used for determining the pixel-to-mm conversion factor.

CHAPTER 5: Results and discussions

5.1 Results from side photos

One of the information of biggest interest which can be calculated from lateral photos is the mean regression rate of the lower surface and upper surface.

Even if not initially requested, the surface mean regression acceleration is also calculated. A verification of a possible inflection point in the function is done and a possible explanation of its presence is provided.

The present work did even more: thanks to the high spatial resolution of the cameras, a study of the evolution in time of the distribution of the local regression rate is attempted.

The mean regression rates for the bottom surface of the hard candy block are plotted in *Table 9* for the inclinations of 30°, 45°, 60° with respect to the horizontal and for the cases of no additional salt added to the water in the aquarium and salinities $S \approx 4.41$ ppt and $S \approx 8.82$ ppt.

It is worth recalling that all the values reported in *Tables 9-10* are negative, because the direction of the normal vector of the surface is considered pointing outward from the solid body.

	$\alpha=30^\circ$	$\alpha=45^\circ$	$\alpha=60^\circ$
No add. NaCl	-3.07e-6 m/s	-3.25e-6 m/s	-2.98e-6 m/s
$S \approx 4.41$ ppt	-3.42e-6 m/s	-3.31e-6 m/s	-3.00e-6 m/s
$S \approx 8.82$ ppt	-3.18e-6 m/s	-2.95e-6 m/s	-2.36e-6 m/s

Table 9 Mean regression rate of the lower surface.

	$\alpha=30^\circ$	$\alpha=45^\circ$	$\alpha=60^\circ$
No add. NaCl	-8.94e-7 m/s	-9.11e-7 m/s	-1.10e-6 m/s
$S \approx 4.41$ ppt	-8.81e-7 mm/s	-8.54e-7 m/s	-8.84e-7 m/s
$S \approx 8.82$ ppt	-1.03e-6 m/s	-9.90e-7 m/s	-8.56e-7 m/s

Table 10 Mean regression rate of the upper surface.

	$\alpha=30^\circ$	$\alpha=45^\circ$	$\alpha=60^\circ$
No add. NaCl	+4.10e-11 m/s ²	-2.46e-11 m/s ²	-1.28e-10 m/s ²
S≈4.41 ppt	+3.52e-11 m/s ²	-1.05e-10 m/s ²	-1.62e-10 m/s ²
S≈8.82 ppt	+5.61e-11 m/s ²	-2.13e-8 m/s ²	-9.52e-11 m/s ²

Table 11 Mean regression acceleration of the lower surface.

	$\alpha=30^\circ$	$\alpha=45^\circ$	$\alpha=60^\circ$
No add. NaCl	+3.23e-11 m/s ²	-1.87e-11 m/s ²	+7.10e-7 m/s ²
S≈4.41 ppt	-5.68e-12 m/s ²	-4.35e-11 m/s ²	-1.87e-11 m/s ²
S≈8.82 ppt	+9.72e-11 m/s ²	-4.30e-11 m/s ²	+9.74e-12 m/s ²

Table 12 Mean regression acceleration of the upper surface.

	$\alpha=30^\circ$	$\alpha=45^\circ$	$\alpha=60^\circ$
No add. NaCl	56'	66'	62'
S≈4.41 ppt	38'	47'	-
S≈8.82 ppt	48'	49'	105'

Table 13 Minutes from the start of the experiment at which there is a flex point in the mean regression acceleration of the lower surface. If '-', then no asymptote was registered.

	$\alpha=30^\circ$	$\alpha=45^\circ$	$\alpha=60^\circ$
No add. NaCl	53'	-	62'
S≈4.41 ppt	37'	62'	68'
S≈8.82 ppt	65'	43'	60'

Table 14 Minutes from the start of the experiment at which there is a flex point in the mean regression acceleration of the upper surface. If '-', then no asymptote was registered.

The data shown in *Tables 9-10* clearly shows how the lower surface has a regression rate which is greater of orders of magnitude with respect to the regression rate of the upper surface. The ratio is expressed in *Table 15*.

	$\alpha=30^\circ$	$\alpha=45^\circ$	$\alpha=60^\circ$
No add. NaCl	3.43	3.57	2.71
S≈4.41 ppt	3.88	3.88	3.39
S≈8.82 ppt	3.09	2.98	2.76

Table 15 Ratio of lower surface's mean regression rate to upper surface's mean regression rate.

Table 15 is quite useful to show that the regression rate is not constant as someone would a priori expect without considering the existence of the boundary layer.

It is also interesting to notice that, by increasing the water salinity for a fixed inclination of the block, the regression rate does not change monotonically.

Furthermore, keeping fixed the salinity and changing the inclination of the block, the same non monotonic behaviour is observed.

Making consideration on the salinity is not easy. While regarding the influence of the inclination angle, apart from the value of the case of no additional added salt at $\alpha = 30^\circ$ whose experiment should be repeat, the other cases show how the regression rate decreases by increasing the inclination with respect to the horizon. After all, the more the block is horizontal, the easier the solute layer “falls” away from the lower surface of the block. In the other extreme case of a perfectly vertical block, the solute layer will indeed remain in the near-wall region while descending downward. This means that the solute increases very easily the concentration gradient flowing downward and therefore the block tends to dissolve slower or, in other words, with a slower regression rate. Furthermore, the smaller the inclination, the more hydrodynamically unstable is the solute layer, and the stronger is the solutal convection induced by dissolution.

To prove this, an experiment with the block perfectly vertical has been carried out. In this case there is no evidence of scalloping on both the surfaces.

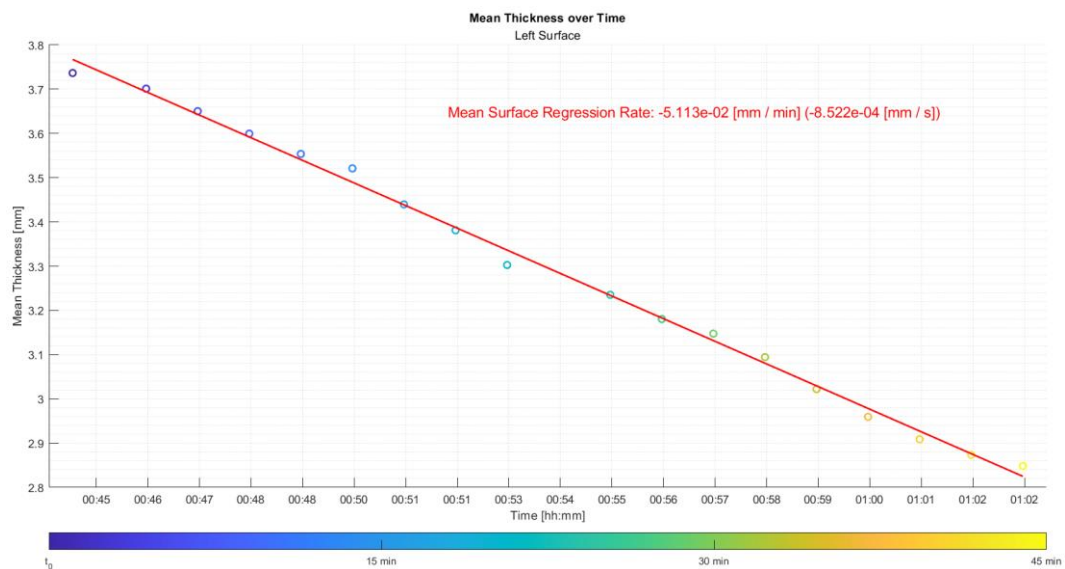


Figure 117 Evolution in time of the thickness of a perfectly vertical dissolving hard candy block.

Fig. 117 clearly shows that in case of a perfectly vertical dissolving block, the regression rate is quasi-perfectly linear and that its module $\dot{h}(t) = -8.52 \cdot 10^{-7}$ m/s is an order of magnitude smaller than the values associated to the lower surface of an inclined block (Table 9) and very similar to most of the values associated to the upper surface of an inclined block (Table 10).

Furthermore, this is an opportunity to recall that the curves approximating the evolution in time of the thickness of an inclined block looks all like Fig. 82. In this curve, three regions can be found. An initial region and a final region where the instantaneous measurements are below the approximating line and a big intermediate region where the opposite happens. Fig. 118 clearly shows this.

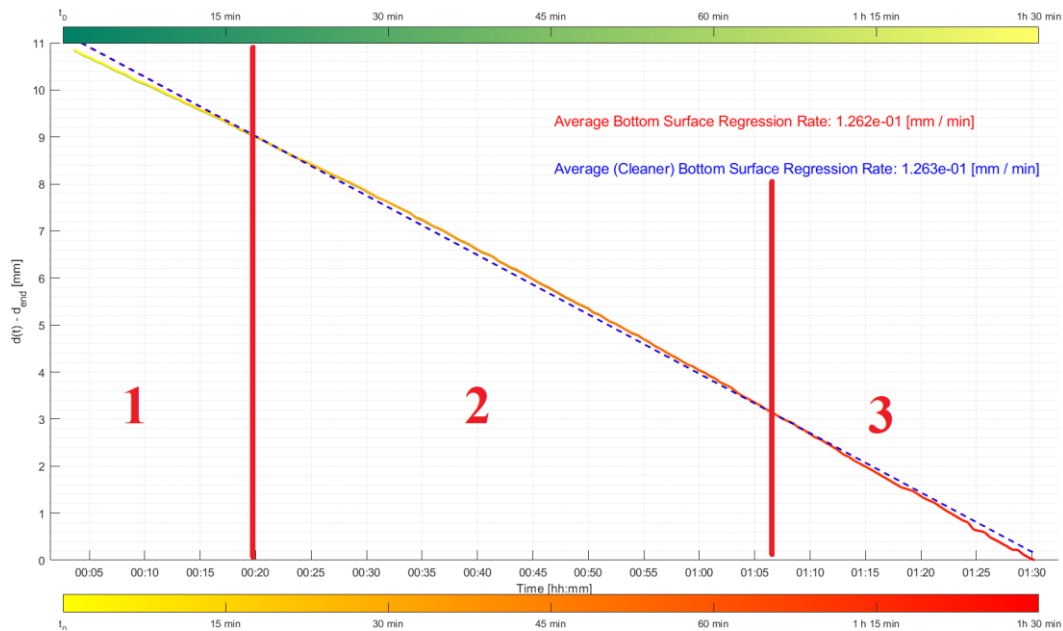


Figure 118 Evolution in time of the thickness of a generic inclined hard candy block.
The three regions described above are quite evident.

This happens because a line approximates all the points within the stencil. But as explained hereafter and can be seen in Fig. 119, the regression rate is not linear. Indeed, in the moment the solute block is immersed into the solvent, there is a peak in the concentration gradient of the overall system. But it is necessary to wait a *system response time* before the regression rate reaches the value it has in the middle of the experiment. After all, as already anticipated in [69] [29], there is an onset time. Whereas, in the final instants of the experiment, there is a lot of dispersed solute in the solvent. Therefore, the concentration gradient is smaller and thus the

instant regression rate calculated from the experimental measurements is lower than the temporal-mean one.

Finally, the higher value in the central region can be explained as simply due to the linear approximation of a non-linear quantity, as anticipated before.

Tables 11-12 are not useful since it is a *mean* regression velocity. Indeed, as just mentioned, the regression velocity in all the experiments is higher at the beginning and decreases as time passes, because the concentration of dissolved solute in the solvent increases in time. Fig. 83 and Fig. 119 are generic curves of the evolution in time of the regression rate that prove what just said. Therefore, considering the mean regression velocity, or even more its sign, is useless. Since, as shown in Fig. 120, its value can be seen as strongly affected by the instant when the curve crosses the zero-line. If most of the curve is above it, then the final mean acceleration is positive, while the opposite happens if most of the curve is below the zero-line. Therefore, Tables 13-14 are more useful than Tables 11-12.

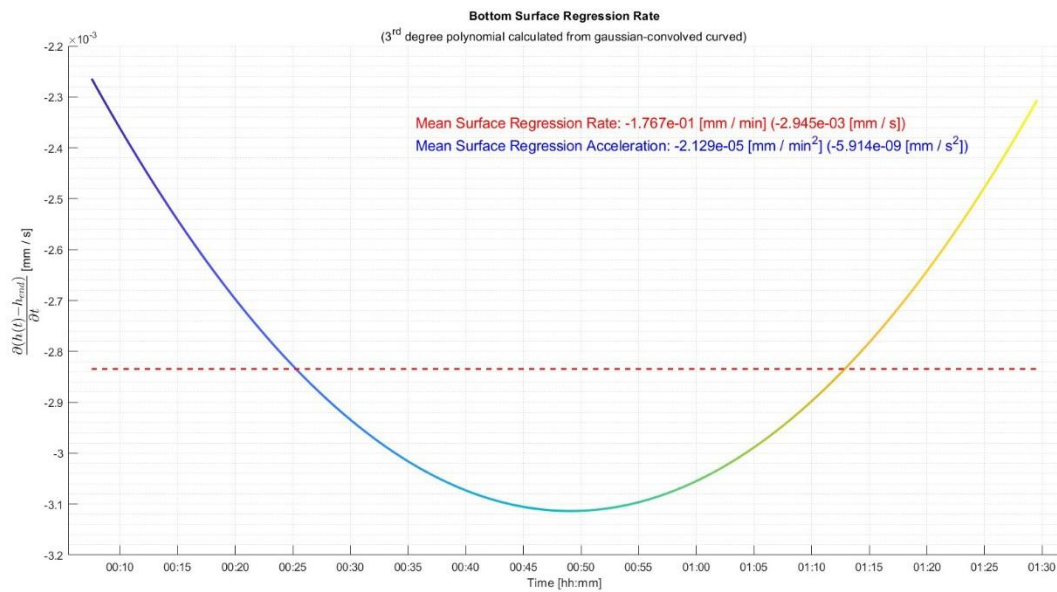


Figure 119 A generic curve showing the evolution of the regression rate in time.

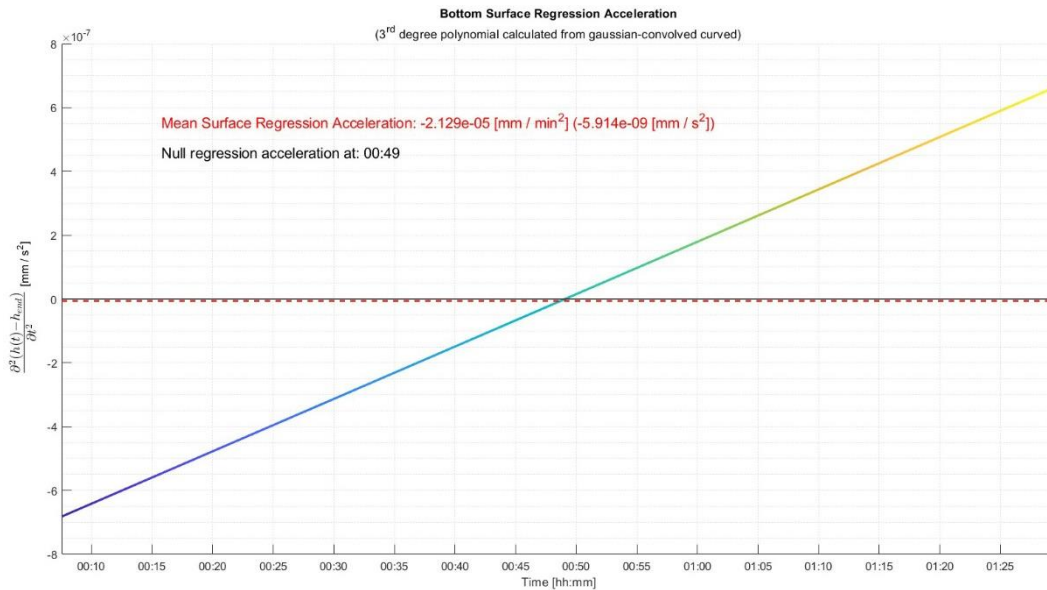


Figure 120 The curve showing the evolution in time of the respective acceleration (parula-coloured) of the regression velocity shown in Fig. 119 and its mean value (red dotted).

Before continuing, it is worth saying that the acceleration is not linear a priori. Indeed, the behaviour of the function approximating acceleration [m/s²] is linear only because the evolution of the thickness [m] in time is approximated with a third-degree function. Anyways, this does not create problems because there is a greater interest in the study of the instant, if exists, when acceleration is zero. And it was confirmed, during the post-processing of several experiments, that increasing the order of the approximating function beyond the third, does not significantly change the final results, but instead increases significantly the corruption of the function, since some coefficients become too small.

Anyways, the instant corresponding to the inflection point indicates when there is a peak in the regression rate. This point identifies the highest deviation between the instantaneous regression rate calculated from experimental results and the approximating function, which is located in the middle region of Fig. 118.

If no inflection point is found, like in the case shown in Table 13 of $\alpha = 60^\circ$ and $S = 4.41 \text{ ppt}$, this does not mean that the regression rate keeps accelerating indefinitely, but that the experiment terminated before the inflection point could have been reached, as clearly proven by Fig. 121.

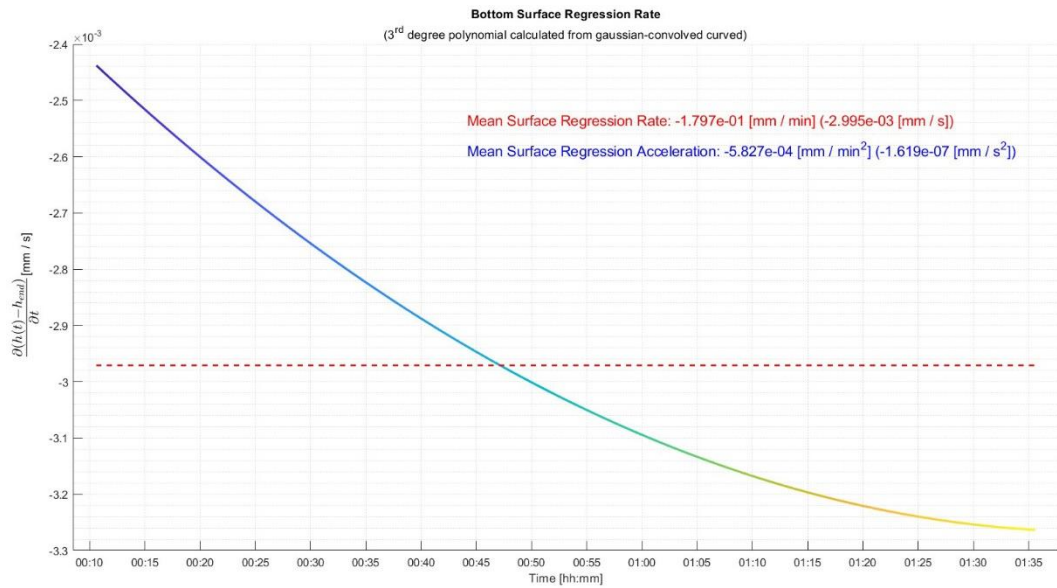


Figure 121 Evolution in time of the regression rate of the lower surface of a block inclined $\alpha = 60^\circ$ with respect to the horizontal and with $S = 4.41$ ppt.

Before the conclusion of the present paragraph, it is good to mention a couple of results regarding the *spatial* evolution of the local regression rate of the lower and upper surfaces of the inclined block.

Fig. 85 shows the spatial evolution of the value referred to the lower surface, while Fig. 122 shows the same graph with fewer curves displayed.

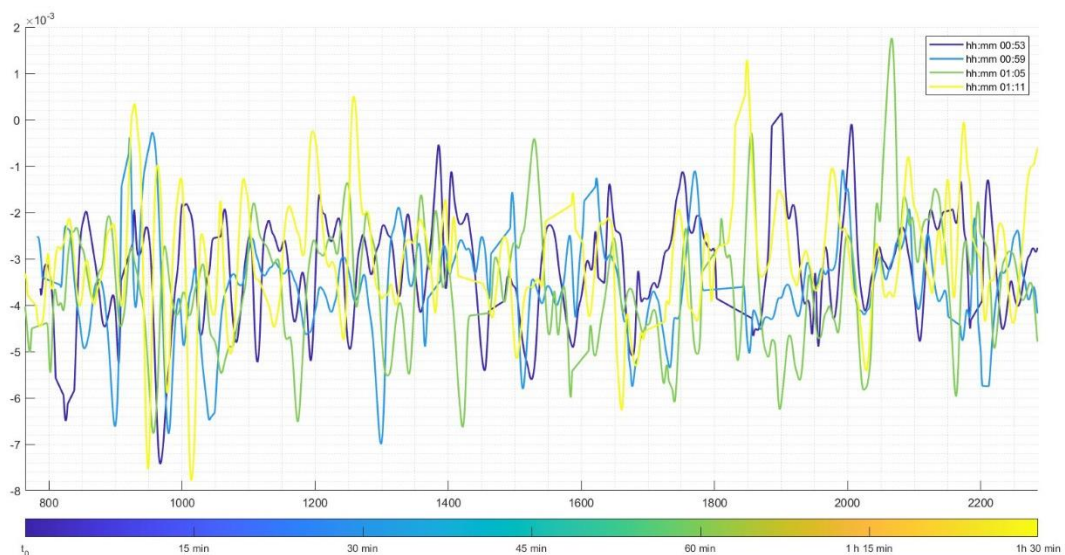


Figure 122 Detail of the graph of the spatial distribution of the regression rate shown in Fig. 85. Referred to the case of a block inclined $\alpha = 45^\circ$ without added salt to the water.

Higher local amplitudes mean a higher regression rate, while the opposite is true for smaller amplitudes. Positive values are physically nonsense, since they should be referred to a surface increasing the position of its surface outwards. The regions of positive values are therefore not considered in the sequent processing. What is worth to notice is that the curves tend to slowly shift to the left in time. The shift is related to the upstream velocity of the pattern. Indeed, positions occupied in an instant by a peak will be occupied after a while by a valley of the dimply lower surface of the dissolving body, and the process repeats. Therefore, the shifting velocity can be also calculated from *Fig. 122*. Anyways, in the present work, it was preferred to calculate the upstream velocity of the patterns only from the frontal photos. Because the side photos are more related to the lateral side, and thus may be affected by unwanted phenomena associated to the boundary region.

The last figure is also useful to calculate the discrete Fourier transform using a fast Fourier transform algorithm, as anticipated in the paragraph 4.1. A couple of results are reported hereafter.

Even if these points may be eventually affected by unwanted phenomena associated to the boundary region, it is necessary to note that they describe quite well a transition that there is in the physical phenomenon studied.

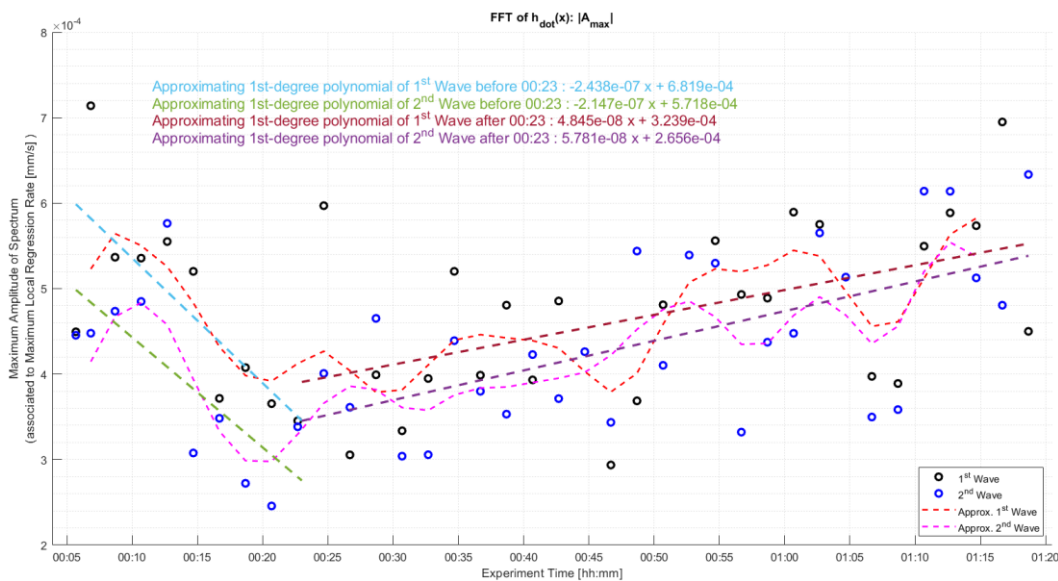


Figure 123 Evolution in time of the amplitude of the two harmonic carrier waves for the case $\alpha = 45^\circ$ and $S = 4.41$ ppt

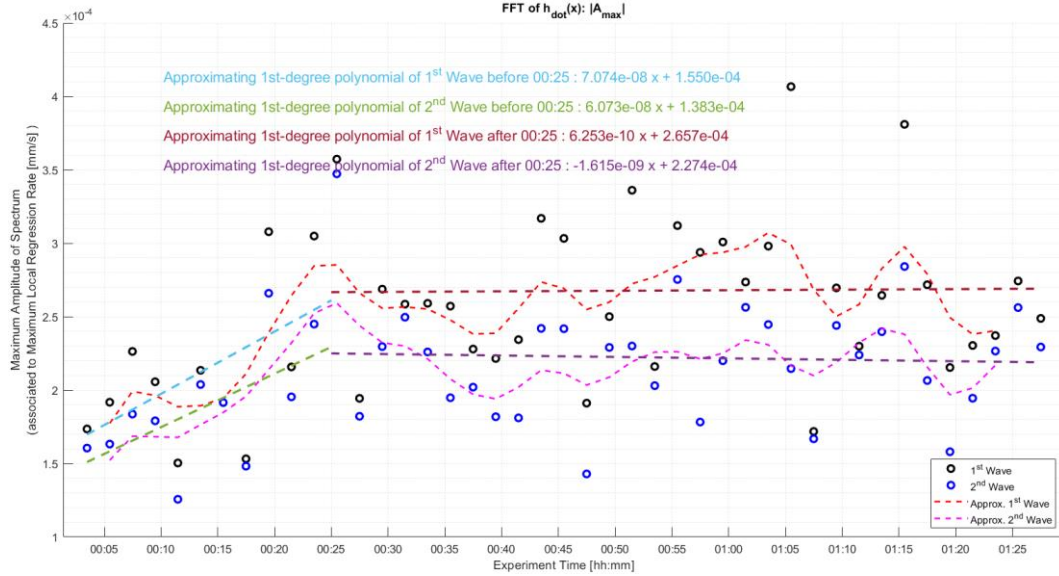


Figure 124 Evolution in time of the amplitude of the two harmonic carrier waves for the case $\alpha = 45^\circ$ and no additional salt added to the water.

Indeed, as visible, it is possible to notice a transition occurring at about 20-25 minutes since the block is immersed. The transition-time depends on the inclination. And the instant shown in Fig. 124 is surprisingly not so different from the mean of the interval at which the transition from flutes to scallop is happening or is under completion.

The corresponding wavelengths associated to the frequencies of the respective carrier waves is found to be within the interval $\lambda \in [1.4, 1.65]$ mm. The mean value is close to three times the characteristic wavelength $\lambda_c \approx 0.53$ mm of the solutal convection instability induced by dissolution applied to the case of a perfectly horizontal block [69]. The same algorithm proposed in the present work applied in the future to the problem of dissolution of a horizontal block could be therefore of interest in determining eventual similarities in the results.

It was also verified that the spatial evolution of the regression rate along the surface pointing downward of the inclined block is not similar *by chance* to a resulting signal made of the superimposition of harmonic signals and noise. To prove this, the discrete Fourier transform using a fast Fourier transform algorithm was applied to the same signal referred to the surface pointing upward, where there is no surface patterning. It was observed that, even if at first, the signal may appear as harmonic,

there is no coherent evolution of the frequency of the respective carrier waves and the frequency (and therefore also the amplitude) of the carrier wave varies in an interval many order of magnitude smaller than the one related to the same quantity of the lower surface, which is shown in *Fig. 86* (and for the amplitude in *Fig. 87*). Thus, it is confirmed that the signal related to the upward pointing surface is not harmonic, and thus the one related to the lower surface must be connected to the self-sculpting.

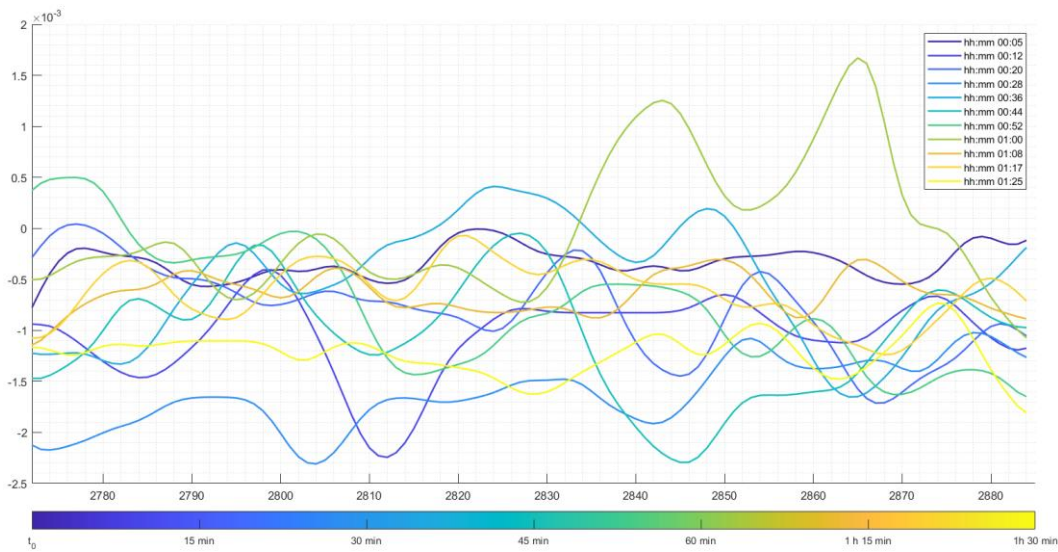


Figure 125 Evolution in time of the local regression rate of the upward pointing surface of a dissolved inclined block.

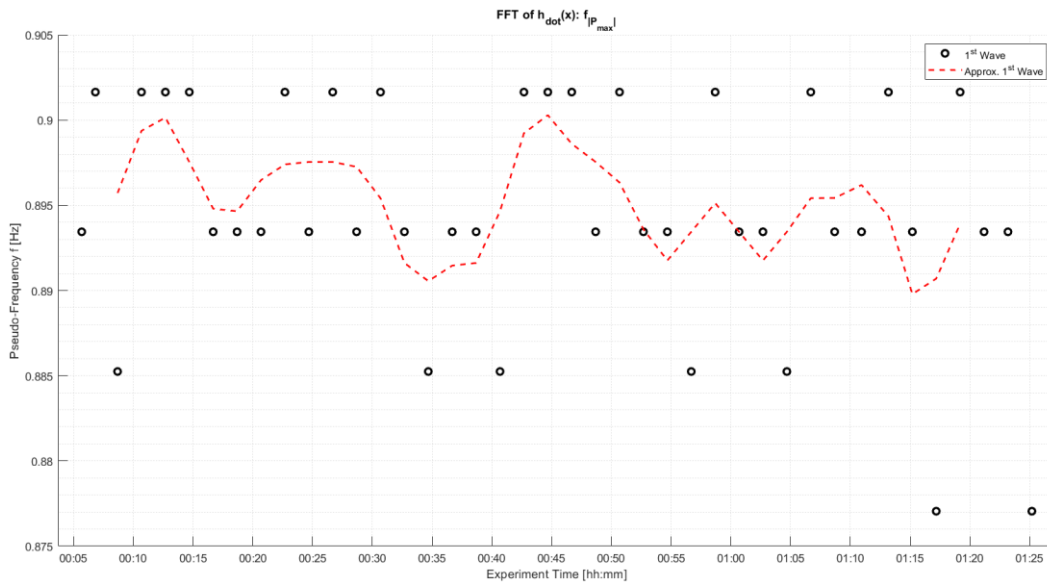


Figure 126 Evolution in time of the frequency of the main harmonic carrier wave of the signal (referred to the surface pointing upward) shown in Fig. 125.

5.2 Results from front photos

It is quite obvious that the results from the side photos must be combined with the ones from the front photos.

The principal results associated to the front photos are related to the determination of coherent dimensions of the patterns on the surface undergoing self-sculpting. Indeed, the coherent structures can be described in terms of vertical and horizontal dimensions and thus, since seem to be repetitive, by the distances in the two directions that separate them. If the distances are found to be constant, then the quantity can be legitimately referred to as wavelength.

The principal graphs obtained have already been presented near the end of paragraph 4.2 and are here reposed for every experiment analysed.

The results are ordered consecutively according to the degree of salinity and secondly according to the inclination angle of the block.

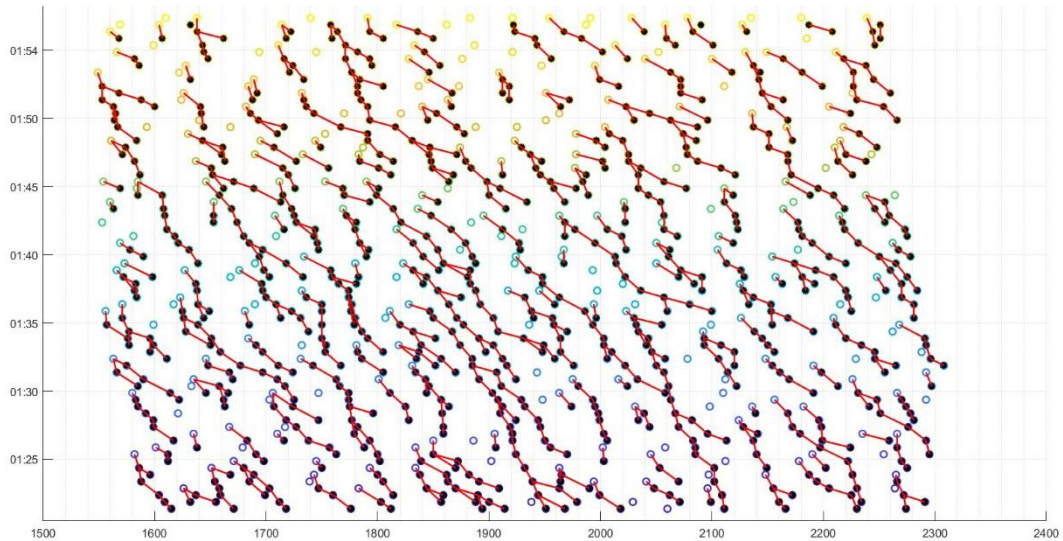


Figure 127 Result from front photos for $\alpha = 30^\circ$ and no additional salt added in the water.

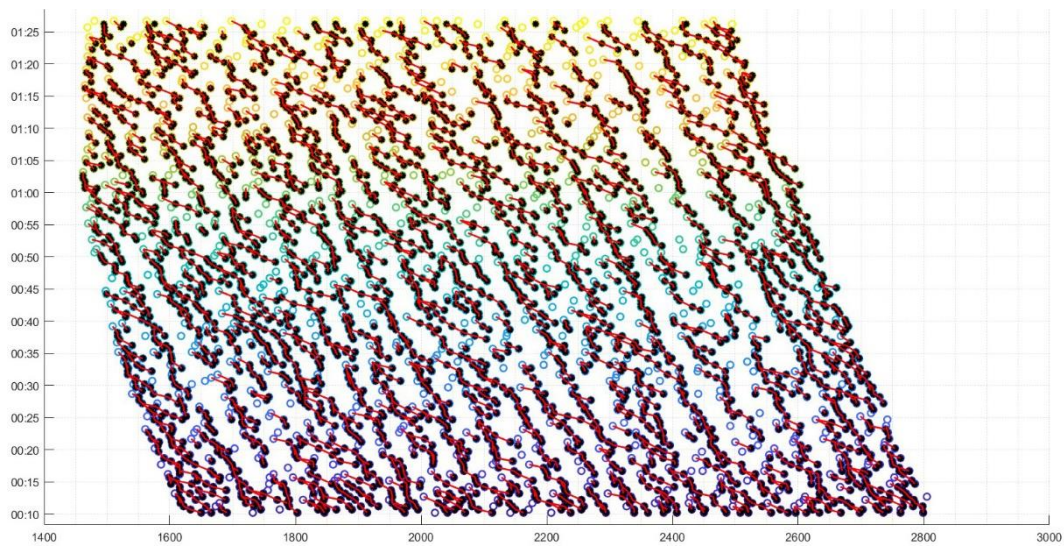


Figure 128 Result from front photos for $\alpha = 45^\circ$ and no additional salt added in the water.

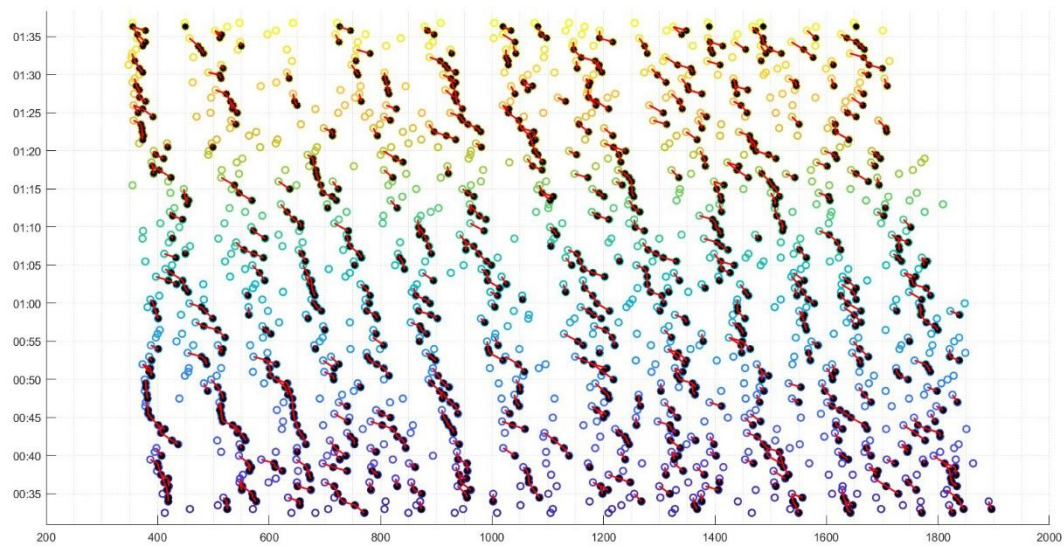


Figure 129 Result from front photos for $\alpha = 60^\circ$ and no additional salt added in the water.

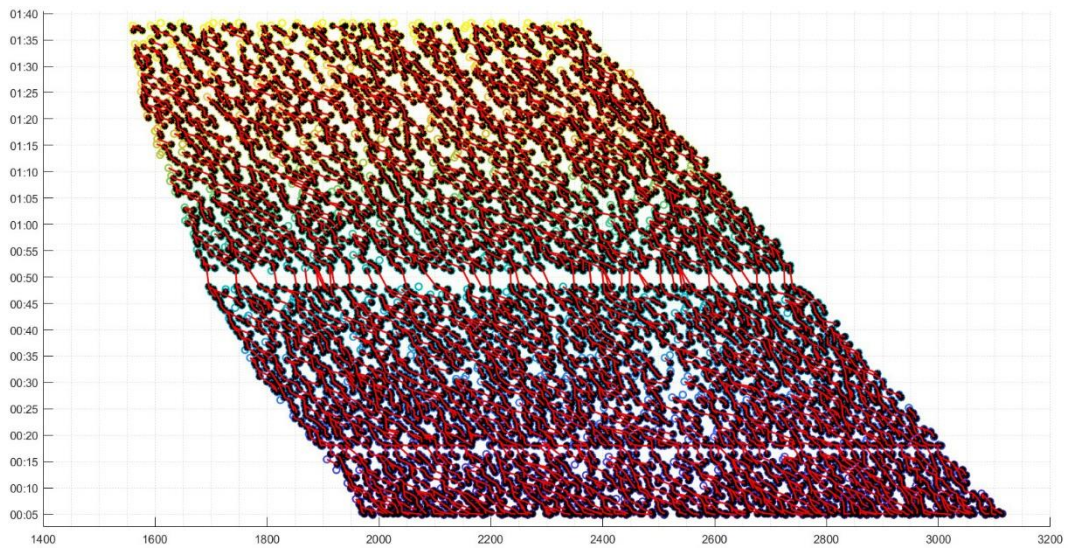


Figure 130 Result from front photos for $\alpha = 30^\circ$ and $S = 4.41$ ppt.

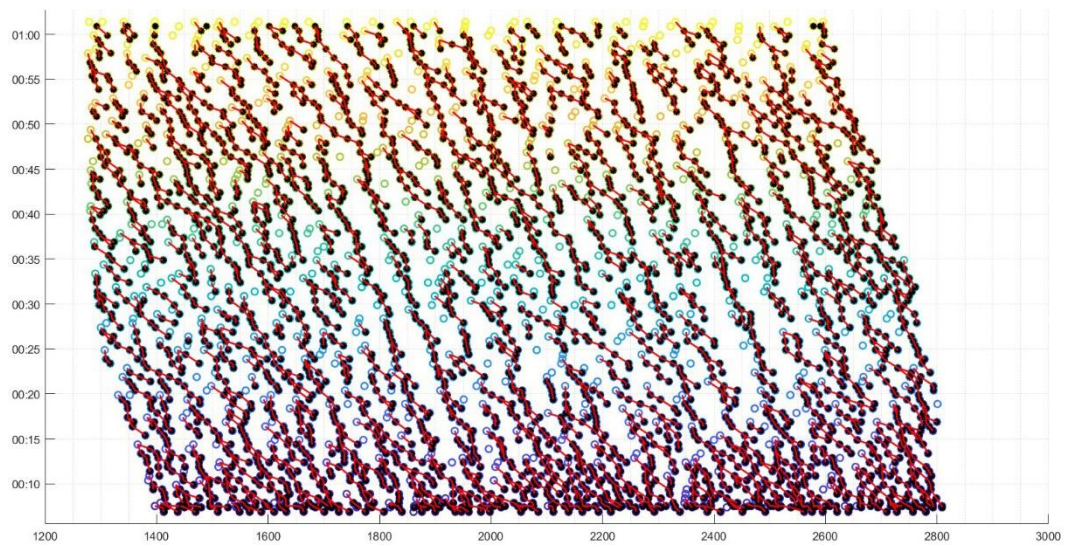


Figure 131 Result from front photos for $\alpha = 45^\circ$ and $S = 4.41$ ppt.

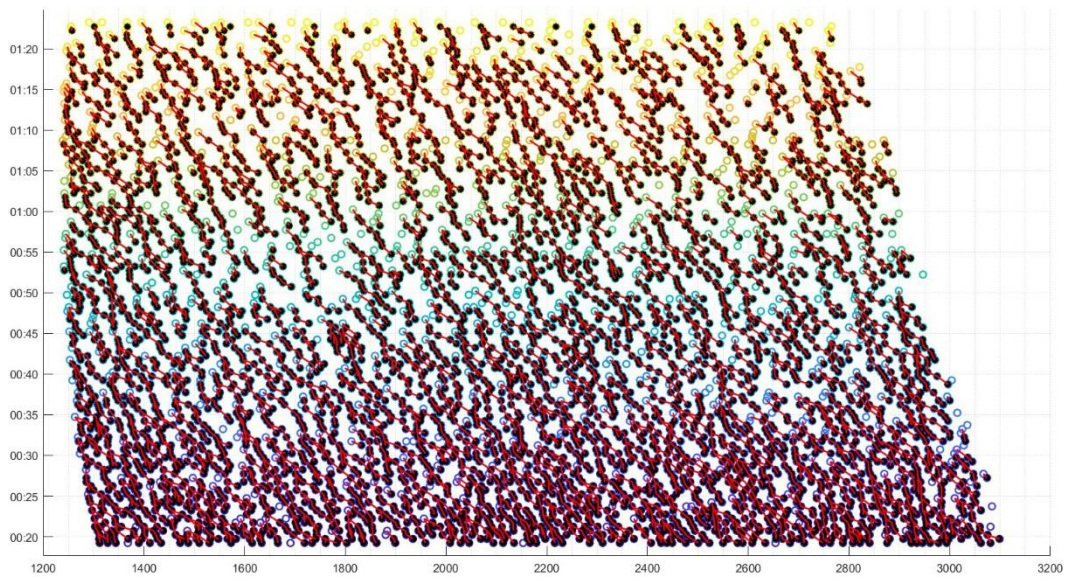


Figure 132 Result from front photos for $\alpha = 60^\circ$ and $S = 4.41$ ppt.

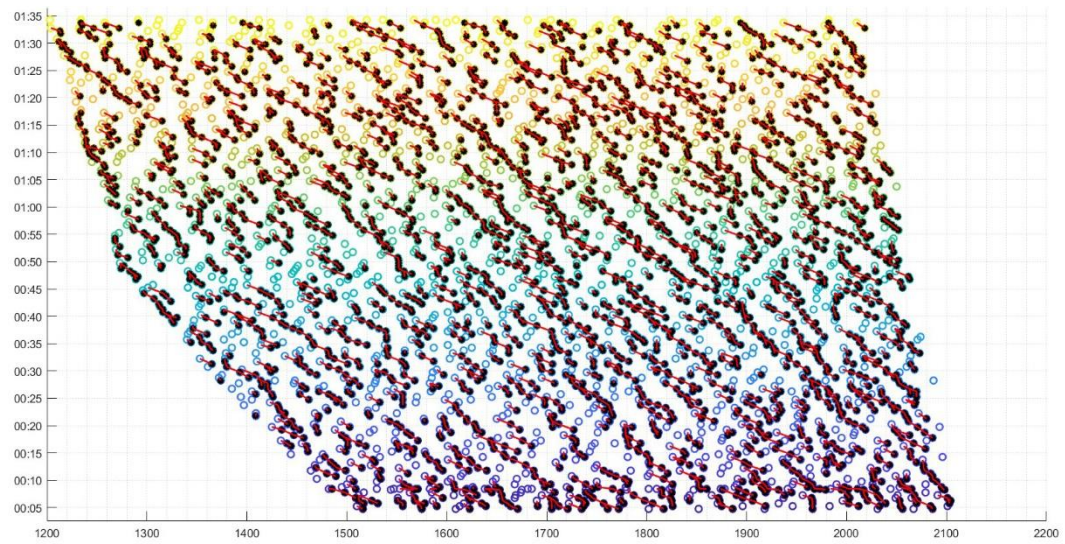


Figure 133 Result from front photos for $\alpha = 30^\circ$ and $S = 8.82$ ppt.

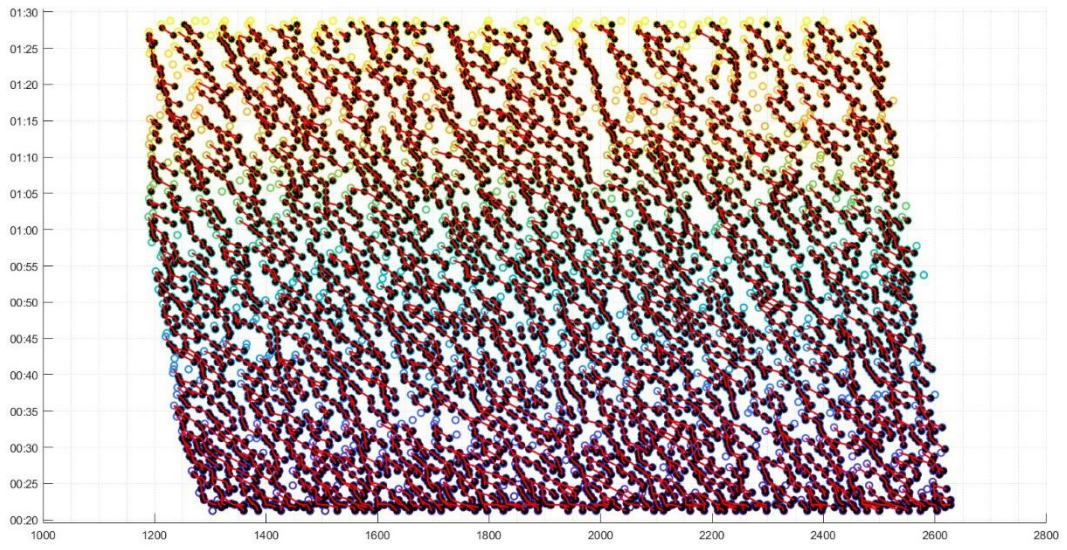


Figure 134 Result from front photos for $\alpha = 45^\circ$ and $S = 8.82$ ppt.

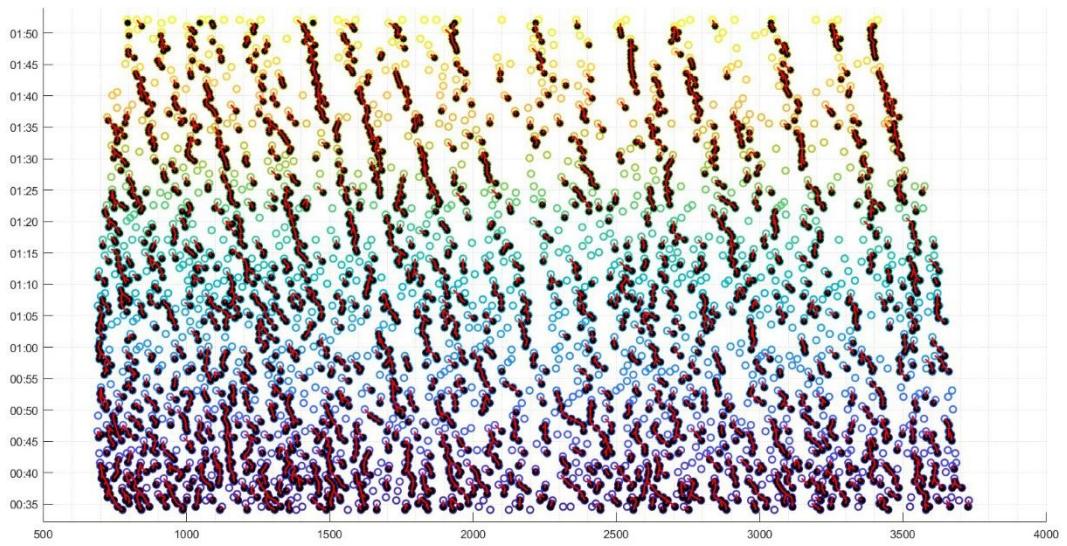


Figure 135 Result from front photos for $\alpha = 60^\circ$ and $S = 8.82$ ppt.

It is quite evident from *Fig. 127-135* that some of them are less dense of points. This is not due to a change in the vertical distance separating the patterns on the front surface of the inclined block. This is only due to a change in the width of the interrogation area.

In the present work, the author preferred to upload, when possible, the results calculated on an interrogation area as big as possible as the surface of the face of the inclined block. But in a few cases, it was not possible. Therefore, cleaner graphs due to a simply narrower surface area were discovered by chance. For a continuation of the present study is therefore suggested to consider that.

The results related to the front photos are all described visually in *Fig. 127-135*. As anticipated, the horizontal distance between a red line connecting cross-correlated points is the vertical peak-to-peak distance between surface patterns. The local inclination of the red lines is related to the instantaneous upstream velocity of the surface pattern considered at that coordinate along the vertical axis of the inclined block.

For reasons only related to a last-minute modification of the section of code showing the graphs, there is still as x -axis the vertical coordinate expressed in pixel's row-number and not in mm. It is hereafter provided a table with the factor (which is a ratio) to be multiplied to the value on the x -axis of the graph to translate the distance in mm.

	$\alpha=30^\circ$	$\alpha=45^\circ$	$\alpha=60^\circ$
No add. NaCl	50/1580.4	50/1449.5	50/1463.8
S\approx4.41 ppt	50/1802.7	50/1567.9	50/1668.6
S\approx8.82 ppt	50/1544.9	50/1565.7	50/1614.0

*Table 16 Factor to be multiplied to the x -axis of the relative graph among *Fig. 127-135* to translate the pixel coordinate into a mm coordinate from the trailing edge of the face of the block.*

Since it is quite difficult to plot in a single graph the evolution in wavelength, it is preferred to leave directly the graphs related to the single cases analysed and to provide instead in a single table the calculated measurements of the vertical distance between the scallops after an hour has passed since the block is set in the aquarium. Since the results are referred to photos taken after an hour, in this case is correct to

call as wavelength the vertical distance separating surface patterns, because the regime is at this point stable.

	$\alpha=30^\circ$	$\alpha=45^\circ$	$\alpha=60^\circ$
No add. NaCl	0.94 mm	2.33 mm	5.66 mm
S\approx4.41 ppt	0.92 mm	2.19 mm	4.42 mm
S\approx8.82 ppt	1.05 mm	2.65 mm	5.59 mm

Table 17 Vertical wavelength of the scallops after one hour since the beginning of the experiment.

The last table illustrates an unexpected dependency on salinity.

Indeed, even if a greater wavelength, by increasing the inclination, was expected by visual observations, the non-monotonicity dependence on the salinity of the solvent could not be anticipated due to the very small difference.

It is worth reminding that a greater wavelength indirectly means that scallops, other than being more distant, should even have longer vertical “legs”. This also means that the valley between a peak and the successive downstream is more extended vertically.

Therefore, the fluid covers a greater wet surface, with the possibility of carrying more solute while moving downstream. Therefore, the concentration should be expected higher, and this would correspond to a lower concentration gradient. This could explain why the wavelength increases by increasing the inclination (*Table 17*) and at the same time the mean regression rate of the lower surface decreases (*Table 9*). This hypothesis seems reasonable.

Unfortunately, a PIV study was not carried out in the present thesis. Therefore, no hypothesis can be drawn regarding the size and the vorticity of eventual recirculating flow within each valley right downstream the crests of scallops.

In conclusion, it was not preferred to show results about the horizontal distance of the patterns, since the values calculated seem to be still too dispersed after an hour. I hope that someone else will be able to improve in the near future the present code written by the author and thus to refine the processed data of this quantity.

5.3 A possible physical mechanism behind scalloping

It is here proposed a possible physical mechanism, which is not based on the idea of *solutal Rayleigh-Bénard instability*, behind the formation of self-sculpted surface patterns induced by dissolution.

The author has nothing against the mentioned theory, but since neither Rayleigh nor Bénard applied their studies on the problem of diffusion of concentration, as anticipated in the paragraph 1.3, the author thinks that a possible explanation not involving RB cells and based instead on the aforementioned other hydrodynamic instability theories could be provided.

The principal motivation is driven by the Rayleigh-Taylor instability of a liquid layer under an inclined plane [26].

The same idea is recalled here in the problem of a dissolving inclined block.

Obviously, the two physical phenomena are different, but the author believes that is legitimate to consider the same hydrodynamic instability behind the first destabilization of the solute layer system.

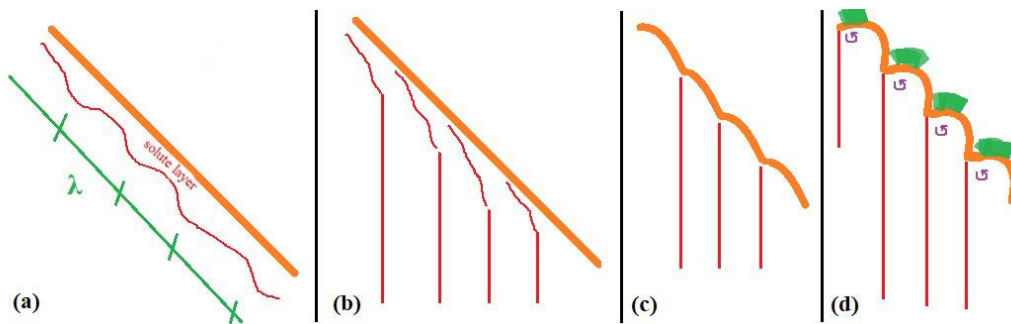


Figure 136 Four principal phases of the proposed physical mechanism behind scalloping.

As soon as the solute body is positioned in the aquarium, it is expected, thanks to dissolution, that it will be formed a solute layer initially locally parallel and directly in contact with the surface of the body. This solute layer is at the beginning “attached” to the surface, thanks to surface tension, and slowly starts to descend along the surface due to the action of gravity.

A fluid layer under an inclined plane is always temporally unstable [26], since the opposed forces of surface tension and gravity act on it. Therefore it will thicken in

some regions (*Fig. 136a*) and a characteristic wavelength, which is associated to the peak-to-peak distance, can be determined based on the inclination angle and the capillary length, as written in *Eq. 19-20*.

It is supposed that is this wavelength to decide the initial position of plumes.

And, even if the position of the plumes may be the non-correct one, the system is able to evolve autonomously in order to reach an equilibrium, as will be legitimately hypothesized in the next paragraph.

The solute layer will therefore behave as in *Fig. 136b*. Basically it reaches the destabilising thickness and evolves into a plume, while right downstream, a “new” solute layer originates, descends and increases its solution concentration, it destabilises and forms a plume, and the process repeats again till the trailing edge of the face is reached.

After all, the process is driven by dissolution and not by the kinematics of the layer, since its inertia and velocity are both very small. Therefore, it is expected an evolution of the surface depending on the local concentration gradient.

Where the thickness of the solute layer is small and the concentration gradient is high, the surface has a higher regression rate, which can be defined as the normal local velocity of the evolving boundary of the surface. While where the thickness of the solute is bigger, then the regression rate is smaller and the surface retrocedes slower in time. Obviously, this extremum is represented by the coordinate of the detaching plume, which evolves in time into a pointed peak, as in *Fig. 136c*.

This process goes on for a while, till the valley between a plume and another is so depressed, that the wetted surface area has increased importantly. In this case the solute layer, which is still laminar, covers a longer distance and thus increases furtherly the maximum solute concentration reached right before detaching from the plume. Thus, from a side, it has a higher inertia with respect to the fluid of the bath, and on the other side, has enough space to furtherly increase its velocity thanks to the acceleration of gravity. It is expected that now, when the layer reaches the position of the plume, it has a non-negligible inertia in order to entrain, thanks to viscosity's shear stresses, the fluid right downstream the plume, thus creating a little recirculation bubble. The related small eddy not only can slowly peel the surface through wall shear-stresses, even if they are very small, but it is in a critical position.

The recirculation region increases the entrainment of outer bath fluid near and downstream the detaching point of the plume, which till now was allowed to become quite asymmetrically sharp. This action, as shown in *Fig. 136d* can explain now the increase in upstream velocity, that is not observed at the beginning of the experiment. Indeed, the pattern is observed to evolve into a stabilised form before increasing suddenly the upstream velocity.

A possible physical mechanism behind the upstream motion is illustrated in *Fig. 137*. Basically, now that the phase illustrated in *Fig.136d* is reached, the local surface right downstream the position of the plume has a higher regression rate with respect to the preceding instants. Therefore, it reaches a position insider than the boundary defined in the previous instant, and by doing so, its position appears to have moved upstream.

Obviously, since the position where the plume detaches is a sharp peak, is more visible even with the naked eye and thus its displacement is more appreciated than other regions on the surface.

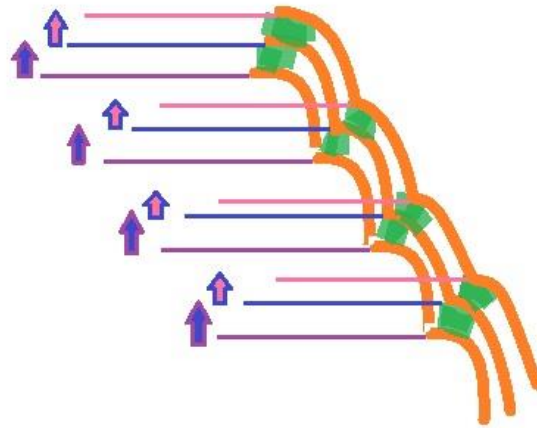


Figure 137 Physical mechanism behind the upstream velocity of scallops.

In conclusion, a physical explanation of the scalloping phenomenon without the need to call the existence of *Rayleigh-Bénard cells* in a *dissolution* problem has been proposed and physically motivated.

There are two considerations the author would like to remark before concluding the present paragraph.

Firstly, *intermittent* plumes [29] [69] can be explained easily as a Kelvin-Helmholtz instability due to the shear stress between the plume and the small recirculating bubble which is induced in the transition between the phase *c* and *d* of *Fig. 136*.

Indeed, even the author observed plumes being *as if* intermitted, but these highlighted a wavy form similar to the one of Kelvin-Helmholtz instability for a concise interval of time. After this interval, the plume appeared to be mostly continuous for the rest of the experiment. Only sporadically it then reassumed a disturbed shape, but this could be also due to the occasional interaction with little-bigger sediments of hard candy transported by the concentration layer. Because it appears to be too sporadic and non-periodic in order to even speak of *frequencies* like the two mentioned papers do.

Anyways, since the author has not performed experiments with salt blocks, he does not comment any more in the present thesis about this observation proposed in the mentioned papers.

The second and last consideration is related to *Eq. 55-58*, which were taken from [30].

As anticipated, the author of the present thesis was not able to find a demonstration of them. But there is only the interest in pointing out that, as anticipated, there was the visual confirmation in the experiments carried out that a relationship between the inclination of the hard candy block and the time when there is a transition from patterns more similar to grooves to patterns more similar to flutes and then to patterns more similar to scallops exists. It was observed that the more inclined is the hard candy block, the longer the groove structure lasts in time before evolving into a flute structure.

In the mentioned formulas, the same dependence is described in *Eq. 58* by the quantity called the *effective gravity*, $g^* = g \times \cos \theta$, which is at denominator. Where θ is the angle with respect to the horizon.

5.4 Scallops as a self-organizing system

Self-organizing systems are able to change their internal structure and their function in response to external circumstances. [28]

As anticipated in paragraph 1.3, the formation of Rayleigh-Bénard cells in nonequilibrium thermodynamics can be considered a self-organizing system. Because it can be said that, by generating a more efficient energy transport through convection, they tend to resist the external perturbations and try to return back to the equilibrium state.

The author dares to suggest that even scallops can be considered in this way. After all, the process is quite *self-regularized* and reaches an asymptotic *equilibrium autonomously*.

Furthermore, many self-organizing systems are characterised by multiple time-scales of their internal and/or external interactions, and possess a hierarchy of structural and/or functional levels in order to react to external inputs [28].

Multiple times-scales are for sure present in the phenomenon, as shown in *Fig. 123-124* and a *hierarchy of structural and functional levels* appears evident too with the existence of different patterns. The patterns do not evolve by chance. After all, there is never a groove developing from a scallop or a secondary scallop transforming into a primary one. And as explained with *Fig. 136*, each pattern seems to have a specific function: the flutes shape the concavity right after the upstream rim; the concavity then enlarges and its sharpen rim allows a small recirculation.

Scallops for sure *react* to external *initial* conditions, as shown by the different results obtained in the first two paragraphs of the present chapter.

Many self-organizing systems are even defined *nonteleological*, i.e., they do not have a specific purpose except their own existence [28].

After all, scallops born due to the existence of a concentration gradient that destabilizes the boundary layer. Their existence can be seen under these perspectives as the aim to reach the null concentration gradient in a more efficient and rapid way, as noted by the compared regression rates of a surface with and

without scalloping. And they even adapt to the surrounding, since as soon as a lower concentration gradient is reached, then the instantaneous regression rate decreases, as shown in *Fig. 119*.

Furthermore, they even have the characteristic of some *hierarchical systems* of being *redundant*: if a scallop is removed mechanically abrading the surface, there are always some nearby which are ready to extend their arms in the now available surface. This is after all what happens when a bubble is seen to impinge while raising upwards against the base of a rim of a scallop. If it gets trapped, then the rim is no more able to keep a recirculating flow in it, and therefore due to the same presence of the bubble, a secondary scallop is created, and thus a secondary neighbouring rim carries out the function of the blocked one. Therefore, the upstream velocity of the pattern is regained, and this causes a spatially non-uniform advance of the rim that frees the bubble. Since there is no more the bubble, then there is no more the necessity of two neighbouring rims, thus they will merge in one as explained in *Fig. 36*.

Therefore, the author of the present thesis would like to propose, with this qualitative description, based on experimental results and evidence, that they are suitable at the pair of Rayleigh-Bénard cells to be considered as a self-organizing system.

In conclusion, as previously said, nonteleological self-organizing systems exists to accomplish a specific purpose. So, what is the specific purpose of scallops?

The answer may be found looking at the asymptotic equilibrium in the dimensions of the coherent structures that is reached at the end of an experiment.

The author proposes that, the explanation of the equilibrium can be found looking at *Fig. 137d*.

If the concentration in the solute layer can furtherly increase, then the recirculating region is expected to increase its vorticity, since the entrainment that drives the recirculating bubble increases due to the increased inertia of the upstream layer. Therefore, it is proposed that the consistency of the final wavelength is found due to the equilibrium between the action performed by the solute layer that tries to take

the greatest concentration as possible (obviously lower than or at maximum equal to the saturated level) toward the plume and the opposed mixing effect due to the action performed by the recirculating region.

Thus, the author supposes, recalling Curl's theory, that the equilibrium should be found in the aim of having the highest and constant Sherwood number.

Since Curl has been now recalled, the author would like to make a final comment on the two theories supported by Curl and Allen.

The author of the present thesis personally supports the idea that *in medio stat virtus*. Both Curl and Allen made a great contribution in exploring the sculpting phenomenon on rocks by water flow, using Plaster of Paris as model. But they made the mistake to believe that their experimental observations and evidence were mainly due to dissolution when, on the contrary, Rayleigh numbers in their experiments are so big that diffusive phenomena cannot be neglected for sure.

They did not agree with each other regarding the last picture of *Fig. 40*. In conclusion, I would like to provide a possible clarification driven by experimental observations.

According to Curl's stable flute theory this should be a fixed pattern that does not change anymore. While Allen's passive bed theory drives him to conclude that when the surface reaches the conjugate state, erosional marks could be destroyed as well as created.

The experiments carried out by the author of the present thesis demonstrate at their final time stage that both Curl and Allen are right, but only partially.

Specifically, it is true that a condition of fixed *dimensions of the coherent structures* is reached. But this does not imply that the coherent structures must stay fixed in space. Indeed, the coherent structures keep moving upwards, as shown in *Fig. 138*, *till the body is completely dissolved*. And since the pattern moves upward, after all, in a *fixed reference system*, the movement can be seen as the transition of peaks into valleys and of valleys into peaks, as shown in *Fig. 122*.

Conclusion and Recommendations

The present work demonstrates quantitatively that even if scalloping on a surface of a dissolving body may appear at a glance as a chaotic behaviour, there is in reality a hidden coherency in the structures when they are analysed statistically. This could be very useful in potential applications in geomorphology and planetary geology, other than in increasing the accuracy of the present mathematical models.

A proposal of the physical mechanism behind scalloping is explained based on detailed experimental observations.

The present proposal even allows to hypothesize scalloping within the class of self-organizing systems.

But honestly additional work is necessary.

The author partially regrets not being able to post-process some of the experiments carried out with other moulds, which were realised from scratch, due to the limited time available in facing a so interesting and elaborate phenomenon.

But is confident in the advancement which will be carried out by future students and researchers on the topic.

Bibliography

- [1] J. B. J. Fourier, *Théorie Analytique de la Chaleur*, Paris: Firmin Didot, 1822.
- [2] A. Fick, «Ueber Diffusion,» *Ann. Phys.*, vol. 170, pp. 59-86, 1855.
- [3] L. Prandtl, «Motions of Fluids with Very Little Viscosity,» 1904. [Online]. Available: <https://ntrs.nasa.gov/citations/19930090813>.
- [4] NASA, «Planetary Cave Rovers,» [Online]. Available: <https://ai.jpl.nasa.gov/public/projects/cave-rovers/>.
- [5] NASA, «Mars Helicopter (Ingenuity),» [Online]. Available: <https://mars.nasa.gov/technology/helicopter/>.
- [6] C. E. Brennen, «Fundamentals of Multiphase Flows,» Cambridge University Press, 2009, p. 19.
- [7] «Encyclopedia Britannica,» [Online]. Available: <https://www.britannica.com/science/phase-state-of-matter>.
- [8] M. Epstein e F. B. Cheung, «Complex Freezing-Melting Interfaces in Fluid Flow,» *Ann. Rev. Fluid. Mech.*, n. 15, pp. 293-319, 1983.
- [9] K. C. Cheng, H. Inaba e R. R. Gilpin, «An experimental investigation of ice formation around an isothermally cooled cylinder in crossflow,» *J. Heat Transfer*, n. 103, pp. 733-738, 1981.
- [10] Y. C. Yen e A. Zehnder, «Melting heat transfer with water jet,» *Int. J. Heat Mass Transfer*, n. 16, pp. 219-223, 1973.
- [11] R. R. Gilpin, «The ablation of ice by a water jet,» *Trans. Can. Soc. Mech. Engrs.*, n. 2, pp. 91-95, 1973.
- [12] C. Thorsness e T. J. Hanratty, «Mass transfer between a flowing fluid and a solid wavy surface,» *AIChE J.*, n. 25, pp. 686-697, 1979.
- [13] J. A. Bilenas e L. M. Jiji, «Variational solution of axisymmetric fluid flow in tubes with surface solidification,» *J. Franklin Inst.*, n. 289, pp. 267-279, 1970.

- [14] M. S. D. Wykes, J. M. Huang, G. A. Hajjar e L. Ristroph, «Self-sculpting of a dissolvable body due to gravitational convection,» *Phys. Rev. Fluids*, vol. 3, n. 4, 2018.
- [15] A. J. Wells e M. G. Worster, «Melting and dissolving of a vertical solid surface with laminar compositional convection,» *J. Fluid Mech.*, vol. 687, pp. 118-140, 2011.
- [16] «Encyclopedia of Mathematics,» [Online]. Available: https://encyclopediaofmath.org/wiki/Stefan_problem.
- [17] J. Štefan, «Ueber einige Probleme der Theorie der Wärmeleitung,» *Wiener Akad. Math. Naturwiss. Abt.*, n. 98, pp. 473-484, 1889.
- [18] C. J. Crepeau, *Jožef Stefan: His Scientific Legacy on the 175th Anniversary of His Birth*, Bentham Books, 2013.
- [19] D. Andreucci, «Lecture notes on the Stefan problem - Università di Roma La Sapienza,» [Online]. Available: https://www.sbai.uniroma1.it/publicazioni/doc/phd_quaderni/02-1-and.pdf.
- [20] T. Jonsson, «On the one dimensional Stefan problem,» 2013. [Online]. Available: <https://www.diva-portal.org/smash/get/diva2:647481/FULLTEXT01.pdf>.
- [21] J. M. Huang, M. J. Shelley e D. B. Stein, «A stable and accurate scheme for solving the Stefan problem coupled with natural convection using the Immersed Boundary Smooth Extension method,» *J. Comp. Phys.*, vol. 432, 2021.
- [22] W. O. Criminale, T. L. Jackson e R. D. Joslin, *Theory and Computation of Hydrodynamic Stability*, Cambridge University Press, 2003.
- [23] P. G. Drazin, *Introduction to Hydrodynamic Stability*, Cambridge University Press, 2002.
- [24] G. K. Batchelor, *An Introduction to Fluid Dynamics*, Cambridge University Press, 1967.
- [25] M. S. Roberts e J. W. Jacobs, «The effects of forced small-wavelength finite-bandwidth initial perturbations and miscibility on the turbulent Rayleigh-Taylor instability,» *J. Fluid Mech.*, vol. 787, pp. 50-83, 2016.
- [26] P.-T. Brun, A. Damiano, P. Rieu, G. Balestra e F. Gallaire, «Rayleigh-Taylor instability under an inclined plane,» *Physics of Fluids*, vol. 27, n. 8, 2015.

- [27] M. G. Velarde e C. Normand, «Convection,» *Scientific American*, vol. 243, n. 1, pp. 92-109, 1980.
- [28] W. Banzhaf, «Self-Organizing Systems,» in *Encyclopedia of Physical Science and Technology*, 3 a cura di, Academic Press, 2003, pp. 589-598.
- [29] J. Philippi, M. Berhanu, J. Derr e S. C. d. Pont, «Solutorial convection induced by dissolution,» *Phys. Rev. Fluids*, vol. 4, n. 10, 2019.
- [30] C. Cohen, M. Berhanu, J. Derr e S. C. d. Pont, «Buoyancy-driven dissolution of inclined blocks: Erosion rate and pattern formation,» *Phys. Rev. Fluids*, vol. 5, n. 5, 2020.
- [31] M. A. Summerfield, *Global Geomorphology*, Routledge, 1991.
- [32] D. Ford e P. Williams, *Karst Hydrogeology and Geomorphology*, John Wiley & Sons Inc., 2007.
- [33] A. Einstein, «The cause of the formation of meanders in the courses of rivers and of the so-called Baer's law,» *Die Naturwissenschaften*, vol. 14, n. 11, pp. 223-224, 1926.
- [34] K. J. W. D. W. E. Perron J. T., «Formation of evenly spaced ridges and valleys,» *Nature*, vol. 460, pp. 502-505, 2009.
- [35] K. Amin, J. M. Huang e L. Ristroph, «The role of shape-dependent flight stability in the origin of oriented meteorites,» *PNAS*, vol. 116, n. 33, pp. 16180-16185, 2019.
- [36] J. M. Huang, J. Tong, M. Shelley e L. Ristroph, «Ultra-sharp pinnacles sculpted by natural convective dissolution,» *PNAS*, vol. 117, n. 38, pp. 23339-23344, 2020.
- [37] D. Bunnell, «The Virtual Cave,» [Online]. Available: <http://www.goodearthgraphics.com/virtcave/>.
- [38] T. Dauxois, T. Peacock, P. Bauer, C. P. Caulfield, C. Cenedese, C. Górlé, G. Haller, G. N. Ivey, P. F. Linden, E. Meiburg, N. Pinardi, N. M. Vriend e A. W. Woods, «Confronting Grand Challenges in environmental fluid dynamics,» *Phys. Rev. Fluids*, vol. 6, n. 2, 2021.
- [39] K.-D. Keller, «Wikipedia: Properties of water,» [Online]. Available: https://en.wikipedia.org/wiki/Properties_of_water.

- [40] F. J. Millero e A. Poisson, «International one-atmosphere equation of state of seawater,» *Deep Sea Research Part A. Oceanographic Research Papers*, vol. 28, n. 6, pp. 625-629, 1981.
- [41] R. Kerr, «Melting driven by vigorous compositional convection,» *J. Fluid Mech.*, vol. 280, pp. 255-285, 1994.
- [42] M. Sugawara, E. Tamura, Y. Satoh, Y. Komatsu, M. Tago e H. Beer, «Visual observations of flow structure and melting front morphology in horizontal ice plate melting from above into a mixture,» *Heat Mass Transfer*, vol. 43, pp. 1009-1018, 2007.
- [43] L.-A. Couston, E. Hester, B. Favier, J. R. Taylor, P. R. Holland e A. Jenkins, «Topography generation by melting and freezing in a turbulent shear flow,» *J. Fluid Mech.*, vol. 911, n. A44, 2021.
- [44] P. Claudin, O. Durán e B. Andreotti, «Dissolution instability and roughening transition,» *J. Fluid Mech.*, vol. 832, n. R2, 2017.
- [45] T. J. S. Huppert H. E., «Ice blocks melting into a salinity gradient,» *J. Fluid Mech.*, vol. 100, n. 2, pp. 367-384, 1980.
- [46] R. Yang, C. J. Howland, H.-R. Liu, R. Verzicco e D. Lohse, «Ice melting in salty water: layering and non-monotonic dependence on the mean salinity,» 2023.
- [47] V. R. L. D. C. C. Yang Y., «Layering and vertical transport in sheared double-diffusive convection in the diffusive regime,» *J. Fluid Mech.*, vol. 933, n. A30, 2022.
- [48] M. Lugeon, «Le striage du lit fluvial,» *Ann. de Géographie*, vol. 24, n. 132, pp. 385-393, 1915.
- [49] J. H. Maxson, «Fluting and Faceting of Rock Fragments,» *J. of Geology*, vol. 48, n. 7, pp. 717-751, 1940.
- [50] J. H. Bretz, «Vadose and Phreatic Features of Limestone Caverns,» *J. Geol.*, vol. 50, n. 6, pp. 675-811, 1942.
- [51] R. P. Sharp, «The Wolf-Creek Glaciers, St. Elias Range, Yukon Territory,» *Geographical Rev.*, vol. 37, n. 1, pp. 26-52, 1947.
- [52] J. Leighly, «Cusped surfaces of melting Ice and Firn,» *Geographical Rev.*, vol. 38, n. 2, pp. 300-306, 1948.

- [53] J. C. Coleman, «An indicator of water-flow in Caves,» *Proc. Univ. Bristol. Speleo. Soc.*, vol. 6, n. 1, pp. 57-67.
- [54] R. L. Curl, «Scallops and Flutes,» *Transactions Cave Research Group of Great Britain*, vol. 7, n. 2, pp. 121-160, 1966.
- [55] P. N. Blumberg e R. L. Curl, «Experimental and theoretical studies of dissolution roughness,» *J. Fluid Mech.*, vol. 65, n. 4, pp. 735-751, 1974.
- [56] J. R. L. Allen, «On the origin of cave flutes and scallops by the enlargement of inhomogeneities,» *Rassegna Speleologica Italiana*, pp. 3-19, February 1972.
- [57] J. R. L. Allen, «Bed forms due to mass transfer in turbulent flows: a kaleidoscope of phenomena,» *J. Fluid Mech.*, vol. 49, n. 1, pp. 49-63, 1971.
- [58] J. R. L. Allen, «Transverse erosional marks of mud and rock: their physical basis and geological significance,» vol. 5, n. 3-4, pp. 167-385, 1971.
- [59] Z. Y. L. D. Villien B., «Surface Dissolution and the Development of Scallops,» *Chem. Eng. Comm.*, vol. 192, n. 1, pp. 125-136, 2006.
- [60] O. Reynolds, «XXIX. An experimental investigation of the circumstances which determine whether the motion of water shall be direct or sinuous, and of the law of resistance in parallel channels,» *Philosophical Transactions of the Royal Society of London*, vol. 174, n. 174, pp. 935-982, 1883.
- [61] S.-E. Lauritzen, «Kvithola at Fauske, northern Norway: an example of ice-contact speleogenesis,» *Norsk Geologisk Tidsskrift*, vol. 66, n. 2, pp. 153-161, 1986.
- [62] J. M. Kay, *Fluid Mechanics and Heat Transfer*, Cambridge University Press, 1963, pp. 170-173.
- [63] G. K. Schlichting H., *Boundary-Layer Theory*, 9 a cura di, Springer-Verlag, 2016, pp. 35-36.
- [64] C. F. Nordin e J. H. Algert, «Spectral analysis of sand waves,» *Proc. Am. Soc. Civil Engrs., J. Hydraulics Div.*, vol. 92, n. 5, pp. 95-114, 1966.
- [65] «Encyclopedia Britannica,» [Online]. Available: <https://www.britannica.com/science/weathering-geology>.
- [66] J. Schürr, «Sur la vitesse de dissolution des sels dans leurs solutions aqueuses,» *J. Phys. Theor. Appl.*, vol. 4, n. 17, pp. 17-26, 1905.

- [67] D. Gechter, P. Huggenberger, P. Ackerer e H. N. Waber, «Genesis and shape of natural solution cavities within salt deposits,» *Water Resour. Res.*, vol. 44, p. W11409, 2008.
- [68] C. Oltéan, F. Golfier e M. A. Buès, «Numerical and experimental investigation of buoyancy-driven dissolution in vertical fracture,» *J. Geophys. Res. Solid Earth*, vol. 118, pp. 2038-2048, 2013.
- [69] M. Berhanu, J. Philippi, S. C. d. Pont e J. Derr, «Solutal convection instability caused by dissolution,» *Physics of Fluids*, vol. 33, n. 7, 2021.
- [70] J. A. Neufeld, M. A. Hesse, A. Riaz, M. A. Hallworth, H. A. Tchelepi e H. E. Huppert, «Convective dissolution of carbon dioxide in saline aquifers,» *Geophys. Res. Lett.*, vol. 37, n. L22404, 2010.
- [71] P. Meakin e B. Jamtveit, «Geological pattern formation by growth and dissolution in aqueous systems,» *Proc. R. Soc.*, vol. 466, n. 659, pp. 659-694, 2010.
- [72] T. S. Sullivan, W. J. Brown, M. D. Kerkel e R. E. Ecke, «Turbulent solutal convection and surface patterning in solid dissolution,» *Phys. Rev. E*, vol. 54, n. 1, pp. 486-495, 1996.
- [73] M. Alkattan, E. H. Oelkers, J.-L. Dandurand. e J. Schott, «Experimental studies of haite dissolution kinetics: 1. The effect of saturation state and the presence of trace metals,» *Chem. Geol.*, vol. 137, n. 201, pp. 201-219, 1997.
- [74] Y. A. Farnam, D. P. Bentz, A. R. Sakulich, D. Flynn e W. J. Weiss, «Measuring Freeze and Thaw Damage in Mortars Containing Deicing Salt Using a Low-Temperature Longitudinal Guarded Comparative Calorimeter and Acoustic Emission,» *Adv. Civ. Eng. Mater.*, vol. 3, n. 1, 2014.
- [75] C. Cohen, M. Berhanu, J. Derr e S. C. d. Pont, «Erosion patterns on dissolving and melting objects,» *Phys. Rev. Fluids*, vol. 1, n. 5, 2016.
- [76] M. v. Meerkerk, C. Poelma e J. Westerweel, «Scanning stereo-PLIF method for free surface measurements in large 3D domains,» *Exp. Fluids*, vol. 61, n. 19, 2020.
- [77] B. Zhao, H. Zeng, Y. Tian e J. Israelachvili, «Adhesion and detachment mechanisms of sugar surfaces from the solid (glassy) to liquid (viscous) state,» *PNAS*, vol. 103, n. 52, 2006.
- [78] H. R. Brown, «Rayleigh–Taylor instability in a finite thickness layer of a viscous fluid,» *Physics of Fluids*, vol. 1, n. 5, pp. 895-896, 1989.

- [79] J. Lister e R. Kerr, «The effect of geometry on the gravitational instability of a buoyant region of viscous fluid,» *J. Fluid Mech.*, vol. 202, pp. 577-594, 1989.
- [80] G. Barra, «The Rheology of Caramel,» 2004. [Online]. Available: https://eprints.nottingham.ac.uk/11837/1/Phd_thesis_Giuseppina_Barra.pdf.
- [81] T. Husband, «ACS: The Sweet Science of Candymaking,» 2014. [Online]. Available: <https://www.acs.org/education/resources/highschool/chemmatters/past-issues/archive-2014-2015/candymaking.html>.
- [82] H. McGee, «On Food and Cooking: The Science and Lore of the Kitchen,» Scribner, 2004, pp. 653-657,680-691.
- [83] H. Y. Roos, *Phase Transitions in Food*, Academic Press, 1995.
- [84] M. Quintas, T. R. S. Brandão, C. L. M. Silva e R. L. Cunha, «Modelling Viscosity Temperature Dependence of Supercooled Sucrose Solutions - The Random-Walk Approach,» *J. Phys. Chem. B*, vol. 111, n. 12, pp. 3192-3196, 2007.
- [85] R. P. Mathlouthi M., «Rheological properties of sucrose solutions and suspensions,» in *Sucrose Properties and Applications*, Springer, 1995.
- [86] P. A. Millero F. J., «International one-atmosphere equation of state of seawater,» *Deep Sea Research Part A. Oceanographic Research Papers*, vol. 28, n. 6, pp. 625-629, 1981.
- [87] E. Nakouzi, R. E. Goldstein e O. Steinbock, «Do Dissolving Objects Converge to a Universal Shape?,» *Langmuir*, vol. 31, n. 14, pp. 4145-4150, 2015.

List of Figures

Figure 1 Possible originating interfaces in liquid-solid phase change problems. .	16
Figure 2 Steady-state ice-layer profile on a flat plate, indicating various flow regimes [3].	17
Figure 3 Temperature and concentration gradients in the case of melting and of dissolving [15].	20
Figure 4 Near-wall temperature, concentration and streamfunction profiles for large Le [15].	21
Figure 5 Sketch of a piecewise constant approximation to a shear layer. Fig. 2.2 in [22].	29
Figure 6 Growth of a sinusoidal disturbance of a vortex sheet with vorticity. Fig. 7.1.3 in [24].	30
Figure 7 Visualization of the vectors acting in a Rayleigh-Taylor instability [20].	32
Figure 8 Scalloped iceberg near Paulet Island, Antarctica. © Phillip Colla.	38
Figure 9 Model of ice scallop due to vigorous compositional convection.	38
Figure 10 Pinnacle karsts in the Tsingy de Bemaraha National Park, Madagascar. © Arthus Bertrand.	39
Figure 11 Tower karsts in Guilin, Guangxi province, China. © VCG Photo.	39
Figure 12 Bed-of-nails morphology from dissolution of an initial porous media. [31].	39
Figure 13 Speleogens in a cave in Borneo. [32] © Dave Bunnell.	40
Figure 14 Sala degli Scallops (transl. “The room of scallops”), Grotta della Lupa, Majella, Italy.	40
Figure 15 Another image of smaller speleogens.	40
Figure 16 Graph of $\rho H_2O T$. [34]	41
Figure 17 Temperature-salinity diagram of H_2O .	41
Figure 18 Possible ice surface melting patterns driven by a buoyancy gradient..	42
Figure 19 Sketch of the melting from below (a) and melting from above (b) configurations [42].	43

Figure 20 Sketch of convective cells and relative streamlines in the near-wall region of the “mountain and valley” structure. [37]	43
Figure 21 In-phase \mathcal{A} and in-quadrature \mathcal{B} shear stress components as a function of the wave number $k\nu u$ * [44].	47
Figure 22 Isocontours of the diffusion coefficient (case a) and of the concentration (case b) within the fluid above a sinusoidally modulated bed (in white). Red (blue) regions correspond to a strong (weak) modulus [44].....	48
Figure 23 Stability of the density/concentration distribution in the region close to the ice surface. Sketches related to melting in water (on the left) and melting in a mixture (on the right) [42].....	49
Figure 24 Dissociation reactions and solubilities of some representative minerals that dissolve congruently in water at 25°C and 1 bar pressure [32].	50
Figure 25 The solubility of calcite and gypsum in water at the standard atmosphere in the temperature interval ranging from 2°C to 25°C [32].	50
Figure 26 Changes of bed geometry with time according to the passive-bed theory (case a) and to the defect model (case b) [58].	52
Figure 27 Crest and critical point geometry of stable flute profile [54].	55
Figure 28 Flute geometry and dissolution-rate and characteristic velocity vectors [55].	56
Figure 29 Characteristic flow regions over one flute period [55].	57
Figure 30 Idealised pattern of flow and associated flow velocity profile in a shallow cavity [56].....	58
Figure 31 Scheme of instabilities and resulting bed forms and flow fields [57]...	60
Figure 32 Mould showing a flute at $Vtd = 1.5$. Current from left to right. The portion of the bed shown in the photo is 10 cm wide [57].....	61
Figure 33 Schematic flow field displaying skin-friction lines and streamlines associated with mature flutes (case a) and mature grooves (case b) [57].	61
Figure 34 Rectilinear furrows [57].	62
Figure 35 Features of ridges and furrows: (a) Evolution in time of the profile. (b) Schematic pattern of skin-friction lines. (c) Three-dimensional illustration of the flow-field [57].....	63

Figure 36 Schematic flow field displaying skin-friction lines and streamlines associated with stages in the development of secondary flutes from longitudinal ridges and furrows [57].	64
Figure 37 Moulds illustrating sequential stages in the development of secondary flutes by the higher-order instability of longitudinal ridges and furrows. They are not referred to the same furrow. Flow from bottom to top [57].	64
Figure 38 Cataloguing of assemblages of transverse erosional marks.	66
Figure 39 Pattern of crests, and their culmination (peaks), in assemblages of polygonal erosional marks [58].	67
Figure 40 Expected development in time of an initial assemblage of transverse erosional marks. Current from top to bottom [58].	67
Figure 41 Conjecture on secondary vortices and bed furrows generated by flank vortices of conjugated marks [58].	68
Figure 42 Phase diagram of NaCl-H ₂ O [74].	72
Figure 43 (a) Physical domain in the numerical simulation. (b) Solutal convection instability near the dissolving interface [69].	73
Figure 44 Schematic view of the dissolution-driven flow on an inclined block of hard candy [30].	77
Figure 45 Evolution in time, from top to bottom, of the dissolution instability [30].	78
Figure 46 Sugar and corn syrup used in the following experiments.	83
Figure 47 Final candy properties depending on the syrup boiling point reached in cooking [82].	84
Figure 48 Chemical arrangement of common sugars [82].	84
Figure 49 State diagram of sucrose. Adapted from [83] and shown in [80].	85
Figure 50 Dependence of the dynamic viscosity of sucrose solutions from temperature and weight concentration $\mu T, wt. \%$. Adapted from Table 6.3 in [85] and shown in [80].	90
Figure 51 Lateral photo (on the left) and frontal photo (on the right) of the same hard candy block, whose dispersed air bubbles were not removed with the vacuum chamber. The base of the block is 134 mm long and 90 mm width.	91
Figure 52 Illustration of the experimental set-up used for the experiments.	92

Figure 53 Photo of an experiment taken behind the point of view of camera A. .	93
Figure 54 Photo of the same experiment taken behind the point of view of camera B.....	93
Figure 55 One of the two moulds with the rectangular base. (It appears distorted only in photo).....	94
Figure 56 Harmonic surface. On the left there is the (negative) resin print on which the silicon mould base on the right was manufactured.	95
Figure 57 Concave mould base to realise a hard candy block with a convex face. In cross-sectional view the surface is an arc of circumference of diameter 170 mm. The two lines of points made of the extrema of the arc of circumference are 125 mm apart.....	95
Figure 58 “V-shaped” base mould.	96
Figure 59 Regression rate influenced by upward pushing bubbles.	96
Figure 60 “U-shaped” base mould.....	97
Figure 61 Mould to realise a half cross-section of a pipe.	98
Figure 62 Evolution in time of the same fixed detail of surface. Each photo is taken after six minutes the preceding one. Photo order is: top-left, top-right, bottom-left, bottom-right. The block is tilted 60° with respect to the horizontal line and the water salinity is $S = 8.81 \text{ ppt}$	101
Figure 63 Evolution in time of the same fixed detail of surface of Fig. 62. The top-left photo is taken after six minutes the bottom-right photo in Fig. 62 was taken. The other three photos are taken at an interval of twelve minutes starting from the top-left photo. Photo order is: top-left, top-right, bottom-left, bottom-right. The block is tilted 60° with respect to the horizontal line and the aquarium water salinity is $S = 8.81 \text{ ppt}$	102
Figure 64 Evolution in time (from top to bottom) of the surface pattern on a hard-candy block inclined 60° with respect to the horizontal line with no salt added to the aquarium water.....	103
Figure 65 Sketch of the different regression rate depending on the surface considered and on the coordinate along the surface. Representation of the system of reference for the angle used.	104

Figure 66 Lateral photos of the experiment to verify the existence and the value of <i>acrit</i>	105
Figure 67 Evolution in time of the surface pattern on a vertical hard-candy block with initial surface inhomogeneities left by trapped bubbles. Time of acquisition of the photo since the start of the experiment: (a) 13 min., (b) 40 min., (c) 70 min., (d) 110 min. All the photos have the same spatial resolution.	107
Figure 68 Evolution in time (from top to bottom) of the pattern on a convex surface on a hard-candy block inclined 45° with respect to the horizontal line with no salt added to the aquarium water. Each photo has the same spatial resolution and is taken 30 minutes after the preceding one.	109
Figure 69 Detail of the top photo in Fig. 70. Regions camped in red point locally downward, while regions camped in blue point locally upward or are locally vertical.....	111
Figure 70 Evolution in time (from top to bottom) of the pattern on a harmonic surface of a hard-candy block inclined 45° with respect to the horizontal line with water salinity $S = 8.81 ppt$. Each photo has the same spatial resolution and is taken 30 minutes after the preceding one.	112
Figure 71 Evolution in time (from top to bottom) of the pattern on the surface of a V-shaped cavity of a hard-candy block inclined 60° with respect to the horizontal line and no salt added to the water. Each photo has the same spatial resolution and is taken 30 minutes after the preceding one.	114
Figure 72 A generic lateral photo.....	118
Figure 73 Additive synthesis of primary colours.....	118
Figure 74 Three main processes (optimised for the lower surface) to detect the body in the photo.....	121
Figure 75 Object detected in the photo shown as Fig. 72 (optimised for the lower surface).....	121
Figure 76 Lower and upper surface contours and relative extrema segmented. .	122
Figure 77 (a) Lower surface according from top to bottom as done by default by MATLAB. (b) Lower surface reorder in 8-connectivity along the direction given by the solute layer. The increasing pixel number is given according to the bottom colorbar.....	123

Figure 78 Variation in time of the overall bottom and upper surface of the dissolving hard candy.....	124
Figure 79 Evolution in time of the boundary of the dissolving hard candy block.	124
Figure 80 Distance calculated for each pixel of the lower surface with respect to the fixed line.....	126
Figure 81 A couple of details of Fig. 80.....	126
Figure 82 Evolution in time of the mean (lower) surface thickness. The red dotted line is the 1 st order approximated regression-rate.....	129
Figure 83 Evolution in time of the (lower) surface regression rate. The horizontal flex point corresponds to null regression acceleration. The horizontal red dotted line is the mean value.....	130
Figure 84 Evolution in time of the (lower) surface regression acceleration. The horizontal red dotted line is the mean value. The horizontal black line intersects the curve at the instant when the acceleration is null, which is the instant associated to the horizontal flex point in Fig. 83.	130
Figure 85 Evolution in time of the local regression rate along the coordinate of the body's lower surface cross-correlated interval.	132
Figure 86 Evolution in time of the frequency of the two harmonic carrier waves found through FFT of the local regression rate defined in the body's surface cross-correlated space interval.....	132
Figure 87 Evolution in time of the wavelength of the two harmonic carrier waves found through FFT of the local regression rate defined in the body's surface cross-correlated space interval.....	133
Figure 88 Evolution in time of the amplitude of the two harmonic carrier waves found through FFT of the local regression rate defined in the body's surface cross-correlated space interval.....	133
Figure 89 Evolution in time of the row position in the photos of the upper and lower horizontal side of the interrogation area. Be aware that the two photos are horizontally compressed.....	136
Figure 90 A generic front photo, with its rectangular interrogation area highlighted.	137

Figure 91 (Workable) spatial domain of the photo defined by the rectangular interrogation area.	137
Figure 92 Binarized domain of detected bubbles and bright defects.	139
Figure 93 Binarized domain of Fig. 92 shown superimposed on Fig. 91, with lower brighter bubble's part coloured in red and upper darker bubble's part coloured in blue.	139
Figure 94 Red pixels correspond to bubbles' lower and brighter part, blue pixels to bubble's upper and darker part, green pixels to restored and thus again workable pixels previously counted among the blue ones. Green pixels can be more easily noted on the top-left corner of the image.	140
Figure 95 Photo 'A'	141
Figure 96 Visualization of the effects of the aforementioned image subtraction. Obviously, in reality, the surface pattern in A is not so evident and is neither so thick in B.	141
Figure 97 Binarized photo highlighting the detected regions of surface patterns.	142
Figure 98 Surface pattern (coloured in red, green or blue) calculated through first derivation of the intensity value along the vertical direction.	143
Figure 99 Working directly on the pixel coordinates associated to surface patterns is not possible. In addition to being discontinuous coordinates, they may even cross each other.	145
Figure 100 Gaussian filtering of the patterns shown in Fig. 98.	146
Figure 101 Sets separated by only one black row are connected. (Only some are marked).	146
Figure 102 Sets separated by a maximum of three black columns are connected.	146
Figure 103 Detail of the calculated skeleton (in red) by thinning of furtherly-connected sets in Fig. 100 along the vertical direction.	147
Figure 104 Detail of the image obtained by furtherly-processed Fig. 98, 100, 103.	148
Figure 105 (a) A connected set. (b) A non-connected set made of connected components.	148

Figure 106 Connection of yellow subsets.	149
Figure 107 Horizontal lines approximating the surface patterns detected and connected thus far.	150
Figure 108 Vertical wavelength between surface patterns (approximated by horizontal lines) calculated by counting the peak-to-peak for each column. Adapted interrogation area in time.	151
Figure 109 Dispersed points indication the distribution along the rows of the photo of the vertical distance between two horizontal lines, which approximates the surface pattern.....	153
Figure 110 With respect to Fig.109, points outside the interval $\mu - \sigma, \mu + \sigma$ are not considered.....	153
Figure 111 Peaks of Fig. 110 distributed along the vertical direction (alias the row) of the photo.....	154
Figure 112 Interpolation of the peak-to-peak points (black) and its gaussian convolution (blue).....	154
Figure 113 Evolution in time of the distribution of the peak-to-peak distance between surface patterns along the vertical direction.	155
Figure 114 Detail of two photos taken at time instants t_1 and $t_2 = t_1 + 240$ s. The detail on the left and on the right is the same, while the detail in the middle is flipped horizontally to show the vertical displacement. The details are made of the same pixels of two different photos taken at different times at a fixed position. It is evident that the surface pattern advances upstream in time.	155
Figure 115 Cross-correlated peak-to-peak distances of the same upstream-advancing surface pattern superimposed on the distributed data shown in Fig. 113.	156
Figure 116 Algorithm used for determining the pixel-to-mm conversion factor.	157
Figure 117 Evolution in time of the thickness of a perfectly vertical dissolving hard candy block.....	161
Figure 118 Evolution in time of the thickness of a generic inclined hard candy block.	162
Figure 119 A generic curve showing the evolution of the regression rate in time.	163

Figure 120 The curve showing the evolution in time of the respective acceleration (parula-coloured) of the regression velocity shown in Fig. 119 and its mean value (red dotted).	164
Figure 121 Evolution in time of the regression rate of the lower surface of a block inclined.....	165
Figure 122 Detail of the graph of the spatial distribution of the regression rate shown in Fig. 85. Referred to the case of a block inclined $\alpha = 45^\circ$ without added salt to the water.	165
Figure 123 Evolution in time of the amplitude of the two harmonic carrier waves	166
Figure 124 Evolution in time of the amplitude of the two harmonic carrier waves	167
Figure 125 Evolution in time of the local regression rate of the upward pointing surface of a dissolved inclined block.	168
Figure 126 Evolution in time of the frequency of the main harmonic carrier wave of the signal (referred to the surface pointing upward) shown in Fig. 125.	168
Figure 127 Result from front photos for $\alpha = 30^\circ$ and no additional salt added in the water.	169
Figure 128 Result from front photos for $\alpha = 45^\circ$ and no additional salt added in the water.	170
Figure 129 Result from front photos for $\alpha = 60^\circ$ and no additional salt added in the water.	170
Figure 130 Result from front photos for $\alpha = 30^\circ$ and $S = 4.41 ppt$	171
Figure 131 Result from front photos for $\alpha = 45^\circ$ and $S = 4.41 ppt$	171
Figure 132 Result from front photos for $\alpha = 60^\circ$ and $S = 4.41 ppt$	172
Figure 133 Result from front photos for $\alpha = 30^\circ$ and $S = 8.82 ppt$	172
Figure 134 Result from front photos for $\alpha = 45^\circ$ and $S = 8.82 ppt$	173
Figure 135 Result from front photos for $\alpha = 60^\circ$ and $S = 8.82 ppt$	173
Figure 136 Four principal phases of the proposed physical mechanism behind scalloping.	176
Figure 137 Physical mechanism behind the upstream velocity of scallops.	178

Acknowledgment

Graduating really means a lot to me.

More than someone could imagine by reading this simple and short phrase.

And even if I have always worked hard, enjoyed the good moments, tried to keep the route in the bad ones, I am aware that the goal I am able to reach today is also thank to the always-supporting relatives and wonderful people, who I am very lucky respectively to have and have met.

Therefore, it is not only a will, but it is also a must taking the opportunity to thank all the people who supported me. And especially those who keep doing it.

My gratitude goes firstly to my family.

This work, together with my university career, would have never seen the light without my parents and my grandparents.

It is also right to thank all my other relatives who have always dedicated interest toward me and what I have been academically doing far from home.

My friends need a special acknowledgement for helping me to live life to the fullest.

Last but not least, I would thank all the experts in the field that helped me to grow. I would like to thank Prof. Stefania Scarsoglio and Professor Sander Gerard Huisman for their huge help and support behind the present work.

I would also like to thank Prof. Daniela Tordella, who even if did not provide direct support for the present thesis, with her lessons out of the ordinary, helped me in understanding which path I want to follow in my future.

I would like to thank everyone of the support staff of the *Physics of Fluids* group of the *University of Twente*, both for their technical support with the experimental setup, and for the bureaucracy with the international documents.

I would like to thank Prof. Marco Amabili. Without him, this could have been a physics, and not an engineering, master's degree thesis.

In conclusion, dear reader, if you are reading the present line after reading the previous pages, you certainly deserve a special thanking too.

Ringraziamenti

Laurearsi significa molto per me.

Più di quanto chiunque possa immaginare, leggendo questa semplice frase.

Ed anche se ho sempre lavorato a testa bassa, ho goduto dei bei momenti ed ho provato a mantenere la rotta in quelli difficili, sono consapevole che il traguardo che sono in grado di raggiungere oggi è anche grazie ai miei parenti ed alle meravigliose persone che sono molto fortunato di avere e di aver conosciuto.

Pertanto, non è solo una volontà, ma è anche un dovere cogliere ora l'opportunità per ringraziare tutte le persone che mi hanno supportato. E specialmente coloro che continuano a farlo.

La mia gratitudine va anzitutto alla mia famiglia.

Questo lavoro, insieme alla mia carriera universitaria, non avrebbe mai visto la luce senza i miei genitori ed i miei nonni.

È anche doveroso ringraziare tutti i restanti parenti, che hanno sempre dedicato interesse nei miei confronti.

Anche i miei amici necessitano un ringraziamento speciale, per avermi aiutato con la loro compagnia a vivere la vita a pieno.

A seguire, ma non per importanza, vorrei ringraziare tutti gli esperti del campo che mi hanno aiutato e permesso di crescere.

Vorrei ringraziare la Professoressa Stefania Scarsoglio ed il Professor Sander Gerard Huisman per il loro incalcolabile aiuto e supporto fornitomi per il presente lavoro.

Vorrei anche ringraziare la Professoressa Daniela Tordella, che sebbene non mi abbia supportato direttamente nella tesi, con le sue lezioni fuori dall'ordinario, mi ha aiutato a comprendere quale strada voglio seguire nel mio futuro.

Vorrei ringraziare tutto lo staff tecnico del *Physics of Fluids group* dell'Università di Twente. Sia per il loro supporto tecnico per gli esperimenti, sia per le commissioni burocratiche con i documenti internazionali.

Vorrei anche ringraziare il Professor Marco Amabili. Senza di lui, probabilmente questa sarebbe stata oggi una Tesi di Laurea in Fisica e non in Ingegneria.

